Title
Microenvironmental Cues Driving CD44-mediated Glioblastoma Invasion through Hyaluronic Acid-rich Matrix

Author
Wolf, Kayla Janean

Publication Date
2020

Peer reviewed|Thesis/dissertation

Microenvironmental Cues Driving CD44-mediated Glioblastoma Invasion through Hyaluronic Acid-rich Matrix

By

Kayla Janean Wolf

A dissertation submitted in partial satisfaction of the

requirements for the degree of

Joint Doctor of Philosophy

with University of California, San Francisco

in

Bioengineering

in the

Graduate Division

of the

University of California, Berkeley

Committee in charge:

Professor Sanjay Kumar, Chair
Professor Tamara Alliston
Professor Matthew Welch

Spring 2020

Abstract

Microenvironmental Cues Driving CD44-mediated Glioblastoma Invasion through Hyaluronic Acid-rich Matrix

by

Kayla Janean Wolf

Joint Doctor of Philosophy in Bioengineering
with University of California, San Francisco

University of California, Berkeley

Professor Sanjay Kumar, Chair

Interactions between tumor cells and the extracellular matrix (ECM) play a critical role in tumor invasion. Glioblastoma (GBM) is a highly malignant primary brain cancer characterized by diffuse infiltration, with tumor cells invading slowly through the hyaluronic acid (HA)-rich parenchyma toward vascular beds and then migrating rapidly along microvasculature rich in collagen, fibronectin, and laminin. Nonetheless, little is known about how cells navigate nonfibrillar 3D matrices, such as the HA-rich brain parenchyma, or how plasticity in cell migration modes between intraparenchymal and perivascular spaces influences invasion. Progress in understanding local infiltration, vascular homing, and perivascular invasion is further limited by the absence of culture models that recapitulate these hallmark processes. The transmembrane receptor CD44 directly facilitates tumor cell invasion by engaging HA in brain matrix and is therefore a likely candidate for mediating invasive plasticity.

In this dissertation, we investigate how topographical cues in the perivascular niche instruct cell invasion modality and how CD44 coordinates with the cytoskeleton to facilitate invasion through HA-rich matrices. We first describe the development of a platform for GBM invasion consisting of a tumor-like cell reservoir and a parallel open channel “vessel” embedded in the 3D HA matrix. We show that this simple paradigm is sufficient to capture multi-step invasion as well as transitions in cell morphology and speed reminiscent of those in GBM. Tumor cells within the model grow into multicellular masses that expand and invade the surrounding HA-rich matrices while extending long (10–100 μm), thin protrusions before encountering the open channel. We then assess how HA signals arise in vivo and how these signals are generally incorporated into in vitro models to mechanistically investigate HA-mediated motility. Finally, we employ our HA hydrogel platform to probe the role of CD44 in cytoskeletal motility. We show that continuous and patient-derived GBM tumor cells interacting with both 2D and 3D HA substrates exploit CD44-based microtentacles (McTNs) to support cell migration. These McTNs are stabilized by a balance between microtubule-driven protrusion and

actomyosin-driven retraction, which are mechanistically coupled by an IQGAP1-CLIP170 complex. Cells approaching vascular structures transition from McTN-based motility to a quasi-2D mesenchymal motility involving actomyosin bundles. McTN-driven motility and/or the transition to mesenchymal motility may represent an important new target for GBM discovery and therapeutics.

This dissertation is dedicated to Isaac

and to Zeke.

Table of Contents

Acknowledgements

I sincerely thank the many people that have given direction, shared technical expertise, and provided personal support throughout my graduate work.

I especially thank my graduate advisor, Professor Sanjay Kumar. I hold the highest respect for Sanjay on both a scientific and personal level and am deeply grateful for his mentorship. Throughout my graduate career, Sanjay has been an active advocate for my scientific training and provided me numerous opportunities to learn through research projects, meetings, writing, and collaborations. Sanjay has consistently prioritized his students' best interests, and this has profoundly impacted my experience for the better. I have truly enjoyed working with Sanjay and hope to carryon even a few of his merits into my future endeavors.

I also sincerely thank the members of my qualifying exam and dissertation committees, including Professor Tamara Alliston, Professor Mohammad Mofrad, Professor Matt Welch, and Professor Phil Messersmith for sharing their expertise end encouraging me to think critically as a scientist. Thank you also to Professor Amy Herr for teaching me how to teach as a graduate student instructor. I appreciate the time that each of these professors has invested in my training and am grateful to have worked with such outstanding people.

Furthermore, I have had the great honor of working with a phenomenal group of labmates, who have brightened even the longest days with their camaraderie. I am incredibly grateful to the past members of the lab for their mentorship (Andy Rape, Badri Ananthanarayanan, Joe Chen, Jason Coombes, Yushan Kim, Elena Kassianidou, Jess Lee, George Lin, Jasmine Hughes, Mike Kang, Stacey Lee, and Phil Kang) and present members for their collegiality (Jieung Baek, Junghwa Cha, Ruoxing Lei, Andy Lopez, Eric Qiao, Emily Carvalho, Erin Akins, Kwasi Amofa, Vivien Tran, and Erika Ding). I have also been privileged to work with an excellent group of rotation students (Callie Jerman, Kwasi Amofa, María Díaz de León Derby, and Charlene Pan), master's students (Julia Lanoha and Jonathan Evans), and undergraduate students (Brian Shing, Caleb Choy, Casey Kraft, Gokul Kannan, and Poojan Shukla). Thanks especially to Kelsey Springer and Katherine Patterson for keeping the lab running and all of us safe. Finally, thank you to my peers in the graduate program, particularly Christina Fuentes, Shaheen Jeeawoody, Sally Winkler, and Xinyi Zhou for sharing both professional insights and deep friendships marked with many lunches.

Lastly, I express my unending gratitude to my family. Thanks to my dad for teaching me to be a farmer, scientist, and engineer long before graduate school. I am grateful for his example and miss him every day. Thank you to my mom for being my greatest cheerleader and always sharing genuine joy over my accomplishments, big and small. My mom has been the epitome of resilience and is an inspiration. Thank you to my husband for challenging me to take risks, encouraging me to learn from failure, and celebrating successes. I am ever grateful for his love, support, and creative sense of humor.

Chapter 1. Dissecting and rebuilding the glioblastoma microenvironment with engineered materials

Parts of this chapter are excerpted with permission from Springer Nature, from the article "Dissecting and rebuilding the glioblastoma microenvironment with engineered materials," by Kayla J. Wolf, Joseph Chen, Jason D. Coombes, Manish K. Aghi, and Sanjay Kumar in *Nature Reviews Materials*, 4, 651-668 (2019).

1.1 Abstract

Glioblastoma (GBM) is the most aggressive and common form of primary brain cancer. Several decades of research have provided great insight into GBM progression; however, the prognosis remains poor, with a median patient survival time of ~15 months. The tumor microenvironment (TME) of GBM plays a crucial role in mediating tumor progression and thus is being explored as a therapeutic target. Progress in the development of treatments targeting the TME is currently limited by a lack of model systems that can accurately recreate the distinct extracellular matrix composition and anatomic features of the brain, such as the blood–brain barrier and axonal tracts. Biomaterials can be applied to develop synthetic models of the GBM TME to mimic physiological and pathophysiological features of the brain, including cellular and extracellular matrix composition, mechanical properties and topography. In this Review, we summarize key features of the GBM microenvironment and discuss different strategies for the engineering of GBM TME models, including 2D and 3D models featuring chemical and mechanical gradients, interfaces and fluid flow. Finally, we highlight the potential of engineered TME models as platforms for mechanistic discovery and drug screening, as well as preclinical testing and precision medicine.

1.2 Introduction

Glioblastoma (GBM) is the most common and aggressive primary central nervous system tumor, with a devastatingly low median patient survival of 15 months[1,2]. Glioblastoma (GBM) comprises 47.7% of all malignant primary central nervous system tumors with a 5 year patient survival of 5.6%.[1] About 95% of patients are diagnosed after age 40 (median age = 65), and no genetic predispositions are known.[3] GBM driver mutations can be traced to astrocyte-like neural stem cells in the subventricular zone[4]; notably, targeting radiotherapy towards the subventricular zone improves patient outcome.[5,6] Primary GBM tumors arise de novo and account for 90% of cases, whereas secondary tumors arise from lower-grade gliomas and account for 10% of cases.[7] Secondary tumors are typically diagnosed in younger patients (mean age = 45 years) and correlate with longer survival.[1,7] Patients with both primary and secondary tumors typically present symptoms of increased intracranial pressure, such as headaches, neurological defects and seizures.[8] The diagnosis of GBM is based on the presence of several histological features including anaplasia, mitotic activity, microvascular proliferation and necrosis.[9] Isocitrate

dehydrogenase (IDH)-mutant status correlates with secondary GBM and better prognosis, possibly because IDH mutation increases genome-wide methylation.[10,11]

Standard treatment consists of surgical resection, followed by chemotherapy and radiotherapy[12]. Surgical resection provides clinical relief, enables tissue acquisition for diagnostic analysis and increases survival.[13] However, GBMs exhibit a diffuse invasion pattern, in which tumor cells either migrate individually or collectively infiltrate healthy tissue beyond the tumor margin[14], making complete surgical resection virtually impossible[13]. Surgical resection must be balanced with the need to preserve precious, intact tissue. Radiotherapy protocols cover a 2 cm margin beyond the visible tumor margin; however, microscopic tumor invasion may spread beyond this distance[15]. Since 2005, alkylating-agent temozolomide (TMZ) combined with radiotherapy has become the standard-of-care for newly diagnosed GBM.[12,16] Methylation of the promoter necessary to express O^6-methylguanine methyltransferase (MGMT), a DNA excision repair enzyme, suppresses reversal of TMZ-induced DNA damage and correlates with increased survival.[17] Despite initial efficacy, tumors ultimately acquire therapeutic resistance and recur.[18] Nitrosureas or a combination of procarbazine, lomustine and vincristine are second-line treatments owing to their higher toxicity and poorer efficacy compared to TMZ.[19,20] Bevacizumab, an antibody-based antiangiogenic therapy, which normalizes the vasculature, was FDA-approved for recurrent GBM in 2009, but was ultimately ineffective at treating GBM in randomized clinical trials.[21–24] Steroids, specifically dexamethasone, are prescribed throughout treatment to ameliorate peritumoral edema and discomfort.[13]

Infiltrating tumor cells are enriched with glioblastoma stem cells (GSCs), which are tumor cells characterized by their ability to recapitulate the vast heterogeneity of GBM cell phenotypes through propagation and differentiation[25]. GSCs are often highly refractory to chemotherapy, driving tumor recurrence and chemoresistance[18]. The tumor microenvironment (TME), which contains extracellular matrix (ECM), interstitial fluid and various stromal cells (for example, astrocytes, macrophages and endothelial cells), is a key regulator of tumor progression[26]. Substantial advances have already been made in understanding microenvironmental contributions to the progression of other cancers, particularly breast cancer[27–30] and pancreatic cancer[31,32]. Therefore, new therapies have also been developed to target the GBM TME[33,34].

Unique features of the brain TME include the blood–brain barrier (BBB), the presence of myelinated and interconnected axon tracts, and a distinct ECM composition, all of which pose specific challenges for treatment[26,35,36]. The BBB, even after losing integrity during tumor progression, is impassable for most chemotherapeutics[37] and is especially impermeable in the actively invading tumor regions, where the BBB is intact[38]. Haptotactic cues from the vascular basement membrane and enrichment of vascular-derived chemotactic cues further drive cell invasion and therapeutic resistance of tumor cells in the perivascular space[35]. Interconnected axon tracts also provide haptotactic cues for cellular invasion and represent a major barrier to surgical resection[39,40]. Furthermore, in contrast to other solid tissues, brain ECM is particularly soft (300–3,000 kPa)[41,42], lacks collagen fibers and is rich in hyaluronic acid (HA), tenascins and chondroitin sulfates[36].

Interestingly, GBMs rarely intravasate and metastasize from the brain, possibly owing to early patient mortality or the unique features of the brain TME[43].

Investigations of TME–tumor interactions are limited by a lack of model systems that accurately represent the human brain microenvironment. Biomaterials and engineered devices offer the possibility to recreate brain-like TMEs, enabling mechanistic discovery and therapeutic screening in environments that mimic tissue more closely than traditional 2D culture paradigms. For example, standard tissue culture plastic and reconstituted basement membrane preparations lack design flexibility and fail to capture key compositional, structural and mechanical features of the brain TME[44–46]. Furthermore, engineered TME models can be tailored to incorporate patient-derived cells and matrix, offering a route towards precision medicine. In this Review, we summarize how the TME drives GBM progression, describe potential therapeutic targets and investigate designs and applications of engineered TME models in research and the clinic. Finally, we outline new directions for designing, fabricating and employing engineered models in patient care.

1.3.1 Glioblastoma microenvironment

The TME provides a dynamic array of signals that drive proliferation, invasion and resistance **(Fig. 1)**. These signals can be broadly categorized into ECM composition, ECM mechanics, topographical cues, interstitial fluid and stromal-cell interactions (Table 1).

TABLE 1. Key signals in the tumor microenvironment.

Signal type	Signal	Signalling effects	Effect on tumor progression	Refs.
Matrix composition	HA	GBM cells increase HA synthesis and degradation	Low MW HA accumulates and promotes GBM cell invasion, GSC stemness and GSC resistance	47–56
	Fibronectin	GBM cells decrease fibronectin expression and crosslinking	Invasion and sensitivity to therapy increase	57–60
	Tenascin C	GBM cells express more tenascin C	Tenascin C increases matrix stiffness and GBM cell invasion and proliferation	61–63
	Laminin	GSCs interact with laminin	GSCs show increased stemness, invasion and proliferation	57,64–66
Matrix mechanics	Elastic modulus	Elastic modulus increases in pseudopalisades and decreases in necrotic core compared to healthy tissue	Increased modulus promotes GBM cell migration and proliferation in vitro	67–75
	Density	GBM cells produce more matrix than non-tumor cells	High matrix density decreases perfusion and	76,77

			increases ECM compaction and cell damage	
Topography	Microvasculature	Tumors exhibit hypervascularity with loss of BBB integrity and change in basement membrane composition	Tumor cells invade rapidly along vasculature	[78,79]
	Myelinated tracts	GBM cells remodel myelin coating	GBM cells invade rapidly along myelinated tracts	[80–84]
Interstitial fluid	Pressure	Tumors exhibit edema	Pressure from edema is a barrier to chemotherapy	[85,86]
	Fluid flow	Convection-enhanced therapy increases flow rates	Fluid flow promotes invasion and proliferation	[87–92]
Stromal and endothelial cell crosstalk	TAMs	GBM-derived osteopontin recruits and maintains TAM phenotype; TAMs secrete complex array of cytokines and growth factors	Immune activity (from cytotoxic T cells) increases; growth factors increase GBM proliferation, survival and migration	[93,94]
	TAAs	GBM cells activate TAAs; TAAs activate tumor cell MMP and uPA expression	Intratumoral immune response decreases; GBM invasion increases and cells become more chemoresistant	[95]
	Vascular endothelial cells	Vascular endothelial cells secrete IL-8	GSC migration, proliferation and stemness increase	[96]
	Neurons	Neurons secrete neuroligin-3	GBM proliferation increases	[97]
	MSCs	MSCs provide exosome cargo such as miR-1587 and secrete IL-6	GSCs proliferation and tumor cell survival increase	[98,99]

GBM, glioblastoma; GSC, glioblastoma stem cell; HA, hyaluronic acid; IL, interleukin; miR, microRNA; MMP, matrix metalloprotease; MSC, mesenchymal stem cell; MW, molecular weight; TAA, tumor-associated astrocyte; TAM, tumor-associated macrophage, TME, tumor microenvironment; uPA, urokinase-type plasminogen activator; ECM, extracellular matrix.

1.3.2 Extracellular Matrix

Normal brain ECM, in contrast to the ECM of other solid tissues, is enriched in glycoproteins, such as tenascins and link proteins, glycosaminoglycans (GAGs), such as HA, and proteoglycans, such as aggrecan, neurocan, versican and phosphacan[100]. Conversely, fibrillar proteins, such as collagen and fibronectin, are relatively sparse[47]. In tumors, the abundance of ECM components is altered; in particular, the level of GAGs is increased by 3–4-fold[101]. Astrocytes and oligodendrocytes produce the majority of brain ECM in normal tissue, but GBM cells also express their own pro-invasive matrix[35,102]. GBM cells can also induce stromal cells to express specific ECM components. In highly angiogenic tumors, tumor cells overexpress tenascins and vitronectin, and stromal cells produce excess laminin, fibronectin and collagen IV[103].

HA, a polyanionic GAG localized primarily in the intraparenchymal region, is the most abundant component of brain ECM[47]. Expressed as a megadalton linear chain in healthy tissue, HA regulates tissue mechanics, organization and hydration. HA also activates cellular signalling through surface receptors such as CD44 and receptor for hyaluronan-mediated motility (RHAMM)[104,105]. The differential signal transduction and functional contributions of CD44 and RHAMM remain incompletely understood; however, it is known that both receptors can drive invasion[48,49,54]. Both tumor and stromal cells produce HA in high-grade gliomas and GBMs overexpress hyaluronan synthase 2 (HAS2)[50,51,55]. Whether downstream signals arising from HA–receptor interactions are pathologic is determined by the molecular weight of HA; low-molecular-weight HA provides pro-invasive cues and high-molecular-weight HA reduces tumor invasion[52,53]. Accordingly, GBM spheroids are less invasive in 3D matrices crosslinked with 500 kDa HA than with 60 kDa or 10 kDa HA[56]. The crucial role of HA in GBM progression motivates the investigation of the effects of the molecular weight, mechanical properties and signalling of HA in engineered TME models.

Laminin, fibronectin and collagen IV are mainly localized in vascular basement membranes[36,106]. Laminin has been shown to be particularly potent in driving GBM progression; however, downstream signalling mechanisms may be isoform specific[107]. For example, in a zebrafish model, laminin α5 increases the formation of blood-vessel-dependent tumors but reduces the migration speed of GBM cells[64]. In human cell culture models, laminin α2 supports GSC growth[66] . Interestingly, GSCs are often propagated on laminin-coated culture dishes, and laminin-binding integrin α6 is necessary for GSC renewal, proliferation and tumor formation[65]. By contrast, fibronectin expression is often decreased in GBMs[57]. Fibronectin assembly reduces GBM cell migration and fibronectin depletion increases migration[58,59]. Pharmacological disruption of fibronectin assembly in orthotopic mouse models also sensitizes tumors to chemotherapy[60]. Thus, assembled fibronectin may inhibit GBM cell invasion but may also reduce the efficacy of chemotherapy. Whether targeted disruption of fibronectin would advance or counteract therapeutic goals remains unclear. Fibrillar collagens, such as collagen I, are not abundant in normal brain tissue; however, non-fibrillar collagen IV is present in basement membranes of the brain vasculature[108,109]. Despite widespread use in engineered TME models[44,46], the role of parenchymal collagen in GBMs in vivo is unclear. Evidence suggests that the structural organization of collagen has an influence on GBMs; accumulation of punctate or non-fibrillar collagen can be correlated with a more invasive phenotype than accumulation of organized fibrillar collagen, which may structurally impede parenchymal invasion[110].

The brain also contains matricellular proteins, which regulate tissue structure and tumor invasion[100]. Tenascin C, which is a large (180–250 kDa) glycoprotein that crosslinks matrix, is particularly important in GBM progression[111,112]. Aggressive gliomas are enriched in tenascin C, which correlates with poorer patient prognosis[63]. Interestingly, glioma ECM stiffness also corresponds with levels of tenascin C but not with levels of type I collagen abundance, vascularity or tumor cell density[63]. Tenascin C further participates in cell–cell crosstalk. Tumor-cell-derived tenascin C interacts with α5β1 and

αvβ6 integrins on T lymphocytes, resulting in reduced mTOR signalling and immunosuppression[62]. Additionally, the presence of tenascin C in collagen I matrices leads to an increase in matrix metalloproteinase (MMP)-12-mediated GBM invasion[61]. Other matricellular proteins, notably agrin, insulin-like growth factor-binding protein (IGFBP) 7 and secreted protein acidic and rich in cysteine (SPARC), are dysregulated in GBM vascular basement membranes, which may contribute to the disruption of the BBB and angiogenesis[78,79]. The matricellular protein osteopontin (Spp1) is further implicated in promoting GBM therapeutic resistance. Osteopontin affects the permissiveness of the TME and maintains the stemness of GSCs through CD44-dependent signalling in the perivascular space[113–115].

The expression of these different ECM components is highly intertwined. For example, silencing uridine diphosphate-glucose 6-dehydrogenase (UGDH), which is an enzyme required for GAG monomer synthesis, results in decreased GAG production and abundance of tenascin C and brevican, leading to a reduction of tumor growth and migration in animal models[116]. Therefore, dissecting the complexity of matrix composition in engineered TME models may uncover targetable drivers of GBM progression.

The mechanical properties of the tumor ECM, for example, matrix density and bulk storage modulus, also play an important role in GBM progression. Like most tumors, GBMs also exhibit an elastic modulus almost twice that of normal tissue, possibly owing to changes in ECM expression and increased compaction[67,68]. However, the elastic modulus varies strongly by region, with a lower modulus observed in necrotic regions (~0.1 kPa) than in the hypercellular core (~10 kPa) and a higher modulus observed in the hypercellular core compared with healthy tissue (1 kPa)[69]. Notably, GBM cell proliferation and migration is mechanosensitive[70,75], although the degree of mechanosensitivity varies between patients[71]. The mechanosensitivity also differs between tumor cell subpopulations, and some GSCs lack mechanosensitivity[72,117]. High matrix modulus (6.9 kPa compared with 0.15 kPa) induces CD44-dependent cell migration and spreading on HA[74]. High matrix modulus (119 kPa compared with 0.08 kPa) also amplifies epidermal growth factor receptor (EGFR) signalling, promoting proliferation[73]. Matrix density is also higher in GBMs than in healthy brain tissue, perhaps owing to compaction caused by matrix overexpression and high cell density. Compaction of GBM cells in vitro further induces expression of collagen IV and VI, vascular endothelial growth factor (VEGF) and the collagen-crosslinking enzyme lysyl oxidase, which is associated with an increase in angiogenesis and matrix elastic modulus[77]. The growing tumor mechanically compresses tissue, damaging neurons and restricting vascular perfusion[76]. GBM ECM remodelling progresses as a positive feedback loop in which tumor cell proliferation and ECM production cause an increase in elastic modulus, which, in turn, further promotes tumor cell proliferation and invasion.

1.3.3 Tumor-stroma interactions

GBM cells most rapidly invade along anatomical tracks, such as the vasculature and myelinated axons[36,40] **(Fig. 1c,d,e)**. As GBM cells invade through the perivascular space

along the vascular basement membrane, they disrupt astrocytic end feet contacts with endothelial cells and weaken the BBB[118] **(Fig. 1e)**. A combination of haptotactic, chemotactic and topographic cues are likely responsible for this pattern of invasion. Many integrin-binding matrix proteins, such as laminin, collagen and fibronectin, are localized at the vascular basement membrane and are relatively sparse in other brain regions[36,106]. Basement membranes have a higher elastic modulus than the surrounding matrix, which may promote a mechanosensitive, integrin-mediated migration[119]. The perivascular space is also rich in paracrine signals from perivascular support cells, as well as nutrients crossing the BBB[120]. The detailed mechanisms of invasion along myelinated axon tracts remain elusive thus far; however, MMP-mediated remodelling of myelin from a non-adhesive to an adhesive substrate is likely involved[81–83,121]. GSCs that migrate along remodelled or deteriorating white-matter tracts gain access to the Notch ligand Jagged1 on exposed nerve fibers, which further promotes invasive growth[84]. Culturing GBM cells on engineered surfaces with linear topographies shows that linear presentation of ECM cues strongly affects migration speed. The resulting constraint and alignment of actin bundles, as well as cytoskeletal polymerization, coordinate rapid, persistent migration[122,123].

Solid tumors exhibit an abnormally high interstitial fluid pressure and volume, mainly owing to leaky vasculature[85,86]. Interstitial fluid flow is most rapid along axon tracts and in perivascular spaces, promoting the distribution of soluble cues, for example, pro-angiogenic factors[87]. Rapid flow in parallel with white-matter tracts leads to an increase in the invasion speed of tumor cells, possibly owing to shear stress or to effects on soluble cue gradients[88]. In vitro and in vivo studies show that interstitial fluid flow promotes migration mediated by the C-X-C chemokine receptor type 4 (CXCR4) receptor and, to a lesser degree, by CD44–HA interactions[89,91,92]. The composition of interstitial fluid substantially varies by tumor region. Lack of dissolved oxygen (hypoxia) and low pH are characteristic of interstitial fluid in the tumor core, which perpetuates necrosis and drives tumor cells towards invasive and pro-angiogenic phenotypes[124]. The high interstitial fluid pressure (IFP) in solid tumors is a major barrier to chemotherapeutic delivery because it prevents the transport of small molecules into the tumor core[86]. Some therapeutic treatments cause a decrease in IFP, which could improve the therapeutic efficacy and reduce oedema. In particular, treatment with bevacizumab in orthotopic GBM models causes a reduction in IFP by ~73%, likely owing to a normalization of the vascularity[24] (Box 1). The importance of interstitial fluid in GBM is well established; however, therapeutic interventions to target interstitial fluid are limited.

Tumor cells and stromal cells in the TME co-evolve during tumor progression. Immune and inflammatory cells, such as infiltrating monocytes and fibroblasts, endothelial cells and glioma-associated mesenchymal stem cells (MSCs), which are located throughout the tumor and in the intraparenchymal region, interact with tumor cells, driving disease progression **(Fig. 1)**. Tumor cells also interact with other intraparenchymal stromal cells, such as astrocytes, pericytes, oligodendrocytes and neurons. A common and crucial function of these non-tumor cells is to secrete signals that modulate tumor cell survival, proliferation and migration. For example, MSCs secrete exosomes and soluble cytokines, such as interleukin-6 (IL-6), which interact with GSCs, increasing their proliferation and

stemness[98,99]. Tumor-associated astrocytes (TAAs) release secreted factors that support tumor cell survival and proliferation, modulate the intratumoral immune response and promote invasion by activating tumor-derived matrix-remodelling enzymes, including MMPs and urokinase-type plasminogen activator (uPA)[95]. GBM cells also extensively interact with microglia and infiltrating tumor-associated macrophages (TAMs) to suppress an antitumor immune response[93,94,114]. Neurons promote proliferation of GBM cells through secretion of soluble factors such as neuroligin-3[97]. Tumor cells also closely interact with vascular endothelial cells (Fig. 1c,e). For example, endothelial cells secrete IL-8 and GSCs upregulate IL-8 receptors, which stimulates migration, growth and stemness[96]. Tumor cells can further directly participate in vessel mimicry by aligning with endothelial cells to form vascular walls or by transdifferentiating into endothelial cells[125,126]. Therefore, the incorporation of the stromal secretome in engineered TMEs is important, owing to its crucial role in regulating tumor cell behaviour, particularly in the context of immunotherapy.

1.4.1 Targeting the microenvironment

The TME substantially changes over time and in the different microregions, particularly during therapeutic treatment. Magnetic resonance imaging (MRI) scans of newly diagnosed patients typically reveal a contrast-enhancing, irregularly shaped GBM tumor border with pseudopalisades or regions of high cell density, surrounding a hypointense region of necrosis[8] (Fig. 1a,b). Necrotic cores are thought to arise once the tumor cell density exceeds a certain threshold at which the cells can no longer be supported by diffusion-based transport of nutrients, gases and metabolites from deteriorating or occluded vasculature. As cells migrate away from hypoxic regions, pseudopalisades form and recruit new vasculature[127] (Fig. 1b,c). As the tumor grows and invades, the adjacent tissue deteriorates (Fig. 1d,e). Neurodegeneration is caused not only by mechanical stresses[76] but also by aberrant levels of tumor-secreted soluble factors, such as the extracellular domain of CD44[128]. Surgical resection of >98% of the gross tumor, including necrotic and pseudopalisading regions, increases overall patient survival[129]. Metabolic, fluorescent dyes can be employed during surgery to improve the identification of the tumor edge, although the clinical benefit is not yet clear[130]. Carmustine-releasing Gliadel wafers can be implanted following surgical resection and may especially benefit patients for whom gross resection is unfeasible; however, the efficacy and safety of this approach remain controversial[131,132]. Tumor-treating fields (alternating electric fields) that disrupt mitosis may also improve patient survival[133,134].

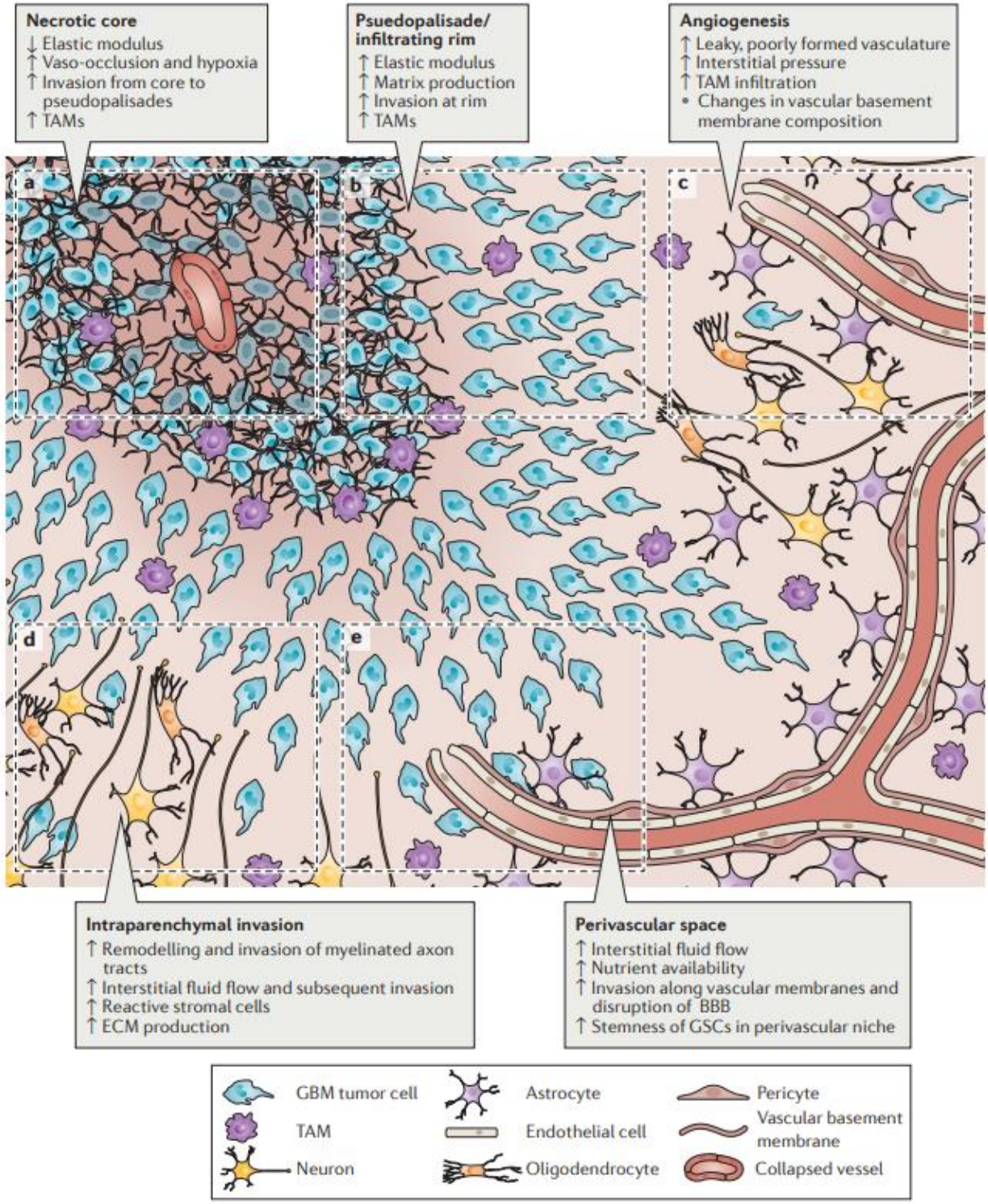

Figure 1. **Schematic of gliobastoma (GBM) regions.** This GBM schematic illustrates changes during tumor progression in the different microenvironmental regions. a) The necrotic core is softer than surrounding tissue and is thought to form after increases in cell density beyond a certain threshold or vaso-occlusive events result in hypoxia. b)

Psuedopalisades are regions of high cell density thought to form as cells migrate away from hypoxic regions. These zones have an increased elastic modulus and matrix production compared to healthy tissue and necrotic regions. GBM cells invade from the outer edge of the cell-dense tumor into healthy tissue at the infiltrating rim. c) GBM tumors show hypervascularity with increased angiogenesis compared to healthy brain tissue. Tumor-associated vasculature is poorly formed, leaky and leads to an increase in interstitial fluid pressure. d) Tumor cells invading through the parenchyma often follow and remodel the surface of myelinated tracts – a region in which high interstitial fluid flow may also drive invasion. e) Tumor cells rapidly invade the vasculature, where they are exposed to nutrients, high interstitial fluid flow and haptotactic cues in basement membranes. The perivascular niche also supports stemness and survival of glioblastoma stem cells (GSCs). TAM, tumor-associated macrophage; ECM, extracellular matrix; BBB, blood-brain barrier.

1.4.2 Glioblastoma stem cell niches

The resection of diffusely invading cells beyond the gross tumor edge poses risks of destroying functional tissue. Even if resection is performed beyond the tumor edge, there is no assurance that all tumor cells can be located and resected5. The clinical need for therapies targeting the remaining tumor cell population has motivated the investigation of how the TME promotes survival, invasion and proliferation of diffusely infiltrating tumor cells. GSCs are especially adept at invading healthy tissue and resisting chemotherapy and radiotherapy, which makes them a key candidate for targeted adjuvant therapies. GSCs reside within specific anatomic niches, which are specialized microenvironments that regulate GSC stemness, proliferation and apoptosis resistance, analogous to tissue stem cell niches[120,135–137]. Importantly, these niches shield GSCs from anticancer therapies by providing pro-survival cues and by anatomically blocking them from therapy exposure[138]. Four unique zones (subarachnoid, perineuronal, perivascular and perinecrotic) have, thus far, been identified that support GSC self-renewal and proliferation[137]. Each zone has a distinct TME composition with niche-specific transcriptional and epigenetic signatures[136,137].

The contributions of the perivascular niche to therapy resistance, infiltration spread and disease progression are perhaps best understood[120,135,139–141]. In the perivascular niche, GSCs and the TME engage in cooperative signalling, promoting neovascularization and GSC maintenance. The leaky vasculature provides access to nutrients, and the endothelium activates Notch-dependent pathways that promote GSC self-renewal and therapy resistance[142]. In turn, GSCs support neovascularization by secreting angiogenic factors such as VEGF[143]. Interestingly, endothelial-derived nitric oxide increases the tumor-initiating capacity of the platelet-derived growth factor receptor (PDGFR)-expressing subset of GSCs[144]. Matrix composition and mechanics of the perivascular niche also drive GSC tumorgenicity[120]. In particular, HA regulates GSC stemness by engaging the HA-specific cell surface receptors RHAMM[145] and CD44 and by activating the transcription of stemness modulators[146]. HA also activates the Toll-like receptor (TLR)

4–nuclear factor (NF)κB pathway to promote stemness; the expression of TLR4 receptors is upregulated during GSC differentiation along with HA synthesis, which increases NFκB activity and suppresses terminal GSC differentiation[147]. Furthermore, altered mechanotransduction caused by niche remodelling stimulates GSC tumorgenicity[148]. For example, a pro-tumorigenic glycocalyx–integrin feedforward loop, in which ECM stiffening induces a mesenchymal transition in GSCs, drives GBM progression correlated with poor prognosis[149–152]. In a brain-mimetic biomaterial platform for the 3D culturing of patient-derived GBM cells, the modulation of both the HA content and of the mechanical properties of the biomaterial are required to recreate the known resistance of GBM cells to the EGFR inhibitor erlotinib, highlighting that the TME can diminish therapeutic efficacy[153].

Although less understood, hypoxic GSC niches also substantially contribute to the maintenance of GSC populations[124,154,155]. Hypoxic niches arise when defective vessels are obstructed or collapse, which leads to a reduction in oxygenation[155]. Cells adapt to low oxygenation by activating hypoxia-inducible factors (HIFs)[124]. Activation of HIF-1α promotes GSC self-renewal and growth and causes pro-invasive protein expression through upregulation of CXCR4, which is a chemokine receptor related to increased migration[154]. Similarly, HIF-2α promotes the expression of Oct4, which is a stem cell marker strongly associated with stemness[156]. Interestingly, HIF-2α is specifically expressed by GSCs and, thus, may serve as a potential GSC-specific marker[156]. Hypoxia may even promote the reprogramming of non-stem GBM cells towards a GSC-like phenotype[156]. Therefore, TME niches play a multifaceted role in regulating GSCs, motivating their investigation in engineered TME models.

1.4.3 Microenvironmental changes

Radiotherapy increases overall patient survival by reducing tumor burden and by improving BBB permeability for chemotherapeutics; however, radiotherapy also triggers the remodelling of the TME, which increases the aggressiveness of tumors at recurrence[157]. In response to radiation, TAMs infiltrate the tumor through the defective BBB and astrocytes adopt a reactive phenotype, which induces tissue inflammation[157]. Moreover, in contrast to bulk tumor cells, GSCs are particularly efficient at evading radiotherapy by activating DNA damage checkpoints to repair DNA damage[158]. The TME promotes tumor cell survival during radiation treatment; for example, in a co-culture of GSCs with astrocytes, signal transducer and activator of transcription 3 (STAT3), signalling is activated in GSCs in response to astrocyte-secreted factors, which increases GSC radiation resistance[159]. Radiation further temporarily induces senescence in GBM cells by triggering a ‘senescence-associated secretory phenotype’, which leads to upregulation of ECM expression, proteolytic enzymes and pro-inflammatory signalling molecules[157]. After exiting senescence, these cells and their microenvironments are primed for invasion and proliferation. GBM cells increase HA production in response to radiation by increasing the expression of HAS2, which correlates with increased invasion41. Senescence also occurs in stromal cells[157] and tumor cells can compensate

for endothelial cell senescence by transdifferentiating into endothelial cells, enabling angiogenesis[160].

The chemotherapeutic temozolomide (TMZ) increases patient survival but can trigger TME remodelling that promotes a resistant, pro-invasive tumor phenotype. Treatment of cultured GBM cells with radiation and TMZ induces an increase in MMP-2 secretion and abundance of matrix-degrading invadopodia[161]. TMZ treatment also alters proteoglycan and GAG composition, with the combination of TMZ and dexamethasone resulting in deterioration of proteoglycan and GAG content[162]. Other agents promote TME remodelling that slows tumor progression. Microtubule inhibitors target cell division, but they can also reduce the invasive capacity of tumor cells by reducing MMP-2 expression[163]. Dexamethasone, which is a steroid traditionally applied for its ability to reduce oedema rather than for its chemotherapeutic properties, also activates fibronectin matrix assembly, resulting in increased cell–cell and cell–matrix adhesions that may slow invasion[57]. However, the role of dexamethasone and other steroids in tumor progression and their interactions with therapeutic interventions are largely unknown. The investigation of treatment-induced TME remodelling in engineered models could unravel these interactions to improve therapeutic strategies.

1.4.4 Targeted therapeutic agents

Targeting therapeutics to the tumor and the TME offer promise to improve patient survival and quality of life[164,165]. Successful clinical treatment of chronic myeloid leukaemia and gastrointestinal stromal tumors with the small-molecule inhibitor imatinib mesylate (Gleevec) targeting mutated kinases demonstrated the potential of targeted therapies[164]. Targeted therapies have also been clinically successful in breast cancer treatment, particularly for the human epidermal growth factor receptor 2 (HER2)-amplified subset[165]. Unfortunately, most of the clinically tested GBM-targeted therapies have shown little efficacy thus far, such as erlotinib targeting the often overexpressed EGFR or PLX3397 targeting colony-stimulating factor 1 receptor (CSF1R) to modulate TAM activity[33,166,167]. Inhibitors targeting the hypervascularity of GBM tumors have come closest to realization and remain a promising strategy (Table 2). The anti-VEGFA therapeutic bevacizumab is currently the only drug approved by the US Food and Drug Administration (FDA) targeting the GBM TME[21–23]. Bevacizumab treatment initially causes a decrease in tumor volume and vascularity, but tumors ultimately adapt with revascularization and increased invasiveness[168]. A more potent pan-VEGF family inhibitor, tivozanib, reduces proliferation and invasion, and is currently undergoing clinical evaluation[169]. Similarly, inhibitors of VEGF receptor tyrosine kinases, such as cediranib and sunitinib, show promise in reducing angiogenesis and normalizing vascularization[170–172]. Other angiogenic targets are also under investigation; for example, the angiopoietin inhibitor AMG 386 reduces vascular permeability and angiogenesis[173,174]. The potential of antiangiogenic therapies motivates the investigation of vascular–tumor interactions in engineered TME models.

TABLE 2. Selected therapeutics targeting the tumor microenvironment in clinical trials.

Therapeutic agent	Target	Effect on tumor progression in preclinical models	Refs.

Microglia and TAMs			
PLX3397	CSF1R inhibitor	↓Microglia, ↓tumor burden, ↓invasion	[167]
Cell receptor–ECM interactions			
Cilengitide	Pentapeptide that blocks activation of αvβ3 and αvβ5 integrins	↓Angiogenesis and tumor growth by blocking of integrins on vascular endothelial and tumor cells	[175]
Hypoxia			
AQ4N	Bioreductive prodrug targeting topoisomerase II in hypoxic cells	↓Hypoxic cells	[176]
Microvascular-related pathways			
Tivozanib	Pan-VEGFR tyrosine kinase inhibitor	↓Proliferation, ↓expression of VCAM-1 and ICAM-1 mediated cell-cell adhesion, and ↓MMP-2-mediated invasion	[169]
Sunitinib	PDGFR and VEGFR inhibitor	↓Angiogenesis, ↓proliferation	[172]
Cediranib	Pan-VEGFR tyrosine kinase inhibitor	↓Angiogenesis, normalization of vasculature	[170,171]
AMG 386	Angiopoietin-1/-2-neutralizing peptibody	↓Vessel permeability, ↓angiogenesis	[173,174]

CSF1R, colony stimulating factor 1 receptor; ICAM-1, intercellular adhesion molecule 1; MMP-2, matrix metalloproteinase 2; PDGFR, platelet-derived growth factor receptor; TAM, tumor-associated macrophage; TME, tumor microenvironment; VCAM-1, vascular cell adhesion molecule 1; VEGFR, vascular endothelial growth factor receptor; ECM, extracellular matrix.

Several other TME features are also explored as targets (Table 2). Efforts to eradicate hypoxic cells within the TME have, overall, been positive in clinical trials in patients with advanced solid tumors[176–179]. Bioreductive prodrugs can be enzymatically reduced in hypoxic regions into cytotoxic products. AQ4N is a bioreductive prodrug targeting topoisomerase II and it has shown promise as an adjuvant therapy in preclinical trials of several cancers, including GBM[179]. Importantly, AQ4N can cross the BBB and was well tolerated in all patients in a phase I study in GBM[176]. Cell–matrix interactions represent another key target for therapies[175,180,181]. Cilengitide is the first integrin inhibitor undergoing clinical testing and initially showed promise for modestly improving survival in both newly diagnosed and recurrent GBM with tolerable toxicity[175]. Cilengitide inhibits integrins αvβ3 and αvβ5, which are overexpressed on GBM cells and vascular endothelial cells. This inhibition disrupts angiogenesis and tumor–matrix interactions needed for migration. However, cilengitide was eventually shown to be ineffective in phase III clinical trials[182], which may be related to poor bioavailability; thus, cilengitide may warrant further investigation[183]. Careful consideration of how the TME influences tumor mechanics and transport can be leveraged to improve drug-delivery methods[180]. For example, convection-enhanced delivery involves catheter insertion directly into the tumor core to continuously deliver a chemotherapy, avoiding perfusion across the BBB and counteracting resistance from increased interstitial pressure[90]. Moreover, a poliovirus-based immunotherapy designed to activate oncolytic T cells has shown promise in improving GBM patient survival and may be combined with molecularly targeted therapeutic strategies[184,185].

1.5.1 Engineering microenvironment models

Experimental models for GBMs range in complexity from 2D cultures on glass or plastic to orthotopic xenografts and genetically engineered mouse models[46]. Traditional 2D models have proven invaluable for investigating some molecular mechanisms governing GBM progression, such as early studies elucidating how MMPs and soluble factors contribute to tumor initiation, invasion and propagation[186]. However, 2D models lack the ECM stiffness and composition, topographical guidance cues and dimensionality of human tissue needed to fully investigate the role of the TME. Orthotopic xenografts of patient-derived GBM cell lines in immunodeficient murine models are commonly used to fully recapitulate the in vivo TME. Orthotopic xenograft models better mimic tumor heterogeneity than in vitro models, with different levels of tumor heterogeneity, depending on the model[187,188]. However, orthotopic xenograft models lack a normal immune response, which is a key parameter in regulating tumor progression and full retention of tumor heterogeneity[45,189]. Furthermore, animal models are more expensive and less scalable than in vitro models, and are often impractical for detailed mechanistic dissection of human pathobiology[190]. The GBM TME substantially affects tumor progression and, thus, engineered TME models offer a valid alternative as experimental GBM models with the potential to overcome the limitations related to animal models[191]. Specific parameters (ECM composition, mechanics, topography and stromal cells) can be incorporated into engineered models to recreate the GBM TME for more precise hypothesis testing (Table 3).

TABLE 3. Engineered glioblastoma models.

Model	Key findings	Refs.
2D matrix models		
PA	Spreading, migration and proliferation increases with matrix stiffness, depending on tumor cell subpopulation and patient	70–73,192
Silicone rubber	Spreading increases with elastic modulus	75
Collagen	Matrix biophysical properties affect phenotype	193,194
HA	CD44 is mechanosensitive; elastic modulus affects miRNA expression	74,195,196
3D matrix models		
Collagen	Dimensionality determines drug resistance; Porosity and density affect invasion speed	194,197 198,199
Collagen-agarose	Cell spreading and motility in collagen requires local matrix stiffening	200,201
HA	Cell invasion through HA mimics invasion in the brain and is slow relative to invasion in highly porous matrices	140,196
Matrigel	Stromal cells in 3D matrix affect GBM phenotype	119,167,16
PEG	MMP degradability enhances cell spreading	202
PNJ	Scaffolds increase stemness of GSCs	203
PCL-HA	HA maintains stemness of GSCs	204
Alginate-chitosan	Scaffolds increased stemness marker expression	205
HA-collagen	HA upregulates invasion	206
HA-gelatin	HA upregulates matrix remodeling	56,207
HA-PEG	Matrix elastic modulus affects ECM deposition	208
Brain-derived ECM	Cells exhibit brain-like invasion in matrix	209,210

Models of heterogeneity		
Elastic modulus patterning	Higher modulus increases cell spreading in 2D and 3D	[211,212]
Orthogonal parameter patterning	Composition and stiffness have non-linear effects on phenotype	[195,213]
Soluble cue gradient	Reduced nutrient and oxygen transport increases secretion of angiogenic factors	[214]
Topographical models		
ECM interface	Interface properties drive invasive morphology	[215,216]
Open channels	Stiffness and pore size have combined effect on invasion	[192]
Electrospun fibers	Linear topographic cues drive rapid invasion	[217–223]
Encapsulated fibers or channels	Cells transition to rapid invasion when encountering linear topographic cues in 3D matrix	[140,206]
Interstitial fluid models		
Flow in Boyden chamber	Interstitial flow drives CXCR4-dependent invasion	[89,91,92]
Multi-parameter microfluidic system		
Pseudopalisade model	Vaso-occlusion drives migration and psuedopalisade formation	[224]
PVN models	Stromal-cell crosstalk affects invasive phenotype	[210,225–227]
Mini-brain with macrophages	GBM cells recruit and influence macrophage polarization	1. [228]
Organoid		
Tumor organoid culture	Tumor organoids maintain heterogeneity and hypoxic gradient	[229]
Stem-cell derived tissue	Engineered neural tissue supports brain-like GBM invasion	[230]

CXCR4, C-X-C chemokine receptor type 4; ECM, extracellular matrix; GBM, glioblastoma; HA, hyaluronic acid; miRNA, microRNA; PA, polyacrylamide; PCL, polycaprolactone; PEG, polyethylene glycol; PNJ, poly(N-isopropylacrylamide-co-Jeffamine M-1000® acrylamide); PVN, perivascular niche; GSC, glioblastoma stem cell.

1.5.2 2D matrix models

A simple approach to incorporating TME components into engineered models is to fabricate 2D substrates featuring ECM ligands and mechanical properties normally present in brain matrix. These modified 2D substrates can be used to explore how matrix mechanics and ECM components affect cell morphology, proliferation and migration (Fig. 2a). The mechanical properties of synthetic substrates, such as polyacrylamide (PA)[70–73,192] and silicone rubber[75], can be well controlled in a physiologically relevant range and coated or conjugated with cell-adhesive matrix proteins, such as laminin or fibronectin. Natural or semi-synthetic polymer matrices, such as collagen[193,194] and HA[74,195,196], typically contain some adhesive ECM cues, but they can also be further modified with ligands. HA gels are particularly advantageous for recapitulating the HA richness of brain ECM. A diverse array of chemistries can be applied in HA gels, such as the addition of methacrylate or thiol groups, to facilitate crosslinking and modification with

peptides[196,231,232]. Synthetic and natural 2D substrates have been applied to demonstrate that GBM cells are mechanoresponsive and that the mechanical response varies between patients and between subpopulations of cells[71,72]. For example, our laboratory has employed 2D HA hydrogels to show that CD44 can transduce mechanical signals from HA to regulate GBM adhesion and invasion[74].

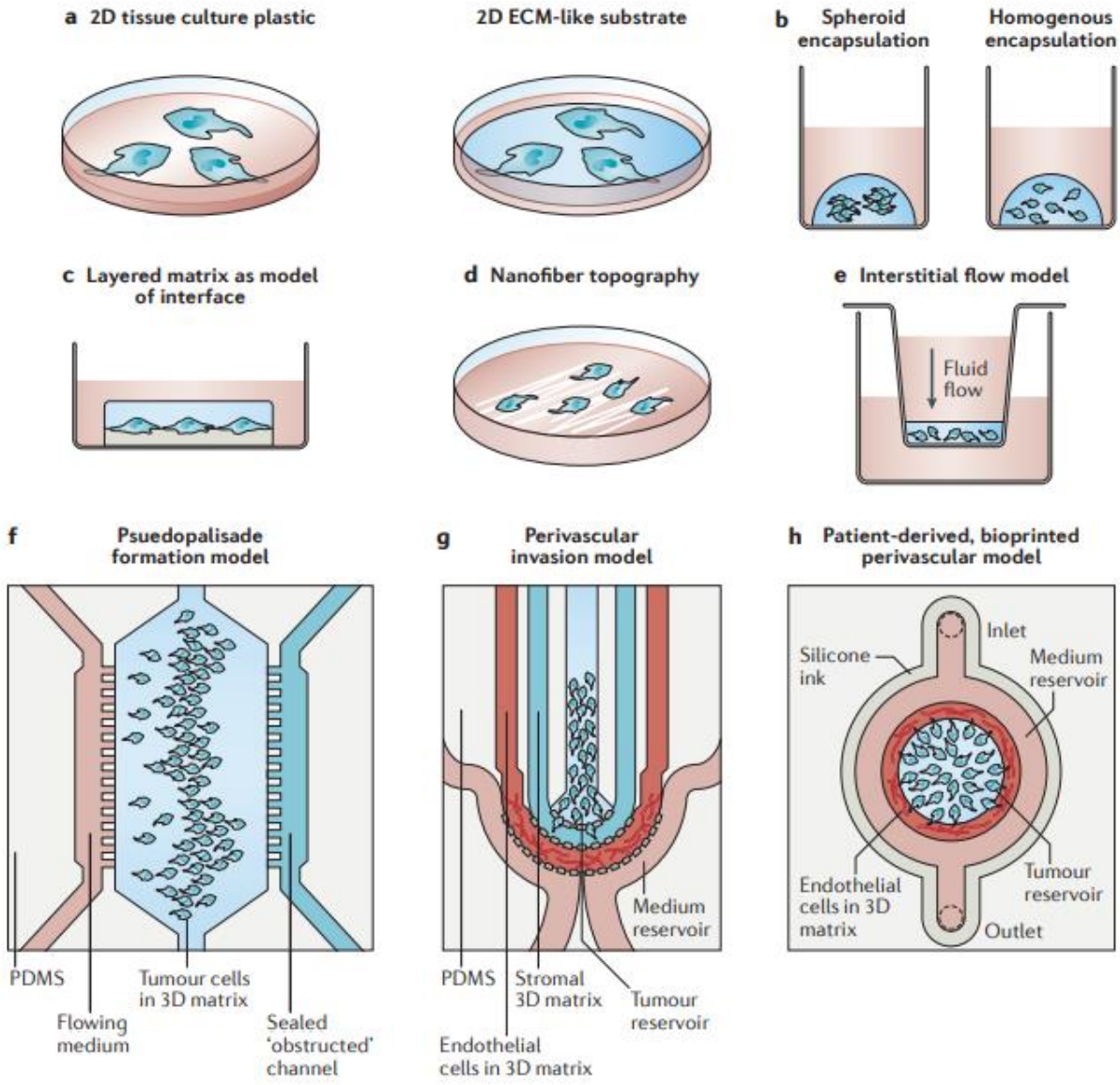

Figure 2. **Engineered glioblastoma models.** a) 2D models often include a matrix layer with tunable mechanical properties and composition. b) In 3D matrices, cells can be encapsulated as spheroids or as single cells. c) Cells can be cultured between extracellular matrix (ECM) layers of distinct composition and mechanics to model cell migration at the interface of the vascular basement membrane and the intraparenchymal matrix. d) Nanofibers with ECM coatings are often used to mimic linear, white matter tracts. e) Media height in a Boyden chamber can be used to generate interstitial flow through matrix-encapsulated cells. f) A microfluidic device with an open (nutrient-rich) and

closed (occluded) channel surrounding matrix-encapsulated cells can be used to test how psuedopalisades form. g) A microfluidic model of the perivascular niche (PVN) containing a glioblastoma stem cell (GSC)-rich tumor reservoir, an intraparenchymal region with stromal matrix and a region of matrix-encapsulated endothelial networks can be used to investigate the role of the PVN in GSC tumorigenicity. h) A bioprinted microfluidic model with a matrix-encapsulated endothelial network arranged concentrically around patient-derived tumor cells can be applied for the development of patient-specific engineered tumor microenvironments (TMEs). Panel f adapted from REF. 223. Panel g adapted from REF. 224. Panel h adapted from REF. 195.

1.5.3 3D matrix models

2D platforms can be rapidly fabricated, are parallelizable and amenable to imaging and culture manipulations; however, owing to their 2D nature, they cannot fully capture brain architecture. By contrast, 3D matrices offer the possibility to incorporate soluble cue gradients, such as an oxygen gradient, and confinement of invading cells, which alters cell morphology and requires the cells to degrade or squeeze through the matrix — as is the case in an in vivo TME. Interestingly, dimensionality alone can profoundly affect cell responses to chemotherapeutics, independent of matrix stiffness or composition[194]. Materials used for 2D substrates, such as collagen[194,197–201] and HA[140,196], can also be employed as 3D scaffolds. However, materials such as PA or polycaprolactone (PCL) requiring harsh solvents or crosslinking reagents during gelation cannot be easily seeded with cells unless they are made highly porous, such that cells can be incorporated into the matrix after gelation. Matrigel, which is a reconstituted basement membrane harvested from mouse sarcoma, is commonly used as 3D matrix because of its rapid, temperature-based gelation, abundance of adhesive sites and compositional complexity[135,233,234]. Collagen and Matrigel are simple to use relative to materials requiring complex synthesis, compatible with 3D cell encapsulation and contain various adhesive sites; however, the collagen-rich composition of both matrices and the fibrous architecture of collagen do not resemble the HA-rich, nanoporous brain matrix. Additionally, Matrigel composition is poorly defined chemically and exhibits batch-to-batch variability. Alternatively, synthetic polyethylene glycol (PEG) gels can be decorated with adhesive peptides and crosslinked with cleavable linkers, enabling precise control over matrix mechanics and composition for GBM modelling. Incorporation of degradability into 3D PEG matrices is not required for GBM cell viability and colony expansion but is essential for mesenchymal-like cell spreading[202]. 3D scaffolds, including electrospun polystyrene (PS) coated with laminin[221], porous PCL scaffolds with incorporated HA[204], poly(N-isopropylacrylamide-co-Jeffamine M-1000 acrylamide) (PNJ) copolymer scaffolds[203] and electrolyte complexes of alginate and chitosan[205], have been applied to demonstrate that dimensionality and matrix cues synergistically support maintenance of GSC stemness. More complex matrices can be fabricated by combining decellularized porcine or patient-derived brain matrix with low amounts of collagen, which better mimics the compositional

complexity of the brain[209,210]. However, these matrices are limited by sample size and require processing steps that destroy the native protein structure.

Cells can be embedded into 3D hydrogels as tumorspheres or as homogeneously dispersed single cells (Fig. 2b). Spheroids recapitulate the soluble cue gradients present in tumors, and spheroids with large diameters (>500 μm) exhibit a hypoxic and sometimes necrotic core[235]. GSCs cultured as tumorspheres in serum-free medium better maintain stemness and heterogeneity than GSCs cultured as single cells in serum-containing medium, and they can be directly encapsulated into matrices[236]. Adherent cells can be grown as tumorspheres using a hanging drop culture[237] or microwells[238] to aggregate cells into spheroids. Homogeneous dispersion of single cells, which are typically encapsulated during matrix gelation, enables evaluation of single-cell morphology, proliferation and colony growth[202,239]. In matrices with large pores, liquid cell suspensions can be dropped onto dehydrated, hydrophilic scaffolds; the cells are then drawn into the bulk 3D matrix after rapid absorption. This approach allows the incorporation of cells into matrices with harsh fabrication chemistries, such as electrospun PS or porous PCL[204,221]. Stromal cells can also be integrated into 3D matrices together with tumor cells but with limited possibilities to control their spatial organization. Stromal cells strongly influence GBM cell behavior; for example, GBM cells cultured with astrocytes and endothelial precursors in 3D HA–collagen matrices exhibit increased migration speed and resistance to STAT3 inhibition as compared to GBM cell culture alone[240].

HA-containing matrices can be fabricated by directly crosslinking the HA backbone[153,196], by complexing HA with polycations such as chitosan[241] or by mixing or conjugating HA into hydrogel networks with collagen[206], gelatin[56,207] or PEG[208]. The nanoporosity (~100–200 nm mesh size) of crosslinked HA gels impedes cell squeezing, necessitates more cell-mediated matrix degradation and leads to slower invasion than matrices with large pores, such as collagen[196,199,231]. HA can also be mechanically incorporated into gelatin matrices with variable elastic moduli and growth factor concentrations. The specific combinations of modulus and growth factor differentially affect proliferation and invasion[242]. Using high-molecular-weight HA, as compared with low-molecular-weight HA, in gelatin matrices leads to an increase in HA production by GBM cells and a decrease in cellular invasion, without changes in HA synthase or hyaluronidase protein expression[56]. The presence of HA in 3D models further induces resistance to the EGFR inhibitor erlotinib, mediated by CD44[243], as well as altered RHAMM, HAS1 and HAS2 gene expression[141]. The effect of HA on resistance to erlotinib depends on the mutant status of EGFR, which can vary between patient-derived lines[244]. Thus, the incorporation of HA into engineered TME models has revealed key mechanisms by which HA drives GBM progression.

1.5.4 Engineering gradients

Mechanical and biochemical ECM cues in the brain are often spatially organized, for example, as gradients or localized hotspots. Spatial organization can be recreated by 2D substrate patterning using photolithographic and microfabrication techniques in

combination with aqueous photochemistries[245,246]. For example, polydimethylsiloxane (PDMS) substrates can be patterned with different stiffnesses by generating stiff posts of defined shapes and sizes, which can be attached to the underside of a thin PDMS membrane. Fibroblasts and myoblasts cultured directly opposite the pillars on the flat upper side of the membrane experience the highest stiffness and show a haptotactic response by migrating towards or along stiff features[211]. Patterning substrates with ECM or mechanical gradients can be used for high-throughput parameter space testing or to examine cell responses to brain-like haptotactic cues. For example, orthogonal patterning of a fibronectin and elastic modulus gradient on an HA hydrogel revealed that GBM cells spread and express oncogenic microRNA in a non-linear manner across the range of the gel[195]. Patterning of 3D substrates is limited by the available patterning method. For example, microfluidic mixing of HA and gelatin precursor solutions with different concentrations results in 3D gelatin–HA gels with gradients of crosslinking density, in HA content and, subsequently, in cell density[213]. Interestingly, cells in these gels showed a biphasic MMP9 expression profile with increasing HA concentration. 3D gels can also be attached to a glass surface, resulting in a non-linear stiffness gradient along the z-axis. Cells encapsulated less than 25 μm from the glass surface spread more and migrate faster than cells located >500 μm from the glass surface independent of matrix density, demonstrating that distance from the glass substrate to the cells within the gel could be used to investigate mechanical effects on GBM[212]. Soluble cue gradients, including oxygen gradients and hypoxia, arise naturally in bulk 3D gels submerged in medium as a function of gel thickness. Cells seeded in 2-mm-thick gelatin hydrogels are exposed to lower rates of nutrient transport and show a pro-angiogenic phenotype with increased VEGF and HIF-1 expression, as compared with cells cultured in 1-mm-thick gelatin hydrogels[214]. Therefore, these TME models can be applied to elucidate the mechanisms by which spatial variation in mechanics, ECM composition and soluble cues influence tumor progression.

1.5.5 Engineering interfaces and topography

Semi-3D materials, often referred to as 2.5D materials, are characterized by a 3D topology arising from multiple 2D topologies. 2.5D systems combine the practicality of fabricating 2D features or patterns with the possibility to incorporate 3D-like constraints. In certain cases, these systems more faithfully recapitulate tissue architecture than ‘true’ 3D matrices. For example, the interface between the vascular basement membrane and the intraparenchymal ECM has been modelled by consecutively layering materials that are representative of the two regions (Fig. 2c). The bottom layer fabricated from Matrigel is analogous to the vascular membrane and the top layer of viscous, soluble HA is analogous to the parnechyma[215]. GBM spheroids seeded at the interface of the two layers show rapid, collective cell migration along the interface when the top layer includes highly viscous HA or viscous methylcellulose, as compared with little invasion when the top layer does not include viscous HA or methylcellulose. Thus, the presence of an interface between a matrix layer and highly viscous solution is sufficient to guide cell invasion along vascular membranes. The migration speed of cells seeded between fibronectin-coated PA and crosslinked HA or crosslinked HA conjugated with the integrin-binding peptide

RGD depends on the degree of ligand–receptor interactions between the cells and the interface, with more interactions slowing invasive migration speed[216]. Semi-3D substrates resembling the brain intraparenchymal region can also be fabricated by layering ECM-producing astrocytes onto plastic to form a parenchyma-like substrate[215]. GBM invasion speed on astrocyte layers inversely correlates with the culture time of astrocytes, which may be a result of ECM accumulation or changes in astrocyte phenotype.

GBM cells rapidly invade along anatomical tracks, specifically in the perivascular space or on myelinated axons[35]. Engineering models of anatomical tracks typically include a linear, topographical feature fabricated on a 2D surface or encapsulated in a 3D matrix. Confinement imposed by microchannels can recapitulate the linear migration and squeezing that cells exhibit when invading tight spaces along anatomical tracks. PA microchannels can be employed to independently modulate pore size and modulus, and have been used in our laboratory to show that matrix modulus and confinement synergize to promote rapid invasion[192]. Alternatively, nanofibers can be applied to study the effects of aligned topographical cues resembling the orientation of white-matter tracts. Interestingly, aligned fibers strongly promote rapid, linear migration[217–220,222,223] (Fig. 2d). To decouple the surface chemistry from the fiber mechanics, electrospun fibers with a ‘core’ material surrounded by a ‘shell’ of a different material were fabricated. The core material determined the modulus, while the shell material determined the surface chemistry. Varying material combinations for the shell and core were employed to demonstrate that GBM cell migration and morphology are sensitive to both nanofiber modulus and ECM coating[223]. The basement membrane composition and topographical features can be recreated within a 3D matrix by coating microfibers with Matrigel and embedding them in 3D matrices. Invading cells that encounter microfibers switch to an invasive mode and rapidly migrate along the fibers[206]. ECM-coated nanofibers also modulate GSC stemness, with laminin-isoform-specific effects[221]. Thus, topographical cues strongly drive invasion, proliferation and resistance, which can be enhanced by other TME signals, such as ECM composition and increasing stiffness.

1.5.6 Interstitial fluid in engineered models

Little is known about how interstitial fluid flow and pressure direct GBM invasion. Interstitial fluid flow can be modelled by seeding hydrogel-encapsulated cells in a Boyden chamber. The top chamber is then filled with excess medium, which creates pressure-driven fluid flow through the membrane pores in parallel to cell migration (Fig. 2e). Using such a model, it could be demonstrated that the interstitial fluid flow activates CXCR4-dependent polarized cell migration in multiple GBM cell lines, including GSCs[91,92]. This CXCR4-dependent invasion was confirmed in a mouse model, in which convection-enhanced therapy was applied to control interstitial flow[89], highlighting the clinical importance of fluid flow for tumor progression and convection-enhanced therapy[89,90].

1.5.7 Microfluidic models with multiple cues

Adding more complexity to TME models improves physiological relevance but, typically, increases the required labor and sacrifices throughput[46]. Microfluidic models can be made complex enough to facilitate construction of TME models with fluid flow, 3D ECM, spatial organization and stromal cell co-culture in a single platform, while allowing imaging, control of parameters and high-throughput screening[247], as well as achieving cost-effectiveness, compared with in vivo models. For example, a device with three parallel, adjacent channels has been developed to test the hypothesis that pseudopalisades form as migrating cells accumulate after a vaso-occlusive event[224] (Fig. 2f) . The outside channels contain flowing medium and the center channel contains a 3D matrix with homogeneously encapsulated cells. Vaso-occlusion can be mimicked by stopping the flow through one channel, which results in a hypoxic gradient. GBM tumor cells migrate away from the occluded channel and form pseudopalisades, supporting the mechanistic hypothesis.

The versatility of microfluidic devices also allows the reconstruction of TME niches. In particular, perivascular niche models can be constructed using parallel, interconnected channels to spatially organize niche layers. GSCs incorporated into such a microfluidic perivascular niche model featuring endothelial cells and the spatial organization of a GBM tumor exhibit morphologies, stemness markers and CXCR4-dependent invasion similar to those observed in vivo[225] (Fig. 2g) . Similarly, in a three-channel device with a tumor reservoir separated by a collagen matrix from an endothelialized, vascular-like reservoir, GSCs are known to precede their differentiated counterparts in invasion. Moreover, GBM pro-invasive genes, including integrins α2 and β3, are upregulated in the presence of endothelial cells[226]. Vascular homing can be studied using a microfluidic device, in which GSCs are encapsulated in a 3D microvascular network[227]. GSCs derived from the subtype of GBM tumors with high PDGFRA expression are particularly prone to vascular homing.

Microfluidic devices have also been developed for preclinical screening. Numerous wells can be included in a single device, seeded with tumorspheres and exposed to orthogonal gradients of chemotherapeutics and nutrients. These devices can serve as platforms for the optimization of drug efficacy and to predict therapeutic resistance[248–250]. However, how these results would translate to decisions for patient care remains unclear, given the difficulty in validating in vitro results with patient outcomes. The efficacy and toxicity of chemotherapeutics are significantly influenced by multiple organ system functions, particularly by the liver metabolism. Intestine and liver models can be added to a GBM model in a microfluidic device to allow chemotherapeutic screening, while considering pro-drug absorption by an intestine-like lumen, as well as metabolism by liver cells[251].

1.5.8 Bioprinting

Bioprinting, or 3D printing of biomatrices and/or cells, can be applied to organize and fabricate 3D matrices and microfluidic models[252,253]. For example, patient-specific GBM models can be bioprinted using concentric rings of endothelial and patient-derived tumor cells encapsulated in a porcine-brain-derived matrix[210] (Fig. 2h). Key tumor features, such

as the hypoxia-induced necrotic core surrounded by pseudopalisades, were observed within the model. Importantly, printed tumors recapitulate clinically observed patterns of tumor resistance to standard therapeutic treatments. The printing of patient-specific tumor models is limited by the sample size of the resected tumor; however, these results demonstrate the feasibility of incorporating a brain-derived matrix into printable bioinks in combination with patient-derived cell lines to test therapeutic responses. Similarly, bioprinted 'mini-brains' comprising a tumor-like, cell-dense region surrounded by a brain-shaped, macrophage-laden gel mimic the spatial organization of TAMs. The GBM cells in this model recruit macrophages and influence macrophage polarization; in turn, macrophages induce GBM invasion[228].

1.5.9 Organoid models of growth and invasion

Instead of recapitulating the complex brain matrix by controlled fabrication, cells can also be seeded into a matrix and stimulated to spontaneously develop into an organoid. To generate GSC organoids, patient tumor samples can be seeded directly into Matrigel suspended in medium. The suspended tumor cells grow into 'tumors' with diameters of 5–10 mm over 5–6 months[229]. In contrast to cell-isolation methods, in which the matrix is degraded and cells are disassociated, this method better preserves patient cell–matrix interactions and tumor heterogeneity, including the proportion of GSCs relative to differentiated cells found in the original patient tumor. During organoid growth, a GSC-rich hypoxic niche is formed at the center of the organoid, which is surrounded by more rapidly dividing cells. Compared with cells cultured in spheroids, cells in organoids better mimic patient tumor phenotype and heterogeneity in orthotopic xenograft models, as well as therapeutic resistance in vitro. Similarly, cerebral organoids with organized, differentiated brain features have been developed for other disease models[254]. These approaches could also be combined to study GBMs. For example, in GSCs seeded in engineered human nervous tissue generated from pluripotent stem cells, the expression of more than 100 genes was upregulated by interactions of GBM cells with stromal cells, many of which relate to ECM remodeling[230]. Therefore, organoid models and engineered tissue can be applied to capture the complexity of tumor TMEs; however, their fabrication is time-intensive, and they are difficult to reproduce. The benefits of complexity often do not outweigh the costs.

1.6 Opportunities for engineered models

Engineered GBM TME models have already provided a wealth of information about the function of the TME in GBM progression, including context-dependent mechanisms of GBM invasion and therapeutic resistance. With improved accuracy and (patho)physiological relevance, GBM TME models will play an important role in the preclinical and clinical pipeline (Fig. 3); for example, platforms incorporating patient-specific tumor samples may eventually aid in predicting therapeutic response and for the tailoring of treatments[224,229,248,255]. Drug responses are currently just as or more robustly predicted by molecular subtype, DNA methylation status and patient age than by in vitro

testing. Furthermore, the limited treatment options in GBM arguably do not yet necessitate complex optimization strategies[1,256,257]. However, validated and reliable engineered models could greatly improve preclinical drug testing. Established mouse models for in vivo screening have already been incorporated as secondary endpoints in GBM clinical trials[258]; however, the time required for model development hinders timely translation into personalized therapies. Engineered TME models would allow therapy screening at shorter timescales. Furthermore, the development of microfluidic models of drug permeability across the BBB could be very valuable for evaluating drug delivery to the central nervous system[259]. Such models are already being developed, but require additional validation and standardization[260].

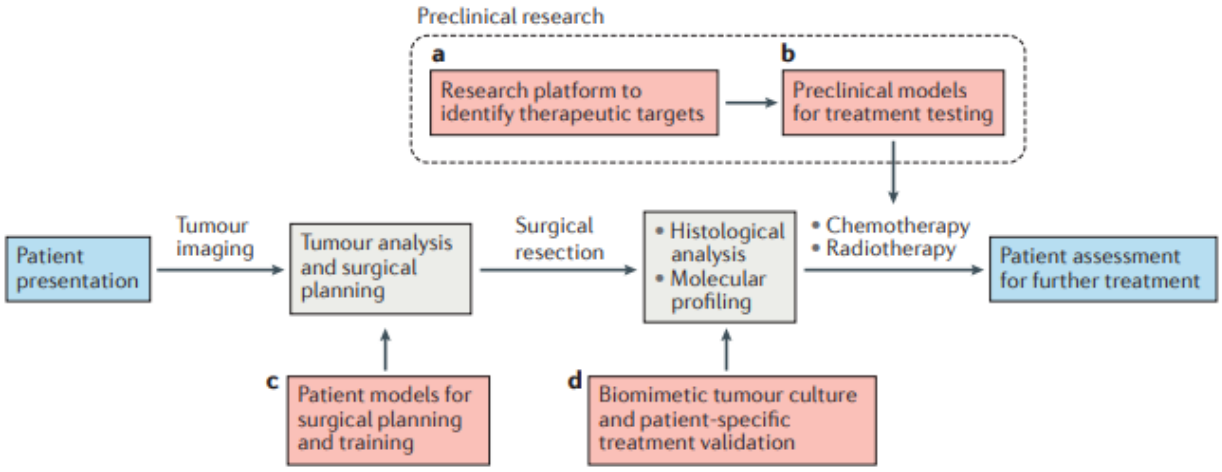

Figure 3. **Glioblastoma microenvironment models in the preclinical and clinical pipeline.** Red dashed lines indicate stages at which engineered models are or could be used. a) Engineered tumor microenvironments (TMEs) have been widely employed as research platforms to investigate the TME and they can be used to identify therapeutic targets. b) With refinement, these platforms can serve as a basis for precision medicine using patient-specific cells and/or matrices. c) Images of tumors from patients can be used to generate mechanically-matched patient-specific models of the tumor and brain anatomy for surgical planning and training. d) After surgical resection, engineered TMEs can aid in maintaining heterogeneity during culture for patient-specific treatment validation. The cells can be selected by molecular profiling and histological analysis.

The translation of patient-specific anatomy to engineered models is also becoming achievable, owing to advances in 3D printing technologies[252]. Full-scale brain models can be generated from patient MRI scans and have proven to be useful in pre-surgical planning, teaching and training[261]. For example, gelatin-based brain models have realistic mechanical properties and can be used for practicing gross resection without damaging intact tissue[262]. Further inclusion of a 3D-printed skull enables surgeons to practice cutting the skull and accessing the tumor site without unnecessarily damaging tissue[263]. Printing of patient-specific anatomical features combined with patient-derived cells and matrix may better recapitulate the gross tumor, facilitating at-scale studies of the TME. Such models could be useful for studying the influence of interstitial fluid on therapeutic

delivery, for example, on drug release from Gliadel wafers or convection-enhanced delivery[90,131].

Machine-learning strategies can also be applied to GBM research. For example, algorithms can be used to extract functionally predictive information about the TME from MRI images. In particular, machine-learning-based parameterization of contrast enhancement in MRI images correlates with gene expression of distinct biological processes, such hypoxia, starvation, matrix remodeling and endothelial permeability[264]. Furthermore, image features can be correlated with tumor subtype and patient survival[265,266]. Patient-specific MRI data can then be combined with other patient characteristics, such as age and Karnofsky Performance Score, to improve diagnosis before surgical resection is performed[267]. Machine learning has also been explored to improve tumor segmentation[268]. This is particularly important for surgical planning but could also be applied for early diagnosis and therapy selection. The information derived from machine-learning algorithms could be combined with other TME modelling technologies to improve their accuracy.

1.7 Perspective and conclusions

The TME has demonstrated potential as a therapeutic target for GBM treatment, owing to its impact on tumor progression. Engineered microenvironments allow the investigation of cell responses in the context of the TME and, thus, facilitate rapid hypothesis testing and screening. However, challenges remain. In particular, the minimal model components necessary to accurately recapitulate in vivo mechanisms need to be determined and the accuracy of models needs to be validated. It remains unclear which of the numerous ECM formulations used in engineered models meet these minimal requirements. A reductionist approach in developing TME models is useful to mimic in vivo GBM cell behavior while avoiding unnecessary costs and complexity. Validation ensures that in vitro discoveries generate useful predictions of clinical relevance. Validation strategies have not yet been fully standardized but generally fall into two categories. First, it must be demonstrated that the physical parameters of the model, such as composition and mechanics, closely match those of brain, to make the model predictive of in vivo behavior. Second, as a measure of model accuracy, cell phenotypes, such as migration, morphology, relative gene expression and chemosensitivity, should be similar to the in vivo phenotype. Ideally, it should further be verified that tumor progression in engineered models is driven by similar biochemical mechanisms as in vivo (for example, signaling pathways governing drug resistance), although this is currently rarely done. An iterative design cycle could be created, in which TME models are systematically tested, and the mechanistic and phenotypic predictions are checked against the in vivo response to refine the model and improve its predictive power.

Practical challenges that limit customizability and complexity include limited throughput and the need for composite fabrication techniques. Co-culture of GBM cells and stromal cells poses particular challenges, such as medium incompatibility, unmatched proliferation rates and long-term viability of primary stromal cells. Similarly, the inclusion of patient-derived cells or matrix in engineered models faces several challenges. Tumor

matrix is difficult to obtain in large quantities and the acclimation of tumor cells to cell culture can alter their phenotype. However, these challenges can certainly be addressed in the future and engineered models offer the opportunity to rapidly and precisely dissect mechanisms of GBM progression, accelerate clinical testing and provide a platform for precision medicine.

1.8 Acknowledgements

The authors gratefully acknowledge financial support from the National Science Foundation (Graduate Research Fellowship to K.J.W.) and the National Institutes of Health (Ruth L. Kirschstein Predoctoral Individual National Research Service Award F31CA228317 to K.J.W.; Ruth L. Kirschstein Postdoctoral Individual National Research Service Award F32CA221366 to J.C.; R21EB025017, R01GM122375 and R01DK118940 to S.K.; and R01CA227136 to M.K.A. and S.K.). J.D.C. has received funding from the European Union's Horizon 2020 research and innovation programme under the Marie Skłodowska-Curie grant agreement no. 752097.

Chapter 2. A 3D topographical model of parenchymal infiltration and perivascular invasion in glioblastoma

Parts of this chapter are excerpted with permission from Elsevier, from the article “A 3D topographical model of parenchymal infiltration and perivascular invasion in glioblastoma”, by Kayla J. Wolf, Stacey Lee, and Sanjay Kumar in *Applied Physics Letters Bioengineering*, 2, 031903 (2018).

2.1 Abstract

Glioblastoma (GBM) is the most common and invasive primary brain cancer. GBM tumors are characterized by diffuse infiltration, with tumor cells invading slowly through the hyaluronic acid (HA)-rich parenchyma toward vascular beds and then migrating rapidly along microvasculature. Progress in understanding local infiltration, vascular homing, and perivascular invasion is limited by the absence of culture models that recapitulate these hallmark processes. Here, we introduce a platform for GBM invasion consisting of a tumor-like cell reservoir and a parallel open channel “vessel” embedded in the 3D HA-RGD matrix. We show that this simple paradigm is sufficient to capture multi-step invasion and transitions in cell morphology and speed reminiscent of those seen in GBM. Specifically, seeded tumor cells grow into multicellular masses that expand and invade the surrounding HA-RGD matrices while extending long (10–100 μm), thin protrusions resembling those observed for GBM in vivo. Upon encountering the channel, cells orient along the channel wall, adopt a 2D-like morphology, and migrate rapidly along the channel. Structured illumination microscopy reveals distinct cytoskeletal architectures for cells invading through the HA matrix versus those migrating along the vascular channel. Substitution of collagen I in place of HA-RGD supports the same sequence of events but with faster local invasion and a more mesenchymal morphology. These results indicate that topographical effects are generalizable across matrix formulations, but the mechanisms underlying invasion are matrix-dependent. We anticipate that our reductionist paradigm should speed the development of mechanistic hypotheses that could be tested in more complex tumor models.

2.2 Introduction

Glioblastoma (GBM) is the most common and malignant primary brain tumor, with a median survival time of 14months and comparatively little improvement in clinical outcome over the past few decades.[269] GBM is characterized by a diffuse, infiltrative pattern of spread in which tumor cells evade surgical resection by migrating away from the tumor mass and resist chemotherapy and radiation.[12,270] Cell interactions with the extracellular matrix (ECM) represent a relatively unexplored potential therapeutic target. Tumor cells hijack ECM to promote survival and invasion, and disruption of cell-ECM interactions shows promise for sensitizing cells to therapeutic intervention.[181] An

important detail of brain ECM is that its composition varies dramatically by region. The ECM surrounding microvasculature is rich in collagen, fibronectin, and laminin, while the parenchymal space is generally devoid of these proteins and instead rich in hyaluronic acid (HA), which supports direct cell adhesion and organizes other matrix components such as tenascin.[36,47,106] Tumor cells invade slowly through the HA-rich parenchyma and then rapidly along vascular tracks, analogous to cars moving on a highway.[35,118,271–273] Chemotactic signals from endothelial and other stromal cells and haptotactic signals from the vascular ECM comprise a perivascular niche (PVN) that promotes invasion and resistance to therapy.[106,113,120,135,138,143]

Despite the established role of the PVN in driving rapid dissemination, mechanisms governing the transition from intraparenchymal to perivascular invasion are not well understood. Investigation of local infiltration, vascular homing, and perivascular invasion is made challenging by the absence of advanced culture models.[186,247,274] Most studies are performed in vitro using rigid, 2D culture dishes. While these simplified paradigms have high scalability and throughput, they do not allow one to control functionally important properties of the brain microenvironment such as stiffness, microarchitecture, dimensionality, and microregional heterogeneity. For example, GBM cells in vivo form microtubes that can signal through interpenetrating networks which are not observed in 2D culture.[275] Animal models offer a fully integrated system but are not amenable to parallelized discovery and screening and lack the tunability needed to quantitatively dissect invasion mechanisms.[190,247,276]

3D culture models derived from natural or synthetic ECM components offer a compromise, in that these systems capture structural aspects of matrix relevant to invasion while retaining some tunability and scalability. For example, implantation of tumorspheres into 3D hydrogels enables integrated investigation of how dimensionality, stiffness, and microarchitecture control invasion.[277] With these concepts in mind, our laboratory has explored the utility of 3D HA hydrogels for investigating GBM invasion. The nanoporous microarchitecture of HA is reminiscent of brain parenchyma, and the elastic modulus is similar to that of brain tissue (300–3000Pa).[41,42] Moreover, morphologic hallmarks of GBM intraparenchymal invasion seen in brain can be recapitulated in 3D HA-RGD gels.[74,196] Still, 3D tumorsphere assays are spatially uniform and thus do not capture the structurally heterogeneous tracks that are closely associated with invasion in vivo.

Early efforts to build microstructural cues into culture models of tumors including GBM have shown great promise in elucidating mechanisms of invasion. For example, confined microchannels have been used to investigate regulation of nuclear squeezing during 3D invasion.[192,278–281] The heterogeneity between the vascular basement membrane and parenchyma has been modeled by layering matrix types, revealing distinct differences in migration depending on the composition of each layer.[215,216] Cells also rapidly follow anatomical tracks, modeled by micropatterned adhesive ligands and electrospun fibers.[223,282] For perivascular invasion specifically, microfluidic devices have been developed to investigate vascular homing and intravasation using separate chambers for endothelial cells, a 3D matrix, and a cell reservoir.[274,283–287] The devices do not

incorporate the cylindrical geometry of vasculature embedded within the 3D matrix, which is vital to understanding how GBM interacts with anatomical tracks. Furthermore, the 3D matrices applied in these systems are often based on fibrillar collagens, which tend not to be abundant in brain outside of vascular compartments. Finally, the chambers are not typically embedded in the matrix, which in principle could allow some cells to invade along the matrix-wall interface instead of invading in 3D until reaching the matrix-vasculature interface. A model of invasion, therefore, should include both a 3D HA-rich matrix to capture aspects of vascular homing and topographical cues to investigate migration along anatomical tracks.

Here, we develop a simple 3D topographical model that enables us to recapitulate multiple stages and features of GBM progression during vascular homing and subsequent migration. Specifically, we find that the incorporation of an open channel as a vessel mimic parallel to a cell reservoir enables imaging of mass expansion, slow invasion through the 3D matrix, and rapid invasion along the channel wall. In a proof-of-principle demonstration, we show that arrival at the vascular channel is accompanied by a transition in tumor cell morphology and invasion speed that is broadly reminiscent of perivascular homing and invasion in GBM. Furthermore, we find that while the overall cell speeds and actin cytoskeletal morphologies underlying the transition are dependent on the matrix type, the relative transition in speed is generalizable across matrices. Thus, while matrix formulation influences mechanisms of invasion, topography can influence invasion within a particular matrix type.

2.3 Methods

HA matrix synthesis

HA hydrogels were synthesized as previously described.[196] Briefly, methacrylic anhydride (Sigma-Aldrich, 94%) was used to functionalize sodium hyaluronate (Lifecore Biomedical, Research Grade, 66 kDa–99 kDa) with methacrylate groups (Me-HA). The extent of methacrylation per disaccharide was quantified by 1H nuclear magnetic resonance spectroscopy (NMR) as detailed previously[288] and found to be 85% for materials used in this study. To add integrin-adhesive functionality, Me-HA was conjugated via Michael Addition with the cysteine-containing RGD peptide Ac-GCGYGRGDSPG-NH2 (Anaspec) at a concentration of 0.5mmol/l. Finally, 3wt. % Me-HA was crosslinked in phenol-free Dulbecco's Modified Eagle's Medium (DMEM) (Invitrogen) with bifunctional thiol dithiothreitol (DTT, Sigma-Aldrich). A concentration of 19mmol/l DTT was selected to yield a shear modulus of 300 Pa. After 1 h of crosslinking, the hydrogels were rinsed and soaked in room temperature phosphate-buffered saline (PBS) for 1 h before cell seeding.

Rheology characterization

The shear modulus of hydrogel formulations was measured using oscillatory rheometry (Anton Parr Physica MCR 310) as described previously.[196] Briefly, hydrogels were first crosslinked by incubation for 1h in a humidified 37 °C chamber. Rheological testing

consisted of frequency sweeps ranging from 100 to 0.1Hz at an amplitude of 0.5% also in a humidified 37 °C chamber. Shear modulus was reported as the average storage modulus for 3 tests per type of matrix composition at an oscillation frequency of 0.5 Hz.

Collagen matrix synthesis

Rat tail collagen I (BD Biosciences) was used to form hydrogels according to the manufacturer's instructions. Briefly, a solution of 1v/v% 1 N NaOH (Carolina Biological Supply), 10v/v% 10 PBS (Fisher BioReagent), and 50 v/v% of 3.84 mg/ml cold collagen I in sterile distilled water was mixed thoroughly on ice. The solution was then pipetted into the desired mold and incubated for 30 min at 37 °C. Finally, solutions were rinsed and soaked for 1 h in room temperature PBS before cell seeding.

Cell culture

U87-MG human glioblastoma cells were obtained from the University of California, Berkeley Tissue Culture Facility, which sources its cultures directly from the ATCC. Cells were cultured in DMEM (Invitrogen) supplemented with 10% calf serum (JR Scientific), 1% penicillin-streptomycin, Minimal Essential Medium (MEM) nonessential amino acids, and sodium pyruvate (Invitrogen). Cells were harvested using 0.25% trypsin-ethylenediaminetetraacetic acid (EDTA) (Thermo Fisher Scientific). Cells were screened bimonthly for mycoplasma and authenticated annually via short tandem repeat analysis. For invasion in PVN model devices, 0.2ll of cells at 5 106 cells/ml were injected. Devices were cultured in 6-well plates with medium being changed every 3–4 days. In devices treated with blebbistatin, medium containing 10 µM blebbistatin was added to the entire well at day 1 and exchanged every 3 days. In other devices, recombinant human epithelial growth factor (EGF) (R&D Systems) at a concentration of 2 µg/ml in 10% serum-containing medium was added to the vessel-like channel and exchanged every 3 days.

Device fabrication

First, the PDMS support was fabricated by mixing a 10:1 mass to mass ratio of Sylgard 184 elastomer with the initiator (Dow Corning). The mixture was pipetted into the desired mold and cured at 80 C for 2h. Horizontal PDMS spacers were first created to separate wires (167 µm diameter, Hamilton) by 500 µm using 500 µm outer diameter glass capillaries (CTech Glass) without attention to height in the z direction, then sliced, and used to space the wires for all subsequent fabrication. The PDMS supports for hydrogels were fabricated by aligning wires with prefabricated horizontal spacers to separate the parallel wires at each end. The wires were spaced between glass coverslips and suspended using 170 µm PDMS strips as vertical spacers. After curing, a 3 mm hole punch and razor blade was used to cut the center of the PDMS support and create space for the hydrogel. The PDMS support was assembled between two 18 mm #1 glass coverslips (VWR) and fastened with a drop of 5-min epoxy (ITW Devcon) at two corners.

To cast the gel, the wires were first reinserted into the assembled device to create a mold. Next, the hydrogel matrix was inserted in the side of the device. Wires were removed

after the hydrogel solution had solidified leaving two open channels. After rinsing and soaking the hydrogels, cells were inserted into the freshly fabricated device using a syringe (Hamilton). Cut wires were used to plug each end of the cell reservoir, and the entire device was placed into the bottom of a 6-well plate and bathed in 3 ml of medium. Cells and gels were equilibrated in medium overnight before imaging. Medium was changed every 3–4days. To introduce diffusible soluble factors into the vessel-like channel, a 33-gauge syringe needle (Jensen Global) was pre-loaded with growth factor and medium of interest and was then inserted into the PDMS support. The opposite end of the open channel was plugged with an additional wire. Diffusion between the open channel and the surrounding bath of medium was blocked in some devices by inserting wires into the PDMS support, fully occluding the channel.

Invasion analysis

For area analysis in HA PVN devices, cells in devices were imaged once every 3days using an Eclipse TE2000 Nikon Microscope with a Plan Fluor Ph1 10 objective. Images were acquired, and large images were stitched using NIS-Elements Software. For each device, the cell reservoir and area of invasion were outlined in ImageJ and normalized to the total cell area from day 1, assumed to be reservoir only. Migration assays were performed by imaging at 15 min intervals for 6 h. ImageJ plugin Manual Tracking was used to track cell movements in each frame and calculate an average cell speed. To analyze single-cell speed transitions, cells were tracked for at least 6 h until a transition event was observed. Only 3 h prior to and directly after a transition, cells were analyzed. The transition point was defined as the time in which the entire nucleus had exited the 3D matrix. Average speed was calculated for cells before and after the transition. All cell motility imaging was performed at least 1 day after seeding in collagen gels and at least 10 days after seeding in HA-RGD gels.

Cell labeling and confocal fluorescence microscopy

Cells in 3D matrices were fixed with a 4 w/v% paraformaldehyde solution (PFA, Alfa Aesar) for 4 h and then permeabilized with 0.5 v/v% Triton-X (Thomas Scientific) solution for 1h. Cells were labeled with 1lg/ml 40,6-diamidino-2-phenylindole (DAPI, Sigma-Aldrich) and 488-labeled phalloidin (Cytoskeleton) by soaking overnight and then washed with PBS thoroughly overnight. After fixation and immunostaining, confocal images were acquired on a Zeiss LSM 780 NLO Axioexaminer upright microscope equipped with a 32-channel GaAsP detector and 2 photomultiplier tubes (PMTs) using a PlanApo Chromat 20 /1.0 water-dipping objective. Samples were illuminated using an Argon multiline laser for excitation at 488 nm and a 405 nm diode laser. Zen 2010 acquisition software was used. Finally, z slices separated by 5 µm were projected in ImageJ using 3D volume viewer. For investigation of cell division within the tumor reservoir, devices that had been cultured for>16days were disassembled and fixed with 4 w/ v% PFA in PBS. The HA matrix was treated with 2500 U/ml hyaluronidase from bovine testes (Sigma) overnight to improve antibody diffusion into the fixed sample. Cells were then labeled with 1lg/ml 40,6-diamidino-2-phenylindole (DAPI, Sigma-Aldrich), Alexa Fluor 546-phalloidin (Thermo-Fisher), monoclonal rabbit anti-Ki-67 primary antibody (Abcam, clone SP6), and Alexa

Fluor-647 polyclonal goat anti-rabbit secondary antibody (Abcam). Stacked confocal images of Ki-67 labeled cells were obtained using a swept-field confocal microscope (Prairie Technologies) with an Olympus LUM Plan FL 60 water immersion objective.

Live/dead cell viability assay

To perform a cell viability assay (Invitrogen), devices that had been cultured for >16 days were disassembled, and cells in 3D matrices were washed with PBS at 37 C for 10min. Gels with cells were then incubated in 2 µM calcein AM and 1 µM ethidium homodimer-1 in PBS for 20min with gentle rocking. Finally, gels were rinsed for 5min with PBS prior to imaging using an Eclipse TE2000 Nikon Microscope with a Plan Fluor Ph1 10 objective.

Structured illumination microscopy (SIM)

For SIM imaging, devices were disassembled by removing the top coverslip and placing the sample face-down onto a #0 coverslip dish (MatTek). To image cells within channels, gels were trimmed with a scalpel and then placed into the dish with PBS for imaging. Cells were imaged directly using an Elyra structured illumination microscope (Zeiss) and a Plan-Apochromat 63 /1.4 Oil DIC M27 objective (Zeiss). Samples were illuminated using an Argon multiline laser for excitation at 488 nm and a 405 nm diode laser. Zen 2010 software was used for image acquisition. For z-stack images, slices were 1µm apart. Finally, z-projections were formed in ImageJ with 2 2 binning using the 3D project. Artifacts caused by imaging deep with 3D HA were minimized by filtering the Fourier transform for images of cells within the HA channel.

3.3.10 Statistical analysis

The sample numbers necessary to obtain a power of 0.8 were estimated prior to experimentation based on estimates from previous studies (G* Power).[289] Each device was fabricated and seeded independently. GraphPad Prism 7 software was used to graph data and perform statistical analysis. Reservoir and invasion areas in each device over time were compared using the Friedman test followed by Dunn's multiple comparison test. Bias in the area of invasion was compared using a paired t-test. Migration speeds within the matrix and the channel were compared as the average of 5 cells in 3 independent devices for each condition to give n1⁄4415 where variability is primarily from cell to cell. Several exclusion criteria were applied when selecting cells for analysis: cells must be clearly visible in all frames of imaging; cells must be leading invasion in the 3D matrix or actively moving in the open channel; and cells must not undergo division during the imaging interval. Data were compared using a student's t-test. For single cell transitions, 2–3 cells were measured in 3 independent devices to give a total of n 1⁄4 7. Data were compared using a paired t-test.

Approvals

This study did not involve human subject research, and so no ethics approval was required.

2.4.1 Results and Discussion

2.4.2 Mimicking vascular tracks embedded within an HA matrix with a simple device

GBM invasion is characterized by tumor expansion, slow invasion through the HA-rich parenchyma, and rapid invasion along vascular tracks **(Fig. 1a)**. During this process, cells transition from a 3D migration mode to a 2D-like migration mode as they follow the interface between the basement membrane and surrounding parenchyma.[118,215,271] We hypothesized that a simple topographic model of the PVN composed of a cell reservoir parallel to an open channel would induce similar progression in invasion **(Fig. 1b)**. Specifically, we hypothesized that by restricting cell invasion to the 3D matrix until cells encountered the open channel, cells would transition from slow migration through the 3D matrix to more rapid migration along the 2D wall of the open channel, analogous to GBM invasion kinetics in vivo.

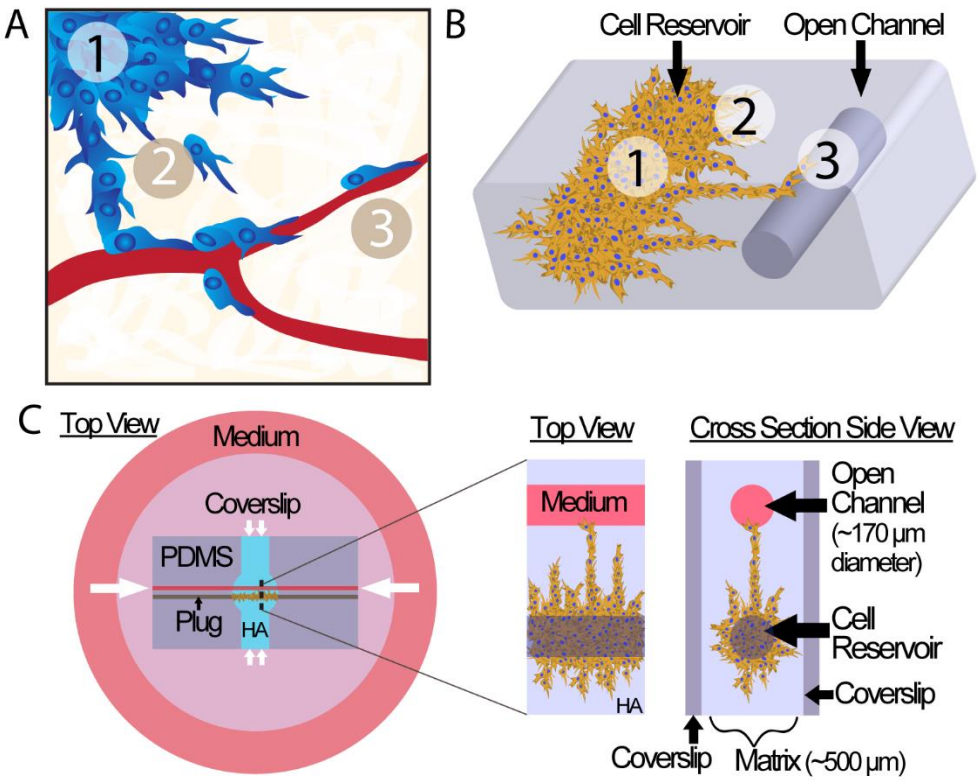

Figure 1. A topographical model of the perivascular niche. (a) Schematic of GBM progression representing (1) tumor expansion, (2) slow invasion through the HA-rich parenchyma, and (3) rapid migration along vascular tracks. (b) GBM progression can be modeled using a simple 3D topographical model of a vessel. (c) Device schematic. The

hydrogel matrix is cast over a mold within a PDMS support and sandwiched between two coverslips to form two open channels. One channel is filled with densely packed cells and plugged to create a tumor-like cell reservoir. White arrows indicate the diffusion of nutrients from surrounding medium to the cell reservoir. The magnified view shows invasion from the cell reservoir to the open channel.

We fabricated a simple device to mimic topographical features of the perivascular niche **(Fig. 1c)**. The device consisted of a tumor-like cell reservoir adjacent to a parallel open channel, both of which were embedded in the 3D matrix. To form the device, we first fabricated two spacers to control the distance between channels and the vertical distance at which the channels were suspended. First, we fabricated a horizontal spacer to control the distance between the parallel channels **(Fig. 2a)**. Vertical spacers consisted of a thin layer of polydimethylsiloxane (PDMS). We then combined horizontal and vertical spacers to mold a PDMS holder with parallel, suspended channels **(Figs. 2b and 3a)**, which was then sandwiched between two glass coverslips which were fastened together **(Fig. 3b)**. The PDMS holder was used to support wires as a mold upon which hydrogel was cast **(Fig. 3c)**. Removal of the wires resulted in two 170 µm diameter parallel channels embedded within the 500 µm thick 3D matrix. We fabricated gels with a shear modulus of 300 Pa. This modulus is both within the range of values typically reported for brain tissue (300–3000 Pa)[41,42] and conducive to maintaining channel integrity during fabrication. One channel was seeded with cells at high density and then plugged on each end to restrict cell migration to the hydrogel only **(Fig. 3d)**. The entire device was then bathed in cell medium, and the other channel was left open to allow passive filling. The cell reservoir and vessel mimic were separated by 500 µm of the 3D matrix through which cells invaded to reach the open channel. Nutrients from medium could diffuse to the cell reservoir either through the open channel or at the sides of the device through the 3D hydrogel.

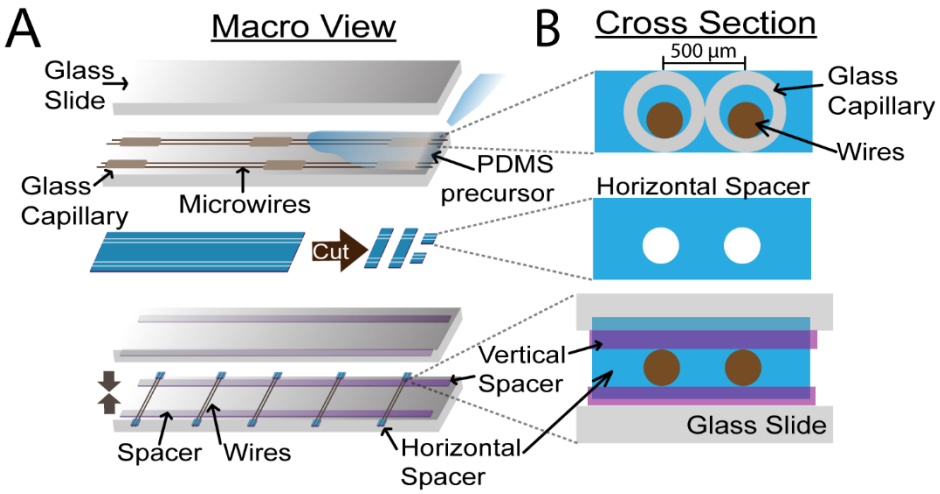

Figure 2. Spacer fabrication to align parallel channels suspended in PDMS. Glass capillaries of known diameter are used to control spacing between microwires during horizontal spacer fabrication. Horizontal spacers are cut from PDMS and then used to control wire-to-wire spacing during PDMS support fabrication. Vertical spacers are used

to suspend microwires. (a) Macro view showing the glass slide and wire alignment. (b) Close-up view of the cross-section of spacer alignment showing control over vertical and horizontal dimensions.

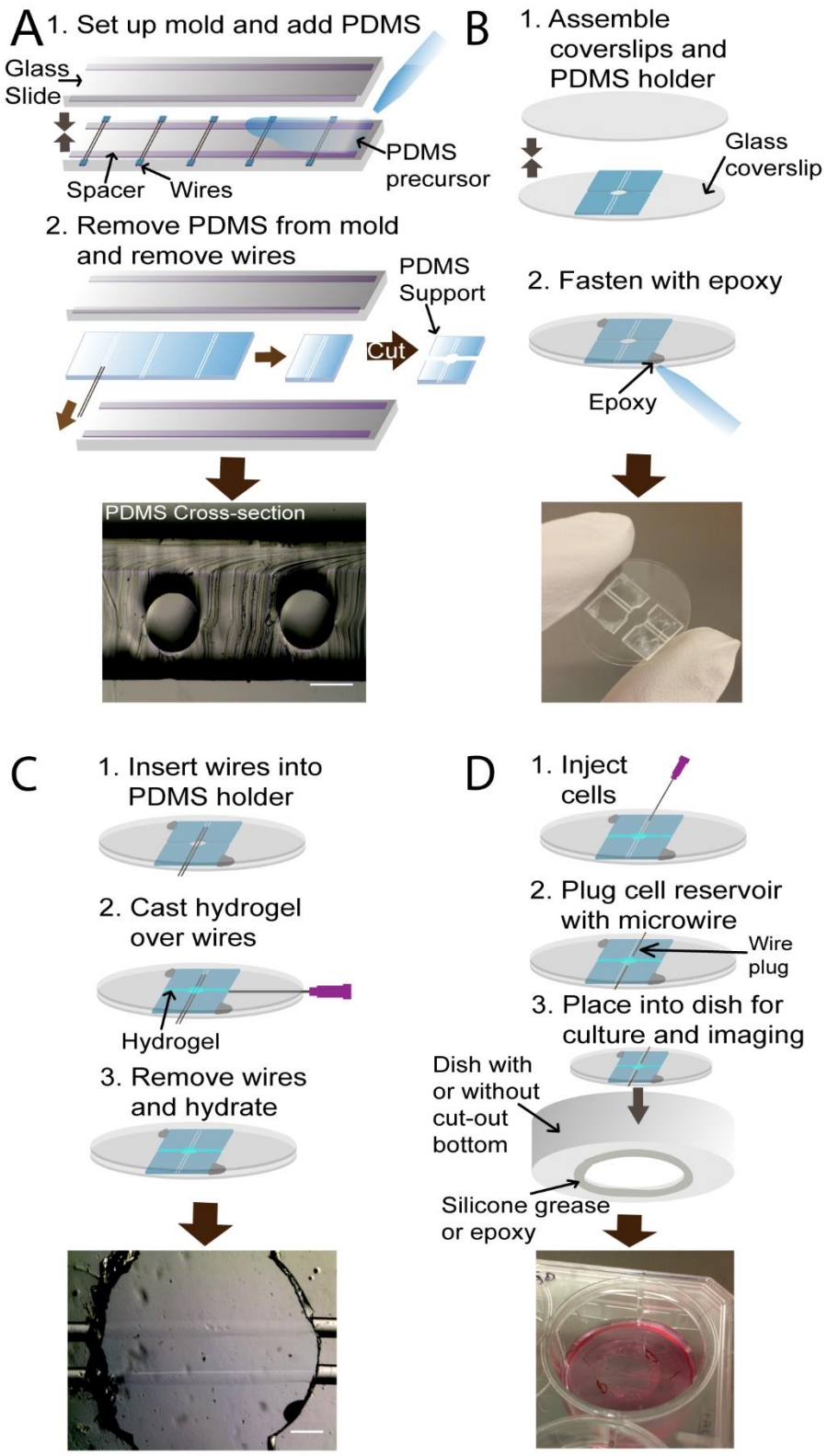

Figure 3. Device fabrication. (a) PDMS supports are fabricated by casting PDMS over a wire mold, curing, and cutting the mold. Scale = 200 µm. (b) PDMS supports are placed between coverslips and fastened with epoxy. (c) Wires are inserted into the device to

mold hydrogel, and the matrix is cast over the wires. Wires are removed leaving open channels. Scale = 500 μm. (d) Cells are injected into the reservoir channel, and plugs are added to prevent cells from migrating out of the channel.

2.4.3 3D topographical model promotes tumor expansion, invasion in masses, and invasion along the channel

To test whether GBM cells would indeed undergo multi-step invasion and follow topographical features within the matrix, we seeded U87-MG human GBM cells into seven devices and tracked invasion for 2–3 weeks. Based on our previous studies, we selected the 3wt. % HA matrix functionalized with 0.5mmol/l RGD as our matrix[74,196] and then tracked tumor expansion and invasion for 2–3 weeks. We chose a 3 wt. % HA concentration to facilitate fabrication of gels with the desired shear modulus of 300 Pa with low enough matrix density to enable cell invasion. We have previously observed in 2D studies that an RGD concentration of 0.5mmol/l promotes cell spreading and formation of broad lamellopodia.[74] Cells began to invade the matrix approximately 4 days after seeding **(Fig. 4a)** and continued to invade in multicellular masses over the next several days, tunneling through the matrix toward the open channel. Cells began to reach the channel around day 13 and reoriented to follow the channel wall **(Fig. 4a)**. Within the channel, cells generally adopted a linear morphology and were spaced further apart than cells packed densely in invading masses.

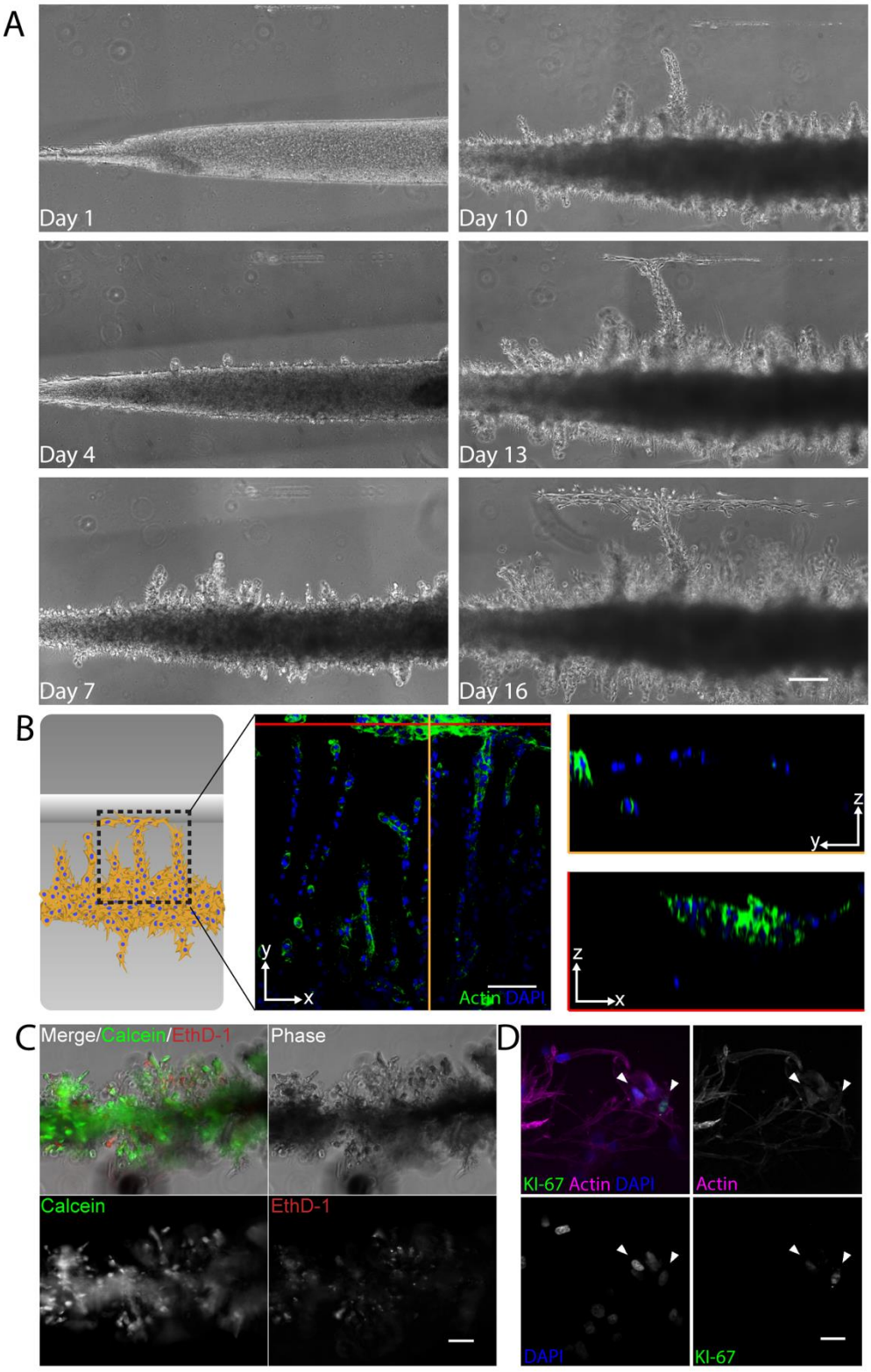

Figure 4. Tumor expansion, 3D invasion, and track-based invasion within the PVN model. (a) Time series for cell expansion and invasion in HA-RGD. Scale = 200 µm. (b) Schematic of the region of interest within gel for z-stack (240 µm, 5 µm slices)

demonstrating that cells generally migrate in the xy plane and that the cells begin to follow the channel after entering. The slice in the xz plane shows migration along the x axis within the channel, and the slice in the yz plane shows minimal migration in the z direction. Scale = 100 µm. (c) Calcein AM to stain viable cells and EthD-1 to stain apoptotic cells demonstrate cell viability within the tumor reservoir. Scale = 100 µm. (d) Z-stack (56 µm in height) of invading cells demonstrating relatively few Ki-67 positive nuclei (indicated by arrowheads). Scale = 20 µm.

Cells invading from the reservoir to the channel were primarily coplanar in xy, tunneling directly toward the open channel, and then migrating along the channel wall (**Fig. 4b**). This highly anisotropic migration suggests the presence of strong, diffusive chemotactic gradients between the reservoir and the channel. While the lack of migration in z may initially seem surprising, solute diffusion is strongly promoted in the xy plane due to the device being covered on top and bottom by coverslips but being open to the medium in all lateral aspects (xy plane). Passive filling of the open channel with medium likely facilitates steeper chemotactic gradients of some medium components due to close proximity to the cell reservoir, further inducing cells to invade directly toward the channel.

To determine whether cells remained viable within the tumor reservoir, we performed a cell viability assay after 16 days in culture and found that most cells stained positive for calcein AM, but not ethidium homodimer (EthD-1) **(Fig. 4c)**. Cells that did stain positive for EthD-1 were not localized to any particular region of the tumor reservoir. We did not observe a necrotic core, which has been observed in larger tumorsphere models (>500 µm diameter).[235] Rather, the cells in the core of the 170 µm diameter reservoirs remain viable despite the high cell density. This is consistent with our observation that the majority of cells within the tumor reservoir are mobile during live imaging experiments. Despite high cell viability, we observed relatively few Ki-67 positive cell nuclei (**Fig. 4d**). Cells with nuclei positive for Ki-67 did not appear to be localized to any particular region of the device; however, more rigorous testing is required to conclusively determine whether any patterns exist. While a number of variables in culture conditions could be responsible, the observed low number of proliferating cells may support the “go or grow” hypothesis. This hypothesis suggests that cells upregulate either invasive mechanisms or proliferative mechanisms, but not both.[40,290] Our platform should be useful for future investigation of the effects of the topographical microenvironment, matrix composition, and culture conditions or drug-treatment on proliferative and invasive phenotypes.

We next sought to observe both expansion and invasion within the model. Invasion in the HA-RGD matrix was visually distinct from expansion of the reservoir mass in phase contrast appearing as a dark region of high cell density **(Fig. 5a)**. Because invasion occurred mostly in the xy plane, we used the area as an approximate measure of expansion and invasion **(Fig. 5a)**. We tracked reservoir growth and cell invasion for 16 days until the first device was fixed for further analysis, normalizing the areas to the total area on day 1 to account for any variance in cell seeding and channel length.

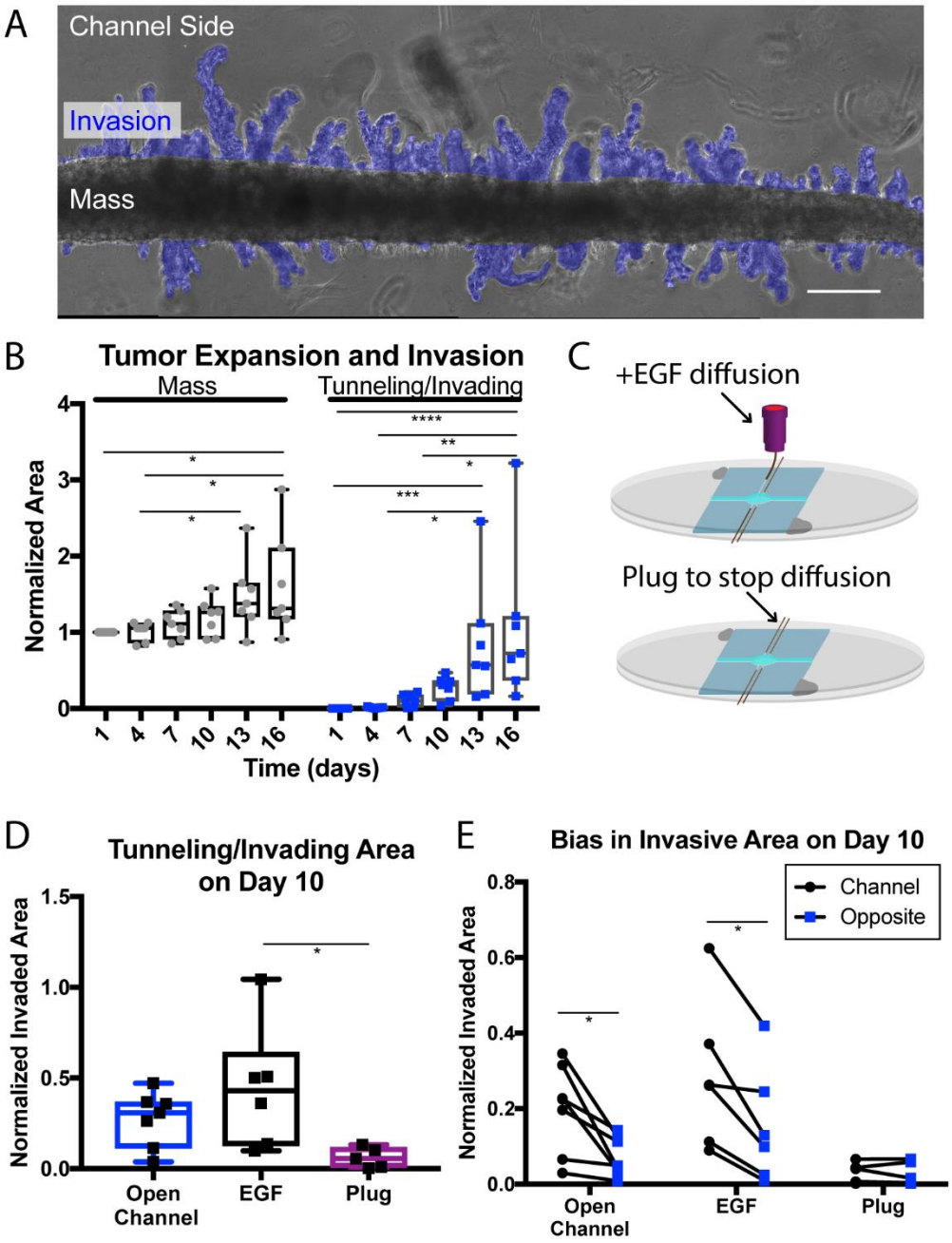

Figure 5. Cell expansion and invasion. (a) Example of invasion quantification showing the area of invasion (blue) as compared to the center mass of cells. Scale = 200 μm. (b) Mass area and tunneling/invading area normalized to the initial area for n1⁄47 devices over the first 16 days after seeding. *, p<0.05; **, p<0.01; ***, p<0.001; ****,p<0.0001 by Friedman's test followed by Dunn's test for multiple comparisons. The center line represents the median, boxes represent the 25th and 75th percentiles, and whiskers represent the min and max. (c) Device schematic for EGF diffusion into the channel and the plugged channel to prevent diffusion. (d) The total area of invading and tunneling cells is higher in the EGF condition compared to that in the plugged channel condition. *, p<0.05 by analysis of variance (ANOVA) followed by Tukey's test for multiple

comparisons, boxes represent the 25th and 75th percentiles, and whiskers represent the min and max. (e) Invading area (blue) on the side nearest the channel compared to the opposite side on day 10 normalized to the total initial area for each device. Each of the lines represents the results obtained with a different device. Significantly more cellular expansion and infiltration are observed on the channel side in devices containing an open channel and EGF diffusion within the channel, but not with a plugged channel (n = 5–7). *, $p < 0.05$ by the paired t-test of the average difference between the channel side and the opposite.

Both the reservoir area and the area of invasion grew over 16 days **(Fig. 5b)**. The reservoir area began to expand earlier than the invaded area in most devices, beginning around day 4 and expanding more rapidly around day 13. The area of invasion did not begin to increase until around day 7 but then expanded more rapidly than the reservoir area. By day 16, the increase in the area was due largely to invasion as opposed to reservoir expansion. These data suggest that some threshold, possibly time or a certain degree of confinement, is required for cells to upregulate invasive mechanisms. Once invasion begins, it proceeds more rapidly than reservoir expansion.

We also observed that invasion was generally biased toward the open channel, despite the fact that the cell mass was surrounded on all sides by an HA matrix bathed in culture medium. We hypothesized that this may be due to a chemotactic effect arising from more rapid diffusion of serum medium components into the open channel. The cell reservoir was much closer to the open channel (500 μm) than to the gel-bath interface at the sides of the device (4 mm). The open channel in close proximity to the reservoir may allow for increased diffusion of some medium components and serve as a chemoattractant. To further investigate the effects of chemotactic gradients within the matrix, we set up two additional conditions. First, we sequestered epithelial growth factor (EGF)-containing medium within the channel **(Fig. 5c)** to allow for EGF diffusion into the channel but not into the surrounding medium. We also set up a control experiment in which we used another wire to plug the open channel on each end, preventing medium component diffusion into the open channel **(Fig. 5c)**. First, we quantified the total area of cell invasion after ten days and found that cells invaded significantly more area in devices treated with EGF compared to those with plugged channels **(Fig. 5d)**. We then quantified and compared the invasion area on the side of the reservoir nearest the open channel with the invasion area opposite. In both the open channel condition and the EGF perfusion condition, we observed significantly more invasion toward the parallel channel compared to the opposite side **(Fig. 5e)**. Together, these results suggest that serum can induce both chemotaxis and chemokinesis, with EGF further enhancing chemokinesis. This also demonstrates that the PVN model can serve as a platform for investigating the effects of other soluble factors within the context of matrix and topographical features.

2.4.4 Cell morphologies in the PVN model resemble tumor cell invasion toward and along vascular tracks

Cell morphology is one indicator of whether cells are interacting with the microenvironment in a manner that captures important features of GBM. We investigated cell morphology in different stages of invasion and locations in the gel **(Fig. 6a)**. Long, thin protrusions generally preceded 3D invasion **(Fig. 6b)**. These protrusions varied in thickness and length. While most protrusions extended between 10 and 50 µm, protrusions occasionally reached>100 µm in length **(Fig. 6c)**. The number, length, and thickness of the protrusions more closely resembled dendritic processes similar to those that have been observed in vivo.[215,271,275] This cell morphology contrasts with elongated cells exhibiting a few short protrusions that can be observed in fibrillar matrices.[291] Together, these results suggest that the HA matrix supports cell invasion that is morphologically similar to that observed in brain parenchyma.

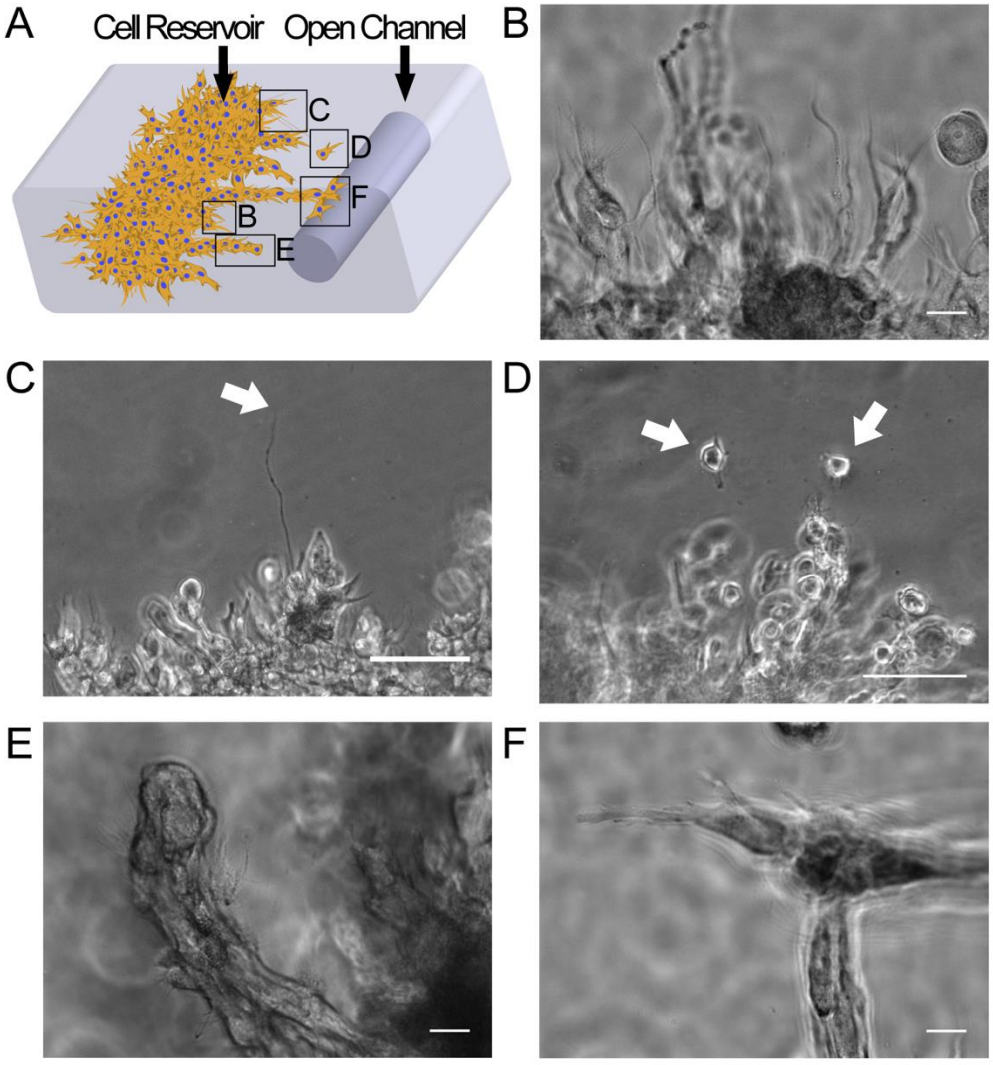

Figure 6. Cell morphologies during invasion. (a) Schematic representing the variety of invasion morphologies depending on the location and stage of invasion. Letters correspond to subsequent figure parts. (b) Invasion is usually preceded by the extension of long protrusions. Scale = 20 µm. (c) Protrusions occasionally reach lengths >100 µm, and the end of protrusion is marked by the arrow. Scale =100 µm. (d) Occasionally single

cells are observed invading the 3D matrix (arrows). Scale = 100 µm. (e) Most cells invade in multicellular “tunnels.” Scale = 20 µm.

We also investigated how cells move at a collective level. GBM cells in vivo move collectively as multicellular strands and less frequently as single cells.[215,271,291–293] While single cells occasionally invaded the 3D matrix **(Fig. 6d)**, invasion was most commonly observed as multicellular masses or “tunnels,” with protrusions extending from the end and sides of these masses **(Fig. 6e)**. This dynamic is consistent with a mechanism in which cells degrade and/or tunnel through the dense 3D matrix during migration. After reaching the open channel, cells changed direction and morphology **(Fig. 6f)**. Cells in the open channel were less rounded and more elongated, aligning parallel to the length of the channel. Thus, an embedded, open channel serving as a topographical model of the PVN is sufficient to recapitulate changes in cell morphology during invasion.

2.4.5 Topographical transitions are observed in multiple 3D matrix types

One of the key features of GBM invasion in vivo that we aimed to recapitulate in this model is rapid migration of cells along vascular tracks relative to the slow interstitial invasion. Having established that cells change the morphology and direction to follow the vessel-mimetic open channel, we investigated whether cells in channels migrated more rapidly than cells in the 3D matrix. Furthermore, we asked whether transitions were induced only by the HA matrix, known to promote cell invasion in the PVN. [294–296] We thus compared HA with collagen I, a fibrous matrix not normally abundant in brain ECM. Choosing a collagen matrix also enabled us to investigate the degree to which the migration mode is dependent on the matrix structure and to explore the versatility of our device in supporting the use of other matrix types.

We observed cell invasion through the 3D matrix and channels in both HA-RGD and collagen I hydrogels and compared cell speeds in these two regions of interest for both matrix types [Fig 7(a)]. Overall, cells in collagen I were more elongated with a more mesenchymal morphology and migrated more rapidly than cells in HA-RGD by approximately a factor of four. In contrast, cells in HA-RGD were more round with numerous dendritic protrusions. Despite the contrast in morphology and overall speed, cells invaded more rapidly (approximately twice the speed) in channels than in the 3D matrix for both matrix types. While the overall speed of invasion is dependent on the matrix type, the topographical cues from the channel drive a change in cell speed that is independent of the matrix composition.

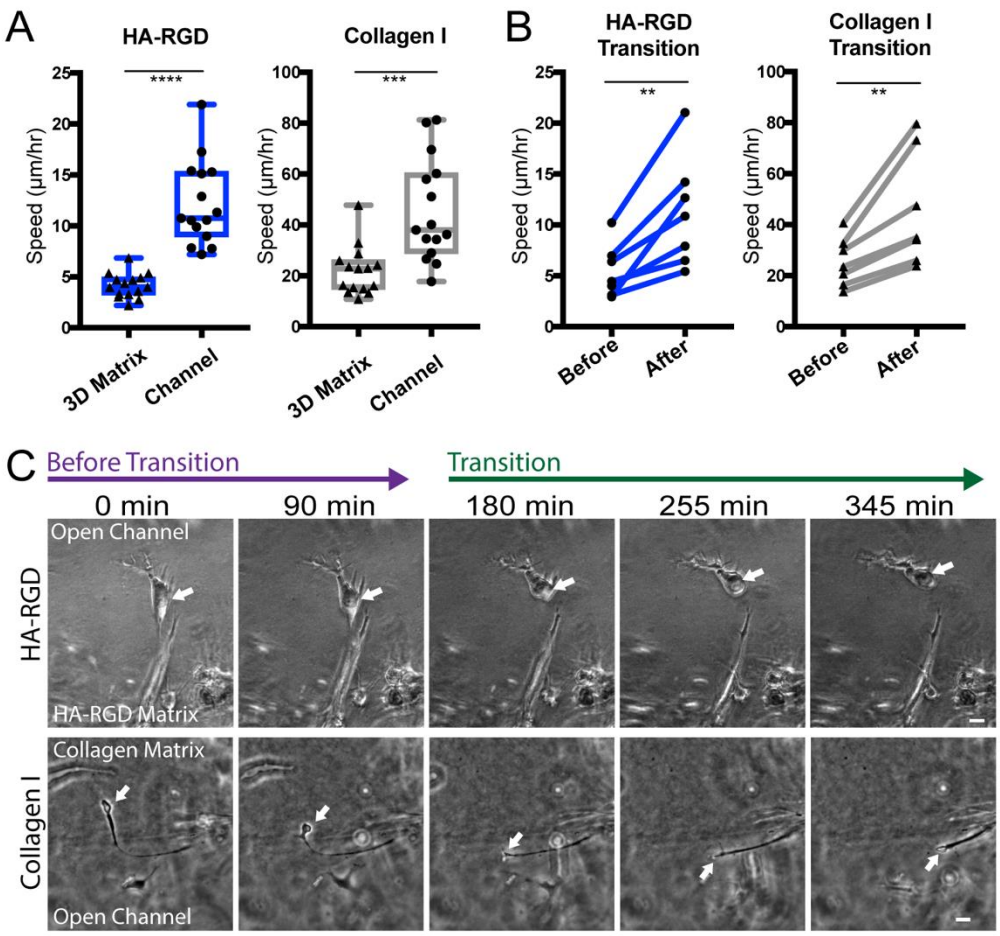

Figure 7. Transitions in the direction, speed, and morphology as cells encounter the open channel. (a) Cell speeds in the 3D matrix are slower than those in channels, ***, $p < 0.001$ by student's t-test. The center line represents the median, boxes represent the 25th and 75th percentiles, and whiskers represent the min and max. (b) Single cell speeds increase after the transition, **, $p < 0.01$ by the paired t-test of average difference between speed before transition and speed after transition. (c) In both HA-RGD and collagen I matrices, cells change the direction to align with the channel. Arrows point to the cell nucleus. Frames at 0 min and 90 min are before the transition of the entire nucleus out of the 3D matrix, while subsequent frames occur after the transition. Scale = 20 μm.

2.4.6 Topography-driven changes in migration speed are instructive rather than selective

The degree to which increased speed exhibited by cells within channels was due to cell-ECM interactions as opposed to cell-cell interactions remained unclear. For example, tumor cells often invade in a communal fashion, with leader cells remodeling the matrix to enable rapid migration of follower cells.[297] It is possible that the difference in migration speed in each topology is driven not by cell-instructive cues but rather by different subpopulations of cells, with one subset more adept at 3D invasion and another more

adept at perivascular invasion. Furthermore, the cell-ECM and cell-cell interactions that underlie single and collective cell migration could depend on the matrix type. Cells in the collagen matrix were more frequently observed moving as single cells and did not invade in the multicellular masses as in HA-RGD. It is likely that the increased pore size and the fibrous structure of collagen were more permissive of cell invasion, either changing or eliminating the role of leader cells.

To begin assessing the relative role of single cells in the transition to perivascular invasion, we quantified the invasion of cells crossing from the 3D matrix to the open channel [Fig. 7(b)]. A transition was defined as the time at which the nucleus fully exited the 3D matrix into the channel. We measured cell speed for a total of 6 h with a transition occurring between the first 3h and the second 3h. Migration speeds before and after the transition were compared [Figs. 7(b) and 7(c)]. Again, cells in the collagen I matrix migrated rapidly compared to HA-RGD. However, in both matrices, individual cells increased their speed after the transition. The speeds before and after the transition were similar to those measured when tracking cells in the 3D matrix or the channel only. We concluded that single cells responded to the open channel topography by increasing speed, leading to overall more rapid invasion along the channel.

2.4.7 Cytoskeletal architecture varies by the location and matrix type

While the increase in cell speed was observed in both matrix types, phase imaging suggested vastly different cell morphologies **(Fig. 7c)**. Specifically, we observed that cells in collagen I or in channels tended to have more linear morphologies in contrast to the rounded, dendritic morphologies seen in HA-RGD. Cytoskeletal architecture, particularly that of the actin cytoskeleton, can reflect mechanisms underlying invasion.[291] We asked whether distinct cytoskeletal architectures were correlated with specific invasion patterns seen in our various matrix formulations (HA, collagen I) and topographies (3D, channel). Following previous studies, we reasoned that actin bundles and stress fibers are more likely to accompany the fast mesenchymal-like migration observed in the open channels and in collagen.[298–300] In contrast, more diffuse cortical actin would be expected within HA-RGD. We therefore applied structured illumination microscopy (SIM) to characterize actin cytoskeletal architecture in each of these scenarios **(Fig. 8)**.

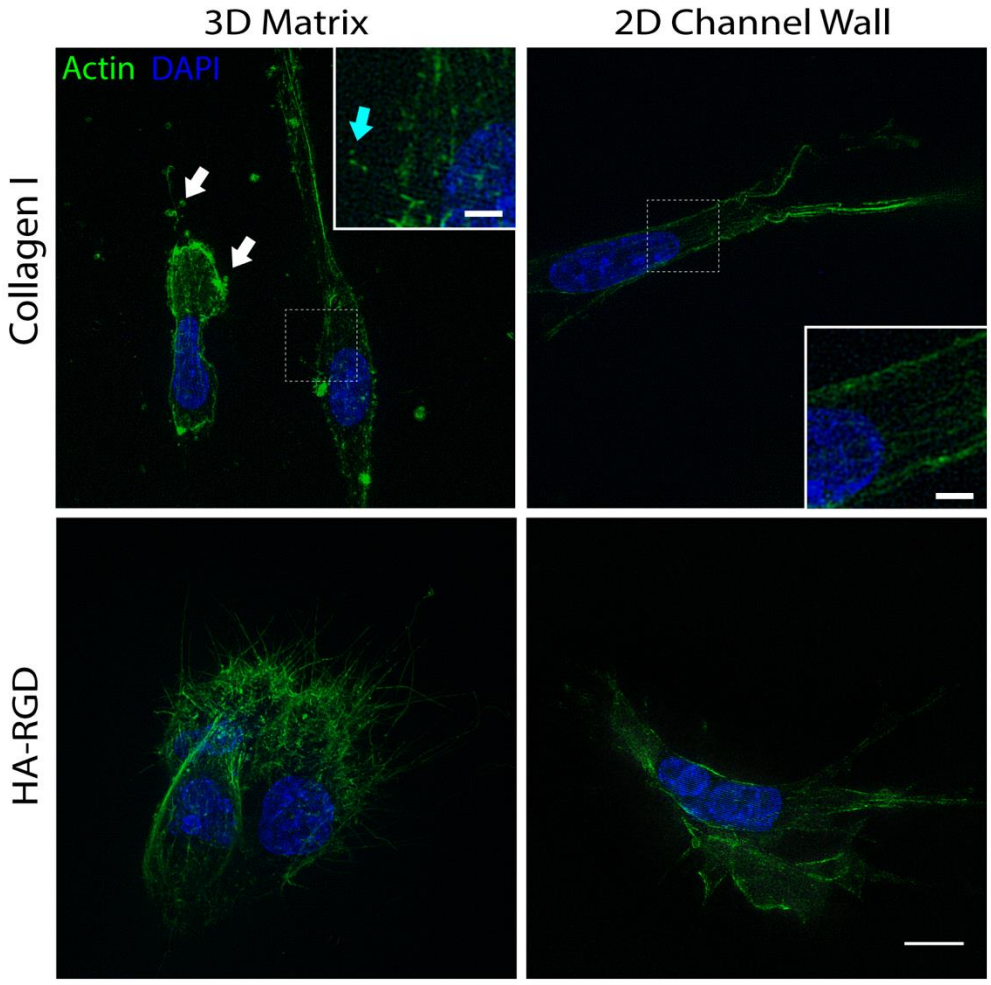

Figure 8. SIM imaging of fixed cells revealing distinct actin architectures. Cells in 3D collagen I gels show evidence of membrane blebbing (white arrows) and nuclear squeezing and also express more numerous short filopodia (blue arrow, inset) than cells in the collagen I channel. Cells in the 3D HA-RGD matrix are densely packed and rounded and express numerous long, thin filopodia. Cells in HA-RGD channels express actin filament bundles and protrusions aligning with the channel wall. Scale = 10 µm; inset scale = 2 µm. Z stacks were 20 µm (top left), 11 µm (top right), 23 µm (bottom left), and 11 µm (bottom right) with 1 µm spacing between slices.

As we anticipated, cells in 3D collagen I assembled long actin filament bundles that align with the direction of migration. This was not the exclusive phenotype, as some cells exhibited an elongated nucleus with membrane blebs, suggesting confined, amoeboid migration. Compared to cells in collagen I channels, cells in 3D collagen expressed short and more numerous filopodia. In contrast to cells in collagen, cells in 3D HA were almost exclusively rounded and had numerous single actin filaments with relatively thin and few filament bundles. Cells in HA-RGD channels were elongated with fewer and longer actin filament-based invasive protrusions. As with collagen I, this was accompanied by assembly of actin bundles aligned in parallel with the channel. Overall, the morphology of cells in 3D was distinct from those in the channel, and the contrast was much greater in

HA-RGD gels. These results explain the hierarchy of migration speeds (channel collagen>3D collagen>channel HA>3D HA). Migration speed is tied to the propensity of the matrix to support actin bundle-driven mesenchymal migration: fastest in a fibrous matrix arranged in a linear channel and slowest in a non-fibrous matrix in 3D. These results also underscore that the migration mode is dependent on the matrix type and that cell morphologies in the HA-RGD matrix compared to collagen I are more similar to those observed in vivo. Still, topography influences the migration mode and speed in a similar fashion within a particular matrix type. While we observed an analogous increase in speed and change in morphology within HA-RGD and collagen I matrices, it is possible that changing cell types or matrix compositions will result in an altogether different type of response to topographical cues. Future investigation of other matrix compositions, possibly with spatial organization of ligands or modulus, may uncover potentially synergistic roles of topography and matrix in promoting invasion.

2.4.8 Integrin engagement and cell contractility promote cell invasion in HA matrices

We then investigated whether integrin engagement and cell contractility were necessary to support invasion into HA-based matrices. While cells are capable of binding to HA-based matrices independent of integrin adhesions, we hypothesized that integrin binding and contractility allow cells to squeeze through the matrix while forming reinforced adhesions that facilitate cell invasion. We compared mass expansion and invasion areas in devices with or without RGD in the matrix and with or without myosin II inhibition through blebbistatin treatment. Blebbistatin treatment significantly reduced the mass expansion of the reservoir **(Fig. 9a)**. Cells in devices lacking RGD or treated with blebbistatin exhibited significantly less invasion and tunneling into the surrounding matrix **(Figs. 9b and 9c)**. Furthermore, we observed different cell morphologies in matrices with or without RGD. Cells invading HA-RGD exhibited long, thin protrusions preceding invasion, while cells in the HA matrix remained largely rounded **(Fig. 9d)**. Thus, cells appeared to transition from a slow, more amoeboidal mode of migration with no RGD and low contractility to a more rapid, mesenchymal mode of migration with RGD in the matrix and uninhibited contractility.

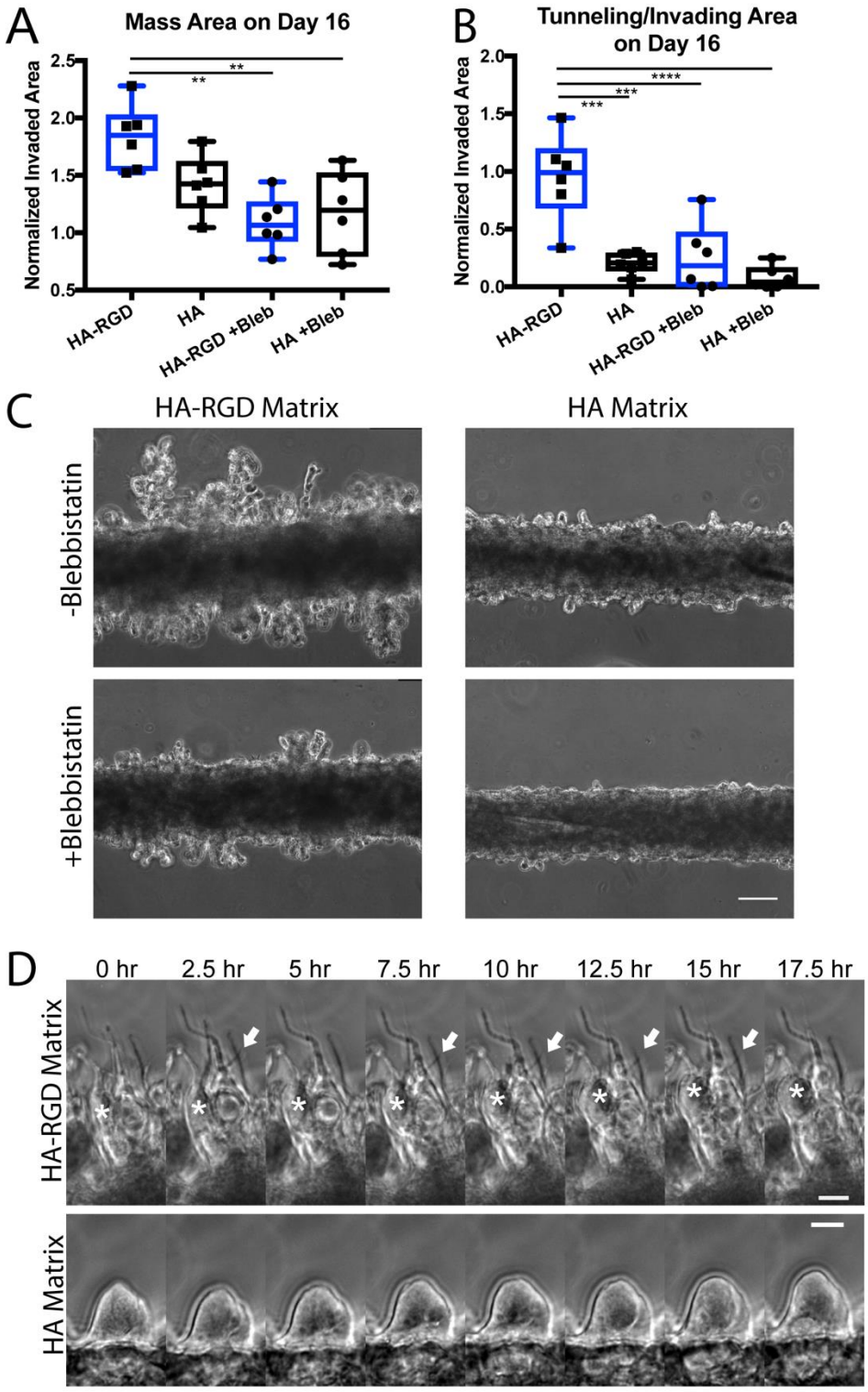

Figure 9. Cell invasion is dependent on integrin engagement and cell contractility. (a) Mass area and (b) tunneling/invading area of cells in HA-RGD and HA matrices treated with or without 10 μM blebbistatin normalized to the initial area on day 1 for n=6 devices

per condition 16 days after seeding. **, p<0.01; ***, p<0.001; ****, p<0.0001 by ANOVA followed by Tukey's test for multiple comparisons. The center line represents the median, boxes represent the 25th and 75th percentiles, and whiskers represent the min and max. (c) Tunneling and invading morphology is decreased with blebbistatin treatment and without the RGD ligand in the matrix. Scale = 100 μm. (d) Invasion in the HA-RGD matrix occurs preceded by thin protrusion extension, while invasion in the HA matrix is not. The arrow indicates protrusion dynamically extending and retracting, and the asterisk indicates the cell shifting toward protrusions.

Compared to our previous results in collagen I matrices, these data suggest that our matrices promote a range of migratory phenotypes with more mesenchymal behavior (collagen I > HA-RGD > HA). These results may also reflect the role of the pore size in regulating invasion. We have previously demonstrated that our HA gels are nanoporous (average mesh size 100–150 nm).[196] Thus, cells are likely to rely on matrix degradation to invade into the gel, resulting in more amoeboidal invasion. Collagen gels, however, have pore sizes on the scale of microns, which enable cell migration without degradation, resulting in faster invasion speeds.[201] As a whole, these experiments demonstrate the possibility of using our platform to investigate the effects of the matrix composition and treatment, which in the future could be leveraged to perform deeper mechanistic studies or conduct screening.

2.5 Conclusions

We have developed a topographical culture model that is sufficient to recapitulate and observe multiple stages of invasion (expansion, matrix infiltration, and invasion along anatomical tracks) with a distinct transition in cell morphology and speed resembling GBM invasion toward and along the PVN. We have demonstrated that the increased speed and the change in the direction are generalizable across matrix types and that distinct actin architectures support these transitions. This work underscores the utility of incorporating topographical cues into 3D invasion models to study multiple modes of invasion relevant to clinical GBM progression. While this study is focused on topographical effects on speed and cell morphology, the platform could be used to conduct screening and investigate cell signaling and mechanistic pathways underlying invasion.

2.6 Acknowledgements

Confocal images were acquired at the CRL Molecular Imaging Center at UC Berkeley, supported by National Science Foundation Grant No. DBI-1041078. We would like to thank Holly Aaron and Jen-Yi Lee for their assistance in training. Additional confocal images were obtained in the Shared Stem Cell Facility, which provided the Prairie Swept Field Confocal Microscope. We thank Dr. Mary West of the CIRM/QB3 Shared Stem Cell Facility at UC Berkeley. Structured illumination microscopy was conducted at the UC Berkeley Biological Imaging Facility, which was supported in part by the National

Institutes of Health S10 program under Award No. 1S10(D018136- 01). The content is solely the responsibility of the authors and does not necessarily represent the official views of the National Institutes of Health. We would like to thank Dr. Steve Ruzin and Dr. Denise Schichnez for their technical assistance and training. Finally, the authors gratefully acknowledge financial support from the following sources: National Science Foundation (Graduate Research Fellowship to K.W.); National Institutes of Health (Ruth L. Kirschstein Predoctoral Individual National Research Service Award No. F31GM119329 to S.L., R21CA174573, R21EB025017, and R01GM122375 to S.K.); and the W.M. Keck Foundation (S.K.).

Chapter 3: Hyaluronic Acid: Incorporating the Bio into the Material

Parts of this chapter are excerpted with permission from Springer Nature, from the article "Hyaluronic Acid: Incorporating the Bio into the Material," by Kayla J. Wolf and Sanjay Kumar in *American Chemical Society Biomaterials Science and Engineering*, 5 (8), 3753-3765 (2019).

3.1 Abstract

In the last few decades, hyaluronic acid (HA) has become increasingly employed as a biomaterial in both clinical and research applications. The abundance of HA in many tissues, together with its amenability to chemical modification, has made HA an attractive material platform for a wide range of applications including regenerative medicine, drug delivery, and scaffolds for cell culture. HA has traditionally been appreciated to modulate tissue mechanics and remodeling through its distinctive biophysical properties and ability to organize other matrix proteins. However, HA can influence cell behavior in much more direct and specific ways by engaging cellular HA receptors, which can trigger signals that influence cell survival, proliferation, adhesion, and migration. In turn, cells modify HA by regulating synthesis and degradation through a dedicated arsenal of enzymes. Optimal design of HA-based biomaterials demands full consideration of these diverse modes of regulation. This review summarizes how HA-based signaling regulates cell behavior and discusses how these signals can be leveraged to create cell-instructive biomaterials.

3.2 Introduction

Hyaluronic acid (HA, also called hyaluronan) is a linear polysaccharide expressed in almost all bodily tissues and fluids at a concentration and molecular weight (MW) that varies by tissue type.[104] The nearly ubiquitous expression of HA is suggestive of both its biological importance as well as its potential for clinical application. HA is amenable to a variety of chemical modifications through three orthogonal functional moieties (hydroxyl, carboxyl, and amide), facilitating its use for numerous applications requiring conjugation or crosslinking.[232,301] While often incorrectly portrayed as an inert or non-adhesive scaffold, HA actually provides a rich abundance of mechanical and biological signals to surrounding cells and tissues.[105,302] Cell surface receptors specific for HA enable cells to respond to the biophysical properties of HA, which can be modulated in vivo by controlling HA abundance, MW, and other factors.[303,304] Cues from HA within the extracellular matrix (ECM) influence cell adhesion, migration, and downstream cell signaling **(Fig. 1).** In turn, cells modify and regulate the HA in the ECM through synthesis, degradation, and organization.[305,306] HA-based signaling is especially important in development, wound healing, and metastatic disease.[53,307–309] Resultant biological signals are critically dependent on the biophysical properties of HA, and thus require consideration in biomaterial design.

Cells bind to HA directly through membrane receptors resulting in transduction of biochemical signals and reinforcement of mechanical linkages that directly mediate adhesion and motility.[49,303] The most studied of these HA cell receptors are CD44 and the Receptor for HA-Mediated Motility (RHAMM) **(Fig. 1)**. CD44 is a transmembrane receptor that binds to extracellular HA through a single binding domain and links indirectly to the actin cytoskeleton by way of ezrin, moesin, or radixin (ERM) family proteins or to the spectrin cytoskeleton through ankyrin proteins.[49] RHAMM contains two HA-binding domains in which HA is bound less tightly than in the HA-binding domain of CD44.[310,311] RHAMM is not a transmembrane receptor, and can exist intracellularly or on the extracellular cell surface in complex with other receptors such as CD44.[311] The reported relationship between RHAMM and CD44 in mediating cell adhesion to HA has been somewhat contradictory and may be context dependent. For example, Lokeshwar and colleagues found RHAMM to be the main mediator of HA binding in primary human endothelial cells.[312] In contrast, Savani and colleagues found that anti-CD44 but not anti-RHAMM antibodies inhibited adhesion of endothelial cells to HA.[313] Similarly conflicting observations have been reported in glioblastomas (GBMs).[54,74] These findings may potentially be reconciled by the fact that RHAMM modifies signaling through CD44, with the degree of modification depending strongly on context. For example, studies of invasive breast cancer cells demonstrate that CD44 and RHAMM coordinate to regulate ERK1/2 signaling and cell motility.[314] Overall, the role of RHAMM and CD44 interactions in cell motility and dependence on the microenvironment remains an open question.

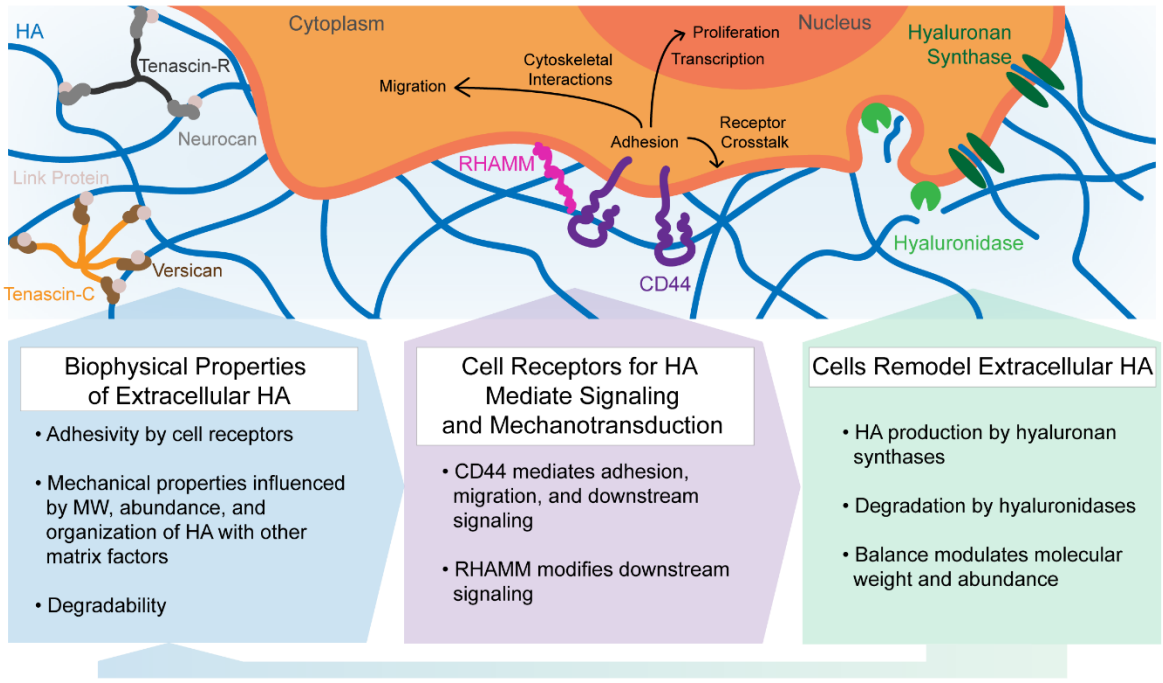

Figure 1. Cells sense biophysical properties of extracellular HA (adhesivity, mechanical properties, and degradability) through surface receptors such as CD44 and RHAMM. These biophysical properties influence cell adhesion, migration, and proliferation through cytoskeletal interactions, transcription, and receptor crosstalk. In turn, cells remodel

extracellular HA through synthesis by hyaluronan synthases and degradation by hyaluronidases.

Independent of its relationship with RHAMM, CD44 plays a critical role in cell motility.[49] For example, CD44 protein expression is increased in highly invasive and/or metastatic cells.[296,315] In GBMs, high CD44 protein levels correlate with the most rapidly invading cell populations,[294] and neutralization or knockdown of CD44 significantly impairs GBM invasion in animal models.[48] CD44 can directly support adhesion and migration, likely through its intracellular cytoskeletal linkages. For example, human prostate cancer cells expressing CD44 mutants lacking the ankyrin binding domain do not adhere to HA.[316] However, the relative contributions of ERM and ankyrin binding to CD44-dependent signaling remains poorly understood and are likely to be context-dependent. CD44 can also complement and potentiate signaling from other surface receptors; for example, Chopra and colleagues found that HA-CD44 binding can increase integrin signaling resulting in cell spreading.[317]

Growing evidence demonstrates that CD44, like integrins, is involved in sensing mechanical signals from the HA matrix. Our laboratory demonstrated that CD44-mediated adhesion and migration depend on the storage modulus of crosslinked HA hydrogels.[74] One possible mechanism governing CD44-mediated mechanosensitivity is that CD44 can undergo force-dependent switching between low affinity and high affinity HA-binding states. The crystal structure of the CD44-HA complex supports this idea, revealing that there are at least two binding conformations.[318] Similarly, molecular dynamics simulations suggest that HA can bind to CD44 in three different conformations, two of which are metastable states that enable low affinity binding.[319] DeGrendele et al. demonstrated that leukocytes adopt a high-affinity state for HA binding during rolling, when adhesive tethers are stressed.[320] Suzuki et al. showed that force experienced by leukocytes during rolling could convert HA-CD44 binding from a low affinity to high affinity state.[321] While these studies differ on the number of proposed binding states, they together strongly suggest that CD44 exhibits force-dependent changes in HA-binding affinity and therefore mechanosensitivity. Shedding of CD44 is also important for CD44-mediated functions, but the role in mechanosensitivity is poorly understood.[322] While there are still numerous open questions regarding CD44-mediated mechanosensitivity and motility, these findings underscore the biological importance of HA mechanics within the ECM.

Several other cell receptors have been reported to bind to HA, although the relative affinities for HA, mechanical roles, and resulting downstream signaling are incompletely understood. Lymphatic Vessel Endothelial Hyaluronan Receptor 1 (LYVE-1) is a lymphatic-specific HA receptor that may play an important immunological function.[323,324] Layilin is a transmembrane protein reported to bind to HA extracellularly and to radixin and merlin proteins intracellularly, but the function is poorly understood.[325,326] HA signaling can also be mediated by Toll like receptors 2 and 4 (TLR2/4),[327–329] but more recent evidence suggests that the signaling effects may not act through a direct ligand-receptor interaction.[330] Finally, tumor necrosis factor-stimulated gene 6 (TSG-6), is a signaling factor that can bind with HA and may enhance CD44-based signaling.[331,332]

Elevated levels of TSG-6 have been observed in the central nervous system following injury.[333]

The biophysical properties of HA can greatly impact the nature of HA-induced cell signaling such that optimized biomaterial design is necessary for appropriate downstream effects. In this review, we begin by discussing key biophysical properties of HA most pertinent to biomaterial design, broadly defined as mechanics, adhesivity, and degradability. We focus on how HA mechanics vary by tissue type and state, and how adhesivity and degradability relate to mechanics. These properties can profoundly influence cell and tissue homeostasis and disease, and we present selected examples from development, wound healing, and tumor progression. Within a biomaterial, the biophysical properties of HA are critically dependent on fabrication methods. Thus, in the second part we discuss how these biophysical properties can be incorporated in biomaterial design, along with the benefits and limitations of various strategies for doing so. As a whole, this review should provide guidance in selecting and achieving optimal biophysical design criteria for a given application.

3.3.1 HA Biophysical Regulation of Cell Behavior within Tissue

HA is a critical driver of a variety of normal and disease processes, including development, wound healing, tissue maintenance, inflammation, and metastasis.[53,105,306–309,334] HA properties, particularly MW and abundance, undergo characteristic changes that support and drive tissue remodeling and homeostasis.[104,305,335] For example, HA levels in tissue tend to be higher during development and play a particularly prominent role in the hematopoietic stem cell niche and central nervous system.[307,336,337] HA is dynamically activated in the early stages of wound healing during which it may promote matrix organization, fibroblast migration, or tissue hydration.[308,334] HA and associated regulatory enzymes are abnormally overexpressed in a variety of tumor types.[53,309] This section will cover the biophysical properties of HA pertaining to adhesivity, organization, and mechanics with a discussion of their interdependency and select examples of biological impact.

3.3.2 HA Adhesivity and Organization Influences Mechanics

HA is a linear and negatively charged polysaccharide composed of disaccharide repeats of D-glucuronic acid and N-acetyl-D-glucosamine **(Fig. 2)**.[338] It is unique among glycosaminoglycans in that it is not a proteoglycan, is synthesized at the plasma membrane instead of the Golgi apparatus, and remains unsulfated and as an unbranched structure within the ECM.[339] Each monomer contains one carboxylic acid, one primary alcohol, and one amide moiety, which are important for biological function and available for chemical modification. The carboxylic acid of the glucuronic acid subunit is effectively deprotonated at physiological pH, giving rise to a polyanionic character.[340]

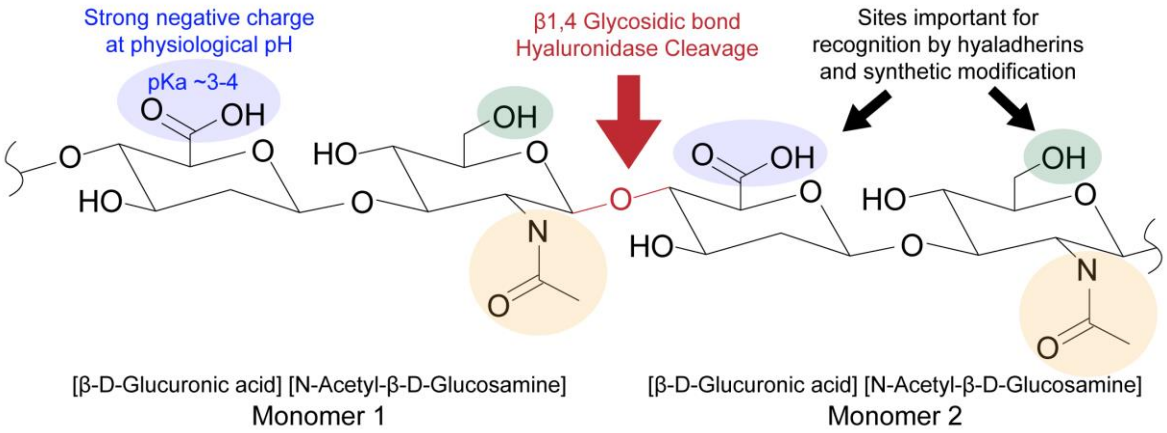

Figure 2. Chemical structure of HA. The carboxylic acid (blue) and primary alcohol (green) are important for both recognition by hyaladherins and for chemical modification. The amide (yellow) also supports adhesion but is less commonly modified.

The mass of an average human adult consists of ~15 g of HA throughout the body, with ~30% of this total turned over daily.[305,339] While some HA is found in virtually all tissue ECMs in the body, the abundance, organization, and MW of HA are strongly tissue-dependent.[104] Solid tissues in rabbit have been reported to have a range from 1 – 500 µg HA /g of wet tissue, while human cartilage contains as much as 2500 µg HA /g of wet tissue.[341,342] While the concentration of HA in most fluids is in the ng/mL to low µg/mL range, the concentration of the vitreous humor is as much as 200 µg/mL[343] and that of the synovial joint is as much as 2-3 mg/mL.[344] HA is traditionally regarded as an extracellular polymer; very little is understood about the intracellular role of HA.[306,345] We focus exclusively on extracellular HA in this review based on its relevance for biomaterial design.

In fluids, HA does not exhibit a well-defined network structure but instead forms entangled networks that contribute to fluid viscosity particularly at high molecular weight (HMW) or with light crosslinking.[346,347] The persistence length of HMW hyaluronan has been estimated to be ~10 nm, approximately 10 monomers, which is around the same length of HA that can bind to a single HA-binding domain.[348] Proteins with HA-binding domains (hyaladherins) contribute to non-covalent assembly of HA *in vivo,* and aspects of this assembly can be mimicked *in vitro*. In the presence of aggrecan, HA forms more ordered structures in solution with higher packing densities. leading to an increase in viscosity.[349] In synovial joint fluid, assembly of these dense, viscous complexes are widely regarded as important for maintaining shear flow while resisting osmotic compression and absorbing compressive force.[349–351]

In solid tissues, HA is non-covalently assembled into a network by a subset of proteoglycans with HA binding domains.[111,309,339] The organization varies by tissue type as well as the local cellular microenvironment **(Fig. 3)**. In the brain, tenascins organize with link proteins and chondroitin sulfate (CS) proteoglycans such as versican, neurocan, and aggrecan to stabilize entangled networks of HA.[111,112] These networks can form perineuronal nets that surround the cell membrane.[352] HA-matrix organization dominates

the intraparenchymal space of brain ECM, which is particularly high in HA content and low in fibrous proteins such as collagen I.[47] In cartilage, HA is also bound and organized by proteoglycans but assembles into an interpenetrating network with collagen fibrils.[353,354] HA-CS binding is mechanically reinforced by complexation with link proteins, which contain binding domains for both HA and CS.[355] The organization and mechanical reinforcement of HA with other proteins is thus important for the mechanical properties of the overall matrix.

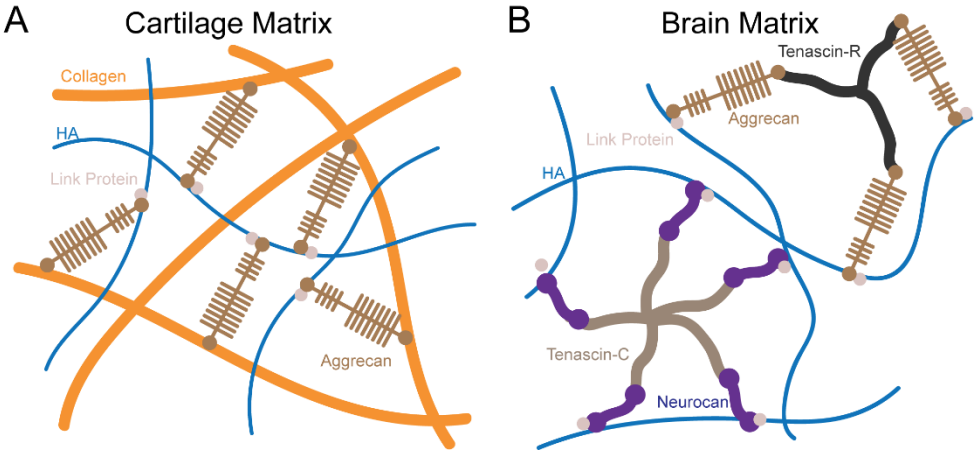

Figure 3. Matrix organization of HA varies by tissue type and cell microenvironment. A) HA organizes as an interpenetrating network that interacts with mechanically-reinforcing collagen fibers in cartilage tissue. B) In contrast, intraparenchymal regions of brain tissue are generally devoid of collagen fibers and HA organizes primarily with chondroitin sulfates.

Hyaladherin-HA binding is generally based on a conserved mechanism involving electrostatic interactions. HA-binding domains, both in matrix proteins and cell receptors, contain positively-charged lysine and arginine residues, which coordinate with the negatively-charged HA backbone and bind 3-6 monomers depending on the hyaladherin type.[356,357] Bano and colleagues investigated hyaladherin-HA affinity by measuring the rupture forces of HA and various hyaladherin binding domains using atomic force microscopy.[358] The rupture force roughly correlated with the number of HA monomers bound by the hyaladherin and ranged from 24-52 pN. Remarkably, reinforcing aggrecan-HA binding by complexing with cartilage link protein effectively increased the binding force above that measured for streptavidin-biotin bonds. This result further supports the idea that HA-binding affinity depends on the length of the HA segment bound as well as underscores the role of HA in supporting ECM mechanical integrity.

3.3.3 Remodeling of HA Alters Mechanics

The MW of HA in the human body varies widely, from tetramers of around 1 kDa to HMW species of around 2 MDa.[335] Changes in MW distribution affect both the physical properties of HA within the ECM as well as cellular biochemical signaling. The effects of MW on the physical properties of ECM stem largely from its contributions to mechanics. Within solutions, increasing MW greatly increases viscosity of HA, reflective of greater entanglement.[359] The mechanical properties of HMW HA are key to the proper function

of synovial joint fluid by resisting compressive forces while allowing shear thinning.[360,361] Increases in low molecular weight (LMW) HA are associated with pathological conditions; for example, osteoarthritis patients exhibit a higher ratio of LMW to HMW HA in synovial fluid compared to healthy patients.[362] Similarly, LMW HA is not commonly found in solid tissue unless the tissue is undergoing either a physiological or pathological remodeling process.[104,305,335] Elevations and other alterations in LMW HA species have been observed in cartilage during aging,[363] as well as in a variety of tumors.[364–366] Broadly, these studies suggest that a shift from HMW to LMW species is associated with plasticity in ECM mechanics and potentially loss of structural integrity.

HA MW can also influence biological processes through biochemical signaling. LMW HA generally stimulates an inflammatory response while HMW HA induces an anti-inflammatory response.[335] In macrophages, LMW HA fragments upregulate inflammatory gene expression contributing to polarization toward a tissue-destructive state.[367] Later work showed that while LMW and HMW HA both activate macrophages, LMW HA induces a pro-inflammatory gene expression profile whereas HMW induces a pro-healing gene expression profile.[368] The mechanisms by which cells sense and respond to MW of HA remain unclear, but experimental studies support several possibilities. It is possible that HA MW may affect cell signaling indirectly through changes in matrix mechanical properties such as increased viscous behavior resulting from increased chain entanglement, but the relative importance of this effect has not been directly demonstrated in vivo. More directly, HMW HA can induce multivalent binding and receptor clustering. Yang et al. showed that HMW HA induces CD44 clustering while HA oligomers of 3 – 10 monosaccharides inhibit clustering, with each reagent exerting differential effects on downstream ERK signaling.[369] From a physical perspective, higher MWs stabilize binding to CD44 such that LMW HA binding is reversible while HMW binding is essentially irreversible.[370] The cumulative effects of binding time and stability could have a range of effects on cell motility and downstream signaling. MW may also affect cellular uptake and downstream intracellular signaling, but this process and mechanistic effects are not well understood.[371]

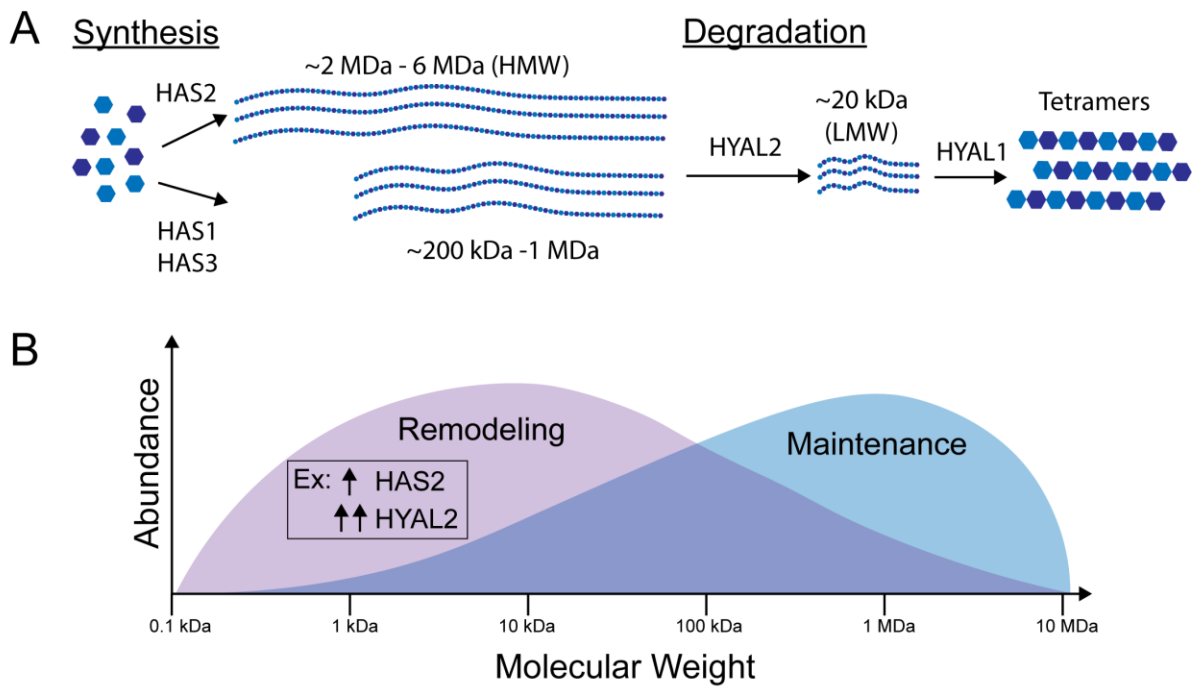

Figure 4. The regulation and role of HA MW in biophysical signaling. A) MW is dependent on expression and activity of hyaluronan synthases and hyaluronidases. HMW HA is synthesized at lengths dependent on the hyaluronan synthase. HMW HA is degraded by HYAL2 to form ~20 kDa fragments which are then further degraded by other hyaluronidases, primarily HYAL1, into tetramer units. B) Human HA is present in a distribution of MWs varying from about 0.1 kDa to 2 MDa. LMW HA elicits a tissue remodeling response, while HMW promotes tissue maintenance. A shift from HMW species to LMW species can be induced by increased synthesis (HAS2) followed by greatly increased degradation (HYAL2) leading to the accumulation of HA fragments.[365,366]

The MW and abundance of HA are mediated by the activity of hyaluronan synthases and hyaluronidases **(Fig. 4A)**. There are three hyaluronan synthases (HAS1, HAS2, HAS3), all of which are multifold transmembrane receptors that vary in expression, rate, and MW of the HA produced. HAS1 has a slower rate of synthesis than HAS2 and HAS3. HAS1 and HAS3 produce lower MW species, while HAS2 can produce very HMW species.[372,373] HAS2 seems to play a particularly significant role in cell invasion and cancer progression. Its expression is elevated in diffusely infiltrating astrocytomas and serves as a prognostic factor.[55] Elevated HAS2 correlates with lower survival in breast cancer[365] and primary brain cancers.[55]

Five hyaluronidases are encoded in the human genome (HYAL1, HYAL2, HYAL3, HYAL4, PH-20/SPAM1), and their expression and function differ by tissue type.[374] Notably, PH-20/SPAM1 is expressed only in testes, while the rest of the hyaluronidases are expressed more broadly. Structures of human HYAL1 show that hyaluronidases bind tetrasaccharides, and the enrichment of arginine residues in the binding cleft suggest the importance of the carboxylic acid on HA for proper recognition.[375] The hyaluronidases

differ in the MW of HA they recognize as well as the MW of their cleavage products. Notably, HYAL2 cleaves HMW HA to ~20 kDa fragments, while other hyaluronidases cleave ~20 kDa fragments to tetrasaccharide products.[374]

Differential expression of enzymes with varying substrates, rates, and products provides a means by which cells can regulate the MW of HA within their environment and resulting shift between inflammatory/pro-metastatic and anti-inflammatory/anti-metastatic signals **(Fig. 4B)**. While this balance remains poorly understood, recent studies are revealing the biological function of this balance. As previously described, tumors are often HA-rich. *In vitro* models suggest that glioblastoma cells upregulate HA synthesis if HA is lacking in the surrounding matrix,[376] and that incorporation of HA into gelatin matrices alters inhibitor sensitivity and upregulates malignancy.[207,243] Interestingly, both HYAL2 and HAS2 gene expression are increased in mesenchymal subtype tumors, and inhibition of HAS2 gene expression results in more dependence on focal adhesion-mediated invasion.[377] A similar pattern of expression is observed in highly invasive breast cancers, which express abnormally high amounts of both HYAL2 and HAS2.[378] This somewhat paradoxical increase in expression of both synthases and hyaluronidases enriches the microenvironment in short, loosely bound, HA fragments.[366] Consistent with this finding, Wu and colleagues observed that LMW HA, but not total HA, correlated with lymph node metastasis and cell invasiveness, and that both hyaluronidases and hyaluronan synthases were overexpressed.[365] Similarly, accumulation of LMW HA and the shift toward a metastatic phenotype results from upregulation of HA synthesis and degradation in prostate cancer.[379,380]

A notable recent study by Tian and colleagues demonstrated the relationship between very HMW HA (10 MDa) and cancer incidence in the naked mole rat, a species in which cancer is rarely observed.[52] By perturbing the abundance of the HMW HA either through HAS2 knockdown or HYAL2 overexpression, naked mole rat cells became highly susceptible to malignant transformation. These results clearly demonstrate the important biological role of HA MW regulation and its therapeutic potential.

3.4.1 Incorporation of HA Biophysical Properties into Biomaterial Design

While HA provides a rich set of biological cues *in vivo*, the biophysical signals arising from HA in biomaterials may dramatically differ depending on the fabrication method. We consider these biophysical properties categorically as relating to either mechanics, adhesivity, or degradability (**Table 1**). We then discuss strategies to achieve these properties in various biomaterial applications with the potential advantages or disadvantages of each strategy.

3.4.2 Applications of HA-based biomaterials

One of the earliest clinical applications of HA was to restore lubrication and enhance stress dissipation (viscosupplementation) in joints as a therapeutic treatment for osteoarthritis.[381] Not long after, HA became more widely used for viscosupplementation in ophthalmology, and eventually otology.[381,382] Early work in these applications revealed

that a main limitation of viscosupplementation was the rapid degradation (<1 day) of the injected HA, thereby reducing the therapeutic benefit.[383] Chemical modification and crosslinking of HA was explored as a means to reduce degradation rates and extend treatment.[384] As methods to chemically modify HA developed, the use of HA has expanded to dermal fillers, tissue regeneration, and drug delivery.[385–389] In many of these applications, the anti-inflammatory, anti-tumorigenic properties of HMW HA have proven attractive. As a drug delivery vehicle, HA can be used to protect peptide or nucleotide therapeutics from rapid degradation or to target cells or tissues with high HA uptake.[390] A number of excellent reviews have been written about the clinical applications of HA matrices.[391–393]

A developing application of HA is for tissue engineering.[394] HA-mediated signaling, particularly that arising from HMW HA, supports survival, proliferation, and stemness. Thus, HA-based biomaterials show promise for encapsulating stem cells and supporting their directed differentiation. As an example, Gerecht and colleagues demonstrated that HA-based hydrogels can maintain stemness of human embryonic stem cells, but that the addition of soluble factors could still induce differentiation in a controllable manner.[395] We have demonstrated that HA-based scaffolds support viability of implanted human pluripotent stem cell-derived dopaminergic neurons and neural progenitor cells for treatment of Parkinson's disease.[396,397] HA-based hydrogels have also been explored as scaffolds for adipose tissue[398,399], cartilage[400], and bone engineering.[401] Because HA is a major component of endogenous ECM and the mechanics of HA can be tuned through a variety of parameters, HA-based biomaterials with controllable mechanics are also used as a research platform in mechanobiology.[186,402–404]

Central to the development of HA-based biomaterials is the presence of three functional moieties (primary alcohol, carboxylic acid, and amide) that can chemically and orthogonally modified, facilitating control of biophysical properties for the desired application.[195,232,301,405,406] Most modifications are made to the carboxylic acid and the primary alcohol, but modifications can also be made to the amide.[232] These modifications support a large backbone diversity, which can then be crosslinked to form a gel or conjugated with peptides, growth factors, or other matrix proteins.[301] HA can also be crosslinked with other polymer backbones to form semi-interpenetrating networks.[407–409] Several excellent reviews have detailed the various chemistries and methodologies used for HA modification.[232,301,405]

3.4.3 Incorporating HA Mechanics into Biomaterial Design

To control mechanical properties of HA-abundant fluids for applications such as viscosupplementation, the concentration and MW of HA are the most important parameters.[346,347] Thus, the viscosity of soluble HA may be easily modulated simply by choosing an appropriate MW range and concentration. For applications requiring solid rather than fluid biomaterials, gelation must be induced through some form of crosslinking. In this case, the backbone MW, the degree of crosslinking, the chemistry of the modification and crosslinker, and the matrix density can all contribute to the bulk matrix properties. Bulk matrix properties can be engineered by tuning any of the

aforementioned parameters, but some strategies may reduce cell viability or motility. Several studies have noted that high density HA matrices restrict cell migration and diffusion of biomacromolecules.[196,410]

One commonly used mechanical parameter of HA and other biological materials is the bulk storage modulus, which is widely understood to be an important effector of cell spreading and motility.[192,411,412] The storage modulus varies widely by tissue type, from a few hundred Pa in soft tissues such as fat, marrow, and brain to tens of MPa in bone.[413] HA materials are most easily fabricated with elastic moduli in the hundreds of Pa to tens of kPa, a range which encompasses most soft tissues.[414] HA hydrogels are often limited for applications in regenerating hard tissues such as cartilage or bone regeneration due to the comparatively low elastic modulus of these materials. One strategy for augmenting the elasticity of HA matrices is to assemble composite polymer networks with stiffer materials. For example, Tavsanli and colleagues used an HA and poly(N,N-dimethylacrylamide) (PDMA) to create hydrogels with high strength and high compressive modulus (in the MPa range) necessary for load-bearing tissues.[415] As described below, a number of investigators have also exploited mixed stiff HA/collagen and HA/gelatin scaffolds for cell culture applications.

While mechanical characterization of solid biomaterials often tends to focus on bulk storage modulus, tissues are typically viscoelastic rather than purely elastic, and this mixed character can greatly influence cell morphology and signaling. Dense HA networks crosslinked with covalent bonds typically exhibit high elasticity with very little viscosity. However, incorporating crosslinks that can dynamically switch between bound and unbound states over experimental time scales results in an increased viscous component. For example, HA viscoelastic properties may be controlled by conjugating cyclodextrins to the HA backbone, which enables supramolecular assembly into structures capable of both storing and dissipating mechanical stresses.[416] Variation of viscoelastic properties in this way influences mesenchymal stem cell (MSC) viability.[403] More recently, Lou et al. employed a dynamic hydrazone bond to crosslink HA polymers within an interpenetrating network of HA and collagen I in order to confer stress relaxation to the hydrogel. Varying the crosslinker affinity, MW of HA, and concentration of HA allowed for tuning of the relaxation time, with faster relaxation times promoting MSC spreading and focal adhesion formation.[417]

Tissue ECM is not spatially homogeneous but rather exhibits temporal and spatial variation in mechanics and composition. Efforts to recapitulate these variations for tissue engineering or mechanobiology research have focused on biomaterial patterning. Because HA modification and crosslinking chemistries are compatible with photoactivation, recent work has focused on developing HA biomaterials with photoresponsive patterned properties. Marklein and Burdick used photoactivated crosslinking to pattern the bulk modulus of a gel from 3 kPa to 100 kPa, a range over which human MSC spreading and proliferation was found to vary.[418] Our own laboratory used orthogonal photoresponsive chemistries to pattern perpendicular gradients of adhesive peptide and increasing modulus into a single gel for a high-resolution investigation of cell response to microenvironment variation.[195] Rosales and colleagues

incorporated a photoswitchable azobenzene moiety that was capable of forming a complex with cyclodextrin in the *trans* conformation and not in the *cis* conformation, allowing for photo-reversible control over the viscoelastic properties of HA.[419] Ongoing work involves investigating the role of dynamic mechanics on cell morphology.
Thin film HA hydrogels (<100 μm) offer the opportunity to apply these materials as interfacial coatings, which may be necessary when a different material is needed to provide basal structural or mechanical properties (e.g. orthopedic implants). For example, HA conjugated with immobilized arginine-glycine-aspartic acid-containing peptides can be coated onto titanium in a polyelectrolyte film with chitosan to improve osteoblast adhesion and reduce bacterial fouling.[420] A number of groups have generated thin films through layer-by-layer deposition with HA and cationic polyelectrolytes such as chitosan and polylysine.[421,422] The storage modulus of the films can be controlled over several orders of magnitude by secondary crosslinking in order to probe cell adhesion and mechanotransduction.[423] For example, Richert et al. showed that the storage modulus of a film could increase from 20 kPa before additional crosslinking to 800 kPa after additional chemical crosslinking.[424] Schneider et al. reported a similar magnitude of change in HA-chitosan films from an initial modulus of 15 kPa to 150 kPa after additional crosslinking, subsequently leading to more fibroblast spreading and adhesion.[425]

As previously mentioned, HA scaffolds within tissue are typically composed of very long HA chains, and use of HMW HA in biomaterials applications strongly influences HA-dependent adhesive signaling and can induce anti-inflammatory effects. However, the high viscosity of HMW HA solutions can make handling and mixing such solutions challenging, particularly in fabrication processes such as micromolding and 3D printing. To this end, supramolecular assembly of HA-based hydrogels has been exploited to enhance shear-thinning.[416,426] Ouyang and colleagues utilized the orthogonal modification of the HA backbone to synthesize a gel that would undergo shear thinning to facilitate 3D printing but could subsequently be stabilized by covalent fixation.[426] With this technology, higher MWs of HA can be incorporated into 3D printed scaffolds as well as other applications requiring rapid mixing or manipulation. Continued consideration of MW should enhance efforts to model tissue using HA-based biomaterials. At least one recent study has successfully incorporated HMW (500 – 750 kDa) HA into culture scaffolds to emulate the MW present in brain matix.[153]

3.4.4 Incorporating Adhesivity and Biodegradability into Biomaterial Design

As previously described, cells express HA-specific receptors that can bind directly to the HA backbone. Given that most solid HA-based biomaterials require modification of the HA backbone, an important question is how chemical modification alters adhesion and adhesion-dependent signaling. The adhesivity of the HA may be dependent on the type and degree of modification and seems to differentially affect specific receptors. For example, since receptor binding pockets typically accommodate around 4-6 HA monomers, it is likely that modifications on a low percentage of monomers (<15%) would only minimally affect HA adhesivity. As an example, modest aldehyde (10% of monomers) or thiol (25% of monomers) backbone modifications do not appear to significantly affect either aggrecan binding to the HA backbone or cell spreading and

adhesion.[427] However, increasing thiol functionalization of the carboxylic acid (from 20% to 40% of monomers) has been reported to reduce biodegradability and neurite extension of encapsulated cortical neurons.[428] Bencherif and colleagues found that degree of methacrylation correlated inversely with cell adhesion and degradation.[429] The sulfonation of hydroxyl groups on the HA backbone also leads to a decrease of platelet adhesion, suggesting the importance of the hydroxyl moiety for some functions.[430] Thus, the changes in HA adhesivity due to backbone modification are nuanced and depend on the degree, type, and site of modification.

The chemistry of the modification may also have specific, context-dependent effects. Increasing divinyl sulfone crosslinking can induce a subcutaneous inflammatory response in vivo, apparently offsetting the anti-inflammatory properties of HMW HA.[431] Both deacetylation of the amide moiety and sulfation of the alcohol moiety of HA can reduce CD44-mediated adhesion to HA, with dual modification further reducing adhesion.[432] While the degree to which modification of the carboxylic acid moiety affects CD44 adhesion is not well known, crystallographic studies suggest that the negative charge and orientation of the carboxylic acid is important for binding to CD44.[318] Modification would likely disrupt rather than enhance this binding. In a similar manner, Lord et al. found that serum proteins were more loosely bound on sulfated photoreactive HA versus non-sulfated HA, and that fibronectin orientation changed with sulfation to affect the degree of cell adhesion.[433]

While the HA backbone can intrinsically support cell adhesion, engagement of integrins is often an important biomaterial design goal, e.g. to promote cell spreading.[434,435] To include these functionalities, peptides or recombinant proteins can be conjugated to the HA backbone which in turn affect cell morphology.[436,437] However, protein conjugation generally requires backbone modification which reduces hyaladherin adhesivity based on the aforementioned studies. Alternatively, other matrix factors can be incorporated into HA-based materials as interpenetrating networks, particularly collagen, Matrigel, and gelatin.[198,400,409,438] The inclusion of other matrix factors adds other types of adhesivity, but can lead to steric hindrance or matrix interactions that change other material properties of the hydrogel.[409]
A variety of studies suggest that while some degree of hyaluronidase recognition and degradation of HA is retained after backbone modification and gelation, these rates are reduced in a manner that depends on the modification site, the degree of modification, and the chemistry of the new functional moiety.[439,440] Acrylation of the primary alcohol of HA has been reported to reduce hyaluronidase-mediated digestion of HA in solution by ~70%, implying that the modification interferes with enzyme binding or activity.[437] While these studies clear indicate that hyaluronidase degradation of matrices is possible, the mechanism by which cells degrade HA-based biomaterials and the relationship with HA MW is poorly understood.

Because the carboxylic acid moiety on HA is important for hyaluronidase recognition, carboxylic acid modifications would be expected to inhibit HA degradation. To this end, complete esterification of the carboxylic group has been observed to prevent degradation by hyaluronidase, while partial esterification of the backbone reduced degradation rate.[441]

In one study, HA degradation rate was observed to depend critically on the degree of adipic dihydrazide modification of HA, with 65% modification reducing the rate nearly ten-fold.[442] In another study, a high degree of biotinylation of HA and other chondroitin sulfates at the carboxylic acid disrupted degradation by hyaluronidases, but partial biotinylation enabled some hyaluronidase-based degradation.[443] Furthermore, increasing crosslink hydrophobicity via the use of hydrazide chemistry reduces hyaluronidase degradation rate.[444] These results together suggest that degradability by hyaluronidase is subject to the modification and crosslinking chemistry, and thus should be a key consideration when designing biomaterials for tissue regeneration or engineering as well as for research platforms in mechanistic studies.

While most modification strategies can be used to reduce HA-based biomaterial degradation, it may be more challenging to retain degradability in applications where both robust mechanics and degradability are desirable. Both properties are valuable in tissue engineering scaffolds and HA-based research platforms in which cells may need to be robustly organized but also be able to modify the microenvironment. The simplest strategy is to minimize the degree of modification to only modestly reduce HA bioactivity. To this end, the degree of modification is controllable to some degree by tailoring reaction conditions.[445] Alternatively, the degradability can be incorporated in the crosslinks through some non-hyaluronidase based degradation mechanism. For example, Sahoo and colleagues used a crosslinking strategy to form an ester linkage with HA that could be rapidly hydrolyzed to yield the native HA backbone structure.[446] Further work showed that the degradation rate could be extended by using a more hydrophobic polycaprolactone-based crosslinker.[447] Several groups have also used matrix metalloproteases (MMP)-degradable peptide crosslinkers.[435,448] MSCs cultured in HA with MMP-sensitive crosslinkers exhibit more rapid sprouting and matrix deposition.[436]

Another option is to not modify the HA backbone at all, but instead rely on non-covalent methods for gelation. For example, HA can be incorporated into an interpenetrating network with collagen in which electrostatic forces result in an HA coating over collagen fibrils.[398] An alternative option that has yet to be explored in great depth is to use native CS or CS mimics to assemble HA matrices. As one example of this possibility, Bernhard and Panitch developed an aggrecan-mimetic peptide that increased the storage modulus of gels for cartilage engineering applications.[449] While the high bond strength between HA and the CS-link protein complex suggests such binding is possible, it is unclear whether this means of crosslinking would be practical for any of the current applications.

Table 1: Potential Advantages and Disadvantages of Strategies Used to Incorporate Key Biophysical Properties of HA into Biomaterial Design.

biophysical property of HA in ECM	strategy for incorporating property into HA biomaterials	potential advantages and disadvantages of strategy
mechanics		
	change HA density	• higher HA density increases both storage and loss modulus[196,346,423] • higher density increases cell confinement and reduces spreading in 3D[196,410,438]
	change molecular weight	• HMW HA offers higher modulus, increased entanglement, and immunosuppressive signaling[335,346,348,359] • LMW HA offers low viscosities and can induce inflammation[335,431]
	HA backbone modification and cross-linking	• enables tunable control of cross-linking[232,301,418,419] • can change viscosity depending on modification[403,416] • can affect hydrophobicity of hydrogel[444,447]
	incorporate interpenetrating / semi-interpenetrating networks	• network can be used to tune mechanical properties[415,422] • HA can interact with networking polymers[198,409,437] • may avoid HA backbone modification[398,449]
adhesivity		
of HA backbone	HA backbone modification	• modification, especially of carboxylic acid and primary alcohol, reduces adhesivity of hyaladherins (cell receptors and ECM)[428–430,432,433] • modifications can cause immunogenic response[431]
of other ECM components	peptide conjugation	• requires backbone modification, which affects HA adhesivity
	form interpenetrating network with other ECM components	• networks may interact with HA backbone[198,334,398,409]
degradability		
of HA backbone	backbone modification	• backbone modification generally reduces degradability[437,439–443]
	cross-linking	• cross-linker can affect degradability[386,447]
of cross-linkers	MMP-cleavable cross-links	• MMP cleavable linkages can enhance 3D cell spreading[436] • relative role of hyaluronidases is unknown
	cross-links degrade by hydrolysis (i.e. esters)	• rates can be controlled by cross-linker type[446,447] • native HA backbone is a product of hydrolysis allowing for hyaluronidase-based degradation[446,447]

3.5 Conclusions and Future Outlook

Based on its bioactivity and versatility, HA is an attractive material platform for a variety of research and technological applications. By carefully considering how HA signaling influences cells and tissues, researchers and engineers can create HA formulations to meet a wide range of design requirements. Central to HA biophysical signaling is its mechanical properties, adhesivity, and degradability. In addition, HA MW has key implications for biophysical signaling, with HMW HA being associated with homeostasis and LMW HA being associated with tissue remodeling.

Various strategies exist for modifying the biophysical cues of HA, each with advantages and limitations that depend on the application. Modification of the HA backbone is a powerful and the most common way to control mechanics, conjugate adhesive ligands, or control degradability. However, backbone modification or crosslinking can reduce the adhesivity of the HA to HA-specific receptors such as CD44 or hamper degradation by hyaluronidases. The degree of modification is still difficult to precisely control using current synthetic methods. Even with these modifications, no strategies to date have captured the complexities of HA organization with other matrix factors and resulting mechanics observed *in vivo*. As a whole, HA is not well suited to applications requiring truly inert or non-degradable biomaterials due to its significant influence on cell signaling and matrix remodeling.

As the field's understanding and appreciation of HA biology continues to expand, future work on HA-based biomaterials should focus on incorporating critical features of HA into biomaterial design and thorough characterization of the downstream effects. First, more attention to HA MW is warranted, given the importance of this parameter to both HA viscoelastic properties and biological effects. Second, the biological importance of HA organization within the ECM remains an open question in the field. As new studies seek to the address this question, chemistries and methodologies should expand to emulate key features of HA organization within biomaterial design. Third, the role of HA degradation in biomaterial performance remains understudied and needs to be addressed for both clinical and research applications. In each of these key areas, the biological effects of HA must be validated to ensure that HA is serving the expected or desired role within the context of the specific biomaterial formulation. With continued progress in all of these areas, the field will be poised to precisely tailor HA formulation for specific applications and better predict how these manipulations influence biological function.

3.6 Acknowledgements

The authors gratefully acknowledge financial support from the following sources: National Science Foundation (Graduate Research Fellowship to K.W.); National Institutes of Health (Ruth L. Kirschstein Predoctoral Individual National Research Service Award No. F31CA228317 to K.W.; R21EB025017, R56DK118940, and R01CA227136 to S.K.).

Chapter 4. A mode of cell adhesion and migration facilitated by CD44-dependent microtentacles

Parts of this chapter are excerpted with permission from , from the article “A mode of cell adhesion and migration facilitated by CD44-dependent microtentacles,” by Kayla J. Wolf, Poojan Shukla, Kelsey Springer, Stacey Lee, Jason D. Coombes, Caleb J. Choy, Samuel J. Kenny, Ke Xu, and Sanjay Kumar in *Proceedings of the National Academy of Sciences*, In press (2020).

4.1 Abstract

The structure and mechanics of many connective tissues are dictated by a collagen-rich extracellular matrix (ECM), where collagen fibers provide topological cues that direct cell migration. However, comparatively little is known about how cells navigate the hyaluronic acid (HA)-rich, nanoporous ECM of brain, a problem with fundamental implications for development, inflammation and tumor invasion. Here, we demonstrate that glioblastoma cells adhere to and invade HA-rich matrix using microtentacles (McTNs), which extend tens of microns from the cell body and are distinct from filopodia. We observe these structures in continuous culture models and primary patient-derived tumor cells, as well as in synthetic HA and organotypic brain slices. High-magnification and super-resolution imaging reveals McTNs are dynamic, CD44-coated tubular protrusions containing microtubules and actin filaments, which respectively drive McTN extension and retraction. Molecular mechanistic studies reveal that McTNs are stabilized by an interplay between microtubule-driven protrusion, actomyosin-driven retraction, and CD44-mediated adhesion, where adhesive and cytoskeletal components are mechanistically coupled by an IQGAP1-CLIP170 complex. McTNs represent a previously unappreciated mechanism through which cells engage nanoporous HA and may represent an important molecular target in physiology and disease.

4.2 Significance

We identify a new mechanism used by tumor cells to adhere to and migrate through nanoporous, three-dimensional extracellular matrix characteristic of brain tissue. In this mechanism, cells engage hyaluronic acid, a key component within brain matrix, by assembling “microtentacles” that can extend tens of microns from the cell body and adhere to the matrix via the CD44 receptor. We also elucidate a molecular mechanism through which these structures can support motility based on the interplay of actin, microtubules, IQGAP1 and CLIP170. Analogous structures have previously been observed in circulating tumor cells and hypothesized to facilitate endothelial attachment and extravasation. Our studies strongly support this concept and further indicate that microtentacles can facilitate adhesion and invasion into tissue.

4.3 Introduction

Tumor cell invasion is critically dependent on interactions with extracellular matrix (ECM) [450]. Glioblastoma (GBM) is the most common and aggressive form of primary brain cancer, with outcomes improving only marginally over the last several decades [12,269]. GBMs are characterized by diffuse infiltration of tumor cells into surrounding healthy tissue, allowing cells to escape surgical resection and engage pro-survival microenvironmental cues that foster resistance to therapy [40]. Targeting cell-ECM interactions in combination with conventional therapies therefore has potential to improve therapeutic outcome [181]. The spatially heterogeneous composition and structure of brain ECM modulates invasion patterns [106]. While the brain is generally richer in hyaluronic acid (HA) than other tissues, the intraparenchymal region is particularly HA-rich and generally lacking in fibrillar contact guidance cues associated with collagen, fibronectin, and laminin normally found in connective tissue [36]. GBMs are more enriched in HA than lower-grade astrocytomas [50], and HA is a potent effector of aggressive invasion in GBM [207,295,451]. Despite the clear functional significance of HA to GBM progression, the mechanisms by which cells invade HA-rich, nonfibrillar 3D matrix are poorly understood.

CD44 is a transmembrane receptor for extracellular HA that plays a critical role in tumor progression and specifically GBM invasion [296]. CD44 is highly overexpressed in GBM compared to healthy tissue and lower grade astrocytomas [294], and CD44 antibody blockade significantly reduces tumor size in rats with grafted C6 gliomas [48]. Furthermore, knockdown (KD) of CD44 in human GBM tumors slows tumor growth and sensitizes tumors to cytotoxic agents [452]. CD44 is also a marker of glioma stem cells (GSCs, also known as tumor initiating cells) and contributes to maintaining stemness [315]. Our laboratory has shown that CD44 is necessary for adhesion and migration on HA hydrogel-based matrix [74]. The intracellular domain of CD44 interacts with the cytoskeleton through direct mechanical linkages or more indirectly through Src family kinase-based activation of Rho GTPase or focal adhesion kinase signaling [49,315]. Specifically, CD44 binds the actin cytoskeleton via ERM family proteins and the spectrin cytoskeleton via ankyrin proteins [49,453,454]. IQGAP1 has also been reported to bind to CD44, which may provide an alternative mechanical linkage to the actin cytoskeleton [455]. The relative roles of these binding interactions remains poorly understood, and may be dependent on the cell type and microenvironment [231]. Although CD44 is a recognized effector of cell invasion and several downstream binding partners have been identified, it remains unclear how the cytoskeleton coordinates to facilitate CD44-mediated invasion. Specifically, the role of CD44 in protrusion formation and tension generation is poorly understood.

Here, we describe a mechanism through which GBM cells engage and invade HA-rich matrix through microtentacles (McTNs). McTNs engage HA via CD44 and are observed in both engineered HA scaffolds and tissue. Actin and microtubules often align in McTNs, undergo retrograde flow, and support tension generation against the ECM. Knockout (KO) of IQGAP1, a known crosslinker of actin and microtubules and regulator of microtubule growth, prevents cell adhesion and McTN formation and reduces migration speed on HA and HA-RGD. This work demonstrates that CD44-HA binding supports adhesion and

migration through the formation of McTNs, which mediate adhesion and motility in HA-rich, nonfibrillar matrix.

4.4 Methods

Cell Lines:
U-251 MG and U-87 MG human glioblastoma cells were obtained from the University of California, Berkeley Tissue Culture Facility, which sources its cultures directly from the ATCC. GSC-11, GSC-268, GSC6-27, GSC-28, GSC-267, GSC-240, GSC-262, GSC-20, and GSC-295 cells were kindly provided from Dr. Joseph McCarty and Dr. Erik Sulman at MD Anderson Cancer Center. L0 cells were originally obtained from Dr. Brent Reynolds and maintained as described in previous publications [72,456,457].

Ex Vivo Mouse Brain Model:
Samples were derived from mice that were cared for by the UC Berkeley Office for Animal Care and Use (OLAC) and all experiments were approved by Berkeley's Institutional Animal Care and Use Committee (ACUC). Brain slice culture was performed following institutional and national regulations in accordance with the American Association for Accreditation of Laboratory Animal Care (AAALAC) using a previously established method [458]. Mouse brain tissue (female, 18 months old) was cut into 1-mm thick slices immediately after transcardial saline perfusion and extraction. Brain slices were cultured in 10% serum medium in the upper chamber of a Boyden (transwell) chamber on top of a 5 µm pore size polyester membrane (Corning) with 10% serum medium in the lower chamber. To each slice, ~1500 U-251 MG cells expressing GFP-tubulin and RFP-LifeAct in 50 µL of media were seeded onto the center of the slice and invasion was tracked using confocal microscopy. After culture, the whole slice was fixed using 4w/v% paraformaldehyde in PBS for 1 hour, placed on a glass-bottom dish, and immediately imaged by SIM.

Laser ablation:
For laser ablation studies, an upright Olympus BX51WI microscope (Olympus Corporation) equipped with Swept Field Confocal Technology (Bruker) and a Ti:Sapphire 2-photon Chameleon Ultra II laser (Coherent) was used. The 2-photon laser was set to 770 nm and ablation was performed using three 20 ms pulses. Live-cell imaging was performed using an Olympus LUMPlanFL N 60x/1.0 water dipping objective. Cells were kept at 37ºC using a stage-top sample heater (Warner Instruments). Images were captured using an EM-CCD camera (Photometrics). The following emission filters were used: The following emission filters were used: Quad FF-01-446/523/600/677-25 (Semrock) and 525/50 ET525/50 (Chroma). PrairieView Software (v. 5.3 U3, Bruker) was used to acquire images.

STORM imaging:
3D-STORM imaging[459,460] was carried out on a homebuilt setup using a Nikon CFI Plan Apo λ 100x oil immersion objective (NA 1.45), as described previously [461,462]. Briefly, the sample was mounted with an imaging buffer consisting of 5% (w/v) glucose, 100 mM

cysteamine, 0.8 mg/mL glucose oxidase, and 40 µg/mL catalase in 1M Tris-HCl (pH 7.5). Dye molecules were photoswitched to the dark state and imaged using either 647- or 560-nm lasers; these lasers were passed through an acousto-optic tunable filter and introduced through an optical fiber into the back focal plane of the microscope and onto the sample at ~2 kW cm-2. A translation stage shifted the laser beams towards the edge of the objective so that light reached the sample at incident angles slightly smaller than the critical angle of the glass-water interface. Single-molecule emission was recorded with an Andor iXon Ultra 897 EM-CCD camera at a framerate of 110 Hz, for a total of ~80,000 frames per image. For 3D-STORM, a cylindrical lens of focal length 1 m was inserted into the imaging path to introduce astigmatism [460]. The raw STORM data were analyzed according to previously described methods [459,460]. Two-color imaging was performed via sequential imaging of targets labeled by Alexa Fluor 647 and CF568.

Cell culture:
U-251 MG and U-87 MG cells were cultured in DMEM (Thermo Fisher Scientific) supplemented with 10% (vol/vol) fetal calf serum (JR Scientific), 1% (vol/vol) penicillin-streptomycin (Thermo Fisher Scientific), 1% (vol/vol) MEM non-essential amino acids (Thermo Fisher Scientific), and 1% (vol/vol) sodium pyruvate (Thermo Fisher Scientific). L0 cells were propagated as neurospheres with serum-free medium (Neurocult NS-A Proliferation kit, Stem Cell Technologies) that contained 20 ng/mL EGF (R&D Systems), 10 ng/mL FGF (R&D Systems), and 0.2% (wt/vol) heparin diluted in PBS (Sigma). Cells were passaged every ~5 days. All GSC cells were propagated as neurospheres in DMEM/F12 basal medium supplemented with 2% (vol/vol) B-27 supplement (Gibco), 20 ng/mL EGF (R&D Systems), and 20 ng/mL FGF (R&D Systems). For experiments on HA gels, medium was supplemented with 0.1% penicillin/streptomycin (Thermo Fisher Scientific). U-87 MG, U-251 MG, and L0 cells were harvested using 0.25% trypsin-EDTA (Thermo Fisher Scientific) except for in preparation for adhesion assays, in which cells were harvested using Accutase cell detachment solution (Innovative Cell Technologies). All GSC cells were harvested using Accutase. L0 and GSC cells were passaged less than 20 times and U-87 MG and U-251 MG cells were passaged less than 30 times. L0 cells have been transcriptionally characterized and classified as the classical subtype of GBM, GSC-11 cells have been classified as the classical subtype, and GSC-20s have been classified as the mesenchymal subtype. Cells were screened on a monthly basis for mycoplasma and validated every six months by Short Tandem Repeat (STR) analysis at the University of California Cell Culture Facility.

Cell line modification:
CD44 shRNA KD cells were previously generated as described.[74] CD44 and IQGAP1 KO cells were developed using established protocols.[463] Briefly, guide RNA primers were cloned into the PX458 backbone (Addgene Plasmid #48138). Two guide RNAs were independently tested for CD44 KO generation, three guide RNAs were independently tested for IQGAP1 KO generation, and one non-targeting guide RNA was used as a control (Table S2). Plasmids were transfected into U-87 MG cells using Viafect Transfection Reagent (Promega). The cells were sorted by fluorescence-activated cell sorting (FACS) for the 2% of cells expressing the highest levels of GFP and clonally expanded. Clones were screened for expression of the target protein by Western blotting.

Potential KO clones were expanded, blotted again as confirmation of the KO, and used for further study. Three non-targeting clones were randomly selected and pooled for further study.

U-251 MG cells stably expressing RFP-LifeAct and GFP-tubulin were generated for studies involving live imaging and ex vivo culture. Cells were first infected with previously generated RFP-LifeAct in pFUG-IP lentiviral particles at an MOI of 5.[464] After three passages, cells were infected with LentiBriteTM GFP-Tubulin lentiviral particles (Millipore Sigma) at an MOI of 20 following manufacturer's directions.

HA hydrogel synthesis:
HA hydrogels were synthesized as previously described.[196] Briefly, methacrylic anhydride (Sigma-Aldrich, 94%) was used to functionalize sodium hyaluronate (Lifecore Biomedical, Research Grade, 66 kDa - 99 kDa) with methacrylate groups. The extent of methacrylation per disaccharide was quantified by 1H NMR as detailed previously and found to be ~85% for materials used in this study. To add integrin-adhesive functionality, methacrylated HA was conjugated via Michael Addition with the cysteine-containing RGD peptide Ac-GCGYGRGDSPG-NH2 (Anaspec) at a concentration of 0.5 mmol/L unless otherwise stated. To add fluorescent tags to the HA backbone, FITC-cysteine (Genscript) at 1 mg/mL dissolved in 20% DMSO and 80% PBS was added to dissolved HA to form a final concentration of 0.1 mg/mL FITC-cysteine in 3w/w% methacrylated HA. Finally, 3% (wt/wt) or 5% (wt/wt) methacrylated HA was crosslinked in phenol-free DMEM (Thermo Fisher Scientific) with bifunctional thiol dithiothreitol (DTT, Thermo Fisher Scientific). A concentration of 204 mmol/L DTT and 5% (wt/wt) HA was selected to yield a shear modulus of ~6.5 kPa for 2D experiments, and a concentration of 19 mmol/L DTT was selected to yield a shear modulus of ~300 kPa for 3D experiments. Previous studies demonstrated the utility of these concentrations and moduli for investigating GBM motility as well as relevance to the modulus of brain tissue.[74,196] Healthy brain ECM elastic modulus is typically between 0.3 to 3 kPa[41,42], and is increased in GBM to around 1-7 kPa.[63] Glass substrates were coated with poly-L-lysine (Sigma-Aldrich) and rinsed prior to gel synthesis to increase adsorption of gels to substrate. 2D gels were flattened by dropping a plasma-treated coverslip onto gel solutions prior to gelation, controlling gel height to be ~120 µm thick. Solutions were crosslinked into gels for 1 h, rinsed, and then soaked in room temperature PBS for at least 1 h before cell seeding.

HA microchannel fabrication:
PDMS channels were created with photolithography and replica molding techniques.[465–467] Photolithography masks were designed with AutoCAD and produced (Artnet Pro). A clean silicon wafer (WaferNet) was spin-coated with SU-8 3005 photoresist (MicroChem Corp.) to create a 5 µm-thick film. After soft baking at 95°C for 3 min, the film was exposed to UV light for 15 sec through the mask, post-baked at 65°C (1 min) and 95°C (2 min). Finally, the wafer was developed and hard-baked at 200°C for 15 min. PDMS monomer and crosslinker were mixed (ratio 10:1, Sylgard® 184 Silicone Elastomer Kit, Dow Corning) and the prepolymer solution was poured onto the wafer. The wafer was degassed under vacuum and then prepolymer was cured for 2 h at 80°C (or overnight at RT). Finally, the PDMS was gently peeled off the wafer. PDMS substrates were washed

with ethanol, dried, and subjected to plasma treatment for 3 min to reduce hydrophobicity. Instead of glass coverslips, PDMS molds with positive features were used to flatten 2D HA gels and imprint negative features during gelation. Cells were seeded onto microchannels after fabrication. Only cells migrating within the 2D were used for analysis.

Fibrin gel formation:
A stock solution of 33 mg/mL fibrinogen (Millipore Sigma) was dissolved for 2 h at 37 °C in 10 mM HEPES buffer and then allowed to settle overnight at 4 °C. A stock solution of thrombin was dissolved at 25 U/mL. Stock solutions were diluted in DMEM to form a final concentration of 3.3 mg/mL fibrinogen and 2 U/mL thrombin. 2D gels were flattened by dropping a plasma-treated coverslip onto gel solutions prior to gelation, controlling gel height to be ~120 μm thick. Solutions were crosslinked into gels for 1 h and rinsed in DMEM prior to cell seeding.

SIM imaging:
Cells on glass, gels, or culture slices were imaged in No. 0 coverslip glass bottom dishes using an Elyra structured illumination microscope (Zeiss) and a Plan-Apochromat 63x/1.4 Oil DIC M27 objective (Zeiss). Samples were illuminated using an Argon multiline laser for excitation at 647 nm, 546 nm, 488 nm and a 405 nm diode laser. Zen 2010 software was used for image acquisition. For z-stack images, slices were 1 μm apart. Finally, z-projections were formed in ImageJ with 2x2 binning using 3D project.

Rheological measurements:
The shear modulus of hydrogel formulations was measured using oscillatory rheometry (Anton Parr Physica MCR 310) as described previously.[196] Briefly, hydrogels were first crosslinked by incubation for 1 h in a humidified 37˚C chamber. Rheological testing consisted of frequency sweeps ranging from 100 to 0.1 Hz at 0.5% amplitude also in a humidified 37˚C chamber. Shear modulus was reported as the average storage modulus for 3 tests per matrix composition at an oscillation frequency of 0.5 Hz.

Centrifugal adhesion assay:
Cells were harvested using Accutase and seeded onto HA gels at a density of 10,000 cells/cm2 and allowed to settle and spread for 30 minutes. Cells were then incubated in inhibitors for an additional 3.5 h before centrifugation; otherwise, cells were centrifuged immediately after 30 minutes. For centrifugation, wells were filled with fresh medium and cell culture plates were sealed with an adhesive plate sealer. The plate was then inverted and centrifuged for 5 minutes at 100g. Cells remaining on hydrogels were then fixed by paraformaldehyde (PFA) and stained with DAPI. Large, seamed images were collected of each gel using an Eclipse TE2000 Nikon Microscope with a Plan Fluor Ph1 10x objective and stitched using stitched NIS-Elements Software. Automated thresholding analysis of the DAPI images was performed on ImageJ to determine a total count of the number of cells on each hydrogel. Each condition was tested in 4-6 wells over at least 3 experiments.

Migration assays:

Cells were seeded onto HA gels at a density of 1000 cells/cm2 and incubated for 4 h. Then, migration assays were performed by imaging cells at 15-minute intervals for 6 h using an Eclipse TE2000 Nikon Microscope with a Plan Fluor Ph1 10x objective and NIS-Elements Software in a 37 ºC, CO2 controlled chamber. The ImageJ plugin Manual Tracking was used to track cell movements in each frame and calculate an average cell speed.

Western blotting:
Cells were lysed in RIPA buffer (Sigma-Aldrich) supplemented with Halt protease and phosphatase inhibitor cocktail (Thermo Fisher Scientific), 4 mg/mL sodium molybdate (Sigma Aldrich, anhydrous), and 4 mg/mL sodium fluoride (Sigma Aldrich,). Equal protein amounts were loaded onto a 4% to 12% gradient bis-tris gel (Thermo Fisher Scientific), and then blotted onto a PVDF membrane (Life Technologies). Membranes were probed with rabbit anti-CD44 antibody (Thermo Fisher Scientific, PA5-21419) or mouse anti-CD44 (R&D Systems, BBA10), anti-IQGAP1 antibody (Abcam, ab86064), and anti-tubulin as a control (Thermo Fisher Scientific, MS-581-P1ABX) or mouse anti-β-actin-peroxidase (Sigma-Aldrich, A3854). Blots were then probed with goat anti-mouse (Thermo Fisher Scientific, 62-6520) or goat anti-rabbit (Thermo Fisher Scientific, 65-6120) secondary HRP-tagged antibodies. Primary antibodies were diluted at 1:2000, except mouse anti-β-actin-peroxidase was diluted at 0.4 µg/mL and mouse anti-CD44 was diluted to 5 µg/mL. Secondary antibodies were diluted at 1:10,000. Membranes were developed using SuperSignal West Dura Chemiluminescent Substrate kit (Thermo Fisher Scientific) and imaged using a ChemiDocXRS+ molecular imager (Bio-Rad).

Pharmacological agents:
Cytochalasin D (Sigma-Aldrich), latrunculin A (Cayman Chemicals), nocodazole (Cell Signaling Technology), colchicine (Sigma-Aldrich), ML-141 (R&D Systems) and blebbistatin (Sigma-Aldrich) were all dissolved at 10 mM in DMSO and stored at -20 ºC until use. Inhibitor solutions were diluted to 10 µM in fresh medium and used to replace medium on cells. Vehicle controls contained 10 µM of DMSO in medium.

Immunofluorescence staining:
Cells were fixed either using PFA or glutaraldehyde (GA). For super-resolution imaging of cytoskeletal structures, cells were fixed first in 0.3% (vol/vol) GA with 0.5% (vol/vol) Triton-X for 30 seconds and then in 3% (vol/vol) GA in cytoskeletal buffer for 20-25 minutes.[468] A 0.1 w/v% sodium borohydride solution in PBS was used to wash cells twice for 5 minutes each to quench excess GA. For confocal imaging of cell morphology, cells were fixed in 4% (wt/vol) PFA for 12 minutes, permeabilized with 0.5% (vol/vol) Triton-X and then washed two times with PBS. For immunostaining, cells were then blocked with 5% (vol/vol) goat serum (GS, Sigma-Aldrich) in PBS for 30 minutes. Primary antibodies were added at 1:200 dilution in 1% (vol/vol) GS except for tubulin antibody, which was added at 1:100 dilution in GS. Primary antibodies were incubated for 1 h at room temperature. After two 5-minute washes in PBS, secondary antibodies at 1:200 dilution were added along with phalloidin and DAPI stains. For cells stained with goat anti-CLIP170 (Novus Biologicals, NBP1-36749) solution, 10 mg/mL BSA in PBS was substituted for goat serum solutions.

Primary antibodies used were rabbit polyclonal anti-CD44 (Thermo Fisher Scientific, PA5-21419), rabbit polyclonal anti-IQGAP1 (Abcam, MS-581-P1ABX), mouse monoclonal anti-tubulin-α Ab-2 (Thermo Fisher Scientific, clone DM1A, MS-581-P1ABX), polyclonal rabbit anti-MYO10 (Sigma-Aldrich, HPA024223), polyclonal goat anti-CLIP170 (Novus Biologicals, NBP1-36749), rabbit polyclonal anti-tubulin, detyrosinated (Millipore. Sigma, AB_609894), mouse monoclonal anti-acetylated tubulin (Millipore Sigma, T7452), and mouse monoclonal anti-tubulin, tyrosine (Millipore Sigma, T9029). Secondary antibodies used were goat anti-mouse Alexa Fluor 568 (Thermo Fisher Scientific, A-11004), goat anti-mouse antibody, Alexa Fluor 488 (Thermo Fisher Scientific, A-11001), goat anti-rabbit Chromeo 546 (Abcam, ab60317), goat anti-rabbit secondary Alexa Fluor 488 antibody (Thermo Fisher Scientific, R37116), goat anti-mouse secondary antibody, Alexa Fluor 405 (Thermo Fisher Scientific, A-31553), polyclonal donkey anti-goat antibody, Alexa Fluor 568 (Thermo Fisher Scientific, A212235), polyclonal goat anti-mouse secondary antibody, Alexa Fluor 647 conjugate (Thermo Fisher Scientific, A21235), goat anti-rabbit Alexa Fluor 647 (Abcam, ab150079). Stains used were DAPI (Sigma-Aldrich, 10236276001), Acti-stain 488 phalloidin (Cytoskeleton, Inc., PDHG1), Alex Fluor 546 phalloidin (Thermo Fisher Scientific, A22283), and Alexa Fluor 647 phalloidin (Cell Signaling Technology, 8940S).

DIC imaging:
HA gels were fabricated on No. 0 coverslip glass bottom dishes (MatTek). Cells were seeded onto the gels at a density of 1000 cells/cm2 and incubated for at least 4 h. Cells were imaged using an Eclipse TE2000 Nikon Microscope equipped with a polarizer, prisms, and analyzer using a Nikon 60x/1.40 Oil Plan Apo VC DIC N2 objective.

The Cancer Genome Atlas gene expression analysis:
Data from the publicly available data browser were queried for expression of *CD44*, *CLIP170*, and *IQGAP1*.[469] The GlioVis data portal analysis tool was used to retrieve mRNA expression data for genes of interest from all available GBM tumor samples in the HG-U133A dataset, and data was analyzed in Prism GraphPad.

McTN formation and retention assays:
Cells were harvested and then suspended into HA solution for a final density of 50 x 10^4 cells/mL and final HA solution of 3% (wt/wt). DTT was then mixed into the solution, and 5 µL drops of the mixture were dropped into the bottom of plate wells without flattening. Plates were incubated at 37 °C in a humidified chamber while being rotated every 2-3 minutes for 15 minutes and then left upside-down for 45 more minutes. After crosslinking, medium was added to the wells to submerge the gel. Gels were incubated for 7 days with a medium change every 2-3 days. Images of cells were imaged using a 20x Nikon phase 2 objective on an Eclipse TE2000 Nikon Microscope. Cells within the gel were randomly selected for imaging. Cells in large clumps, adhered to the bottom of the plate, or near the outer edge of the gel were excluded from analysis. Cells were imaged on Day 7 for both McTN formation and retention assays. In retention assays, cells were imaged for 45 minutes at 5-minute intervals before the addition of inhibitor and then for an additional 45 minutes after the addition of inhibitor.

Quantification and statistical analysis:
The number of samples necessary to achieve power of 0.8 were estimated using G*Power using previous or preliminary data. Statistical significance was calculated by the indicated tests using GraphPad/Prism. For all experiments, N values were the sum of replicates collected over 3 independent experiments. Statistical details (exact value of N and what N represents, statistical test used for comparison, definition of center, dispersion and precision measures, and definition of significance) can be found in figure legends.

4.5.1 Results

4.5.2 GBM cell adhesion and migration on HA is associated with extension of microtentacles (McTNs)

We had shown that CD44 is necessary for adhesion to HA in previous work, with CD44 KD or antibody blockade abrogating adhesion to HA-based hydrogels [74]. However, the contributions of CD44 to force generation through the cytoskeleton remained unknown. To gain additional mechanistic insight into this result, we seeded both continuous GBM cells and GSCs on HA and performed phase and differential interference contrast (DIC) imaging. Cells exhibited partially rounded cell bodies surrounded by long, thin protrusions closely associated with the HA visible at high magnification (**Fig. 1A, Fig. S1**). The protrusions were positive for CD44 (**Fig. 1B**), with 65 ± 18% staining positive for both F-actin and tubulin in U-87 MG cells and 56 ± 17% in U-251 MG cells (**Fig. 1B, Fig. S2**). Structured illumination microscopy (SIM) imaging revealed a fan of actin filaments supported by several microtubules interspersed throughout the protrusions in both continuous U-87 MG cells (**Fig. 1C**) and GSC-11 primary tumor-initiating cells (**Fig. 1D**). Acetylated microtubules were located in the center of the cell body and not in protrusions, suggesting that microtubules in protrusions are relatively dynamic (**Fig. S3A**) [470]. Tyrosinated microtubules, which regulate neuronal growth cone organization and are required for interaction with certain microtubule binding proteins such as CLIP170, extended extensively into protrusions (**Fig. S3B**) [471,472]. Detyrosinated tubulin, a marker of long-lived microtubules, was found interspersed along microtubules in protrusions consistent with previous studies (**Fig. S3C**) [473].

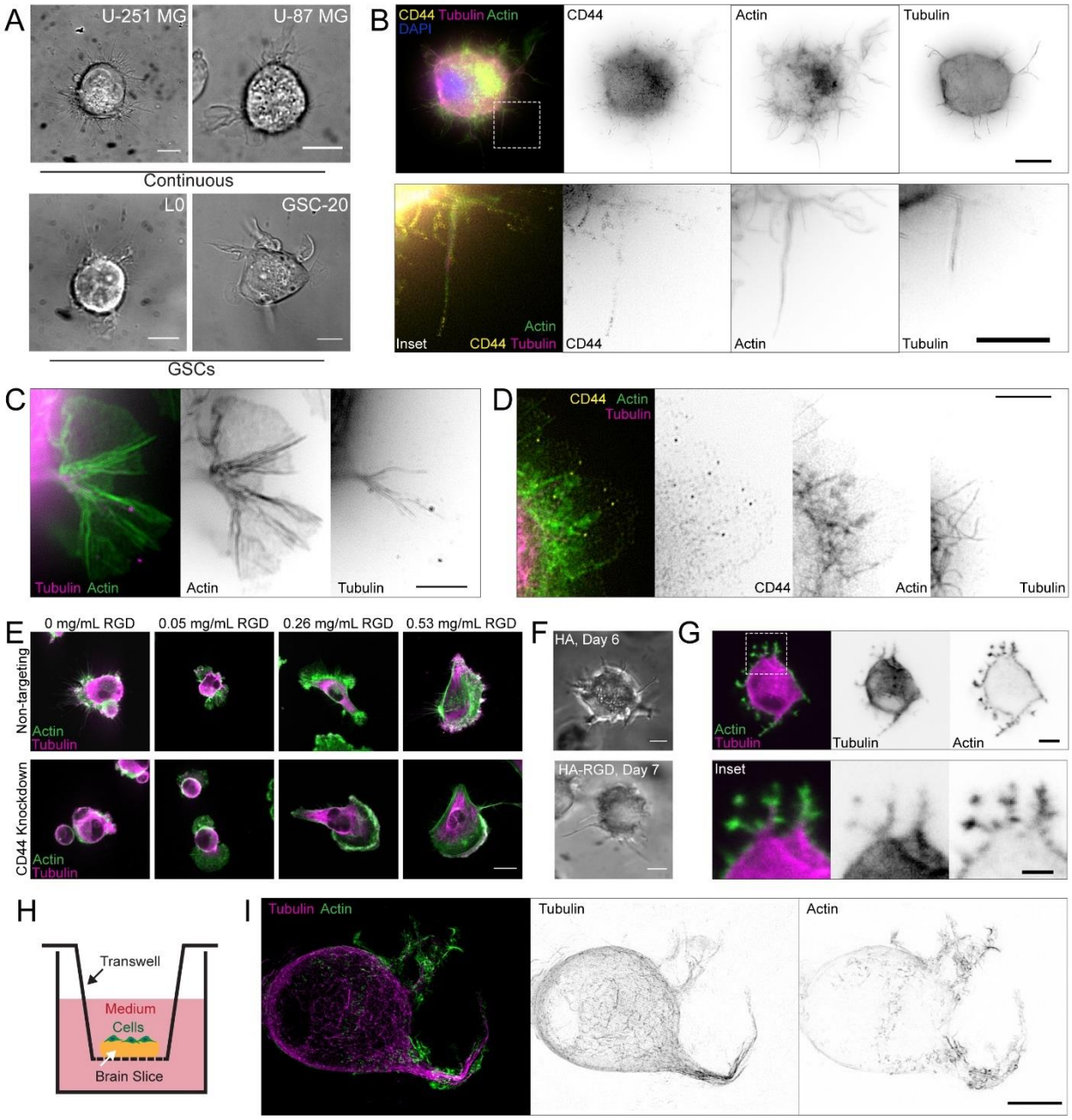

Figure 1. Cells interacting with HA express actin- and microtubule-positive McTNs. A) DIC imaging of live cells demonstrates that both continuous GBM cells and GSCs exhibit long, thin protrusions on HA. Scale=10 µm. B) SIM imaging of U-251 MG cells on HA demonstrates that protrusions are CD44 positive and frequently actin- and microtubule-positive. Scale=10 µm. C) SIM imaging shows parallel actin filaments and microtubules in the core of protrusions of U-87 MG cells on HA. Scale=5 µm. D) GSC-11 cells express actin- and tubulin-positive protrusions. Scale=5 µm. E) CD44 shRNA KD U-251 MG cells seeded on HA or HA-RGD can form lamellipodia and large actin bundles at high RGD concentrations similar to the non-targeting control but are unable to spread or form protrusions on HA without RGD. Scale=20 µm. F) U-251 MG cells cultured for 6 days in

3D HA and 7 days in HA-RGD. Scale=10 µm. G) GFP-tubulin and RFP-LifeAct-expressing U-251 MG cell embedded in 3D HA and imaged by confocal microscopy. Scale =10 µm. H) Schematic of *ex vivo* tissue culture slice model showing cells seeded onto brain tissue slices immersed in medium within a transmembrane insert. I) GFP-tubulin and RFP-LifeAct expressing U-251 MG cell after 1 day of culture in *ex vivo* tissue culture slice model as a Z-stack projection (12 slices, 1 µm spacing). Scale=10 µm.

Although the distribution of microtubules within protrusions and overall length varied by cell type, all cells expressed F-actin and microtubule-positive protrusions on HA. Furthermore, cells on HA generally lacked thick actin bundles and large lamellipodia typically observed on 2D, integrin-engaging substrates [474–476]. The morphology of these protrusions, particularly their microtubule and actin architecture, seemed reminiscent of microtubule-positive microtentacles (McTNs) that have been described in circulating breast cancer cells and implicated in endothelial docking and extravasation [462,477–479]. Thus, we refer to these protrusions as McTNs. However, a key difference between McTNs in circulating breast cancer cells and invading GBM cells is that GBM cells associate with a solid-state ECM and rarely enter the circulatory system [43], suggesting drastically different functions.

To determine how McTNs might be affected by the presence of integrin ligands normally expected to promote lamellipodia, focal adhesions, and stress fibers, we investigated the effects of varying RGD concentration on cell morphology. With increasing RGD concentration, lamellipodia and large actin bundles increasingly dominated the phenotype in cells with both shRNA KD of CD44 and a non-targeting control (**Fig 1E**). In contrast, only the control cells were able to spread and form McTNs on HA. Fibrin contains both integrin-adhesive sites and binds CD44, although the CD44-fibrin(ogen) interaction is weaker than CD44-HA [480,481]. Cells seeded on 2D fibrin gels also exhibited lamellipodia and large actin bundles consistent with cells on HA-RGD (**Fig. S4**). Integrin-engagement is thus necessary for actin bundling and lamellipodia formation, and CD44-substrate binding alone is not sufficient to generate these morphologies.

When cells were encapsulated in HA with a 3D topology characteristic of brain parenchyma, cells not only retained McTNs but lost the intervening fan-like regions of actin (**Fig. 1F**). Cells in both 3D HA and 3D HA-RGD formed protrusions similar in size, length, and frequency and over similar timescales (**Fig. 1F**). McTNs in 3D (~1 week) formed much more slowly than in 2D (~minutes), consistent with a need for extensive remodeling for McTN formation. Furthermore, the similarity in morphology between cells in 3D HA and 3D HA-RGD suggests that McTNs may be more prominent in 3D even when integrin ligands are available. The protrusions exhibited by U-251 MG cells expressing GFP-tubulin and RFP-LifeAct in 3D HA were also actin- and tubulin-positive, with microtubules occupying the core of the protrusions and extending into the protrusion ends (**Fig. 1G**). We have previously demonstrated that U-87 cells invade HA-RGD by tunneling into the bulk matrix over the course of several weeks and that invasion is preceded by elaboration of long protrusions [140]. We observe here that U-251 MG tumorspheres cultured in HA for 10 days exhibit protrusions into matrix and initial tunneling (**Fig. S5A**). These protrusions may be involved in matrix degradation, as larger

protrusions and tunneling cells are only observed in regions where the HA is degraded (**Fig. S5B**). These observations also suggest a mechanism by which cells move through nanoporous HA, which requires degradation to form a sufficiently large defect in the gel before cell migration can occur.

While 2D and 3D HA gels recapitulate some features of brain ECM, such as dimensionality, bulk elastic modulus, and HA-richness, this matrix does not fully capture the complexity of brain tissue. *Ex vivo* slice models have proven a valuable paradigm that retains the complexity of tissue while remaining amenable to high-resolution imaging [271,482]. We therefore seeded U-251 MG cells on *ex vivo* tissue culture slices, placed the slices on Boyden chamber (transwell) filters, and allowed the cells to invade for 24 hours **(Fig. 1H)**. SIM imaging of invaded cells revealed actin- and microtubule-positive McTNs of similar cytoskeletal composition to those observed in 2D and 3D culture (**Fig. 1I**). The consistency in cytoskeletal morphology between the HA platform and brain tissue culture supports the physiological significance of McTNs in driving adhesion and migration in brain tissue.

4.5.3 McTN structure and function depend on CD44

Given the abundance of the HA receptor CD44 on the McTN surface, we next investigated functional contributions of CD44 to McTN morphology and function. When we applied stochastic optical reconstruction microscopy (STORM) to image cells on HA, we observed that CD44 randomly distributed across the entire cell membrane, completely covering the periphery of McTNs (**Fig. 2A**). This is in contrast to previous reports of CD44 clustering into microdomains in other cell types, which has been hypothesized to increase interactions between CD44 and certain membrane proteins [483]. The broad distribution of CD44 even on membrane surfaces not in contact with the HA is consistent with our earlier finding that CD44-mediated adhesion to HA is rapid (minutes) and driven by many weak contacts. This is in contrast to integrin/focal adhesion-based attachment, which requires much longer maturation times (hours) and is associated with fewer, stronger, and more discrete adhesive structures [74].

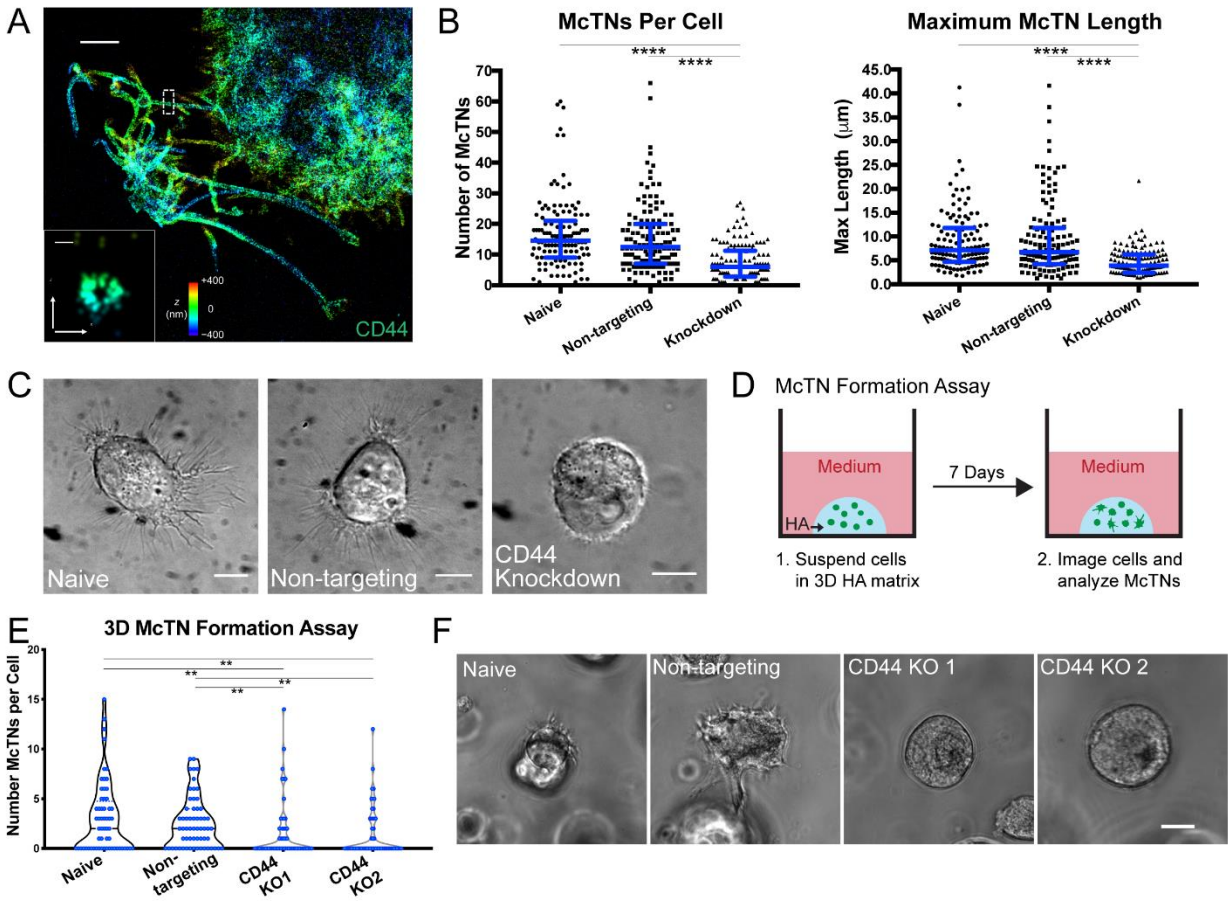

Figure 2. McTNs are CD44-dependent. A) STORM imaging of CD44-covered McTNs at periphery of U-251 MG cell on HA with inset showing transverse axis. Colors indicate z position. Scale=2 μm, inset=100 nm. B) shRNA KD of CD44 in U-251 MG cells on HA leads to a reduction of McTN number and length. N=130 total cells from 3 independent experiments. ****, $p<0.0001$ by Kruskal-Wallis test followed by Dunn's Multiple Comparisons test. Blue lines represent median with interquartile range. C) DIC imaging of spread naïve and non-targeting U-251 MG cells compared to rounded and poorly adhered shRNA CD44 KD cells. Scale=10 μm. D) Schematic of McTN formation assay in which cells are suspended in 3D HA, cultured for 7 days, and then imaged. E) Number of McTNs formed per naïve and non-targeting U-87 MG cells compared to CD44 KO controls. N=60 total cells analyzed from 3 independent experiments. **, $p<0.01$ by Kruskal-Wallis test followed by Dunn's Multiple Comparisons test. F) Example phase images of cells from the high McTN expressing population in naïve and non-targeting cells and the population expressing no McTNs in the CD44 KO cells. Scale=10 μm.

We assessed the role of CD44 in McTN formation by counting the number of observable McTNs per cell from a population of randomly selected naïve, non-targeting, and shRNA CD44 KD cells seeded on 2D HA. Using the same data set, we measured the length of the longest McTN for each cell. CD44 KD cells expressed significantly fewer protrusions per cell (**Fig. 2B**). Similarly, CD44 KD cells generally did not form long protrusions. In particular, the population of cells expressing the most and longest McTNs was almost

completely absent in CD44 KD cells. The KD cells remained rounded and extended only short protrusions, consistent with poor adhesion to the matrix (**Fig. 2C**).

As noted earlier, McTN formation is much slower in 3D than in 2D HA (days vs. hours), which strongly implies McTN formation within 3D nanoporous HA requires cells to degrade or otherwise remodel the surrounding matrix. To explore the functional importance of CD44 while accounting for these radically different kinetics, we designed a McTN formation assay in which cells were cultured in 3D HA for a week and then imaged within a single plane, and any visible McTNs were counted (**Fig. 2D**). During this extended period, we were concerned that the intrinsic heterogeneities associated with shRNA-mediated KD could allow selective pressures to artifactually enrich the population in cells with high CD44 expression. To avoid this confounding issue, we applied CRISPR-based gene editing to generate CD44 KO U-87 MG cells, for which we validated the lack of CD44 function through an inability to adhere to bare HA (**Fig. S6**). In CD44 KO cells we observed between 0 and ~15 McTNs/cell, with most cells having <5 McTNs within the imaging plane (**Fig. 2E**). While this does not account for protrusions extending in the z-direction, the results are overall consistent with 2D data (**Fig. 2B**). Again, we observed a subpopulation of cells with more numerous McTNs in controls that was not present in CD44 KO cells (**Fig 2E**). Furthermore, a larger proportion of CD44 KO cells expressed no McTNs. Cells expressing no McTNs were completely rounded and did not appear to productively engage the surrounding matrix (**Fig. 2F**). The finding that some CD44 KO cells are able to express McTNs in 3D matrix may result from several alternative mechanisms that emerge in the absence of CD44-HA binding. First, other hyaladherins such as RHAMM not strongly bound in 2D may engage more tightly in 3D matrix and compensate for CD44. Another possibility is that cells cultured in 3D HA over the course of a week secrete matrix components that engage adhesive receptors. Collectively, these data strongly indicate that McTN formation is largely CD44-dependent.

4.5.4 McTNs uniquely depend on microtubules over actin, Cdc42, and Myosin X

We next examined the extent to which McTNs depend on actin and microtubules. Cytochalasin D-mediated inhibition of actin polymerization increased both the number and length of McTNs, whereas nocodazole-based inhibition of microtubule polymerization reduced both the number of McTNs and the maximum protrusion length (**Fig. 3A**). Addition of cytochalasin D to CD44 knockout cells, however, did not generate significant growth of McTNs, indicating the necessity of CD44-HA adhesion to reinforce McTN formation and extension (**Fig. S7**). The few, short McTNs that formed were likely microtubules that began to protrude but could not stabilize and grow. Notably, McTN number and length were insensitive to the Cdc42 inhibitor ML141 (**Fig. 3A**), implying that these structures are not filopodia [484]. DIC imaging of cells during inhibitor treatment revealed that previously existing McTNs not only persisted but continued to grow after cytochalasin D treatment, and were accompanied by induction of new McTNs (**Fig. 3B**). In contrast, colchicine treatment produced an initial collapse of most McTNs, followed by slow collapse of the remaining McTNs (**Fig. 3B**). Addition of cytochalasin D and nocodazole did not reduce localization of CD44 to the cell membrane (**Fig. S8**). Thus,

McTNs are functionally distinct from filopodia, with McTN formation and protrusion along the matrix promoted by microtubule polymerization and restricted by actin polymerization.

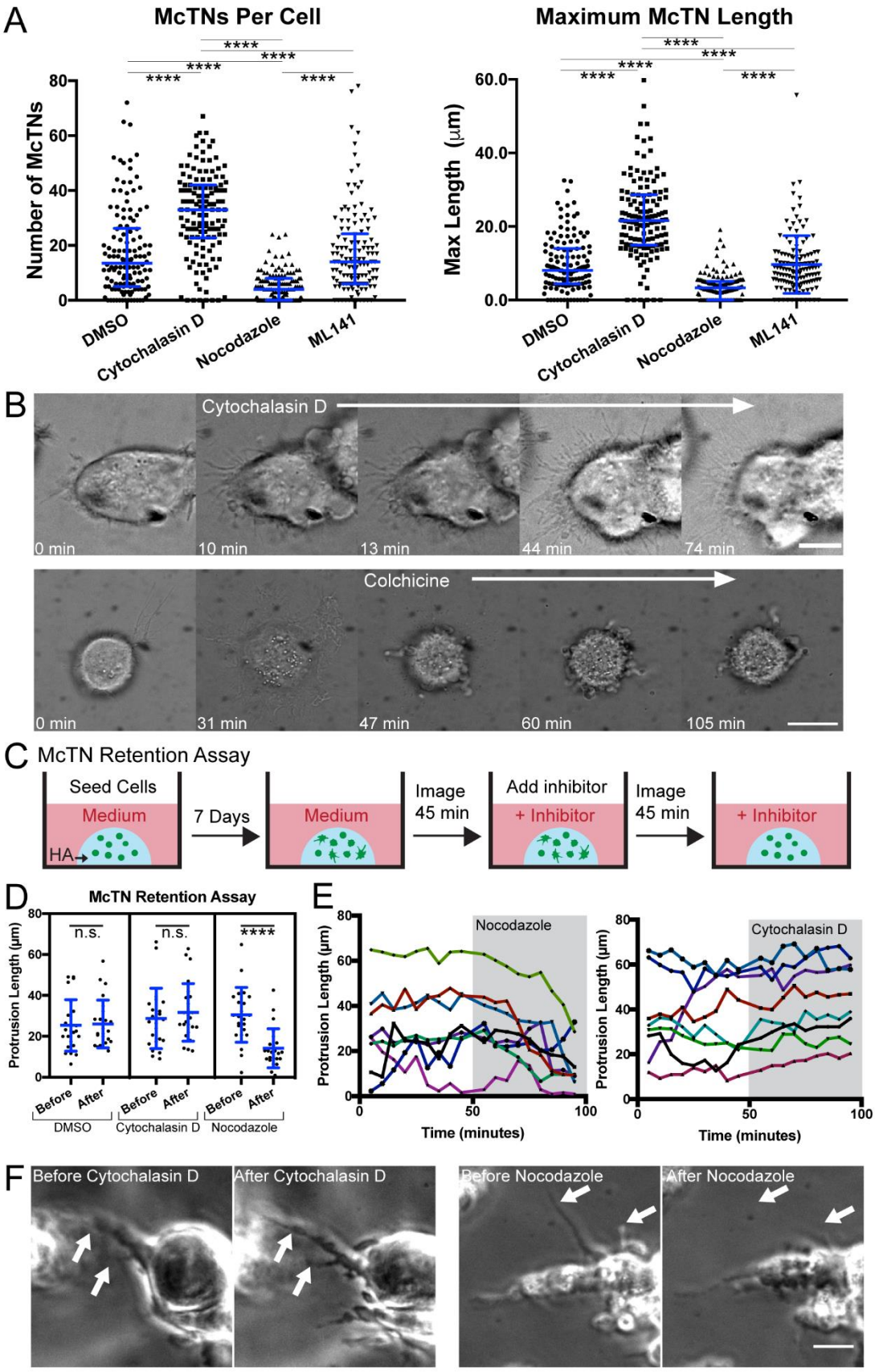
A
McTNs Per Cell
Number of McTNs
Maximum McTN Length
Max Length (μm)
DMSO
Cytochalasin D
Nocodazole
ML141
****
B
Cytochalasin D
0 min
10 min
13 min
44 min
74 min
Colchicine
0 min
31 min
47 min
60 min
105 min
C
McTN Retention Assay
Seed Cells
Medium
HA
7 Days
Image
45 min
Add inhibitor
+ Inhibitor
D
McTN Retention Assay
Protrusion Length (μm)
n.s.
****
Before
After
DMSO
Cytochalasin D
Nocodazole
E
Nocodazole
Cytochalasin D
Protrusion Length (μm)
Time (minutes)
F
Before Cytochalasin D
After Cytochalasin D
Before Nocodazole
After Nocodazole

Figure 3. McTNs are distinct from filopodia and are stabilized by a balance between microtubules and actin. A) Number of McTNs per U-251 MG cell and maximum McTN length per cell. N=130 total cells analyzed from 3 independent experiments, ****, p<0.0001 by Kruskal-Wallis test followed by Dunn's Multiple Comparisons test. Blue lines represent median with interquartile range. B) DIC imaging of U-251 MG cells shows McTNs increase in length and number with cytochalasin D treatment, while McTNs collapse with colchicine treatment. Scale=10 µm. C) Schematic showing McTN formation assay. Cells are seeded in 3D HA and cultured for 7 days. Cells are imaged for at least 45 minutes, an inhibitor is added, and then cells are again imaged for 45 minutes while McTN lengths are tracked. D) Length of tracked McTNs at 45 minutes before inhibitor addition compared to 45 minutes after inhibitor addition in U-87 MG cells. N=24 McTNs from 12 cells analyzed. ****, p<0.001, with lengths before and after each inhibitor compared by a paired t-test. Blue lines represent mean and standard deviation. E) Lengths of example individual protrusions tracked before and after inhibitor treatment. F) Examples of tracked protrusions (white arrows) 45 minutes before inhibitor addition and 45 minutes after inhibitor addition. Scale=20 µm.

To explore these regulatory concepts in 3D, we modified our McTN formation assay **(Fig. 2D)** to quantify McTN retention. Specifically, cells were cultured for 1 week to allow for McTNs to grow and then imaged for 45 minutes prior to inhibitor treatment and 45 minutes after treatment (**Fig. 3C**). We hypothesized that if microtubules were truly critical to McTN retention, inhibition of microtubules would result in McTN collapse but inhibition of actin would not. Comparing the lengths of individual McTNs 45 minutes prior to inhibitor treatment and 45 minutes after inhibitor treatment showed that DMSO and cytochalasin D treatment did not significantly affect protrusion length but nocodazole treatment resulted in decreased McTN length (**Fig 3D**). Observation of individual protrusions suggested that while McTNs collapsed gradually after nocodazole treatment, McTNs were largely unaffected by cytochalasin D treatment (**Fig. 3E, F**). The lack of McTN growth in response to microtubule disruption is consistent with a model in which McTN extension requires degradation and remodeling of the HA, which would be expected to occur over days. Together, these results suggest a similar microtubule dependence of McTNs in 3D matrix as observed on 2D matrix.

To gain additional insight into McTN ultrastructure, we revisited STORM to investigate cytoskeletal organization in these structures (**Fig. 4A**). In DMSO-treated controls, cell protrusions were composed of linear actin filaments that extended to the tips of some protrusions with interspersed and co-aligned microtubules. Notably, cells on HA lacked large actin bundles or lamellipodia. After cytochalasin D treatment, filamentous actin organization was not discernable, and microtubules dominated the core of long protrusions. Nocodazole treatment disrupted nearly all microtubule structures, with some short microtubule fragments present at the periphery. Nocodazole-treated cells expressed short actin filaments around the periphery. As a whole, nocodazole-treated cells were rounded and did not appear to interact with the HA, consistent with our previous results. We also used SIM to examine the localization of myosin X, a recognized filopodial tip marker thought to contribute to actin polymerization and traction force generation [485]. While these cells did not strongly express myosin X at the tips of filopodia even when

seeded on HA-RGD, some myosin X was present in the lamellipodia of cells on HA-RGD (**Fig. 4B**). In contrast, cells on HA expressed almost no myosin X in protrusions. Together, these results underscore mechanistic differences between filopodia and McTNs.

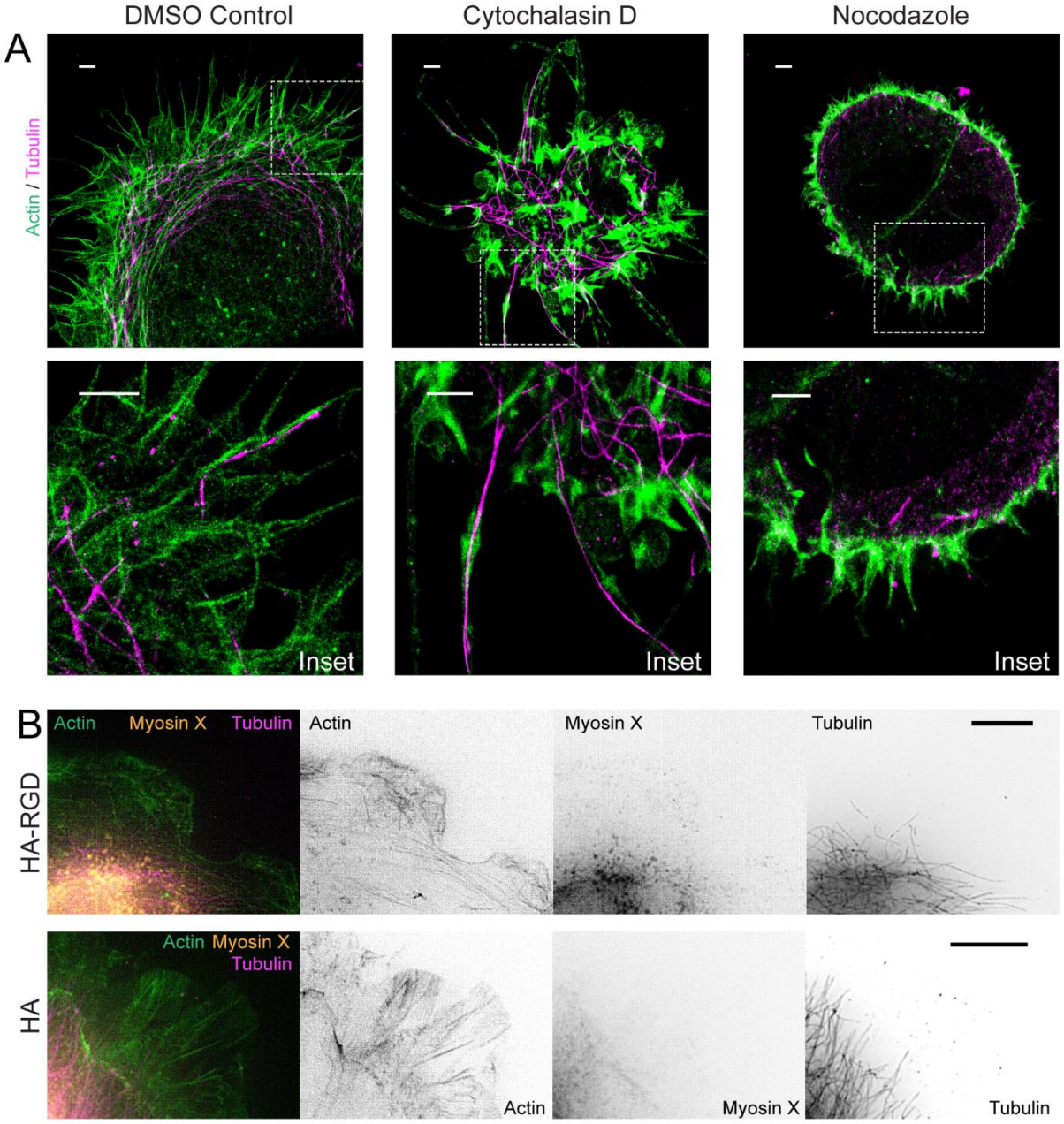

Figure 4. Organization of microtubules and actin within McTNs. A) STORM imaging of U-251 MG cells treated with DMSO as a control shows actin filaments extending around the cell periphery with microtubules interspersed and extending to the ends of McTN tips. After cytochalasin D treatment, most protrusions contain microtubules at the core. Cells treated with nocodazole adhere poorly to HA, remain rounded, and express only short, actin-positive protrusions at the periphery. Scale=2 µm. B) U-251 MG cells on bare HA

matrix do not express myosin X at the cell periphery. Cells on HA-RGD express some myosin X at the leading edge compared to cells on HA. Scale=5 µm.

4.5.5 McTNs are dynamic and participate in cell adhesion and motility

To gain deeper mechanistic insight into the dynamic interplay of microtubules and actin in McTNs, we applied live-cell SIM imaging to cells on HA expressing GFP-tubulin and RFP-LifeAct. While control cells on glass exhibited more traditional migratory structures in which microtubules and actin were not strongly colocalized along with short filopodial structures decorated the leading edge, cells on HA displayed a different morphology **(Fig. 5A, B)**. Cells on bare HA exhibited strong colocalization of actin filaments and microtubules in linear protrusions. Furthermore, colocalized actin filaments and microtubules underwent retrograde flow at the leading edge of the cell at qualitatively similar rates (**Fig. 5B**). Cells on HA-RGD rarely showed colocalization of actin and microtubules, with actin filaments again outlining the cell periphery (**Fig. 5C**). Retrograde flow on HA-RGD also appeared to be much slower than on bare HA.

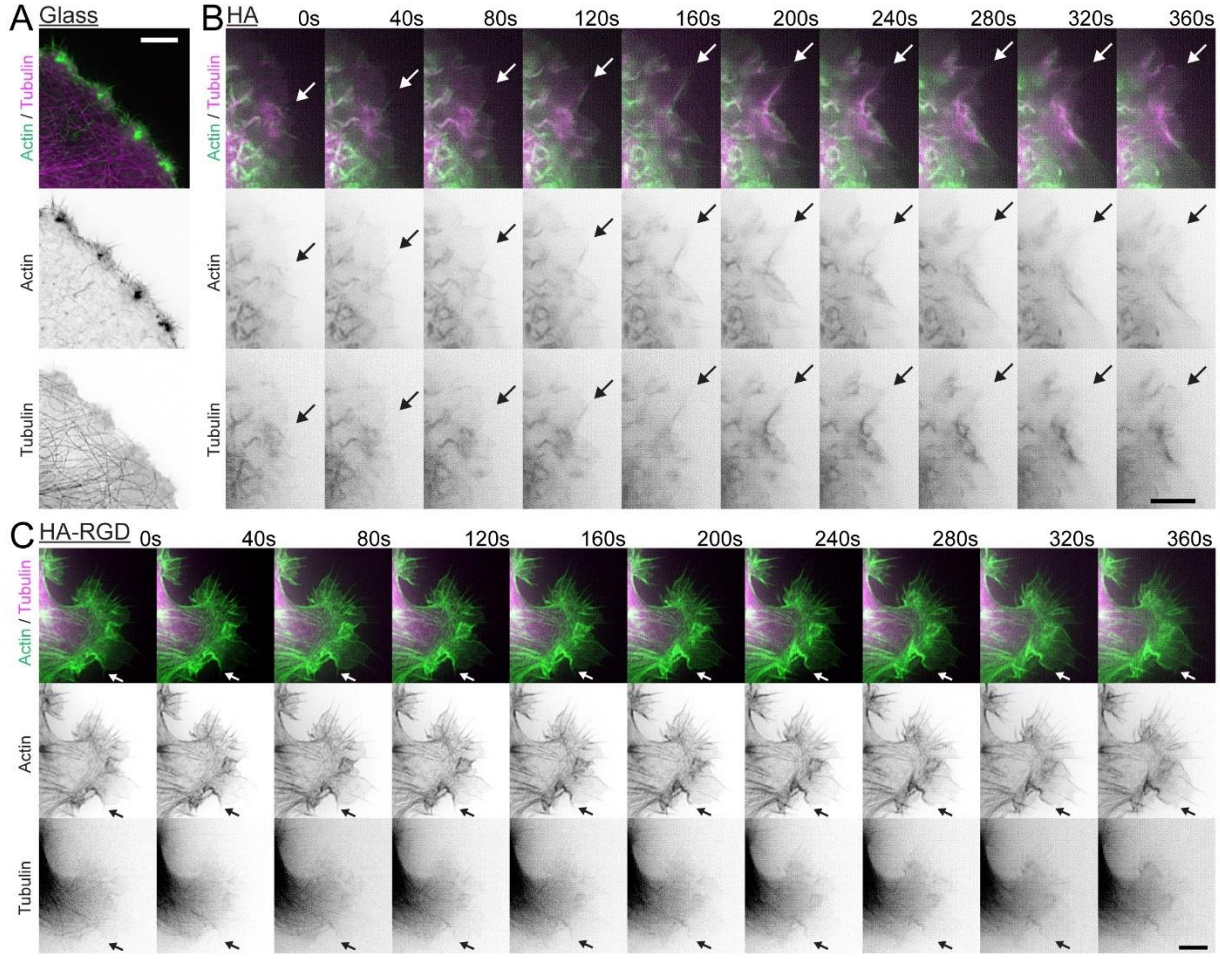

Figure 5. Microtubules and actin align and undergo coordinated retrograde flow in McTNs. A) On glass, U-251 MG cells express short actin filaments. Scale=5 µm. B)

Microtubules and actin grow in parallel and undergo retrograde flow in U-251 MG cells on HA. Arrow shows an example microtubule and actin microfilament in parallel. Scale=5 µm. C) Microtubule and actin are less strongly colocalized in U-251 MG cells on HA-RGD compared to HA. Arrow shows an example where microtubule is growing in parallel with actin. Scale=5 µm.

To investigate the role of McTNs in cell adhesion, mechanics, and motility, we pharmacologically manipulated McTN dynamics while probing these processes in several different *in vitro* paradigms. Using a centrifugal adhesion assay, we found that disruption of microtubules reduced adhesion while disruption of actin polymerization increased adhesion in both U-87 MG and U-251 MG cells (**Fig. 6A, Fig. S9A**). These results were consistent with our previous observations that nocodazole-treated cells are rounded on HA while cytochalasin D-treated cells express more and longer McTNs. In contrast, disruption of microtubule polymerization did not affect adhesion to HA-RGD (**Fig. 6B**). Disruption of either microtubules or actin decreased 2D random migration on HA, with actin disruption resulting in a more extreme reduction of motility (**Fig. 6C, Fig. S9B**). However, disruption of microtubules did not affect 2D migration on HA-RGD, despite affecting cell morphology and spreading (**Fig. 6D, Fig. S10A**). This implies that cells on HA as opposed to HA-RGD treated with microtubule polymerization inhibitors do not adhere strongly enough to generate traction forces necessary for migration. The loss of microtubule-mediated signaling may also or alternatively reduce F-actin assembly, thereby reducing the area of adhesion and number of adhesive bonds engaged with the surface. Conversely, cells treated with actin polymerization inhibitors can adhere strongly but cannot generate sufficient actomyosin-based traction to support motility. Moderate inhibition of myosin II-mediated contractility by blebbistatin resulted in an increase in HA adhesion and decrease of migration speed on 2D HA substrates (**Fig. 6A,C**). These results mirrored trends observed with actin polymerization inhibitors although to a lesser extreme. To characterize migration in environments characteristic of confined geometries found in tissue, we seeded cells onto HA or HA-RGD microchannels. We saw a similar relative effect of inhibitors on migration of cells in HA-microchannels as on 2D matrix (**Fig. 6E**). Microtubule disruption slowed migration of cells on HA-RGD microchannels (**Fig. 6F**) but did not prevent cells from attaching and spreading to some degree in HA-RGD channels (**Fig. S10B**). SIM imaging revealed that blebbistatin treatment resulted in longer, thinner McTNs with more prominent microtubule-based structures than with DMSO alone (**Fig. 6G**). Microtubule-driven protrusion or microtubule-based signaling and CD44-mediated adhesion thus seem to balance actomyosin-driven contractility in McTN-based motility (**Fig. 6H**). In contrast, integrin-RGD binding strengthens adhesion and reinforces actin bundles, which reduces the need for mechanical balance by microtubule polymerization or signaling.

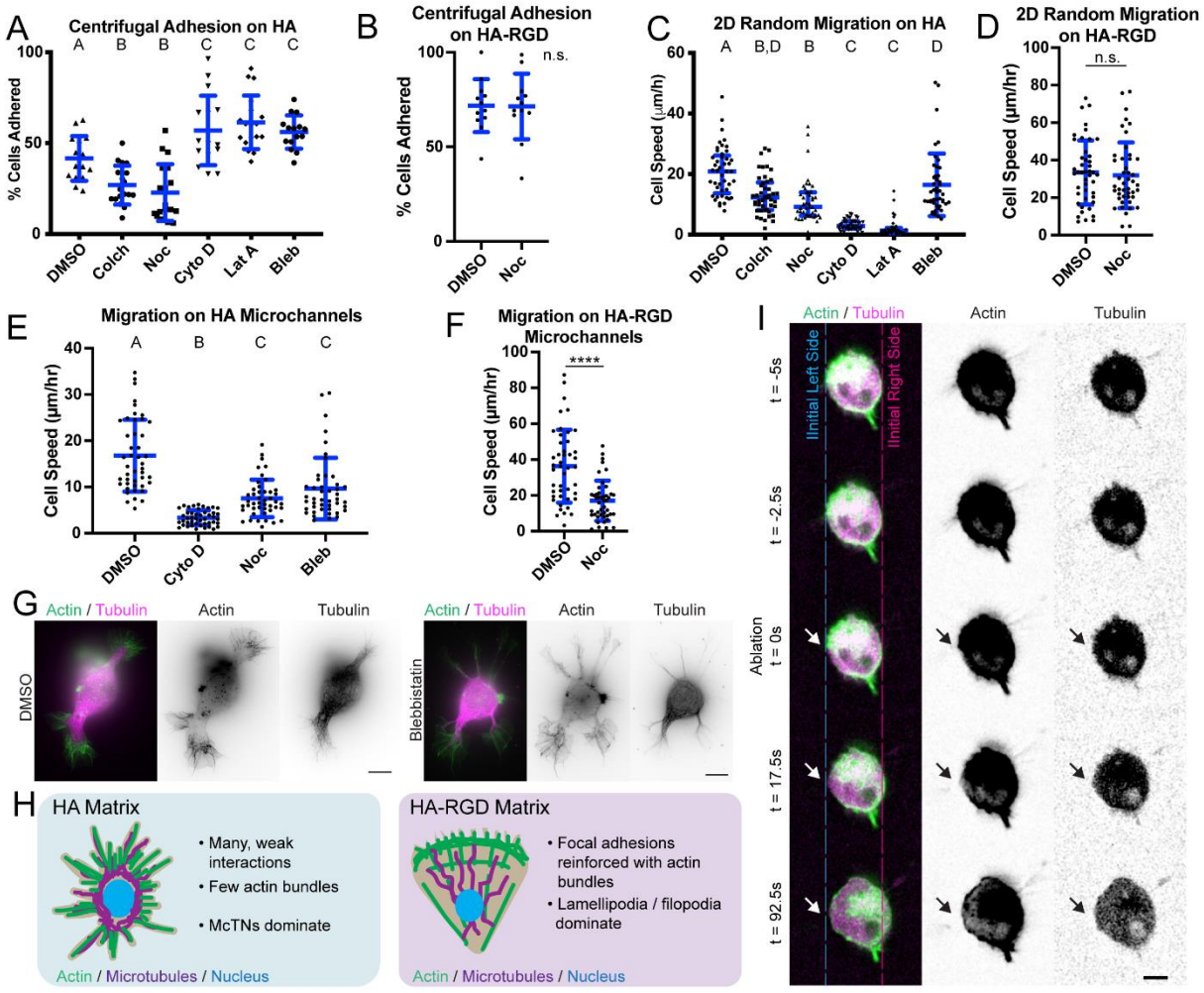

Figure 6. McTNs facilitate cell adhesion and motility on HA. A) Centrifugal adhesion assay for U-87 MG cells interacting with HA. N=15-18 total gels analyzed from 3 independent experiments. A, B, and C represent statistical families with a significant difference of $p<0.05$ by ANOVA followed with Tukey-Kramer Multiple Comparisons test. Blue lines represent mean and standard deviation. B) Centrifugal adhesion assay for U-87 MG cells interacting with HA-RGD. N=12 total gels analyzed from 3 independent experiments, with no significant difference by Student's t-test. Blue lines represent mean and standard deviation. C) Random 2D migration speeds of U-87 MG cells on HA. N=45 total cells analyzed from 3 independent experiments. A, B, C, and D represent statistical families with a significant difference of $p<0.05$ by ANOVA followed with Tukey-Kramer Multiple Comparisons test. Blue lines represent mean and standard deviation. D) Random 2D migration speeds of U-87 MG cells on HA-RGD. N=45 total cells analyzed from 3 independent experiments. No significant difference detected by Student's t-test. Blue lines represent mean and standard deviation. E) 1D random migration of U-87 MG cells on microchannels in HA. N=45 total cells analyzed from 3 independent experiments. A, B, and C represent statistical families with a significant difference of $p<0.05$ by ANOVA followed with Tukey-Kramer Multiple Comparisons test. Blue lines represent mean and standard deviation. F) 1D random migration of U-87 MG cells on microchannels in HA-RGD. N=45 total cells analyzed from 3 independent experiments. ****, $p<0.0001$ by

Student's t-test. G) SIM imaging of U-87 MG cells treated with blebbistatin compared with cells treated with the vehicle control DMSO. Scale=10 µm. H) Schematic of cell morphology on HA compared to HA-RGD. Cells on HA exhibit McTNs. I) Laser ablation of McTN in U-251 MG cell expressing GFP-tubulin and RFP-LifeAct. Arrow indicates ablation site. Scale=10 µm.

Based on this model, we hypothesized that McTNs must bear tension. Laser ablation of an McTN extending from a U-251 MG cell on an HA directly verified this hypothesis (**Fig. 6I**). After ablation, the microtubule component was no longer visible, presumably due to rapid microtubule depolymerization induced by the ablation [486]. The cell body shifted away from the site of laser ablation, implying that the ablated McTN had been maintaining a tensile force between the cell body and HA.

4.5.6 McTN formation requires IQGAP1

The coupling of cytoskeletal forces to cell traction and motility in integrin-based adhesion has traditionally been framed in terms of a motor-clutch model [487,488]. In this paradigm, actin polymerization advances the leading edge and establishes matrix adhesions, which act as clutches that transmit myosin-based centripetal forces to the matrix to allow forward translocation of the cell. Based on our SIM imaging revealing close coupling between actin and microtubule dynamics, we hypothesized that an analogous motor-clutch mechanism may be at play in McTNs, with McTNs acting as the protrusive element. Such a model would require specific proteins to couple microtubules, actin, and CD44. The IQGAP1/CLIP170 complex is a natural candidate in this regard. IQGAP1 has previously been shown to complex with the microtubule-binding protein CLIP170, where it can participate in microtubule capture to membrane-localized Rac1 and Cdc42 in the leading edge of fibroblasts [489]. Crosslinking of actin and microtubules via IQGAP1 and CLIP170 has also been implicated in neuronal dendrite and axonal growth cone extension [490]. IQGAP1 positive protrusions have been identified in brain tissue culture [491], and IQGAP1 has previously been suggested as a biomarker for aggressive GBM [492]. Given that IQGAP1 can also bind to CD44 and is important for HA binding by CD44 [455], we asked whether IQGAP1, CLIP170 and CD44 collectively contribute to McTN formation, cell adhesion, and cell motility.

SIM imaging of cells on HA revealed colocalization of IQGAP1, CLIP170, actin, and microtubules in McTNs (**Fig. 7A**). IQGAP1 strongly colocalized to actin both in cells on HA and HA-RGD, where it is available for complexation with CLIP170 (**Fig. S11A,B**). Protrusions positive for actin and microtubules were also positive for IQGAP1 and CLIP170, with 71 ± 18% of protrusions positive for all four components (**Fig. S11C**). To test functional contributions of IQGAP1 to McTN formation, we used CRISPR/Cas9 gene editing to knock out IQGAP1 in U-87 MG cells (**Fig. S11D**). Fewer IQGAP1 KO cells formed long McTNs (>10 µm) than controls (**Fig. S11E**). IQGAP1 KO cells also exhibited more blebbing than controls, perhaps indicating a more contractile state (**Fig. S11F-G**) [493]. IQGAP1 KO cells still spread on HA-RGD, albeit with a more circular, less polarized morphology (**Fig. S12**), possibly reflecting IQGAP1's association with actin and Rho GTPases [494]. Consistent with these morphological observations, IQGAP1 KO had no

effect on cell adhesion to HA-RGD but dramatically reduced adhesion to HA (**Fig. 7C**). The random 2D migration speed of IQGAP1 KO cells was moderately reduced both on HA and HA-RGD (**Fig. 7D**). Thus, RGD-integrin binding is largely preserved in the absence of IQGAP1, but CD44-mediated binding to HA-rich matrix is largely abrogated.

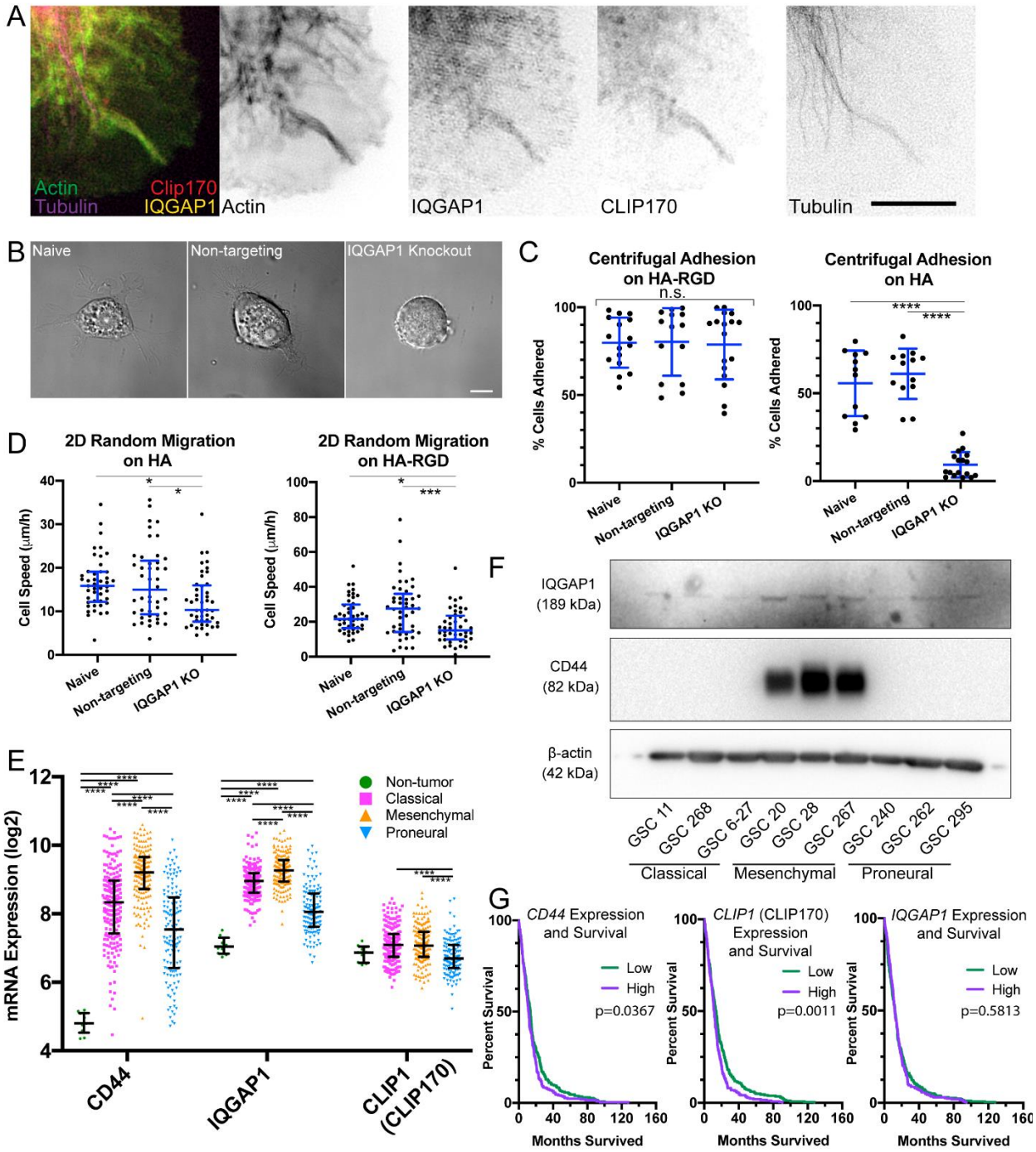

Figure 7. McTNs are mechanically coupled to the cytoskeleton and ECM through CD44, IQGAP1, and CLIP170. A) SIM of U-87 MG cell on HA demonstrating that IQGAP1, CLIP170, tubulin, and actin are colocalized in McTNs. Scale=5 μm. B) DIC imaging demonstrates that IQGAP1 KO cells remain rounded on HA compared to naïve and non-targeting controls. Scale=10 μm. C) IQGAP1 KO reduces adhesion to HA but not HA-RGD. N=13-17 total gels analyzed from 3 independent experiments. ****, p<0.001 by one-way ANOVA followed by Tukey-Kramer Multiple Comparisons test. Blue lines represent mean and standard deviation D) IQGAP1 KO reduces 2D migration speed on both HA and HA-RGD. N=45 total cells analyzed from 3 independent experiments. *, p<0.05; ***, p<0.001, by one-way ANOVA followed by Tukey-Kramer Multiple Comparisons test. Blue lines represent mean and standard deviation. E) Plot of log2 transformed mRNA levels obtained from TCGA of CD44, IQGAP1, and CLIP1 by subtype. Black lines represent median and interquartile range. N=10 non-tumor, 199 classical, 166 mesenchymal, and 137 proneural samples from independent patients analyzed. ****, p<0.001 by one-way ANOVA followed by Tukey-Kramer's Multiple Comparisons test using log2 transformed mRNA expression levels and compared between subtypes for each gene. F) Western blot of IQGAP1, CD44, and -actin in patient derived GSC cells indicates variable yet ubiquitous IQGAP1 expression, but high CD44 expression only in cells of the mesenchymal subtype. Blot was first probed for CD44 and -actin, followed by stripping and probing for IQGAP1 G) Kaplan-Meier survival correlating with high or low levels of CD44, CLIP170, and IQGAP1 mRNA with median expression level used as cutoff. N=262 patients in the high expression group and N=263 patients in the low expression group. p values determined by log-rank Mantel-Cox comparison.

To more deeply explore the disease relevance of these findings, we analyzed the Cancer Genome Atlas (TCGA) to explore associations between *IQGAP1*, *CLIP1* (CLIP170), and *CD44* gene expression and GBM. *CD44* and *IQGAP1* gene expression were strongly correlated (Pearson's product-moment coefficient of 0.61). Both *CD44* and *IQGAP1* are highly overexpressed in GBM (**Fig. 7E**). Furthermore, *IQGAP1*, *CLIP1* (CLIP170), and *CD44* show GBM subtype-specific expression patterns, with the highest expression levels in the most aggressive mesenchymal subtype and the lowest expression levels in the least aggressive proneural subtype. We also probed the CD44 and IQGAP1 status in a panel of GSCs which have been previously characterized by subtype [152] (**Fig. 7F**). Consistent with results from the TCGA, we observed a dramatic upregulation in CD44 as well as an upregulation of IQGAP1 in the mesenchymal subtype compared to the proneural and classical subtypes. All of the cell lines expressed levels of CD44s detectable by Western blotting except GSC 268 and GSC 6-27, and isoform expression of CD44 was not observed (**Fig. 7F, Fig. S6A, Fig. S13**). While low IQGAP1 expression in histological samples has been associated with longer patient survival relative to samples with high expression [492], no correlation was observed between gene expression and survival using median expression as a cutoff for survival analysis (**Fig. 7G**). CD44 and CLIP1 (CLIP170) gene expression correlated with patient survival (**Fig. 7G**). The significant but modest survival difference correlated with high compared to low CD44 expression is consistent with previous findings that an intermediate level of CD44 the strongest correlation with poor patient survival [482].

4.6 Discussion

Here, we investigated molecular and biophysical mechanisms through which GBM cells adhere to HA. We find that GBM cells interact with HA via McTNs, which are long, thin protrusions rich in the HA-receptor CD44, which we show is necessary for cell adhesion and McTN stability. Motility assays and laser ablation show that McTNs are stabilized by a balance of actomyosin-driven contraction, microtubule-driven protrusion, and CD44-mediated adhesion. Mechanical coupling of actin and microtubules with McTNs appears to be reinforced by a complex of IQGAP1 and CLIP170, and loss of IQGAP1 specifically disrupts adhesion and motility on HA.

McTNs, defined as microtubule-positive protrusions that elongate following actin depolymerization, have been observed in circulating tumor cells (CTCs), where they are believed to facilitate endothelial adhesion prior to extravasation [477–479]. However, to our knowledge, these structures have not been previously appreciated in the context of 2D or 3D migration in or on a solid-state matrix. It is therefore informative to compare McTNs to canonically described migratory processes. McTNs share some morphological similarities with filopodia, such as the high aspect ratio and presence of actin filaments [495]. However, the lack of Cdc42-dependence and myosin X-positivity, together with the dependence on CD44 and microtubules for formation and elongation, suggest that McTNs are structurally and functionally distinct from filopodia. McTNs in 3D show some similarities with pseudopodia, although pseudopodia are usually observed in a context of integrin adhesion in fibrillar matrix rather than nanoporous matrix lacking integrin ligands [496,497]. Nonetheless, additional characterization and comparison of molecular composition and dynamics are necessary to establish the degree of similarity between these protrusions and develop a more rigorous operational definition. Our findings may also offer mechanistic insight into GBM progression *in vivo*. Micronemes, microtubes, and other long, protrusive structures have been described in GBMs, yet their molecular characteristics and mechanisms of formation remain incompletely elucidated. In particular, McTNs bear several key similarities to recently reported membrane microtubes, which are postulated to connect cells into a multicellular network that facilitates exchange of resistance factors [275]. Key similarities are the inclusion of actin and microtubules, lack of myosin X, and similar morphology. While it is not clear that McTNs are functionally related to microtubes, our results and model may offer mechanistic insights in to how microtubes and related processes arise in GBM.

These data also provide insights into how CD44 supports cell motility. Our HA platform enables us to isolate and investigate the role of CD44-HA binding in driving invasion. Importantly, CD44 is sufficient to drive the formation of tension-bearing protrusions that enable motility in the complete absence of integrin ligands. We have previously demonstrated that CD44-HA binding occurs more rapidly than integrin binding[74], and imaging in this study suggests CD44 covers the membrane rather than localizing to specific binding regions analogous to integrins in focal adhesions. Furthermore, CD44-mediated adhesion alone does not support strong actin bundling or the formation of large

lamellipodia. These findings support a model in which CD44 binding is characterized by many rapid weak interactions with the ECM whereas integrin binding which is characterized by fewer, slow, mechanically reinforced interactions. These two systems give rise to fundamentally different cytoskeletal architectures. Microtubule polymerization, through mechanical reinforcement and/or modulation of tubulin-mediated signaling, reduces retrograde actin flow or upregulates F-actin assembly that balances actomyosin-based contractility [498,499]. With the lack of reinforced, localized cell-matrix interactions in the context of CD44-HA binding and low integrin binding found in cells in HA-rich matrix, more internal protrusive forces or signaling cues from microtubules may be needed to balance actomyosin contractility [122]. Consistent with this idea, microtubule-based motility is increasingly recognized as key to migration through tightly confined channels or soft 3D matrix in which focal adhesion formation may be restricted [122,500]. Furthermore, GBM cells have been reported to migrate despite treatment with pharmacological inhibitors of actin polymerization [501]. This may also explain why we observed McTNs in both 3D HA and HA-RGD but not in 2D HA and HA-RGD, with much greater prominence in 3D than in 2D.

Several studies have identified IQGAP1 as an important marker of GBM invasion, but the mechanisms underlying the expression of this biomarker remain poorly understood [491,492,494]. In particular, IQGAP1-positive processes protruding from GBM cells have been identified in brain tissue culture slices [491]. Our work suggests that IQGAP1 may be contributing directly to invasive McTN machinery through the coupling of actin and microtubules in complex with CLIP170 and possibly CD44. Nonetheless, it is important to acknowledge that CD44, IQGAP1, and microtubules can all trigger other types of intracellular signals which likely contribute to migratory phenotypes. Microtubule disruption releases monomeric tubulin potentially along with actin regulatory factors, which could in turn promote actin polymerization and contractility [498,502,503]. CD44, IQGAP1, and microtubules all upregulate and depend to some degree on Rac1 signaling [497,504]. It is possible that disrupting one of these components also reduces Rac1 signaling, which in turn impedes McTN growth. While the nature of the relationship between IQGAP1, CLIP170, CD44, actin, and microtubules remains to be further elucidated, our study suggests strong interplay that is particularly important in the context of low-integrin, high-CD44 engagement compared to high-integrin engagement.

While targeting CD44 is effective in reducing tumor invasion in animal models[48,452], initial clinical studies of antibodies targeting one isoform of CD44 in breast or squamous cell carcinoma failed due to high toxicity from non-specific interactions with CD44 in other organs such as skin [505,506]. Our findings highlight the need to understand the role of CD44-cytoskeletal interactions to elucidate more specific targets. These findings also underscore compositional and mechanistic differences in protrusions forming in microenvironments lacking nonfibrillar guidance cues and rich in HA. McTN function should be further studied to better understand the relevance of these structures in disease progression, such as how McTNs participate in matrix remodeling or whether they facilitate cell-cell communication. Given the morphological similarities between McTNs and protrusions involved in invasion and cell-cell communication *in vivo*[271,275], establishment of functional similarities could generate new mechanistic insight and

therapeutic targets difficult to elucidate in animal models. Finally, understanding how McTN expression relates to molecular subtype and tumor recurrence would focus efforts to target McTN-based motility in patients who would most benefit.

4.7 Acknowledgements

Confocal images were acquired at the CIRM/QB3 Shared Stem Cell Facility at UC Berkeley, which provided the Olympus BX51WI microscope with Swept Field Confocal technology. We thank Mary West for assistance and training. Structured illumination microscopy was conducted at the UC Berkeley Biological Imaging Facility, which was supported in part by the National Institutes of Health S10 program under award number 1S10OD018136-01. The content is solely the responsibility of the authors and does not necessarily represent the official views of the National Institutes of Health. We thank Dr. Steve Ruzin and Dr. Denise Schichnes for their technical assistance and training. We also thank the following groups and individuals: Dr. Joe McCarty and Dr. Erik Sulman at MD Anderson Cancer Center for providing the GSC patient-derived cells, Dr. David Schaffer for sharing equipment for Western blot and immunohistochemistry analysis, Hector Nolla for technical assistance with flow cytometry, and the Northwest Animal Care Facility. Finally, we gratefully acknowledge financial support from the following sources: National Institutes of Health (F31CA228317 to K.W.; F31GM119329 to S.L.; R21CA174573, R21EB016359, and R01GM122375 to S.Kumar), the European Union's Horizon 2020 research and innovation programme under the Marie Sklodowska-Curie grant agreement (No. 752097 to J.C.), and the W.M. Keck Foundation (S.Kumar). K.X. is a Chan Zuckerberg Biohub Investigator and acknowledges support from NSF under CHE-1554717.

Chapter 5. Conclusions

Interactions between tumor cells and their microenvironment facilitate aggressive tumor progression but remain a relatively unexplored therapeutic target. In this dissertation, we investigated interactions of glioblastoma (GBM) cells with matrix and topographical cues in a hyaluronic acid (HA)-rich microenvironment. In Chapter 1, we reviewed the contributions of the microenvironment to GBM progression and how the microenvironment can be studied using model systems. Importantly, in vitro model systems enable detailed mechanistic analysis of tumor invasion while avoiding limitations of orthotopic xenograft animal models (e.g. cost, scalability, and lack of normal immune response). With improved validation, these model systems can potentially accelerate therapeutic development and improve patient-specific treatments.

In Chapter 2, we developed an in vitro model of intraparenchymal invasion and vascular invasion that can specifically capture the transition between these invasive modalities. Our work demonstrates that cells transitioning from a 3D mode of invasion in the intraparenchymal-like region to a quasi-2D mode of invasion in the vascular-like region increase invasion speed and change cytoskeletal morphology. These topographical effects are generalizable across matrix formulations, although the mechanisms underlying invasion are matrix dependent. We also found that the change in topography is cell instructive as opposed to selective. While many model systems of 3D invasion have utilized collagen I or Matrigel, our model integrates topographical cues into HA. This matrix better represents the brain microenvironment and can serve as a platform for introducing vasculature and stromal cells for further investigation.

We then reviewed how HA specifically gives rise to biological signaling, and how these signals can be integrated into model systems in Chapter 3. HA is not inert, but rather is an active signaling molecule through its mechanics, adhesivity, and degradability. Incorporating these properties into in vitro models is critical for understanding HA biology and designing HA-based platforms that precisely guide cell behavior. We also discussed how HA-based signaling can be explored systematically using HA-based platforms. While integrin-based motility is appreciated as the main driver of adhesion and migration, other transmembrane receptors can also contribute significantly to cell motility. Our work in Chapter 4 leveraged HA-based platforms to show that CD44, a transmembrane receptor for HA, facilitates GBM adhesion and migration in HA-rich matrices. CD44-dependent microtentacles (McTN) mediate this migration and adhesion and serve as a protrusive unit through which cells can apply force and generate tension on HA. McTNs are stabilized by a combination of actin and microtubule polymerization and are mechanistically coupled through IQGAP1/CLIP170. Our work suggests McTNs and CD44-dependent motility as a potential therapeutic target.

Collectively, this work demonstrates how topography, HA, and CD44 guide cell behavior and underscores the importance of investigating cell-HA interactions, prompting investigation into the reciprocal relationship of CD44 and the HA network in tissue. While we have demonstrated that CD44 is sufficient to support adhesion and motility in HA, the contributions of CD44 to motility in more complex environments remains poorly

understood. Our work in Chapter 4 suggests that CD44-driven motility is most important in the context of HA-rich environments with low-integrin availability. Understanding how CD44 contributes to adhesion and migration in environments with high integrin-ligand availability, fibrillar structures, or increasing dimensionality (2D vs. 3D) would provide fundamental insight into CD44-mediated mechanobiology and invasion. We also have not yet completely characterized the role of CD44 in applying traction force. While studies have measured forces applied by single integrins or how traction is distributed through focal adhesions on the single-cell and multicellular scale, we have yet to quantify traction force applied at any scale through CD44.

Our also work suggests that McTNs play important functional roles in the invasion of HA-rich matrices, but we have not yet deeply investigated these functions. In particular, the finding that McTNs precede invasion suggests that McTNs likely play a role in matrix remodeling through secretion and degradation. In this way, McTNs in HA-rich matrices may function analogous to invadopodia in collagen-rich matrices. Future studies should examine the role of actin and microtubule balance and the contributions of the CLIP170/IQGAP1 complex. We have not investigated the extent to which these molecular players interact directly through mechanical force transmission versus more indirectly through diffusion of a soluble signal, nor have we examined how binding of these components affects cytoskeletal force distribution and traction force. A more thorough characterization of mechanisms governing McTN formation and function will better define how McTNs and other known cell protrusions relate.

Finally, there is a major gap in our understanding of how cells mechanically sense, navigate, and modify the HA network in engineered matrices and whole tissue. HA molecular weight is a key regulator of HA-based signaling that we have not explored in this dissertation, and the mechanisms underlying the importance of molecular weight are relatively unexplored. It is possible that HA concentration and molecular weight vary across tumor microenvironments, and that this variation directly influences to tumor progression. The degree to which HA contributes to mechanics at the tissue level and how cells modify the HA network, especially with respect to molecular weight, also remains largely unknown. Given that hyaluronidases are already used in other cancer types to improve chemotherapeutic delivery by reducing diffusion barriers, a more thorough understanding of how HA guides tumor progression could improve treatment precision. Future studies of CD44-HA interactions will illuminate new avenues for HA-targeted therapies and will fundamentally influence the development of engineered HA matrices for tissue engineering and modeling.

References:

1. Ostrom, Q. T. *et al.* CBTRUS Statistical Report: Primary Brain and Other Central Nervous System Tumors Diagnosed in the United States in 2011–2015. *Neuro. Oncol.* **20**, iv1–iv86 (2018).
2. Koshy, M. *et al.* Improved survival time trends for glioblastoma using the SEER 17 population-based registries. *J. Neurooncol.* **107**, 207–212 (2012).
3. Tamimi, A. F. & Juweid, M. *Epidemiology and Outcome of Glioblastoma*. *Glioblastoma* (Codon Publications, 2017). doi:10.15586/CODON.GLIOBLASTOMA.2017.CH8.
4. Lee, J. H. J.-H. J.-K. J.-H. J. E. J. H. *et al.* Human glioblastoma arises from subventricular zone cells with low-level driver mutations. *Nature* **560**, 243–247 (2018).
5. Khalifa, J. *et al.* Subventricular zones: new key targets for glioblastoma treatment. *Radiat. Oncol.* **12**, 67 (2017).
6. Chen, L. *et al.* Increased Subventricular Zone Radiation Dose Correlates With Survival in Glioblastoma Patients After Gross Total Resection. *Int. J. Radiat. Oncol.* **86**, 616–622 (2013).
7. Ohgaki, H. & Kleihues, P. Genetic pathways to primary and secondary glioblastoma. *Am. J. Pathol.* **170**, 1445–53 (2007).
8. Davis, M. E. Glioblastoma: Overview of Disease and Treatment. *Clin. J. Oncol. Nurs.* **20**, S2-8 (2016).
9. Gupta, A. & Dwivedi, T. A Simplified Overview of World Health Organization Classification Update of Central Nervous System Tumors 2016. *J. Neurosci. Rural Pract.* **8**, 629–641 (2017).
10. Yan, H. *et al. IDH1* and *IDH2* Mutations in Gliomas. *N. Engl. J. Med.* **360**, 765–773 (2009).
11. Hartmann, C. *et al.* Patients with IDH1 wild type anaplastic astrocytomas exhibit worse prognosis than IDH1-mutated glioblastomas, and IDH1 mutation status accounts for the unfavorable prognostic effect of higher age: implications for classification of gliomas. *Acta Neuropathol.* **120**, 707–718 (2010).
12. Stupp, R. *et al.* Effects of radiotherapy with concomitant and adjuvant temozolomide versus radiotherapy alone on survival in glioblastoma in a randomised phase III study: 5-year analysis of the EORTC-NCIC trial. *Lancet. Oncol.* **10**, 459–66 (2009).
13. Young, R. M., Jamshidi, A., Davis, G. & Sherman, J. H. Current trends in the surgical management and treatment of adult glioblastoma. *Ann. Transl. Med.* **3**, 121 (2015).
14. Watanabe, M., Tanaka, R. & Takeda, N. Magnetic resonance imaging and histopathology of cerebral gliomas. *Neuroradiology* **34**, 463–469 (1992).
15. Sherriff, J. *et al.* Patterns of relapse in glioblastoma multiforme following concomitant chemoradiotherapy with temozolomide. *Br. J. Radiol.* **86**, 20120414 (2013).
16. Mutter, N. & Stupp, R. Temozolomide: a milestone in neuro-oncology and beyond? *Expert Rev. Anticancer Ther.* **6**, 1187–1204 (2006).
17. Hegi, M. E. *et al.* Clinical trial substantiates the predictive value of O-6-methylguanine-DNA methyltransferase promoter methylation in glioblastoma

patients treated with temozolomide. *Clin. Cancer Res.* **10**, 1871–4 (2004).
18. Franceschi, E. *et al.* Treatment options for recurrent glioblastoma: pitfalls and future trends. *Expert Rev. Anticancer Ther.* **9**, 613–619 (2009).
19. Kappelle, A. C. *et al.* PCV chemotherapy for recurrent glioblastoma multiforme. *Neurology* **56**, 118–120 (2001).
20. Weller, M., Cloughesy, T., Perry, J. R. & Wick, W. Standards of care for treatment of recurrent glioblastoma--are we there yet? *Neuro. Oncol.* **15**, 4–27 (2013).
21. Kreisl, T. N. *et al.* Phase II Trial of Single-Agent Bevacizumab Followed by Bevacizumab Plus Irinotecan at Tumor Progression in Recurrent Glioblastoma. *J. Clin. Oncol.* **27**, 740–745 (2009).
22. Wenger, K. J. *et al.* Bevacizumab as a last-line treatment for glioblastoma following failure of radiotherapy, temozolomide and lomustine. *Oncol. Lett.* **14**, 1141–1146 (2017).
23. Friedman, H. S. *et al.* Bevacizumab Alone and in Combination With Irinotecan in Recurrent Glioblastoma. *J. Clin. Oncol.* **27**, 4733–4740 (2009).
24. Lee, C. G. *et al.* Anti-Vascular endothelial growth factor treatment augments tumor radiation response under normoxic or hypoxic conditions. *Cancer Res.* **60**, 5565–70 (2000).
25. Eyler, C. E. & Rich, J. N. Survival of the fittest: cancer stem cells in therapeutic resistance and angiogenesis. *J. Clin. Oncol.* **26**, 2839–45 (2008).
26. Quail, D. F. & Joyce, J. A. The Microenvironmental Landscape of Brain Tumors. *Cancer Cell* **31**, 326–341 (2017).
27. Levental, K. R. *et al.* Matrix Crosslinking Forces Tumor Progression by Enhancing Integrin Signaling. *Cell* **139**, 891–906 (2009).
28. Nakasone, E. S. *et al.* Imaging Tumor-Stroma Interactions during Chemotherapy Reveals Contributions of the Microenvironment to Resistance. *Cancer Cell* **21**, 488–503 (2012).
29. Ghajar, C. M. *et al.* The perivascular niche regulates breast tumour dormancy. *Nat. Cell Biol.* **15**, 807–17 (2013).
30. Provenzano, P. P., Inman, D. R., Eliceiri, K. W. & Keely, P. J. Matrix density-induced mechanoregulation of breast cell phenotype, signaling and gene expression through a FAK-ERK linkage. *Oncogene* **28**, 4326–43 (2009).
31. Elahi-Gedwillo, K. Y., Carlson, M., Zettervall, J. & Provenzano, P. P. Antifibrotic Therapy Disrupts Stromal Barriers and Modulates the Immune Landscape in Pancreatic Ductal Adenocarcinoma. *Cancer Res.* **79**, 372–386 (2019).
32. Provenzano, P. P. *et al.* Enzymatic Targeting of the Stroma Ablates Physical Barriers to Treatment of Pancreatic Ductal Adenocarcinoma. *Cancer Cell* **21**, 418–429 (2012).
33. De Vleeschouwer, S. & Bergers, G. *Glioblastoma: To Target the Tumor Cell or the Microenvironment? Glioblastoma* (Codon Publications, 2017).
34. Jain, A. *et al.* Guiding intracortical brain tumour cells to an extracortical cytotoxic hydrogel using aligned polymeric nanofibres. *Nat. Mater.* **13**, 308–316 (2014).
35. Gritsenko, P. G., Ilina, O. & Friedl, P. Interstitial guidance of cancer invasion. *J. Pathol.* **226**, 185–199 (2012).
36. Bellail, A. C., Hunter, S. B., Brat, D. J., Tan, C. & Van Meir, E. G. Microregional extracellular matrix heterogeneity in brain modulates glioma cell invasion. *Int. J.*

Biochem. Cell Biol. **36**, 1046–69 (2004).
37. van Tellingen, O. *et al.* Overcoming the blood–brain tumor barrier for effective glioblastoma treatment. *Drug Resist. Updat.* **19**, 1–12 (2015).
38. de Vries, N. A., Beijnen, J. H., Boogerd, W. & van Tellingen, O. Blood–brain barrier and chemotherapeutic treatment of brain tumors. *Expert Rev. Neurother.* **6**, 1199–1209 (2006).
39. Nimsky, C. *et al.* Preoperative and Intraoperative Diffusion Tensor Imaging-based Fiber Tracking in Glioma Surgery. *Neurosurgery* **56**, 130–138 (2005).
40. Giese, A., Bjerkvig, R., Berens, M. E. & Westphal, M. Cost of migration: invasion of malignant gliomas and implications for treatment. *J. Clin. Oncol.* **21**, 1624–36 (2003).
41. Miller, K., Chinzei, K., Orssengo, G. & Bednarz, P. Mechanical properties of brain tissue in-vivo: experiment and computer simulation. *J. Biomech.* **33**, 1369–76 (2000).
42. Budday, S. *et al.* Mechanical properties of gray and white matter brain tissue by indentation. *J. Mech. Behav. Biomed. Mater.* **46**, 318–30 (2015).
43. Bernstein, J. J. & Woodard, C. A. Glioblastoma cells do not intravasate into blood vessels. *Neurosurgery* **36**, 124–32 (1995).
44. Nakod, P. S., Kim, Y. & Rao, S. S. Biomimetic models to examine microenvironmental regulation of glioblastoma stem cells. *Cancer Lett.* **429**, 41–53 (2018).
45. Lenting, K., Verhaak, R., ter Laan, M., Wesseling, P. & Leenders, W. Glioma: experimental models and reality. *Acta Neuropathol.* **133**, 263–282 (2017).
46. Xiao, W., Sohrabi, A. & Seidlits, S. K. Integrating the glioblastoma microenvironment into engineered experimental models. *Futur. Sci. OA* **3**, FSO189 (2017).
47. Zimmermann, D. R. & Dours-Zimmermann, M. T. Extracellular matrix of the central nervous system: from neglect to challenge. *Histochem Cell Biol* **130**, 635–653 (2008).
48. Breyer, R. *et al.* Disruption of intracerebral progression of rat C6 glioblastoma by in vivo treatment with anti-CD44 monoclonal antibody. *J. Neurosurg.* **62**, 140–149 (2000).
49. Ponta, H., Sherman, L. & Herrlich, P. A. CD44: from adhesion molecules to signalling regulators. *Nat. Rev. Mol. Cell Biol.* **4**, 33–45 (2003).
50. Delpech, B. *et al.* Hyaluronan and hyaluronectin in the extracellular matrix of human brain tumour stroma. *Eur. J. Cancer* **29A**, 1012–7 (1993).
51. Yoo, K.-C. *et al.* Proinvasive extracellular matrix remodeling in tumor microenvironment in response to radiation. *Oncogene* **37**, 3317–3328 (2018).
52. Tian, X. *et al.* High-molecular-mass hyaluronan mediates the cancer resistance of the naked mole rat. *Nature* **499**, 346–349 (2013).
53. Chanmee, T., Ontong, P. & Itano, N. Mini-review Hyaluronan: A modulator of the tumor microenvironment. *Cancer Lett.* **375**, 20–30 (2016).
54. Akiyama, Y. *et al.* Hyaluronate Receptors Mediating Glioma Cell Migration and Proliferation. *J. Neurooncol.* **53**, 115–127 (2001).
55. Valkonen, M. *et al.* Elevated expression of hyaluronan synthase 2 associates with decreased survival in diffusely infiltrating astrocytomas. *BMC Cancer* **18**, 664

(2018).
56. Chen, J.-W. E. *et al.* Influence of Hyaluronic Acid Transitions in Tumor Microenvironment on Glioblastoma Malignancy and Invasive Behavior. *Front. Mater.* **5**, 39 (2018).
57. Shannon, S. *et al.* Dexamethasone-Mediated Activation of Fibronectin Matrix Assembly Reduces Dispersal of Primary Human Glioblastoma Cells. *PLoS One* **10**, e0135951 (2015).
58. Serres, E. *et al.* Fibronectin expression in glioblastomas promotes cell cohesion, collective invasion of basement membrane in vitro and orthotopic tumor growth in mice. *Oncogene* **33**, 3451–3462 (2014).
59. Sabari, J. *et al.* Fibronectin Matrix Assembly Suppresses Dispersal of Glioblastoma Cells. *PLoS One* **6**, e24810 (2011).
60. Yuan, L. *et al.* Transglutaminase 2 inhibitor, KCC009, disrupts fibronectin assembly in the extracellular matrix and sensitizes orthotopic glioblastomas to chemotherapy. *Oncogene* **26**, 2563–2573 (2007).
61. Sarkar, S., Nuttall, R. K., Liu, S., Edwards, D. R. & Yong, V. W. Tenascin-C Stimulates Glioma Cell Invasion through Matrix Metalloproteinase-12. *Cancer Res.* **66**, 11771–11780 (2006).
62. Mirzaei, R. *et al.* Brain tumor-initiating cells export tenascin-C associated with exosomes to suppress T cell activity. *Oncoimmunology* **7**, e1478647 (2018).
63. Miroshnikova, Y. A. *et al.* Tissue mechanics promote IDH1-dependent HIF1α–tenascin C feedback to regulate glioblastoma aggression. *Nat. Cell Biol.* **18**, 1336–1345 (2016).
64. Gamble, J. T. *et al.* Quantification of glioblastoma progression in zebrafish xenografts: Adhesion to laminin alpha 5 promotes glioblastoma microtumor formation and inhibits cell invasion. *Biochem. Biophys. Res. Commun.* **506**, 833–839 (2018).
65. Lathia, J. D. *et al.* Integrin alpha 6 regulates glioblastoma stem cells. *Cell Stem Cell* **6**, 421–32 (2010).
66. Lathia, J. D. *et al.* Laminin alpha 2 enables glioblastoma stem cell growth. *Ann. Neurol.* **72**, 766–778 (2012).
67. Chauvet, D. *et al.* In Vivo Measurement of Brain Tumor Elasticity Using Intraoperative Shear Wave Elastography. *Eur. J. Ultrasound* **37**, 584–590 (2015).
68. Stewart, D. C., Rubiano, A., Dyson, K. & Simmons, C. S. Mechanical characterization of human brain tumors from patients and comparison to potential surgical phantoms. *PLoS One* **12**, e0177561 (2017).
69. Ciasca, G. *et al.* Nano-mechanical signature of brain tumours. *Nanoscale* **8**, 19629–19643 (2016).
70. Ulrich, T. A. *et al.* The mechanical rigidity of the extracellular matrix regulates the structure, motility, and proliferation of glioma cells. *Cancer Res.* **69**, 4167–74 (2009).
71. Grundy, T. J. *et al.* Differential response of patient-derived primary glioblastoma cells to environmental stiffness. *Sci. Rep.* **6**, 23353 (2016).
72. Wong, S. Y. *et al.* Constitutive activation of myosin-dependent contractility sensitizes glioma tumor-initiating cells to mechanical inputs and reduces tissue invasion. *Cancer Res.* **75**, 1113–1122 (2015).

73. Umesh, V., Rape, A. D., Ulrich, T. A. & Kumar, S. Microenvironmental Stiffness Enhances Glioma Cell Proliferation by Stimulating Epidermal Growth Factor Receptor Signaling. *PLoS One* **9**, e101771 (2014).
74. Kim, Y. & Kumar, S. CD44-mediated adhesion to hyaluronic acid contributes to mechanosensing and invasive motility. *Mol. Cancer Res.* **12**, 1416–29 (2014).
75. Thomas, T. W. & DiMilla, P. A. Spreading and motility of human glioblastoma cells on sheets of silicone rubber depend on substratum compliance. *Med. Biol. Eng. Comput.* **38**, 360–70 (2000).
76. Seano, G. *et al.* Solid stress in brain tumours causes neuronal loss and neurological dysfunction and can be reversed by lithium. *Nat. Biomed. Eng.* **3**, 230–245 (2019).
77. Mammoto, T. *et al.* Role of Collagen Matrix in Tumor Angiogenesis and Glioblastoma Multiforme Progression. *Am. J. Pathol.* **183**, 1293–1305 (2013).
78. Rascher, G. *et al.* Extracellular matrix and the blood-brain barrier in glioblastoma multiforme: spatial segregation of tenascin and agrin. *Acta Neuropathol.* **104**, 85–91 (2002).
79. Pen, A., Moreno, M. J., Martin, J. & Stanimirovic, D. B. Molecular markers of extracellular matrix remodeling in glioblastoma vessels: Microarray study of laser-captured glioblastoma vessels. *Glia* **55**, 559–572 (2007).
80. Giese, A. *et al.* Migration of Human Glioma Cells on Myelin. *Neurosurgery* **38**, 755–764 (1996).
81. Hensel, T., Amberger, V. & Schwab, M. A metalloprotease activity from C6 glioma cells inactivates the myelin-associated neurite growth inhibitors and can be neutralized by antibodies. *Br. J. Cancer* **78**, 1564–1572 (1998).
82. Amberger, V. R., Hensel, T., Ogata, N. & Schwab, M. E. Spreading and migration of human glioma and rat C6 cells on central nervous system myelin in vitro is correlated with tumor malignancy and involves a metalloproteolytic activity. *Cancer Res.* **58**, 149–58 (1998).
83. Oellers, P., Schröer, U., Senner, V., Paulus, W. & Thanos, S. Rocks are expressed in brain tumors and are required for glioma-cell migration on myelinated axons. *Glia* **57**, 499–509 (2009).
84. Wang, J. *et al.* Invasion of white matter tracts by glioma stem cells is regulated by a NOTCH1–SOX2 positive-feedback loop. *Nat. Neurosci.* **22**, 91–105 (2019).
85. Swartz, M. A. & Fleury, M. E. Interstitial Flow and Its Effects in Soft Tissues. *Annu. Rev. Biomed. Eng.* **9**, 229–256 (2007).
86. Heldin, C.-H., Rubin, K., Pietras, K., Ostman, A. & Östman, A. High interstitial fluid pressure - an obstacle in cancer therapy. *Nat. Rev. Cancer* **4**, 806–13 (2004).
87. Abbott, N. J. Evidence for bulk flow of brain interstitial fluid: significance for physiology and pathology. *Neurochem. Int.* **45**, 545–552 (2004).
88. Geer, C. P. & Grossman, S. A. Interstitial fluid flow along white matter tracts: A potentially important mechanism for the dissemination of primary brain tumors. *J. Neurooncol.* **32**, 193–201 (1997).
89. Cornelison, R. C., Brennan, C. E., Kingsmore, K. M. & Munson, J. M. Convective forces increase CXCR4-dependent glioblastoma cell invasion in GL261 murine model. *Sci. Rep.* **8**, 17057 (2018).
90. Vogelbaum, M. A. & Aghi, M. K. Convection-enhanced delivery for the treatment

of glioblastoma. *Neuro. Oncol.* **17**, ii3–ii8 (2015).
91. Kingsmore, K. M. *et al.* Interstitial flow differentially increases patient-derived glioblastoma stem cell invasion *via* CXCR4, CXCL12, and CD44-mediated mechanisms. *Integr. Biol.* **8**, 1246–1260 (2016).
92. Munson, J. M., Bellamkonda, R. V. & Swartz, M. A. Interstitial flow in a 3D microenvironment increases glioma invasion by a CXCR4-dependent mechanism. *Cancer Res.* **73**, 1536–46 (2013).
93. Poon, C. C., Sarkar, S., Yong, V. W. & Kelly, J. J. P. Glioblastoma-associated microglia and macrophages: targets for therapies to improve prognosis. *Brain* **140**, 1548–1560 (2017).
94. Hambardzumyan, D., Gutmann, D. H. & Kettenmann, H. The role of microglia and macrophages in glioma maintenance and progression. *Nat. Neurosci.* **19**, 20–7 (2016).
95. Brandao, M., Simon, T., Critchley, G. & Giamas, G. Astrocytes, the rising stars of the glioblastoma microenvironment. *Glia* **67**, 779–790 (2019).
96. Infanger, D. W. *et al.* Glioblastoma Stem Cells Are Regulated by Interleukin-8 Signaling in a Tumoral Perivascular Niche. *Cancer Res.* **73**, 7079–7089 (2013).
97. Venkatesh, H. S. *et al.* Neuronal Activity Promotes Glioma Growth through Neuroligin-3 Secretion. *Cell* **161**, 803–16 (2015).
98. Figueroa, J. *et al.* Exosomes from Glioma-Associated Mesenchymal Stem Cells Increase the Tumorigenicity of Glioma Stem-like Cells via Transfer of miR-1587. *Cancer Res.* **77**, 5808–5819 (2017).
99. Hossain, A. *et al.* Mesenchymal Stem Cells Isolated From Human Gliomas Increase Proliferation and Maintain Stemness of Glioma Stem Cells Through the IL-6/gp130/STAT3 Pathway. *Stem Cells* **33**, 2400–2415 (2015).
100. Novak, U. & Kaye, A. H. Extracellular matrix and the brain: components and function. *J. Clin. Neurosci.* **7**, 280–290 (2000).
101. Bertolotto, A., Magrassi, M. L., Orsi, L., Sitia, C. & Schiffer, D. Glycosaminoglycan changes in human gliomas. A biochemical study. *J. Neurooncol.* **4**, 43–48 (1986).
102. Chintala, S. K., Sawaya, R., Gokaslan, Z. L., Fuller, G. & Rao, J. S. Immunohistochemical localization of extracellular matrix proteins in human glioma, both in vivo and in vitro. *Cancer Lett.* **101**, 107–114 (1996).
103. Mahesparan, R. *et al.* Expression of extracellular matrix components in a highly infiltrative in vivo glioma model. *Acta Neuropathol.* **105**, 49–57 (2003).
104. Cowman, M. K., Lee, H.-G., Schwertfeger, K. L., McCarthy, J. B. & Turley, E. A. The Content and Size of Hyaluronan in Biological Fluids and Tissues. *Front. Immunol.* **6**, 261 (2015).
105. Dicker, K. T. *et al.* Hyaluronan: A simple polysaccharide with diverse biological functions. *Acta Biomater.* **10**, 1558–1570 (2014).
106. Candece L. Gladson. The Extracellular Matrix of Gliomas: Modulation of Cell Function. *J. Neuropathol. Exp. Neurol.* **58**, 1029–1040 (1999).
107. Ljubimova, J. Y., Fujita, M., Khazenzon, N. M., Ljubimov, A. V & Black, K. L. Changes in laminin isoforms associated with brain tumor invasion and angiogenesis. *Front. Biosci.* **11**, 81–8 (2006).
108. Ogawa, K., Oguchi, M., Nakashima, Y. & Yamabe, H. Distribution of collagen Type IV in brain tumors: An immunohistochemical study. *J. Neurooncol.* **7**, 357–

366 (1989).
109. Rojiani, A. M. & Dorovini-Zis, K. Glomeruloid vascular structures in glioblastoma multiforme: an immunohistochemical and ultrastructural study. *J. Neurosurg.* **85**, 1078–1084 (1996).
110. Pointer, K. B. *et al.* Association of collagen architecture with glioblastoma patient survival. *J Neurosurg* **126**, 1812–1821 (2017).
111. Rauch, U. Brain matrix: structure, turnover and necessity. *Biochem. Soc. Trans.* **35**, 656–60 (2007).
112. Lundell, A. *et al.* Structural Basis for Interactions between Tenascins and Lectican C-Type Lectin Domains: Evidence for a Crosslinking Role for Tenascins. *Structure* **12**, 1495–1506 (2004).
113. Pietras, A. *et al.* Osteopontin-CD44 Signaling in the Glioma Perivascular Niche Enhances Cancer Stem Cell Phenotypes and Promotes Aggressive Tumor Growth. *Cell Stem Cell* **14**, 357–369 (2014).
114. Wei, J. *et al.* Osteopontin mediates glioblastoma-associated macrophage infiltration and is a potential therapeutic target. *J. Clin. Invest.* **129**, 137–149 (2018).
115. Lamour, V. *et al.* Targeting osteopontin suppresses glioblastoma stem-like cell character and tumorigenicity *in vivo*. *Int. J. Cancer* **137**, 1047–1057 (2015).
116. Oyinlade, O. *et al.* Targeting UDP-α-d-glucose 6-dehydrogenase inhibits glioblastoma growth and migration. *Oncogene* **37**, 2615–2629 (2018).
117. Ruiz-Ontañon, P. *et al.* Cellular Plasticity Confers Migratory and Invasive Advantages to a Population of Glioblastoma-Initiating Cells that Infiltrate Peritumoral Tissue. *Stem Cells* **31**, 1075–1085 (2013).
118. Watkins, S. *et al.* Disruption of astrocyte-vascular coupling and the blood-brain barrier by invading glioma cells. *Nat. Commun.* **5**, 4196 (2014).
119. Candiello, J. *et al.* Biomechanical properties of native basement membranes. *FEBS J.* **274**, 2897–2908 (2007).
120. Charles, N. & Holland, E. C. The perivascular niche microenvironment in brain tumor progression. *Cell Cycle* **9**, 3012–21 (2010).
121. Giese, A., Westphal, M., Giesexs, A. & Westphal, M. No Title. *Neurosurgery* **39**, (1996).
122. Balzer, E. M. *et al.* Physical confinement alters tumor cell adhesion and migration phenotypes. *FASEB J.* **26**, 4045–56 (2012).
123. Monzo, P. *et al.* Mechanical confinement triggers glioma linear migration dependent on formin FHOD3. *Mol. Biol. Cell* **27**, 1246–61 (2016).
124. Monteiro, A., Hill, R., Pilkington, G. & Madureira, P. The Role of Hypoxia in Glioblastoma Invasion. *Cells* **6**, 45 (2017).
125. Soda, Y. *et al.* Transdifferentiation of glioblastoma cells into vascular endothelial cells. *Proc. Natl. Acad. Sci.* **108**, 4272–4280 (2011).
126. Hardee, M. E. & Zagzag, D. Mechanisms of Glioma-Associated Neovascularization. *Am. J. Pathol.* **181**, 1126–1141 (2012).
127. Brat, D. J. *et al.* Pseudopalisades in glioblastoma are hypoxic, express extracellular matrix proteases, and are formed by an actively migrating cell population. *Cancer Res.* **64**, 920–7 (2004).
128. Lim, S. *et al.* Glioblastoma-secreted soluble CD44 activates tau pathology in the

brain. *Exp. Mol. Med.* **50**, 5 (2018).
129. Lacroix, M. *et al.* A multivariate analysis of 416 patients with glioblastoma multiforme: prognosis, extent of resection, and survival. *J. Neurosurg.* **95**, 190–198 (2001).
130. Shinoda, J. *et al.* Fluorescence-guided resection of glioblastoma multiforme by using high-dose fluorescein sodium. *J. Neurosurg.* **99**, 597–603 (2003).
131. Bregy, A. *et al.* The role of Gliadel wafers in the treatment of high-grade gliomas. *Expert Rev. Anticancer Ther.* **13**, 1453–1461 (2013).
132. Perry, J., Chambers, A., Spithoff, K. & Laperriere, N. Gliadel wafers in the treatment of malignant glioma: a systematic review. *Curr. Oncol.* **14**, 189–94 (2007).
133. Stupp, R. *et al.* Effect of Tumor-Treating Fields Plus Maintenance Temozolomide vs Maintenance Temozolomide Alone on Survival in Patients With Glioblastoma. *JAMA* **318**, 2306 (2017).
134. Davies, A. M., Weinberg, U. & Palti, Y. Tumor treating fields: a new frontier in cancer therapy. *Ann. N. Y. Acad. Sci.* **1291**, 86–95 (2013).
135. Calabrese, C. *et al.* A Perivascular Niche for Brain Tumor Stem Cells. *Cancer Cell* **11**, 69–82 (2007).
136. Borovski, T., De Sousa E Melo, F., Vermeulen, L. & Medema, J. P. Cancer stem cell niche: the place to be. *Cancer Res.* **71**, 634–9 (2011).
137. Silver, D. J. & Lathia, J. D. Revealing the glioma cancer stem cell interactome, one niche at a time. *J. Pathol.* **244**, 260–264 (2018).
138. Brooks, M. D., Sengupta, R., Snyder, S. C. & Rubin, J. B. Hitting Them Where They Live: Targeting the Glioblastoma Perivascular Stem Cell Niche. *Curr. Pathobiol. Rep.* **1**, 101–110 (2013).
139. Shiraki, Y. *et al.* Significance of perivascular tumour cells defined by CD109 expression in progression of glioma. *J. Pathol.* **243**, 468–480 (2017).
140. Wolf, K. J., Lee, S. & Kumar, S. A 3D topographical model of parenchymal infiltration and perivascular invasion in glioblastoma. *APL Bioeng.* **2**, 031903 (2018).
141. Ngo, M. T. & Harley, B. A. C. Perivascular signals alter global gene expression profile of glioblastoma and response to temozolomide in a gelatin hydrogel. *Biomaterials* **198**, 122–134 (2019).
142. Zhu, T. S. *et al.* Endothelial cells create a stem cell niche in glioblastoma by providing NOTCH ligands that nurture self-renewal of cancer stem-like cells. *Cancer Res.* **71**, 6061–72 (2011).
143. Bao, S. *et al.* Stem cell-like glioma cells promote tumor angiogenesis through vascular endothelial growth factor. *Cancer Res.* **66**, 7843–8 (2006).
144. Charles, N. *et al.* Perivascular nitric oxide activates notch signaling and promotes stem-like character in PDGF-induced glioma cells. *Cell Stem Cell* **6**, 141–52 (2010).
145. Tilghman, J. *et al.* HMMR maintains the stemness and tumorigenicity of glioblastoma stem-like cells. *Cancer Res.* **74**, 3168–79 (2014).
146. Chanmee, T., Ontong, P., Kimata, K. & Itano, N. Key Roles of Hyaluronan and Its CD44 Receptor in the Stemness and Survival of Cancer Stem Cells. *Front. Oncol.* **5**, 180 (2015).

147. Ferrandez, E., Gutierrez, O., Segundo, D. S. & Fernandez-Luna, J. L. NFκB activation in differentiating glioblastoma stem-like cells is promoted by hyaluronic acid signaling through TLR4. *Sci. Rep.* **8**, 6341 (2018).
148. Chen, J. & Kumar, S. Biophysical regulation of cancer stem/initiating cells: Implications for disease mechanisms and translation. *Curr. Opin. Biomed. Eng.* **1**, 87–95 (2017).
149. Barnes, J. M. *et al.* A tension-mediated glycocalyx–integrin feedback loop promotes mesenchymal-like glioblastoma. *Nat. Cell Biol.* **20**, 1203–1214 (2018).
150. Iwadate, Y. Epithelial-mesenchymal transition in glioblastoma progression. *Oncol. Lett.* **11**, 1615–1620 (2016).
151. Lau, J. *et al.* STAT3 blockade inhibits a radiation-induced proneural-to-mesenchymal transition in glioma. *Cancer Res.* **75**, 4302 (2015).
152. Bhat, K. P. L. *et al.* Mesenchymal Differentiation Mediated by NF-κB Promotes Radiation Resistance in Glioblastoma. *Cancer Cell* **24**, 331–346 (2013).
153. Xiao, W. *et al.* Brain-Mimetic 3D Culture Platforms Allow Investigation of Cooperative Effects of Extracellular Matrix Features on Therapeutic Resistance in Glioblastoma. *Cancer Res.* **78**, 1358–1370 (2018).
154. Soeda, A. *et al.* Hypoxia promotes expansion of the CD133-positive glioma stem cells through activation of HIF-1α. *Oncogene* **28**, 3949–3959 (2009).
155. Colwell, N. *et al.* Hypoxia in the glioblastoma microenvironment: shaping the phenotype of cancer stem-like cells. *Neuro. Oncol.* **19**, 887–896 (2017).
156. Heddleston, J. M., Li, Z., McLendon, R. E., Hjelmeland, A. B. & Rich, J. N. The hypoxic microenvironment maintains glioblastoma stem cells and promotes reprogramming towards a cancer stem cell phenotype. *Cell Cycle* **8**, 3274–3284 (2009).
157. Gupta, K. & Burns, T. C. Radiation-Induced Alterations in the Recurrent Glioblastoma Microenvironment: Therapeutic Implications. *Front. Oncol.* **8**, 503 (2018).
158. Bao, S. *et al.* Glioma stem cells promote radioresistance by preferential activation of the DNA damage response. *Nature* **444**, 756–760 (2006).
159. Rath, B. H., Wahba, A., Camphausen, K. & Tofilon, P. J. Coculture with astrocytes reduces the radiosensitivity of glioblastoma stem-like cells and identifies additional targets for radiosensitization. *Cancer Med.* **4**, 1705–16 (2015).
160. De Pascalis, I. *et al.* Endothelial trans-differentiation in glioblastoma recurring after radiotherapy. *Mod. Pathol.* **31**, 1361–1366 (2018).
161. Mao, L. *et al.* Enhancement of invadopodia activity in glioma cells by sublethal doses of irradiation and temozolomide. *J. Neurosurg.* **129**, 598–610 (2018).
162. Tsidulko, A. Y. *et al.* Conventional Anti-glioblastoma Chemotherapy Affects Proteoglycan Composition of Brain Extracellular Matrix in Rat Experimental Model in vivo. *Front. Pharmacol.* **9**, 1104 (2018).
163. Yoshida, D., Piepmeier, J. M., Bergenheim, T., Henriksson, R. & Teramoto, A. Suppression of matrix metalloproteinase-2-mediated cell invasion in U87MG, human glioma cells by anti-microtubule agent: in vitro study. *Br. J. Cancer* **77**, 21–5 (1998).
164. Sawyers, C. Targeted cancer therapy. *Nature* **432**, 294–297 (2004).
165. Higgins, M. J. & Baselga, J. Targeted therapies for breast cancer. *J. Clin. Invest.*

121, 3797–803 (2011).
166. Westphal, M., Maire, C. L. & Lamszus, K. EGFR as a Target for Glioblastoma Treatment: An Unfulfilled Promise. *CNS Drugs* **31**, 723 (2017).
167. Butowski, N. *et al.* Orally administered colony stimulating factor 1 receptor inhibitor PLX3397 in recurrent glioblastoma: an Ivy Foundation Early Phase Clinical Trials Consortium phase II study. *Neuro. Oncol.* **18**, 557–564 (2016).
168. Pàez-Ribes, M. *et al.* Antiangiogenic Therapy Elicits Malignant Progression of Tumors to Increased Local Invasion and Distant Metastasis. *Cancer Cell* **15**, 220–231 (2009).
169. Momeny, M. *et al.* Blockade of vascular endothelial growth factor receptors by tivozanib has potential anti-tumour effects on human glioblastoma cells. *Sci. Rep.* **7**, 44075 (2017).
170. Batchelor, T. T. *et al.* Phase II study of cediranib, an oral pan-vascular endothelial growth factor receptor tyrosine kinase inhibitor, in patients with recurrent glioblastoma. *J. Clin. Oncol.* **28**, 2817–23 (2010).
171. Batchelor, T. T. *et al.* Phase III randomized trial comparing the efficacy of cediranib as monotherapy, and in combination with lomustine, versus lomustine alone in patients with recurrent glioblastoma. *J. Clin. Oncol.* **31**, 3212–8 (2013).
172. Kreisl, T. N. *et al.* Continuous daily sunitinib for recurrent glioblastoma. *J. Neurooncol.* **111**, 41–48 (2013).
173. Neal, J. & Wakelee, H. AMG-386, a selective angiopoietin-1/-2-neutralizing peptibody for the potential treatment of cancer. *Curr. Opin. Mol. Ther.* **12**, 487–95 (2010).
174. Reardon, D. A. *et al.* A review of VEGF/VEGFR-targeted therapeutics for recurrent glioblastoma. *J. Natl. Compr. Canc. Netw.* **9**, 414–27 (2011).
175. Scaringi, C., Minniti, G., Caporello, P. & Enrici, R. M. Integrin inhibitor cilengitide for the treatment of glioblastoma: a brief overview of current clinical results. *Anticancer Res.* **32**, 4213–23 (2012).
176. Albertella, M. R. *et al.* Hypoxia-Selective Targeting by the Bioreductive Prodrug AQ4N in Patients with Solid Tumors: Results of a Phase I Study. *Clin. Cancer Res.* **14**, 1096–1104 (2008).
177. Fang, H. & DeClerck, Y. A. Targeting the Tumor Microenvironment: From Understanding Pathways to Effective Clinical Trials. *Cancer Res.* **73**, 4965–4977 (2013).
178. Papadopoulos, K. P. *et al.* A Phase 1 Open-Label, Accelerated Dose-Escalation Study of the Hypoxia-Activated Prodrug AQ4N in Patients with Advanced Malignancies. *Clin. Cancer Res.* **14**, 7110–7115 (2008).
179. Patterson, L. H. & McKeown, S. R. AQ4N: a new approach to hypoxia-activated cancer chemotherapy. *Br. J. Cancer* **83**, 1589–93 (2000).
180. Jain, K. K. A Critical Overview of Targeted Therapies for Glioblastoma. *Front. Oncol.* **8**, 419 (2018).
181. Carbonell, W. S., DeLay, M., Jahangiri, A., Park, C. C. & Aghi, M. K. β1 integrin targeting potentiates antiangiogenic therapy and inhibits the growth of bevacizumab-resistant glioblastoma. *Cancer Res.* **73**, 3145–54 (2013).
182. Stupp, R. *et al.* Cilengitide combined with standard treatment for patients with newly diagnosed glioblastoma with methylated MGMT promoter (CENTRIC

EORTC 26071-22072 study): a multicentre, randomised, open-label, phase 3 trial. *Lancet Oncol.* **15**, 1100–1108 (2014).
183. Tucci, M., Stucci, S. & Silvestris, F. Does cilengitide deserve another chance? *Lancet. Oncol.* **15**, e584-5 (2014).
184. Brown, M. C. *et al.* Cancer immunotherapy with recombinant poliovirus induces IFN-dominant activation of dendritic cells and tumor antigen-specific CTLs. *Sci. Transl. Med.* **9**, eaan4220 (2017).
185. Desjardins, A. *et al.* Recurrent Glioblastoma Treated with Recombinant Poliovirus. *N. Engl. J. Med.* **379**, 150–161 (2018).
186. Rape, A., Ananthanarayanan, B. & Kumar, S. Engineering strategies to mimic the glioblastoma microenvironment. *Adv. Drug Deliv. Rev.* **79**–**80**, 172–183 (2014).
187. Stylli, S. S., Luwor, R. B., Ware, T. M. B., Tan, F. & Kaye, A. H. Mouse models of glioma. *J. Clin. Neurosci.* **22**, 619–626 (2015).
188. Joo, K. M. *et al.* Patient-Specific Orthotopic Glioblastoma Xenograft Models Recapitulate the Histopathology and Biology of Human Glioblastomas In Situ. *Cell Rep.* **3**, 260–273 (2013).
189. Simeonova, I. & Huillard, E. In vivo models of brain tumors: roles of genetically engineered mouse models in understanding tumor biology and use in preclinical studies. *Cell. Mol. Life Sci.* **71**, 4007–4026 (2014).
190. Ismail Kola, J. L. Can the pharmaceutical industry reduce attrition rates? *Nat. Rev. Drug Discov.* **3**, 711–715 (2004).
191. Wu, M. & Swartz, M. A. Modeling tumor microenvironments in vitro. *J. Biomech. Eng.* **136**, 021011 (2014).
192. Pathak, A. & Kumar, S. Independent regulation of tumor cell migration by matrix stiffness and confinement. *Proc. Natl. Acad. Sci. U. S. A.* **109**, 10334–9 (2012).
193. Diao, W. *et al.* Behaviors of Glioblastoma Cells in in Vitro Microenvironments. *Sci. Rep.* **9**, 85 (2019).
194. Fernandez-Fuente, G., Mollinedo, P., Grande, L., Vazquez-Barquero, A. & Fernandez-Luna, J. L. Culture Dimensionality Influences the Resistance of Glioblastoma Stem-like Cells to Multikinase Inhibitors. *Mol. Cancer Ther.* **13**, 1664–1672 (2014).
195. Rape, A. D., Zibinsky, M., Murthy, N. & Kumar, S. A synthetic hydrogel for the high-throughput study of cell–ECM interactions. *Nat. Commun.* **6**, 8129 (2015).
196. Ananthanarayanan, B., Kim, Y. & Kumar, S. Elucidating the mechanobiology of malignant brain tumors using a brain matrix-mimetic hyaluronic acid hydrogel platform. *Biomaterials* **32**, 7913–7923 (2011).
197. Kaphle, P., Li, Y. & Yao, L. The mechanical and pharmacological regulation of glioblastoma cell migration in 3D matrices. *J. Cell. Physiol.* **234**, 3948–3960 (2019).
198. Yang, Y. *et al.* Influence of chondroitin sulfate and hyaluronic acid on structure, mechanical properties, and glioma invasion of collagen I gels. *Biomaterials* **32**, 7932–7940 (2011).
199. Yang, Y., Motte, S. & Kaufman, L. J. Pore size variable type I collagen gels and their interaction with glioma cells. *Biomaterials* **31**, 5678–5688 (2010).
200. Ulrich, T. A., Lee, T. G., Shon, H. K., Moon, D. W. & Kumar, S. Microscale mechanisms of agarose-induced disruption of collagen remodeling. *Biomaterials*

32, 5633–5642 (2011).
201. Ulrich, T. A., Jain, A., Tanner, K., MacKay, J. L. & Kumar, S. Probing cellular mechanobiology in three-dimensional culture with collagen–agarose matrices. *Biomaterials* **31**, 1875–1884 (2010).
202. Wang, C., Tong, X., Jiang, X. & Yang, F. Effect of matrix metalloproteinase-mediated matrix degradation on glioblastoma cell behavior in 3D PEG-based hydrogels. *J. Biomed. Mater. Res. A* **105**, 770–778 (2017).
203. Heffernan, J. M. *et al.* PNIPAAm-co-Jeffamine® (PNJ) scaffolds as in vitro models for niche enrichment of glioblastoma stem-like cells. *Biomaterials* **143**, 149–158 (2017).
204. Martínez-Ramos, C. & Lebourg, M. Three-dimensional constructs using hyaluronan cell carrier as a tool for the study of cancer stem cells. *J. Biomed. Mater. Res. Part B Appl. Biomater.* **103**, 1249–1257 (2015).
205. Kievit, F. M. *et al.* Modeling the tumor microenvironment using chitosan-alginate scaffolds to control the stem-like state of glioblastoma cells. *Biomater. Sci.* **4**, 610–613 (2016).
206. Herrera-Perez, M., Voytik-Harbin, S. L. & Rickus, J. L. Extracellular Matrix Properties Regulate the Migratory Response of Glioblastoma Stem Cells in Three-Dimensional Culture. *Tissue Eng. Part A* **21**, 2572–82 (2015).
207. Pedron, S., Becka, E. & Harley, B. A. C. C. Regulation of glioma cell phenotype in 3D matrices by hyaluronic acid. *Biomaterials* **34**, 7408–17 (2013).
208. Wang, C., Tong, X. & Yang, F. Bioengineered 3D Brain Tumor Model To Elucidate the Effects of Matrix Stiffness on Glioblastoma Cell Behavior Using PEG-Based Hydrogels. *Mol. Pharm.* **11**, 2115–2125 (2014).
209. Koh, I. *et al.* The mode and dynamics of glioblastoma cell invasion into a decellularized tissue-derived extracellular matrix-based three-dimensional tumor model. *Sci. Rep.* **8**, 4608 (2018).
210. Yi, H.-G. *et al.* A bioprinted human-glioblastoma-on-a-chip for the identification of patient-specific responses to chemoradiotherapy. *Nat. Biomed. Eng.* **[Epub Ahea**, (2019).
211. Cortese, B., Gigli, G. & Riehle, M. Mechanical Gradient Cues for Guided Cell Motility and Control of Cell Behavior on Uniform Substrates. *Adv. Funct. Mater.* **19**, 2961–2968 (2009).
212. Rao, S. S. *et al.* Inherent Interfacial Mechanical Gradients in 3D Hydrogels Influence Tumor Cell Behaviors. *PLoS One* **7**, e35852 (2012).
213. Pedron, S., Becka, E. & Harley, B. A. Spatially Gradated Hydrogel Platform as a 3D Engineered Tumor Microenvironment. *Adv. Mater.* **27**, 1567–1572 (2015).
214. Pedron, S. & Harley, B. A. C. Impact of the biophysical features of a 3D gelatin microenvironment on glioblastoma malignancy. *J. Biomed. Mater. Res. Part A* **101**, 3404–3415 (2013).
215. Gritsenko, P., Leenders, W. & Friedl, P. Recapitulating in vivo-like plasticity of glioma cell invasion along blood vessels and in astrocyte-rich stroma. *Histochem. Cell Biol.* **148**, 1–12 (2017).
216. Rape, A. D. & Kumar, S. A composite hydrogel platform for the dissection of tumor cell migration at tissue interfaces. *Biomaterials* **35**, 8846–53 (2014).
217. Beliveau, A., Thomas, G., Gong, J., Wen, Q. & Jain, A. Aligned Nanotopography

Promotes a Migratory State in Glioblastoma Multiforme Tumor Cells. *Sci. Rep.* **6**, 26143 (2016).
218. Sharma, P., Sheets, K., Elankumaran, S. & Nain, A. S. The mechanistic influence of aligned nanofibers on cell shape, migration and blebbing dynamics of glioma cells. *Integr. Biol.* **5**, 1036–1044 (2013).
219. Grodecki, J. *et al.* Glioma-astrocyte interactions on white matter tract-mimetic aligned electrospun nanofibers. *Biotechnol. Prog.* **31**, 1406–1415 (2015).
220. Agudelo-Garcia, P. A. *et al.* Glioma cell migration on three-dimensional nanofiber scaffolds is regulated by substrate topography and abolished by inhibition of STAT3 signaling. *Neoplasia* **13**, 831–40 (2011).
221. Ma, N. K. L. *et al.* Collaboration of 3D context and extracellular matrix in the development of glioma stemness in a 3D model. *Biomaterials* **78**, 62–73 (2016).
222. Kievit, F. M. *et al.* Aligned Chitosan-Polycaprolactone Polyblend Nanofibers Promote the Migration of Glioblastoma Cells. *Adv. Healthc. Mater.* **2**, 1651–1659 (2013).
223. Rao, S. S. *et al.* Mimicking white matter tract topography using core–shell electrospun nanofibers to examine migration of malignant brain tumors. *Biomaterials* **34**, 5181–5190 (2013).
224. Ayuso, J. M. *et al.* Glioblastoma on a microfluidic chip: Generating pseudopalisades and enhancing aggressiveness through blood vessel obstruction events. *Neuro. Oncol.* **19**, 503–513 (2017).
225. Truong, D. *et al.* A three-dimensional (3D) organotypic microfluidic model for glioma stem cells – Vascular interactions. *Biomaterials* **198**, 63–77 (2019).
226. Chonan, Y., Taki, S., Sampetrean, O., Saya, H. & Sudo, R. Endothelium-induced three-dimensional invasion of heterogeneous glioma initiating cells in a microfluidic coculture platform. *Integr. Biol.* **9**, 762–773 (2017).
227. Xiao, Y. *et al.* Ex vivo Dynamics of Human Glioblastoma Cells in a Microvasculature-on-a-Chip System Correlates with Tumor Heterogeneity and Subtypes. *Adv. Sci.* **6**, 1801531 (2019).
228. Heinrich, M. A. *et al.* 3D-Bioprinted Mini-Brain: A Glioblastoma Model to Study Cellular Interactions and Therapeutics. *Adv. Mater.* **31**, 1806590 (2019).
229. Hubert, C. G. *et al.* A Three-Dimensional Organoid Culture System Derived from Human Glioblastomas Recapitulates the Hypoxic Gradients and Cancer Stem Cell Heterogeneity of Tumors Found In Vivo. *Cancer Res.* **76**, 2465–77 (2016).
230. Nayernia, Z. *et al.* The relationship between brain tumor cell invasion of engineered neural tissues and in vivo features of glioblastoma. *Biomaterials* **34**, 8279–8290 (2013).
231. Wolf, K. J. & Kumar, S. Hyaluronic Acid: Incorporating the Bio into the Material. *ACS Biomater. Sci. Eng.* **5**, 3753–3765 (2019).
232. Schanté, C. E., Zuber, G., Herlin, C. & Vandamme, T. F. Chemical modifications of hyaluronic acid for the synthesis of derivatives for a broad range of biomedical applications. *Carbohydr. Polym.* **85**, 469–489 (2011).
233. Ylivinkka, I. *et al.* Motility of glioblastoma cells is driven by netrin-1 induced gain of stemness. *J. Exp. Clin. Cancer Res.* **36**, 9 (2017).
234. Kumar, K. K. *et al.* Glioma stem cell invasion through regulation of the interconnected ERK , integrin α 6 and N-cadherin signaling pathway ☆. *Cell.*

Signal. **24**, 2076–2084 (2012).
235. Weiswald, L.-B., Bellet, D. & Dangles-Marie, V. Spherical cancer models in tumor biology. *Neoplasia* **17**, 1–15 (2015).
236. Lee, J. *et al.* Tumor stem cells derived from glioblastomas cultured in bFGF and EGF more closely mirror the phenotype and genotype of primary tumors than do serum-cultured cell lines. *Cancer Cell* **9**, 391–403 (2006).
237. Timmins, N. E. & Nielsen, L. K. Generation of multicellular tumor spheroids by the hanging-drop method. *Methods Mol. Med.* **140**, 141–51 (2007).
238. Mirab, F., Kang, Y. J. & Majd, S. Preparation and characterization of size-controlled glioma spheroids using agarose hydrogel microwells. *PLoS One* **14**, e0211078 (2019).
239. Zhang, X.-P. *et al.* Notch activation promotes cell proliferation and the formation of neural stem cell-like colonies in human glioma cells. *Mol. Cell. Biochem.* **307**, 101–108 (2007).
240. Herrera-Perez, R. M. *et al.* Presence of stromal cells in a bioengineered tumor microenvironment alters glioblastoma migration and response to STAT3 inhibition. *PLoS One* **13**, e0194183 (2018).
241. Florczyk, S. J. *et al.* Porous chitosan-hyaluronic acid scaffolds as a mimic of glioblastoma microenvironment ECM. *Biomaterials* **34**, 10143–10150 (2013).
242. Heffernan, J. M., Overstreet, D. J., Le, L. D., Vernon, B. L. & Sirianni, R. W. Bioengineered Scaffolds for 3D Analysis of Glioblastoma Proliferation and Invasion. *Ann. Biomed. Eng.* **43**, 1965–1977 (2014).
243. Pedron, S., Hanselman, J. S., Schroeder, M. A., Sarkaria, J. N. & Harley, B. A. C. Extracellular Hyaluronic Acid Influences the Efficacy of EGFR Tyrosine Kinase Inhibitors in a Biomaterial Model of Glioblastoma. *Adv. Healthc. Mater.* **6**, 1700529 (2017).
244. Pedron, S. *et al.* Hyaluronic acid-functionalized gelatin hydrogels reveal extracellular matrix signals temper the efficacy of erlotinib against patient-derived glioblastoma specimens. *Biomaterials* 119371 (2019).
245. Shin, H. Fabrication methods of an engineered microenvironment for analysis of cell–biomaterial interactions. *Biomaterials* **28**, 126–133 (2007).
246. Brown, T. E. & Anseth, K. S. Spatiotemporal hydrogel biomaterials for regenerative medicine. *Chem. Soc. Rev.* **46**, 6532–6552 (2017).
247. Sung, K. E. & Beebe, D. J. Microfluidic 3D models of cancer. *Adv. Drug Deliv. Rev.* **79**–**80**, 68–78 (2014).
248. Akay, M. *et al.* Drug Screening of Human GBM Spheroids in Brain Cancer Chip. *Sci. Rep.* **8**, 15423 (2018).
249. Han, J. *et al.* Rapid emergence and mechanisms of resistance by U87 glioblastoma cells to doxorubicin in an in vitro tumor microfluidic ecology. *Proc. Natl. Acad. Sci.* **113**, 14283–14288 (2016).
250. Fan, Y. *et al.* Engineering a Brain Cancer Chip for High-throughput Drug Screening. *Sci. Rep.* **6**, 25062 (2016).
251. Jie, M. *et al.* Evaluation of drug combination for glioblastoma based on an intestine–liver metabolic model on microchip. *Analyst* **142**, 3629–3638 (2017).
252. Dai, X., Ma, C., Lan, Q. & Xu, T. 3D bioprinted glioma stem cells for brain tumor model and applications of drug susceptibility. *Biofabrication* **8**, 045005 (2016).

253. Wang, X. *et al.* Bioprinting of glioma stem cells improves their endotheliogenic potential. *Colloids Surfaces B Biointerfaces* **171**, 629–637 (2018).
254. Hattori, N. Cerebral organoids model human brain development and microcephaly. *Mov. Disord.* **29**, 185–185 (2014).
255. Huang, Y., Agrawal, B., Clark, P. A., Williams, J. C. & Kuo, J. S. Evaluation of Cancer Stem Cell Migration Using Compartmentalizing Microfluidic Devices and Live Cell Imaging. *J. Vis. Exp* **58**, 3297 (2011).
256. Piccolo, S. R. & Frey, L. J. Clinical and molecular models of glioblastoma multiforme survival. *Int. J. Data Min. Bioinform.* **7**, 245–65 (2013).
257. Verhaak, R. G. W. *et al.* Integrated Genomic Analysis Identifies Clinically Relevant Subtypes of Glioblastoma Characterized by Abnormalities in PDGFRA, IDH1, EGFR, and NF1. *Cancer Cell* **17**, 98–110 (2010).
258. Molecular Profiling in Guiding Individualized Treatment Plan in Adults With Recurrent/Progressive Glioblastoma - Full Text View - ClinicalTrials.gov.
259. Wang, Y. I., Abaci, H. E. & Shuler, M. L. Microfluidic blood-brain barrier model provides in vivo-like barrier properties for drug permeability screening. *Biotechnol. Bioeng.* **114**, 184–194 (2017).
260. van der Helm, M. W., van der Meer, A. D., Eijkel, J. C. T., van den Berg, A. & Segerink, L. I. Microfluidic organ-on-chip technology for blood-brain barrier research. *Tissue Barriers* **4**, e1142493 (2016).
261. Randazzo, M., Pisapia, J. M., Singh, N. & Thawani, J. P. 3D printing in neurosurgery: A systematic review. *Surg. Neurol. Int.* **7**, S801–S809 (2016).
262. Ploch, C. C., Mansi, C. S. S. A., Jayamohan, J. & Kuhl, E. Using 3D Printing to Create Personalized Brain Models for Neurosurgical Training and Preoperative Planning. *World Neurosurg.* **90**, 668–674 (2016).
263. Naftulin, J. S., Kimchi, E. Y. & Cash, S. S. Streamlined, Inexpensive 3D Printing of the Brain and Skull. *PLoS One* **10**, e0136198 (2015).
264. Treiber, J. M. *et al.* Molecular physiology of contrast enhancement in glioblastomas: An analysis of The Cancer Imaging Archive (TCIA). *J. Clin. Neurosci.* **55**, 86–92 (2018).
265. Gevaert, O. *et al.* Glioblastoma Multiforme: Exploratory Radiogenomic Analysis by Using Quantitative Image Features. *Radiology* **273**, 168–174 (2014).
266. Chow, D. *et al.* Imaging Genetic Heterogeneity in Glioblastoma and Other Glial Tumors: Review of Current Methods and Future Directions. *Am. J. Roentgenol.* **210**, 30–38 (2018).
267. Lao, J. *et al.* A Deep Learning-Based Radiomics Model for Prediction of Survival in Glioblastoma Multiforme. *Sci. Rep.* **7**, 10353 (2017).
268. Dupont, C., Betrouni, N., Reyns, N. & Vermandel, M. On Image Segmentation Methods Applied to Glioblastoma: State of Art and New Trends. *IRBM* **37**, 131–143 (2016).
269. Ostrom, Q. T. *et al.* CBTRUS Statistical Report: Primary Brain and Central Nervous System Tumors Diagnosed in the United States in 2008-2012. *Neuro. Oncol.* **17**, iv1–iv62 (2015).
270. Xie, Q., Mittal, S. & Berens, M. E. Targeting adaptive glioblastoma: an overview of proliferation and invasion. *Neuro. Oncol.* **16**, 1575–84 (2014).
271. Hirata, E. *et al.* In vivo fluorescence resonance energy transfer imaging reveals

differential activation of Rho-family GTPases in glioblastoma cell invasion. *J. Cell Sci.* **125**, 858–868 (2012).
272. Te Boekhorst, V. & Friedl, P. *Plasticity of Cancer Cell Invasion— Mechanisms and Implications for Therapy*. *Molecular and Cellular Basis of Metastasis: Road to Therapy* vol. 132 (Elsevier Inc., 2016).
273. Giesexs, A. & Westphal, M. Glioma Invasion in the Central Nervous System. *Neurosurgery* **39**, 235–252 (1996).
274. Malandrino, A., Kamm, R. D. & Moeendarbary, E. In Vitro Modeling of Mechanics in Cancer Metastasis. *ACS Biomater. Sci. Eng.* acsbiomaterials.7b00041 (2017) doi:10.1021/acsbiomaterials.7b00041.
275. Osswald, M. *et al.* Brain tumor cells interconnect to a functional and resistant network. *Nature* **528**, 93–98 (2015).
276. Knight, A. Systematic reviews of animal experiments demonstrate poor human clinical and toxicological utility. *Altern. Lab. Anim.* **35**, 641–59 (2007).
277. Kunz-Schughart, L. A., Freyer, J. P., Hofstaedter, F. & Ebner, R. The Use of 3-D Cultures for High-Throughput Screening: The Multicellular Spheroid Model. *J. Biomol. Screen.* **9**, 273–285 (2004).
278. Carey, S. P. *et al.* Comparative mechanisms of cancer cell migration through 3D matrix and physiological microtracks. *Am. J. Physiol. Cell Physiol.* **308**, ajpcell.00225.2014 (2014).
279. Thomas, D. G. *et al.* Non-muscle myosin IIB is critical for nuclear translocation during 3D invasion. *J. Cell Biol.* **210**, 583–94 (2015).
280. Irimia, D. & Toner, M. No Title. **1**, (2009).
281. Cha, J. *et al.* Tapered Microtract Array Platform for Antimigratory Drug Screening of Human Glioblastoma Multiforme. *Adv. Healthc. Mater.* **4**, 405–411 (2015).
282. Johnson, J. *et al.* Quantitative analysis of complex glioma cell migration on electrospun polycaprolactone using time-lapse microscopy. *Tissue Eng. Part C. Methods* **15**, 531–40 (2009).
283. Zervantonakis, I. K. *et al.* Three-dimensional microfluidic model for tumor cell intravasation and endothelial barrier function. *Proc. Natl. Acad. Sci. U. S. A.* **109**, 13515–20 (2012).
284. Bersini, S. *et al.* A microfluidic 3D in vitro model for specificity of breast cancer metastasis to bone. *Biomaterials* **35**, 2454–61 (2014).
285. Chen, M. B., Whisler, J. A., Jeon, J. S. & Kamm, R. D. Mechanisms of tumor cell extravasation in an in vitro microvascular network platform. *Integr. Biol.* **5**, 1262 (2013).
286. Zhang, Q., Liu, T. & Qin, J. No Title. **12**, (2012).
287. Sun, S. *et al.* Protein alterations associated with temozolomide resistance in subclones of human glioblastoma cell lines. *J. Neurooncol.* **107**, 89–100 (2012).
288. Smeds, K. A. & Grinstaff, M. W. Photocrosslinkable polysaccharides forin situ hydrogel formation. *J. Biomed. Mater. Res.* **54**, 115–121 (2001).
289. Faul, F., Erdfelder, E., Lang, A.-G. & Buchner, A. G*Power 3: a flexible statistical power analysis program for the social, behavioral, and biomedical sciences. *Behav. Res. Methods* **39**, 175–91 (2007).
290. Jensen, S. S. *et al.* Establishment and Characterization of a Tumor Stem Cell-Based Glioblastoma Invasion Model. *PLoS One* **11**, e0159746 (2016).

291. Friedl, P. & Wolf, K. Tumour-cell invasion and migration: diversity and escape mechanisms. *Nat. Rev. Cancer* **3**, 362–74 (2003).
292. Winkler, F. *et al.* Imaging glioma cell invasion *in vivo* reveals mechanisms of dissemination and peritumoral angiogenesis. *Glia* **57**, 1306–1315 (2009).
293. Assanah, M. C. *et al.* PDGF stimulates the massive expansion of glial progenitors in the neonatal forebrain. *Glia* **57**, 1835–1847 (2009).
294. Yoshida, T., Matsuda, Y., Naito, Z. & Ishiwata, T. CD44 in human glioma correlates with histopathological grade and cell migration. *Pathol. Int.* **62**, 463–470 (2012).
295. Park, J. B., Kwak, H.-J. & Lee, S.-H. Role of hyaluronan in glioma invasion. *Cell Adh. Migr.* **2**, 202–7 (2008).
296. Toole, B. P. Hyaluronan-CD44 Interactions in Cancer: Paradoxes and Possibilities. *Clin. Cancer Res.* **15**, 7462–7468 (2009).
297. Tse, J. M. *et al.* Mechanical compression drives cancer cells toward invasive phenotype. *Proc. Natl. Acad. Sci. U. S. A.* **109**, 911–6 (2012).
298. Sanz-Moreno, V. & Marshall, C. J. The plasticity of cytoskeletal dynamics underlying neoplastic cell migration. *Curr. Opin. Cell Biol.* **22**, 690–696 (2010).
299. Moreno-Bueno, G. *et al.* The morphological and molecular features of the epithelial-to-mesenchymal transition. *Nat. Protoc.* **4**, 1591–1613 (2009).
300. Paňková, K., Rösel, D., Novotný, M. & Brábek, J. The molecular mechanisms of transition between mesenchymal and amoeboid invasiveness in tumor cells. *Cell. Mol. Life Sci.* **67**, 63–71 (2010).
301. Highley, C. B., Prestwich, G. D. & Burdick, J. A. Recent advances in hyaluronic acid hydrogels for biomedical applications. *Curr. Opin. Biotechnol.* **40**, 35–40 (2016).
302. Girish, K. S. & Kemparaju, K. The magic glue hyaluronan and its eraser hyaluronidase: A biological overview. (2007) doi:10.1016/j.lfs.2007.02.037.
303. Toole, B. P. *Hyaluronan and its binding proteins, the hyaladherins*. *Current Opinion in Cell Biology* vol. 2 https://ac.els-cdn.com/095506749090081O/1-s2.0-095506749090081O-main.pdf?_tid=972edc25-0b24-4356-aa19-975687e759f7&acdnat=1538589312_bf0869795fad745860a7535b97c31d1b (1990).
304. Day, A. J. & Prestwich, G. D. Hyaluronan-binding proteins: tying up the giant. *J. Biol. Chem.* **277**, 4585–8 (2002).
305. Stern, R. Hyaluronan catabolism: a new metabolic pathway. *Eur. J. Cell Biol.* **83**, 317–325 (2004).
306. Lee, J. Y. & Spicer, A. P. Hyaluronan: a multifunctional, megaDalton, stealth molecule. *Curr. Opin. Cell Biol.* **12**, 581–586 (2000).
307. Khaing, Z. Z. & Seidlits, S. K. Hyaluronic acid and neural stem cells: implications for biomaterial design. *J. Mater. Chem. B* (2015).
308. MANUSKIATTI, W. & MAIBACH, H. I. HYALURONIC ACID AND SKIN: WOUND HEALING AND AGING. *Int. J. Dermatol.* **35**, 539–544 (1996).
309. Toole, B. P. Hyaluronan: from extracellular glue to pericellular cue. *Nat. Rev. Cancer* **4**, 528–539 (2004).
310. Ziebell, M. R. & Prestwich, G. D. Interactions of peptide mimics of hyaluronic acid with the receptor for hyaluronan mediated motility (RHAMM). *J. Comput. Aided.*

Mol. Des. **18**, 597–614 (2004).
311. Maxwell, C. A. *et al.* Cell-surface and mitotic-spindle RHAMM: moonlighting or dual oncogenic functions? *J. Cell Sci.* **121**, 925–32 (2008).
312. Lokeshwar, V. B. & Selzer, M. G. Differences in hyaluronic acid-mediated functions and signaling in arterial, microvessel and vein-derived human endothelial cells. *J. Biol. Chem.* **275**, 27641–9 (2000).
313. Savani, R. C. *et al.* Differential involvement of the hyaluronan (HA) receptors CD44 and receptor for HA-mediated motility in endothelial cell function and angiogenesis. *J. Biol. Chem.* **276**, 36770–8 (2001).
314. Hamilton, S. R. *et al.* The Hyaluronan Receptors CD44 and Rhamm (CD168) Form Complexes with ERK1 , 2 That Sustain High Basal Motility in Breast Cancer Cells * □. **282**, 16667–16680 (2007).
315. Zöller, M. CD44: can a cancer-initiating cell profit from an abundantly expressed molecule? *Nat. Rev. Cancer* **11**, 254–67 (2011).
316. Zhu, D. & Bourguignon, L. Y. Interaction between CD44 and the repeat domain of ankyrin promotes hyaluronic acid-mediated ovarian tumor cell migration. *J. Cell. Physiol.* **183**, 182–95 (2000).
317. Chopra, A. *et al.* Augmentation of integrin-mediated mechanotransduction by hyaluronic acid. *Biomaterials* **35**, 71–82 (2014).
318. Banerji, S. *et al.* Structures of the Cd44–hyaluronan complex provide insight into a fundamental carbohydrate- protein interaction. doi:10.1038/nsmb1201.
319. Vuorio, J., Vattulainen, I. & Martinez-Seara, H. Atomistic fingerprint of hyaluronan–CD44 binding. *PLOS Comput. Biol.* **13**, e1005663 (2017).
320. DeGrendele, H. C., Estess, P. & Siegelman, M. H. Requirement for CD44 in Activated T Cell Extravasation into an Inflammatory Site. *Science (80-.).* **278**, 672–675 (1997).
321. Suzuki, T. *et al.* Mechanical force effect on the two-state equilibrium of the hyaluronan-binding domain of CD44 in cell rolling. *Proc. Natl. Acad. Sci.* **112**, 6991–6996 (2015).
322. Stamenkovic, I. & Yu, Q. Shedding Light on Proteolytic Cleavage of CD44: The Responsible Sheddase and Functional Significance of Shedding. *J. Invest. Dermatol.* **129**, 1321–1324 (2009).
323. Banerji, S. *et al.* LYVE-1, a new homologue of the CD44 glycoprotein, is a lymph-specific receptor for hyaluronan. *J. Cell Biol.* **144**, 789–801 (1999).
324. Jackson, D. G. Immunological functions of hyaluronan and its receptors in the lymphatics. *Immunol. Rev.* **230**, 216–231 (2009).
325. Bono, P., Rubin, K., Higgins, J. M. G. & Hynes, R. O. Layilin, a Novel Integral Membrane Protein, Is a Hyaluronan Receptor. *Mol. Biol. Cell* **12**, 891–900 (2001).
326. Layilin, a cell surface hyaluronan receptor, interacts with merlin and radixin. *Exp. Cell Res.* **308**, 177–187 (2005).
327. Scheibner, K. A. *et al.* Hyaluronan fragments act as an endogenous danger signal by engaging TLR2. *J. Immunol.* **177**, 1272–81 (2006).
328. Termeer, C. *et al.* Oligosaccharides of Hyaluronan activate dendritic cells via toll-like receptor 4. *J. Exp. Med.* **195**, 99–111 (2002).
329. Gariboldi, S. *et al.* Low molecular weight hyaluronic acid increases the self-defense of skin epithelium by induction of beta-defensin 2 via TLR2 and TLR4. *J.*

Immunol. **181**, 2103–10 (2008).
330. Ebid, R., Lichtnekert, J. & Anders, H.-J. Hyaluronan is not a ligand but a regulator of toll-like receptor signaling in mesangial cells: role of extracellular matrix in innate immunity. *ISRN Nephrol.* **2014**, 714081 (2014).
331. Mahoney, D. J., Blundell, C. D. & Day, A. J. Mapping the hyaluronan-binding site on the link module from human tumor necrosis factor-stimulated gene-6 by site-directed mutagenesis. *J. Biol. Chem.* **276**, 22764–71 (2001).
332. Parkar, A. A. & Day, A. J. Overlapping sites on the Link module of human TSG-6 mediate binding to hyaluronan and chondroitin-4-sulphate. *FEBS Lett.* **410**, 413–417 (1997).
333. Coulson-Thomas, V. J. *et al.* Tumor Necrosis Factor-stimulated Gene-6 (TSG-6) Is Constitutively Expressed in Adult Central Nervous System (CNS) and Associated with Astrocyte-mediated Glial Scar Formation following Spinal Cord Injury. *J. Biol. Chem.* **291**, 19939–52 (2016).
334. Weigel, P. H., Frost, S. J., McGary, C. T. & LeBoeuf, R. D. The role of hyaluronic acid in inflammation and wound healing. *Int. J. Tissue React.* **10**, 355–65 (1988).
335. Stern, R., ASARI, A. A. & Sugahara, K. N. Hyaluronan fragments: An information-rich system. *Eur. J. Cell Biol.* **85**, 699–715 (2006).
336. Marei, W. F., Ghafari, F. & Fouladi-Nashta, A. A. Role of hyaluronic acid in maturation and further early embryo development of bovine oocytes. *Theriogenology* **78**, 670–677 (2012).
337. Haylock, D. N. & Nilsson, S. K. The role of hyaluronic acid in hemopoietic stem cell biology. *Regen. Med.* **1**, 437–445 (2006).
338. MEYER, K. Chemical structure of hyaluronic acid. *Fed. Proc.* **17**, 1075–7 (1958).
339. Fraser, J. R. E., Laurent, T. C. & Laurent, U. B. G. Hyaluronan: its nature, distribution, functions and turnover. *J. Intern. Med.* **242**, 27–33 (1997).
340. Park, J. W. & Chakrabarti, B. Optical characteristics of carboxyl group in relation to the circular dichroic properties and dissociation constants of glycosaminoglycans. *Biochim. Biophys. Acta* **544**, 667–75 (1978).
341. Laurent, U. B. G. & Tengblad, A. Determination of hyaluronate in biological samples by a specific radioassay technique. *Anal. Biochem.* **109**, 386–394 (1980).
342. Armstrong, S. E. & Bell, D. R. Measurement of high-molecular-weight hyaluronan in solid tissue using agarose gel electrophoresis. *Anal. Biochem.* **308**, 255–64 (2002).
343. Osterlin, S. On the molecular biology of the vitreous in the aphakic eye. *Acta Ophthalmol.* **55**, 353–61 (1977).
344. Dahl, L. B., Dahl, I. M., Engström-Laurent, A. & Granath, K. Concentration and molecular weight of sodium hyaluronate in synovial fluid from patients with rheumatoid arthritis and other arthropathies. *Ann. Rheum. Dis.* **44**, 817–22 (1985).
345. Hascall, V. C. *et al.* Intracellular hyaluronan: a new frontier for inflammation? *Biochim. Biophys. Acta - Gen. Subj.* **1673**, 3–12 (2004).
346. Wendy E. Krause, †, Enrico G. Bellomo, ‡ and & Ralph H. Colby*, ‡. Rheology of Sodium Hyaluronate under Physiological Conditions. (2001) doi:10.1021/BM0055798.
347. Milas, M. *et al.* Comparative rheological behavior of hyaluronan from bacterial and

animal sources with cross-linked hyaluronan (hylan) in aqueous solution. *Biopolymers* **59**, 191–204 (2001).
348. Oelschlaeger, C., Cota Pinto Coelho, M. & Willenbacher, N. Chain Flexibility and Dynamics of Polysaccharide Hyaluronan in Entangled Solutions: A High Frequency Rheology and Diffusing Wave Spectroscopy Study. *Biomacromolecules* **14**, 3689–3696 (2013).
349. Horkay, F., Basser, P. J., Hecht, A.-M. & Geissler, E. Gel-like behavior in aggrecan assemblies. *J. Chem. Phys.* **128**, 135103 (2008).
350. Zhu, W., Mow, V. C., Rosenberg, L. C. & Tang, L.-H. Determination of kinetic changes of aggrecan-hyaluronan interactions in solution from its rheological properties. *J. Biomech.* **27**, 571–579 (1994).
351. Nishimura, M. *et al.* Role of chondroitin sulfate–hyaluronan interactions in the viscoelastic properties of extracellular matrices and fluids. *Biochim. Biophys. Acta - Gen. Subj.* **1380**, 1–9 (1998).
352. Galtrey, C. M. & Fawcett, J. W. The role of chondroitin sulfate proteoglycans in regeneration and plasticity in the central nervous system. *Brain Res. Rev.* **54**, 1–18 (2007).
353. Dijkgraaf, L. C., De Bont, L. G. M., Boering, -Geert & Liem, R. S. B. *Normal Cartilage Structure, Biochemistry, and Metabolism: A Review of the Literature*. *J Oral Maxillofac Surg* vol. 53 https://www.joms.org/article/0278-2391(95)90283-X/pdf (1995).
354. Roughley, P. J. & Lee, E. R. Cartilage proteoglycans: Structure and potential functions. *Microsc. Res. Tech.* **28**, 385–397 (1994).
355. Tang, L.-H., Buckwalter, J. A. & Rosenberg, L. C. Effect of link protein concentration on articular cartilage proteoglycan aggregation. *J. Orthop. Res.* **14**, 334–339 (1996).
356. Bajorath, J., Greenfield, B., Munro, S. B., Day, A. J. & Aruffo, A. Identification of CD44 residues important for hyaluronan binding and delineation of the binding site. *J. Biol. Chem.* **273**, 338–43 (1998).
357. Kahmann, J. D. *et al.* Localization and characterization of the hyaluronan-binding site on the Link module from human TSG-6.
358. Bano, F., Tammi, M. I., Kang, D. W., Harris, E. N. & Richter, R. P. Single-Molecule Unbinding Forces between the Polysaccharide Hyaluronan and Its Binding Proteins. *Biophys. J.* **114**, 2910–2922 (2018).
359. Kobayashi, Y., Okamoto, A. & Nishinari, K. Viscoelasticity of hyaluronic acid with different molecular weights. *Biorheology* **31**, 235–244 (1994).
360. Schurz, J. & Ribitsch, V. Rheology of synovial fluid. *Biorheology* **24**, 385–99 (1987).
361. Zhang, Z. & Christopher, G. F. The nonlinear viscoelasticity of hyaluronic acid and its role in joint lubrication. *Soft Matter* **11**, 2596–603 (2015).
362. Bjelle, A., Andersson, T. & Granath, K. Molecular Weight Distribution of Hyaluronic Acid of Human Synovial Fluid in Rheumatic Diseases. *Scand. J. Rheumatol.* **12**, 133–138 (1983).
363. Holmes, M. W., Bayliss, M. T. & Muir, H. Hyaluronic acid in human articular cartilage. Age-related changes in content and size. *Biochem. J.* **250**, 435–41 (1988).

364. Lokeshwar, V. B. *et al.* Stromal and Epithelial Expression of Tumor Markers Hyaluronic Acid and HYAL1 Hyaluronidase in Prostate Cancer. *J. Biol. Chem.* **276**, 11922–11932 (2001).
365. Wu, M. *et al.* A novel role of low molecular weight hyaluronan in breast cancer metastasis. *FASEB J.* **29**, 1290–1298 (2015).
366. McAtee, C. O., Barycki, J. J. & Simpson, M. A. Emerging roles for hyaluronidase in cancer metastasis and therapy. *Adv. Cancer Res.* **123**, 1–34 (2014).
367. McKee, C. M. *et al.* Hyaluronan (HA) fragments induce chemokine gene expression in alveolar macrophages. The role of HA size and CD44. *J. Clin. Invest.* **98**, 2403–13 (1996).
368. Rayahin, J. E., Buhrman, J. S., Zhang, Y., Koh, T. J. & Gemeinhart, R. A. High and low molecular weight hyaluronic acid differentially influence macrophage activation. *ACS Biomater. Sci. Eng.* **1**, 481–493 (2015).
369. Yang, C. *et al.* The high and low molecular weight forms of hyaluronan have distinct effects on CD44 clustering. *J. Biol. Chem.* **287**, 43094–107 (2012).
370. Wolny, P. M. *et al.* Analysis of CD44-hyaluronan interactions in an artificial membrane system: insights into the distinct binding properties of high and low molecular weight hyaluronan. *J. Biol. Chem.* **285**, 30170–80 (2010).
371. Cyphert, J. M., Trempus, C. S. & Garantziotis, S. *Size Matters: Molecular Weight Specificity of Hyaluronan Effects in Cell Biology*. *International Journal of Cell Biology* vol. 2015 1–8 (Hindawi, 2015).
372. Itano, N. & Kimata, K. Mammalian Hyaluronan Synthases. *IUBMB Life (International Union Biochem. Mol. Biol. Life)* **54**, 195–199 (2002).
373. Itano, N. *et al.* Three isoforms of mammalian hyaluronan synthases have distinct enzymatic properties. *J. Biol. Chem.* **274**, 25085–92 (1999).
374. and, R. S. & Mark J. Jedrzejas*, ‡. Hyaluronidases: Their Genomics, Structures, and Mechanisms of Action. (2006) doi:10.1021/CR050247K.
375. Kinlin L. Chao, Lavanya Muthukumar, and & Herzberg*, O. Structure of Human Hyaluronidase-1, a Hyaluronan Hydrolyzing Enzyme Involved in Tumor Growth and Angiogenesis†,‡. (2007) doi:10.1021/BI700382G.
376. Chen, J.-W. E., Pedron, S. & Harley, B. A. C. The Combined Influence of Hydrogel Stiffness and Matrix-Bound Hyaluronic Acid Content on Glioblastoma Invasion. *Macromol. Biosci.* **17**, 1700018 (2017).
377. Cha, J., Kang, S.-G. & Kim, P. Strategies of Mesenchymal Invasion of Patient-derived Brain Tumors: Microenvironmental Adaptation. *Sci. Rep.* **6**, 24912 (2016).
378. Heldin, P. *et al.* Deregulation of hyaluronan synthesis, degradation and binding promotes breast cancer. *J. Biochem.* **154**, 395–408 (2013).
379. Bharadwaj, A. G. *et al.* Spontaneous metastasis of prostate cancer is promoted by excess hyaluronan synthesis and processing. *Am. J. Pathol.* **174**, 1027–36 (2009).
380. Kovar, J. L., Johnson, M. A., Volcheck, W. M., Chen, J. & Simpson, M. A. Hyaluronidase Expression Induces Prostate Tumor Metastasis in an Orthotopic Mouse Model. *Am. J. Pathol.* **169**, 1415–1426 (2006).
381. Balazs, E. A. Therapeutic use of hyaluronan. *Struct. Chem.* **20**, 341–349 (2009).
382. Balazs, E. A. & Denlinger, J. L. Clinical uses of hyaluronan. *Ciba Found. Symp.* **143**, 265–75; discussion 275-80, 281–5 (1989).

383. Brown, T., Laurent, U. & Fraser. Turnover of hyaluronan in synovial joints: elimination of labelled hyaluronan from the knee joint of the rabbit. *Exp. Physiol.* **76**, 125–134 (1991).
384. Adams, M. E. An analysis of clinical studies of the use of crosslinked hyaluronan, hylan, in the treatment of osteoarthritis. *J. Rheumatol. Suppl.* **39**, 16–8 (1993).
385. Collins, M. N. & Birkinshaw, C. Hyaluronic acid based scaffolds for tissue engineering-A review. *Carbohydr. Polym.* **92**, 1262–1279 (2013).
386. Prestwich, G. D. Hyaluronic acid-based clinical biomaterials derived for cell and molecule delivery in regenerative medicine. *J. Control. Release* **155**, 193–199 (2011).
387. Arsiwala, S. Z. Current Trends in Facial Rejuvenation with Fillers. *J. Cutan. Aesthet. Surg.* **8**, 125–6 (2015).
388. Tezel, A. & Fredrickson, G. H. The science of hyaluronic acid dermal fillers. *J. Cosmet. Laser Ther.* **10**, 35–42 (2008).
389. Price, R. D., Berry, M. G. & Navsaria, H. A. Hyaluronic acid: the scientific and clinical evidence. *J. Plast. Reconstr. Aesthetic Surg.* **60**, 1110–1119 (2007).
390. Oh, E. J. *et al.* Target specific and long-acting delivery of protein, peptide, and nucleotide therapeutics using hyaluronic acid derivatives. *J. Control. Release* **141**, 2–12.
391. Köwitsch, A., Zhou, G. & Groth, T. Medical application of glycosaminoglycans: a review. *J. Tissue Eng. Regen. Med.* **12**, e23–e41 (2018).
392. Medical Applications of Hyaluronan. in *Hyaluronic Acid* 143–192 (John Wiley & Sons, Ltd, 2015). doi:10.1002/9781118695920.ch6.
393. Kogan, G., Šoltés, L., Stern, R. & Gemeiner, P. Hyaluronic acid: a natural biopolymer with a broad range of biomedical and industrial applications. *Biotechnol. Lett.* **29**, 17–25 (2006).
394. Burdick, J. A. & Prestwich, G. D. Hyaluronic Acid Hydrogels for Biomedical Applications. *Adv. Mater.* **23**, H41–H56 (2011).
395. Gerecht, S. *et al.* Hyaluronic acid hydrogel for controlled self-renewal and differentiation of human embryonic stem cells. *Proc. Natl. Acad. Sci. U. S. A.* **104**, 11298–303 (2007).
396. Adil, M. M. *et al.* Engineered hydrogels increase the post-transplantation survival of encapsulated hESC-derived midbrain dopaminergic neurons. *Biomaterials* **136**, 1–11 (2017).
397. Adil, M. M. *et al.* Dopaminergic Neurons Transplanted Using Cell-Instructive Biomaterials Alleviate Parkinsonism in Rodents. *Adv. Funct. Mater.* 1804144 (2018) doi:10.1002/adfm.201804144.
398. Xin, X., Borzacchiello, A., Netti, P. A., Ambrosio, L. & Nicolais, L. Hyaluronic-acid-based semi-interpenetrating materials. *J. Biomater. Sci. Polym. Ed.* **15**, 1223–36 (2004).
399. Tan, H., Rubin, J. P. & Marra, K. G. Injectable in situ forming biodegradable chitosan-hyaluronic acid based hydrogels for adipose tissue regeneration. *Organogenesis* **6**, 173–80.
400. TAN, H., WU, J., LAO, L. & GAO, C. Gelatin/chitosan/hyaluronan scaffold integrated with PLGA microspheres for cartilage tissue engineering. *Acta Biomater.* **5**, 328–337 (2009).

401. Kim, J. *et al.* Bone regeneration using hyaluronic acid-based hydrogel with bone morphogenic protein-2 and human mesenchymal stem cells. *Biomaterials* **28**, 1830–1837 (2007).
402. Boudou, T., Crouzier, T., Nicolas, C., Ren, K. & Picart, C. Polyelectrolyte Multilayer Nanofilms Used as Thin Materials for Cell Mechano-Sensitivity Studies. *Macromol. Biosci.* **11**, 77–89 (2011).
403. Eddhahak, A. & Zidi, M. Influence of viscoelastic properties of an hyaluronic acid-based hydrogel on viability of mesenchymal stem cells. *Biomed. Mater. Eng.* **26**, 103–114 (2015).
404. Cha, J. & Kim, P. Biomimetic Strategies for the Glioblastoma Microenvironment. *Front. Mater.* **4**, 45 (2017).
405. Volpi, N., Schiller, J., Stern, R. & Soltes, L. Role, Metabolism, Chemical Modifications and Applications of Hyaluronan. *Curr. Med. Chem.* **16**, 1718–1745 (2009).
406. Lim, H. J. *et al.* Response to di-functionalized hyaluronic acid with orthogonal chemistry grafting at independent modification sites in rodent models of neural differentiation and spinal cord injury †. *J. Mater. Chem. B* **4**, 6865 (2016).
407. Nistor, M. T., Chiriac, A. P., Nita, L. E., Vasile, C. & Bercea, M. Semi-interpenetrated polymer networks of hyaluronic acid modified with poly(aspartic acid). *J. Polym. Res.* **20**, 86 (2013).
408. Chen, Q. *et al.* Semi-interpenetrating network hyaluronic acid microgel delivery systems in micro-flow. *J. Colloid Interface Sci.* **519**, 174–185 (2018).
409. Brigham, M. D. *et al.* Mechanically Robust and Bioadhesive Collagen and Photocrosslinkable Hyaluronic Acid Semi-Interpenetrating Networks. *Tissue Eng. Part A* **15**, 1645–1653 (2009).
410. Erickson, I. E. *et al.* Macromer density influences mesenchymal stem cell chondrogenesis and maturation in photocrosslinked hyaluronic acid hydrogels. *Osteoarthr. Cartil.* **17**, 1639–1648 (2009).
411. Ulrich, T. A., Pardo, E. M. D. J. & Kumar, S. The Mechanical Rigidity of the Extracellular Matrix Regulates the Structure , Motility , and Proliferation of Glioma Cells. *Cancer Res.* **69**, 4167–4175 (2009).
412. Keung, A. J., de Juan-Pardo, E. M., Schaffer, D. V. & Kumar, S. Rho GTPases Mediate the Mechanosensitive Lineage Commitment of Neural Stem Cells. *Stem Cells* **29**, 1886–1897 (2011).
413. Handorf, A. M., Zhou, Y., Halanski, M. A. & Li, W.-J. Tissue Stiffness Dictates Development, Homeostasis, and Disease Progression. *Organogenesis* **11**, 1–15 (2015).
414. Discher, D. E., Janmey, P. & Wang, Y.-L. Tissue cells feel and respond to the stiffness of their substrate. *Science* **310**, 1139–43 (2005).
415. Tavsanli, B., Can, V. & Okay, O. Mechanically strong triple network hydrogels based on hyaluronan and poly(N,N-dimethylacrylamide). *Soft Matter* **11**, 8517–8524 (2015).
416. Rodell, C. B., Kaminski, A. L. & Burdick, J. A. Rational Design of Network Properties in Guest–Host Assembled and Shear-Thinning Hyaluronic Acid Hydrogels. *Biomacromolecules* **14**, 4125–4134 (2013).
417. Lou, J., Stowers, R., Nam, S., Xia, Y. & Chaudhuri, O. Stress relaxing hyaluronic

acid-collagen hydrogels promote cell spreading, fiber remodeling, and focal adhesion formation in 3D cell culture. *Biomaterials* **154**, 213–222 (2018).
418. Marklein, R. A. & Burdick, J. A. Spatially controlled hydrogel mechanics to modulate stem cell interactions. *Soft Matter* **6**, 136–143.
419. Adrianne, R., Christopher, R., Minna, C., Jason, B. & Kristi, A. Supramolecular hyaluronic acid-based hydrogels with dynamic viscoelasticity. *Front. Bioeng. Biotechnol.* **4**, (2016).
420. Chua, P.-H., Neoh, K.-G., Kang, E.-T. & Wang, W. Surface functionalization of titanium with hyaluronic acid/chitosan polyelectrolyte multilayers and RGD for promoting osteoblast functions and inhibiting bacterial adhesion. *Biomaterials* **29**, 1412–1421 (2008).
421. C. Picart, *,†,‖ *et al.* Buildup Mechanism for Poly(l-lysine)/Hyaluronic Acid Films onto a Solid Surface. (2001) doi:10.1021/LA010848G.
422. Salomäki, M. & Kankare, J. Influence of Synthetic Polyelectrolytes on the Growth and Properties of Hyaluronan−Chitosan Multilayers. *Biomacromolecules* **10**, 294–301 (2009).
423. Schneider, A. *et al.* Polyelectrolyte Multilayers with a Tunable Young's Modulus: Influence of Film Stiffness on Cell Adhesion. *Langmuir* **22**, 1193–1200 (2006).
424. Ludovic Richert, †, Adam J. Engler, ‡, Dennis E. Discher, ‡ and & Catherine Picart*, †,§. Elasticity of Native and Cross-Linked Polyelectrolyte Multilayer Films. (2004) doi:10.1021/BM0498023.
425. Schneider, A., Richert, L., Francius, G., Voegel, J.-C. & Picart, C. Elasticity, biodegradability and cell adhesive properties of chitosan/hyaluronan multilayer films. *Biomed. Mater.* **2**, S45–S51 (2007).
426. Ouyang, L., Highley, C. B., Rodell, C. B., Sun, W. & Burdick, J. A. 3D Printing of Shear-Thinning Hyaluronic Acid Hydrogels with Secondary Cross-Linking. *ACS Biomater. Sci. Eng.* **2**, 1743–1751 (2016).
427. Köwitsch, A. *et al.* Bioactivity of immobilized hyaluronic acid derivatives regarding protein adsorption and cell adhesion. *Biotechnol. Appl. Biochem.* **58**, 376–389 (2011).
428. Eng, D., Caplan, M., Preul, M. & Panitch, A. Hyaluronan scaffolds: A balance between backbone functionalization and bioactivity. *Acta Biomater.* **6**, 2407–2414 (2010).
429. Bencherif, S. A. *et al.* Influence of the degree of methacrylation on hyaluronic acid hydrogels properties. *Biomaterials* **29**, 1739–1749 (2008).
430. Lian Cen, K. G. Neoh, *, Yali Li, and & Kang, E. T. Assessment of in Vitro Bioactivity of Hyaluronic Acid and Sulfated Hyaluronic Acid Functionalized Electroactive Polymer†. (2004) doi:10.1021/BM040048V.
431. Ibrahim, S., Kang, Q. K. & Ramamurthi, A. The impact of hyaluronic acid oligomer content on physical, mechanical, and biologic properties of divinyl sulfone-crosslinked hyaluronic acid hydrogels. *J. Biomed. Mater. Res. Part A* **9999A**, NA-NA (2010).
432. Bhattacharya, D. S. *et al.* Impact of structurally modifying hyaluronic acid on CD44 interaction †. *J. Mater. Chem. B* **5**, 8183 (2017).
433. Lord, M. S., Pasqui, D., Barbucci, R. & Milthorpe, B. K. Protein adsorption on

derivatives of hyaluronic acid and subsequent cellular response. *J. Biomed. Mater. Res. Part A* **91A**, 635–646 (2009).
434. Zhu, X. *et al.* Directing three-dimensional multicellular morphogenesis by self-organization of vascular mesenchymal cells in hyaluronic acid hydrogels. *J. Biol. Eng.* **11**, 12 (2017).
435. Kim, J. *et al.* Synthesis and characterization of matrix metalloprotease sensitive-low molecular weight hyaluronic acid based hydrogels. *J. Mater. Sci. Mater. Med.* **19**, 3311–3318 (2008).
436. Lei, Y., Gojgini, S., Lam, J. & Segura, T. The spreading, migration and proliferation of mouse mesenchymal stem cells cultured inside hyaluronic acid hydrogels. *Biomaterials* **32**, 39–47 (2011).
437. Park, Y. D., Tirelli, N. & Hubbell, J. A. *Photopolymerized hyaluronic acid-based hydrogels and interpenetrating networks*. *Biomaterials* vol. 24 https://ac.els-cdn.com/S0142961202004209/1-s2.0-S0142961202004209-main.pdf?_tid=c41b39b4-280b-4a72-a7f2-7e99bf780b24&acdnat=1535387665_5fb35a70b706cfde3db0779ce15952b2 (2003).
438. Kutty, J. K., Cho, E., Soo Lee, J., Vyavahare, N. R. & Webb, K. The effect of hyaluronic acid incorporation on fibroblast spreading and proliferation within PEG-diacrylate based semi-interpenetrating networks. *Biomaterials* **28**, 4928–4938 (2007).
439. Nimmo, C. M., Owen, S. C. & Shoichet, M. S. Diels-Alder Click Cross-Linked Hyaluronic Acid Hydrogels for Tissue Engineering. *Biomacromolecules* **12**, 824–830 (2011).
440. Oh, E. J. *et al.* Control of the molecular degradation of hyaluronic acid hydrogels for tissue augmentation. *J. Biomed. Mater. Res. Part A* **86A**, 685–693 (2008).
441. Zhong, S. P. *et al.* Biodegradation of hyaluronic acid derivatives by hyaluronidase. *Biomaterials* **15**, 359–365 (1994).
442. Bulpitt, P. & Aeschlimann, D. New strategy for chemical modification of hyaluronic acid: Preparation of functionalized derivatives and their use in the formation of novel biocompatible hydrogels. *J. Biomed. Mater. Res.* **47**, 152–169 (1999).
443. Altgärde, N. *et al.* Probing the biofunctionality of biotinylated hyaluronan and chondroitin sulfate by hyaluronidase degradation and aggrecan interaction. *Acta Biomater.* **9**, 8158–8166 (2013).
444. Prestwich, G. D., Marecak, D. M., Marecek, J. F., Vercruysse, K. P. & Ziebell, M. R. *Controlled chemical modification of hyaluronic acid: synthesis, applications, and biodegradation of hydrazide derivatives*. *Journal of Controlled Release* vol. 53 https://www.sciencedirect.com/science/article/pii/S0168365997002423 (1998).
445. Oudshoorn, M. H. M., Rissmann, R., Bouwstra, J. A. & Hennink, W. E. Synthesis of methacrylated hyaluronic acid with tailored degree of substitution. *Polymer (Guildf).* **48**, 1915–1920 (2007).
446. Sahoo, S., Chung, C., Khetan, S. & Burdick, J. A. Hydrolytically Degradable Hyaluronic Acid Hydrogels with Controlled Temporal Structures. *Biomacromolecules* **9**, 1088–1092 (2008).
447. Chung, C., Beecham, M., Mauck, R. L. & Burdick, J. A. The influence of degradation characteristics of hyaluronic acid hydrogels on in vitro neocartilage

formation by mesenchymal stem cells. *Biomaterials* **30**, 4287–4296 (2009).
448. Wei, Z., Lewis, D. M., Xu, Y. & Gerecht, S. Dual Cross-Linked Biofunctional and Self-Healing Networks to Generate User-Defined Modular Gradient Hydrogel Constructs. *Adv. Healthc. Mater.* **6**, 1700523 (2017).
449. Bernhard, J. C. & Panitch, A. Synthesis and characterization of an aggrecan mimic. *Acta Biomater.* **8**, 1543–1550 (2012).
450. Bissell, M. J. & Radisky, D. Putting tumours in context. *Nat. Rev. Cancer* **1**, 46–54 (2001).
451. Ward, J. A., Huang, L., Guo, H., Ghatak, S. & Toole, B. P. Perturbation of Hyaluronan Interactions Inhibits Malignant Properties of Glioma Cells. *Am. J. Pathol.* **162**, 1403–1409 (2003).
452. Xu, Y., Stamenkovic, I. & Yu, Q. CD44 attenuates activation of the hippo signaling pathway and is a prime therapeutic target for glioblastoma. *Cancer Res.* **70**, 2455–64 (2010).
453. Clucas, J. *et al.* ERM proteins in cancer progression. *J. Cell Sci.* **127**, 267–75 (2014).
454. Zhu, D. & Bourguignon, L. Y. W. The ankyrin-binding domain of CD44s is involved in regulating hyaluronic acid-mediated functions and prostate tumor cell transformation. *Cell Motil. Cytoskeleton* **39**, 209–222 (1998).
455. Bourguignon, L. Y. W., Gilad, E., Rothman, K. & Peyrollier, K. Hyaluronan-CD44 interaction with IQGAP1 promotes Cdc42 and ERK signaling, leading to actin binding, Elk-1/estrogen receptor transcriptional activation, and ovarian cancer progression. *J. Biol. Chem.* **280**, 11961–72 (2005).
456. Deleyrolle, L. P. *et al.* Evidence for label-retaining tumour-initiating cells in human glioblastoma. *Brain* **134**, 1331–1343 (2011).
457. Lin, J.-M. G. *et al.* Linking invasive motility to protein expression in single tumor cells. *Lab Chip* **18**, 371–384 (2018).
458. Jung, S. *et al.* Brain tumor invasion model system using organotypic brain-slice culture as an alternative to in vivo model. *J. Cancer Res. Clin. Oncol.* **128**, 469–476 (2002).
459. Rust, M. J., Bates, M. & Zhuang, X. Sub-diffraction-limit imaging by stochastic optical reconstruction microscopy (STORM). *Nat. Methods* **3**, 793–796 (2006).
460. Huang, B., Wang, W., Bates, M. & Zhuang, X. Three-Dimensional Super-Resolution Imaging by Stochastic Optical Reconstruction Microscopy. *Science (80-.).* **319**, 810–813 (2008).
461. Wojcik, M., Hauser, M., Li, W., Moon, S. & Xu, K. Graphene-enabled electron microscopy and correlated super-resolution microscopy of wet cells. *Nat. Commun.* **6**, 7384 (2015).
462. Killilea, A. N. *et al.* Cytoskeletal organization in microtentacles. *Exp. Cell Res.* **357**, 291–298 (2017).
463. Ran, F. A. *et al.* Genome engineering using the CRISPR-Cas9 system. *Nat. Protoc.* **8**, 2281–308 (2013).
464. Lee, J. P., Kassianidou, E., MacDonald, J. I., Francis, M. B. & Kumar, S. N-terminal specific conjugation of extracellular matrix proteins to 2-pyridinecarboxaldehyde functionalized polyacrylamide hydrogels. *Biomaterials* **102**, 268–276 (2016).

465. Xia, Y. *et al.* Replica molding using polymeric materials: A practical step toward nanomanufacturing. *Adv. Mater.* **9**, 147–149 (1997).
466. Gates, B. D. *et al.* New Approaches to Nanofabrication: Molding, Printing, and Other Techniques. *Chem. Rev.* **105**, 1171–1196 (2005).
467. Rianna, C., Radmacher, M. & Kumar, S. Direct Evidence that Tumor Cells Soften when Navigating Confined Spaces. *Mol. Biol. Cell* In press. (2020).
468. Xu, K., Babcock, H. P. & Zhuang, X. Dual-objective STORM reveals three-dimensional filament organization in the actin cytoskeleton. *Nat. Methods* **9**, 185–188 (2012).
469. Bowman, R. L., Wang, Q., Carro, A., Verhaak, R. G. W. & Squatrito, M. GlioVis data portal for visualization and analysis of brain tumor expression datasets. *Neuro. Oncol.* **19**, 139–141 (2017).
470. Wloga, D., Joachimiak, E. & Fabczak, H. Tubulin Post-Translational Modifications and Microtubule Dynamics. *Int. J. Mol. Sci.* **18**, E2207 (2017).
471. Bieling, P. *et al.* CLIP-170 tracks growing microtubule ends by dynamically recognizing composite EB1/tubulin-binding sites. *J. Cell Biol.* **183**, 1223–1233 (2008).
472. Marcos, S. *et al.* Tubulin Tyrosination Is Required for the Proper Organization and Pathfinding of the Growth Cone. *PLoS One* **4**, e5405 (2009).
473. Song, Y. & Brady, S. T. Post-translational modifications of tubulin: pathways to functional diversity of microtubules. *Trends Cell Biol.* **25**, 125–36 (2015).
474. Olson, M. F. & Sahai, E. The actin cytoskeleton in cancer cell motility. *Clin. Exp. Metastasis* **26**, 273–287 (2009).
475. Arnold, M. *et al.* Activation of Integrin Function by Nanopatterned Adhesive Interfaces. *ChemPhysChem* **5**, 383–388 (2004).
476. Rottner, K. & Stradal, T. E. Actin dynamics and turnover in cell motility. *Curr. Opin. Cell Biol.* **23**, 569–578 (2011).
477. Whipple, R. A., Cheung, A. M. & Martin, S. S. Detyrosinated microtubule protrusions in suspended mammary epithelial cells promote reattachment. *Exp. Cell Res.* **313**, 1326–36 (2007).
478. Whipple, R. A. *et al.* Vimentin filaments support extension of tubulin-based microtentacles in detached breast tumor cells. *Cancer Res.* **68**, 5678–5688 (2008).
479. Matrone, M. a *et al.* Metastatic breast tumors express increased tau, which promotes microtentacle formation and the reattachment of detached breast tumor cells. *Oncogene* **29**, 3217–27 (2010).
480. Adams, R. A., Passino, M., Sachs, B. D., Nuriel, T. & Akassoglou, K. Fibrin mechanisms and functions in nervous system pathology. *Mol. Interv.* **4**, 163–76 (2004).
481. Raman, P. S., Alves, C. S., Wirtz, D. & Konstantopoulos, K. Distinct Kinetic and Molecular Requirements Govern CD44 Binding to Hyaluronan versus Fibrin(ogen). *Biophys. J.* **103**, 415–423 (2012).
482. Klank, R. L. *et al.* Biphasic Dependence of Glioma Survival and Cell Migration on CD44 Expression Level. *CellReports* **18**, 23–31 (2016).
483. Ilangumaran, S., Briol, A. & Hoessli, D. C. CD44 selectively associates with active Src family protein tyrosine kinases Lck and Fyn in glycosphingolipid-rich plasma

membrane domains of human peripheral blood lymphocytes. *Blood* **91**, 3901–8 (1998).
484. Heasman, S. J. & Ridley, A. J. Mammalian Rho GTPases: new insights into their functions from in vivo studies. *Nat. Rev. Mol. Cell Biol.* **9**, 690–701 (2008).
485. Sousa, A. D. & Cheney, R. E. Myosin-X: a molecular motor at the cell's fingertips. *Trends Cell Biol.* **15**, 533–539 (2005).
486. Heisterkamp, A. *et al.* Pulse energy dependence of subcellular dissection by femtosecond laser pulses. *Opt. Express* **13**, 3690–3696 (2005).
487. Chan, C. E. & Odde, D. J. Traction Dynamics of Filopodia on Compliant Substrates. *Science (80-.).* **322**, 1687–1691 (2008).
488. Mitchison, T. & Kirschner, M. Cytoskeletal dynamics and nerve growth. *Neuron* **1**, 761–772 (1988).
489. Fukata, M. *et al.* Rac1 and Cdc42 Capture Microtubules through IQGAP1 and CLIP-170. *Cell* **109**, 873–885 (2002).
490. Coles, C. H. & Bradke, F. Coordinating Neuronal Actin–Microtubule Dynamics. *Curr. Biol.* **25**, R677–R691 (2015).
491. Rotoli, D. *et al.* IQGAP1 in Podosomes/Invadosomes Is Involved in the Progression of Glioblastoma Multiforme Depending on the Tumor Status. *Int. J. Mol. Sci.* **18**, 150 (2017).
492. Mcdonald, K. L. *et al.* IQGAP1 and IGFBP2: Valuable Biomarkers for Determining Prognosis in Glioma Patients. *J. Neuropathol. Exp. Neurol.* **66**, 405–417 (2007).
493. Paluch, E. K. & Raz, E. The role and regulation of blebs in cell migration. *Curr. Opin. Cell Biol.* **25**, 582–90 (2013).
494. Noritake, J., Watanabe, T., Sato, K., Wang, S. & Kaibuchi, K. IQGAP1: a key regulator of adhesion and migration. *J. Cell Sci.* **118**, 2085–92 (2005).
495. Murphy, D. A. & Courtneidge, S. A. The 'ins' and 'outs' of podosomes and invadopodia: characteristics, formation and function. *Nat. Rev. Mol. Cell Biol.* **12**, 413–426 (2011).
496. Bard, J. B. & Hay, E. D. The behavior of fibroblasts from the developing avian cornea. Morphology and movement in situ and in vitro. *J. Cell Biol.* **67**, 400–18 (1975).
497. Bouchet, B. P. & Akhmanova, A. Microtubules in 3D cell motility. *J. Cell Sci.* **130**, 39–50 (2017).
498. Prahl, L. S. *et al.* Microtubule-Based Control of Motor-Clutch System Mechanics in Glioma Cell Migration Correspondence. *Cell Rep.* **25**, 2591–2604 (2018).
499. Stamenović, D., Mijailovich, S. M., Tolić-Nørrelykke, I. M., Chen, J. & Wang, N. Cell prestress. II. Contribution of microtubules. *Am. J. Physiol. Physiol.* **282**, C617–C624 (2002).
500. Rhee, S., Jiang, H., Ho, C.-H. & Grinnell, F. Microtubule function in fibroblast spreading is modulated according to the tension state of cell-matrix interactions. *Proc. Natl. Acad. Sci. U. S. A.* **104**, 5425–30 (2007).
501. Panopoulos, A., Howell, M., Fotedar, R., Margolis, R. L. & Blanchoin, L. Glioblastoma motility occurs in the absence of actin polymer. *Mol. Biol. Cell* **22**, 2212–2220 (2011).
502. Heck, J. N. *et al.* Microtubules regulate GEF-H1 in response to extracellular matrix stiffness. *Mol. Biol. Cell* **23**, 2583–2592 (2012).

503. Cheng, I. K. *et al.* GEF-H1 over-expression in hepatocellular carcinoma promotes cell motility via activation of RhoA signalling. *J. Pathol.* **228**, 575–585 (2012).
504. Marhaba, R. & Zöller, M. CD44 in cancer progression: adhesion, migration and growth regulation. *J. Mol. Histol.* **35**, 211–31 (2004).
505. Tijink, B. M. *et al.* A Phase I Dose Escalation Study with Anti-CD44v6 Bivatuzumab Mertansine in Patients with Incurable Squamous Cell Carcinoma of the Head and Neck or Esophagus. *Clinical Cancer Research* vol. 9 6064–6072 (2006).
506. Rupp, U. *et al.* Safety and pharmacokinetics of bivatuzumab mertansine in patients with CD44v6-positive metastatic breast cancer: final results of a phase I study. *Anticancer. Drugs* **18**, 477–85 (2007).
507. Lichti, C. F. *et al.* Integrated Chromosome 19 Transcriptomic and Proteomic Data Sets Derived from Glioma Cancer Stem-Cell Lines. *J. Proteome Res.* **13**, 191–199 (2014).

Appendix. Supplementary Figures and Tables for Chapter 4

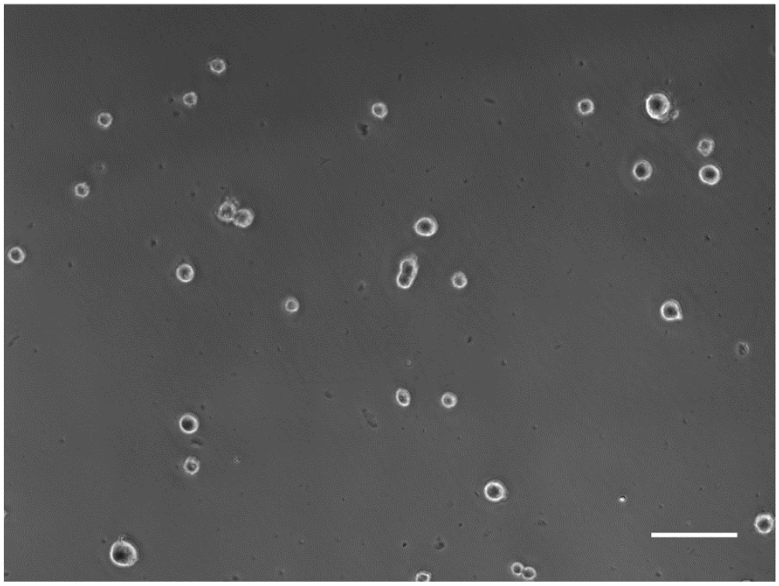

Figure S1. U-87 MG cells on HA matrix appear rounded and without cell protrusions using phase imaging with 10x magnification. Higher magnification is necessary to observe protrusions on HA matrix. Scale=100 µm.

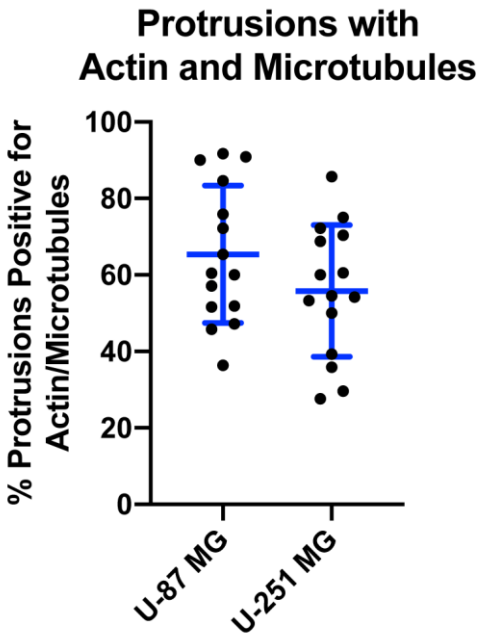

Figure S2. Percentage of protrusions positive for both actin and microtubules. N=15 total cells analyzed from 3 independent experiments. Blue lines represent mean and standard deviation.

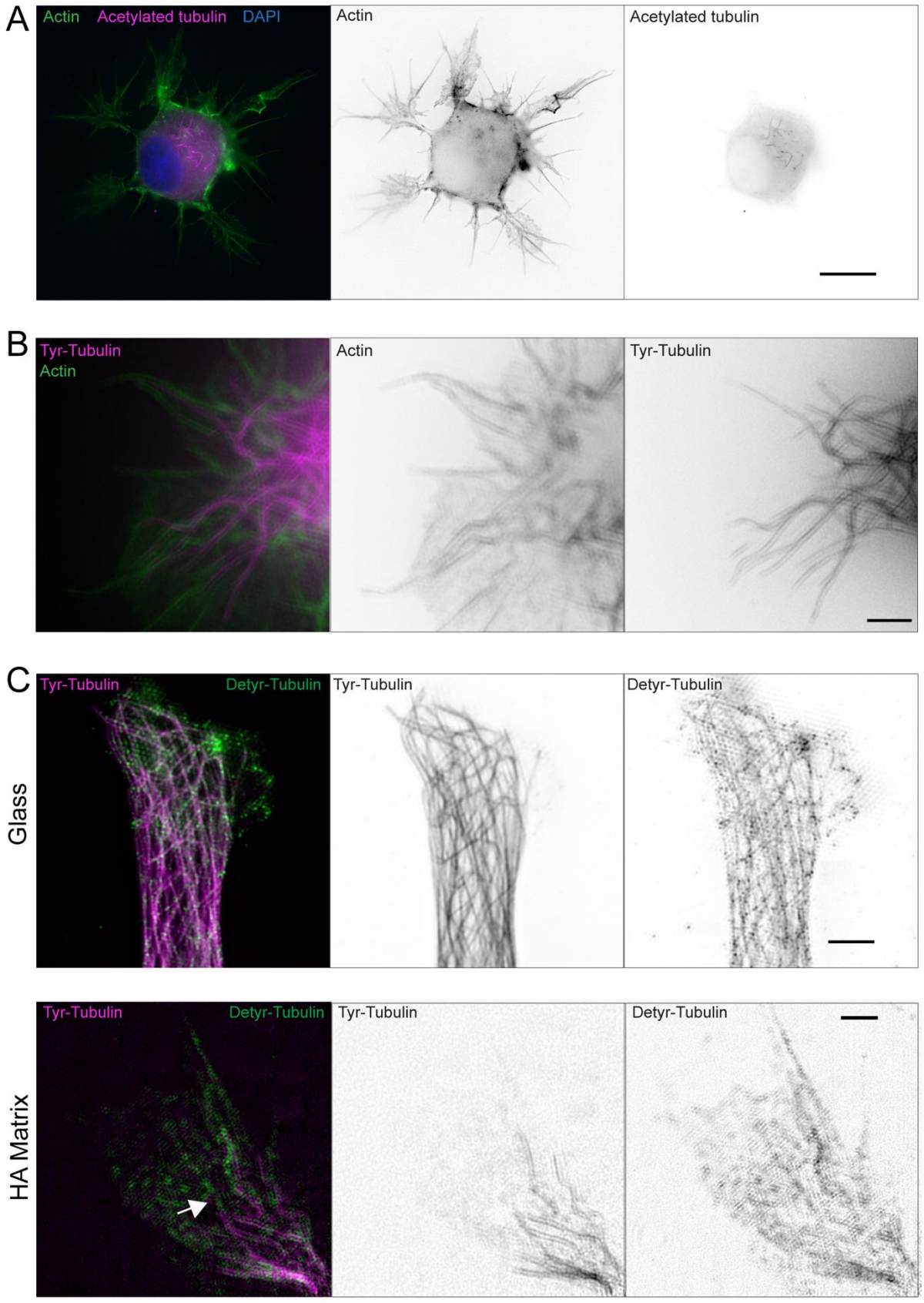
A
Actin
Acetylated tubulin
DAPI
Actin
Acetylated tubulin
B
Tyr-Tubulin
Actin
Actin
Tyr-Tubulin
C
Glass
Tyr-Tubulin
Detyr-Tubulin
Tyr-Tubulin
Detyr-Tubulin
HA Matrix
Tyr-Tubulin
Detyr-Tubulin
Tyr-Tubulin
Detyr-Tubulin

Figure S3. Post-translational modifications of tubulin in protrusions. A) Acetylated microtubules do not extend into McTNs, but rather are restricted to the cell body. Scale=10 µm. B) Tyrosinated microtubules (Tyr-tubulin) are found within protrusions. Scale=2 µm. C) On glass, detyrosinated tubulin (Detyr-tubulin) is found interspersed along tyrosinated microtubules as well as in fragmented or monomeric tubulin. On HA matrix, detyrosinated tubulin is also found interspersed along tyrosinated microtubules as well as more diffusely at the periphery of protrusions. Arrow indicates an apparent transition along a microtubule from being composed of detyrosinated and tyrosinated tubulin to being composed of detyrosinated tubulin. Scale=2 µm.

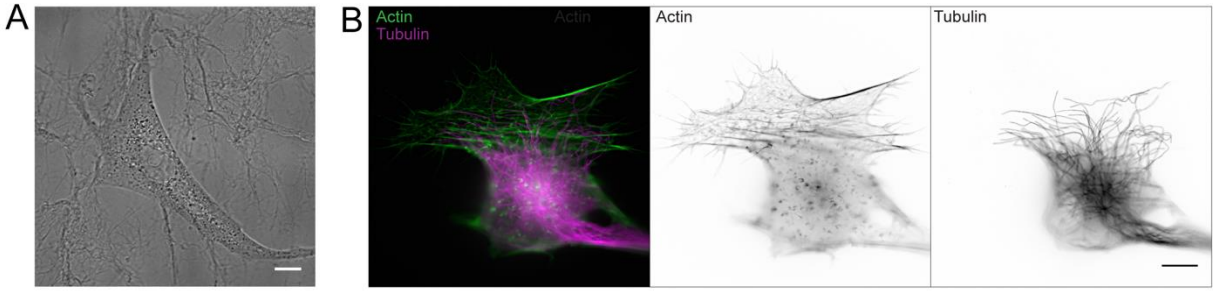

Figure S4. U-87 MG cells seeded on 2D fibrin gels. A) DIC imaging reveals cells exhibit lamellipodia. Scale=10 µm. B) SIM imaging of U-87 MG cells on fibrin reveals cells exhibit lamellipodia with thick actin bundling and without microtubules extending into actin-based protrusions. Scale=10 µm.

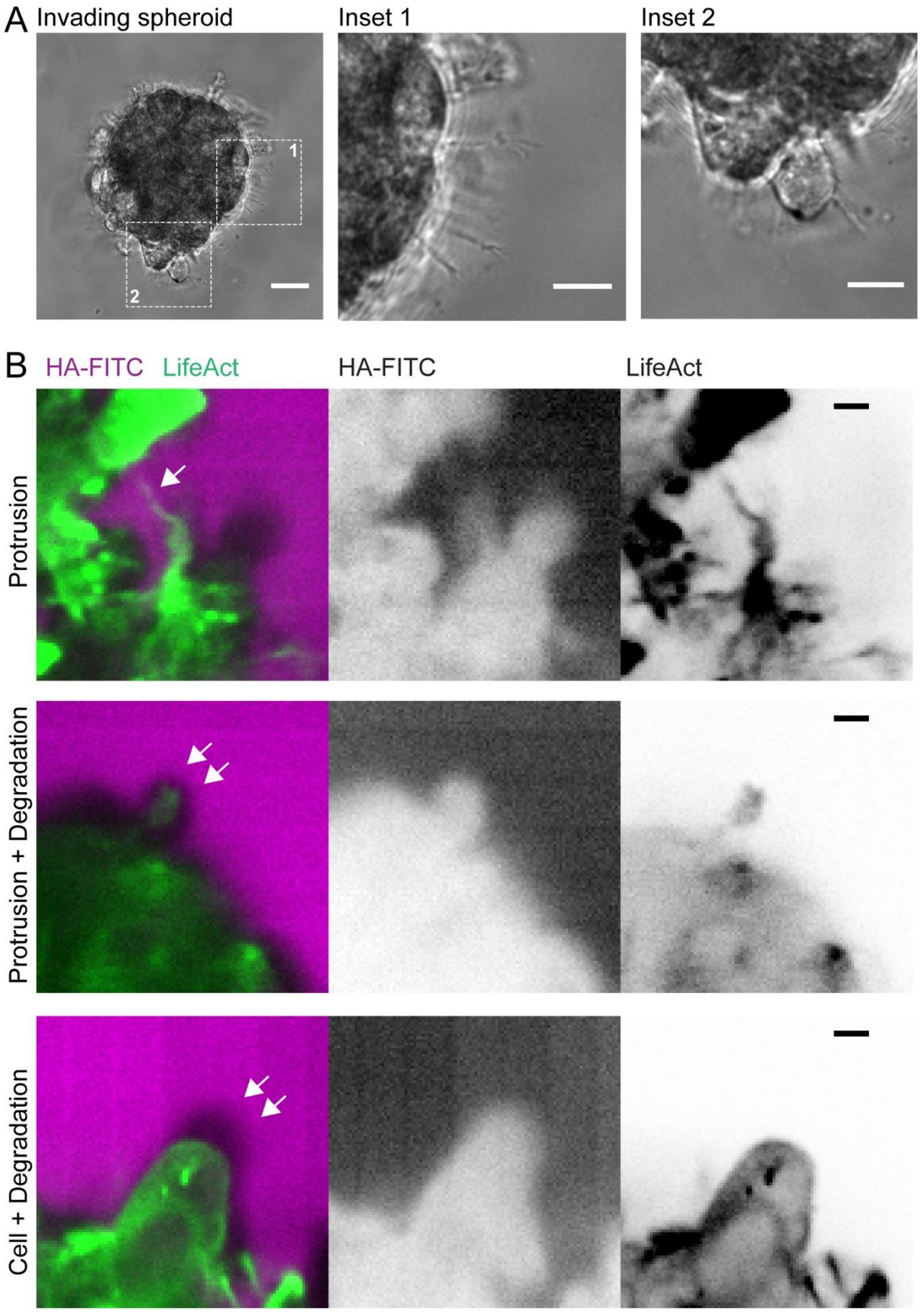
A
Invading spheroid
Inset 1
Inset 2
1
2
B
HA-FITC LifeAct
HA-FITC
LifeAct
Protrusion
Protrusion + Degradation
Cell + Degradation

Figure S5. McTNs may precede degradation into HA-matrix. A) U-251 MG spheroid cultured for 10 days in HA matrix exhibits McTNs and initial cell invasion into the matrix. Scale=20 µm. Inset 1 shows protrusions forming along spheroid periphery. Scale=10 µm. Inset 2 shows cell invasion preceded by McTN formation. Scale=10 µm. B) Confocal images of modes of invasion U-251 MG spheroids expressing GFP-tubulin and RFP-LifeAct and cultured for 10 days in HA-matrix tagged with FITC. The high intensity of HA-FITC masks the fluorescence of GFP-tubulin. Small protrusions can be seen in matrix with little degradation (single arrow). Larger protrusions are observed larger defects of matrix, and cell migration is observed only in sufficiently large HA matrix defects (double arrows). Scale=10 µm.

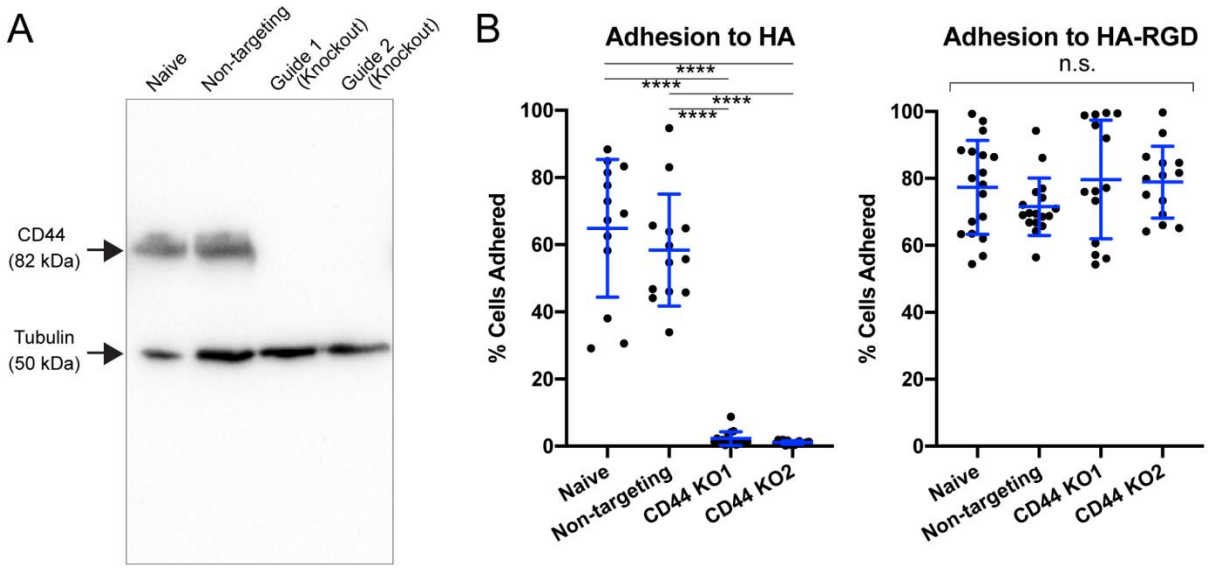

Figure S6. Validation of CD44 KO cells. A) Western blot showing U-87 MG naïve cells, non-targeting cells, and two clones with treated each with one CD44-targeting guide. Both guides gave rise to a KO. B) Centrifugal adhesion assays demonstrating that CD44 KO dramatically reduces adhesion to HA matrix but does not significantly affect adhesion to HA-RGD. N=13-18 total gels from 3 independent experiments. ****, $p<0.0001$ by ANOVA followed by Tukey-Kramer's Multiple Comparison's test. Blue lines represent mean and standard deviation.

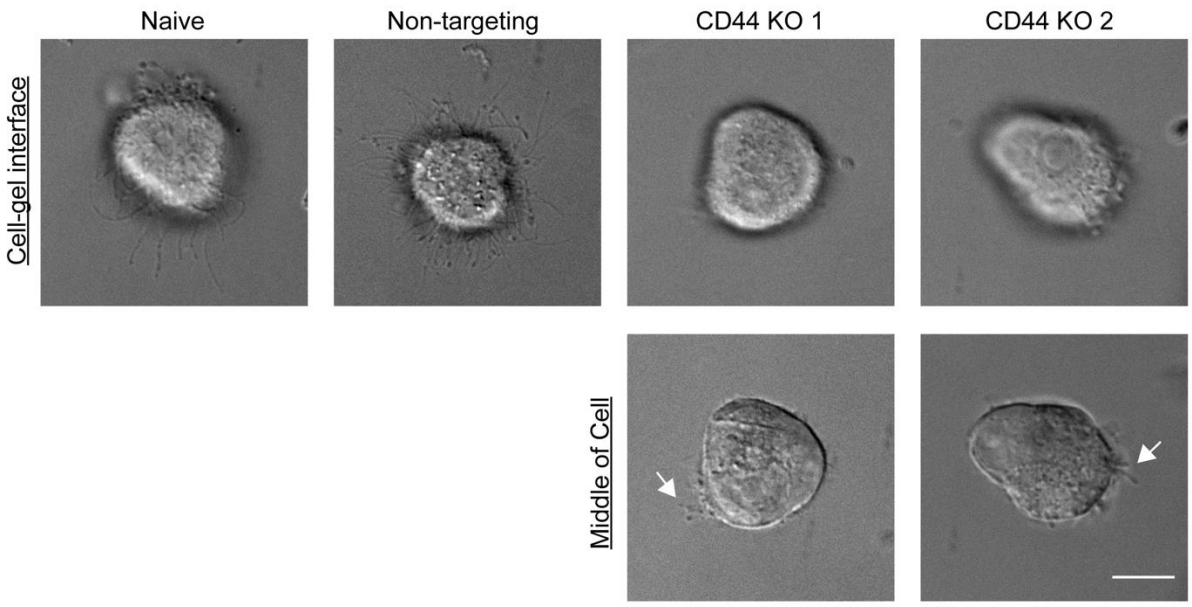

Figure S7. Cytochalasin D treatment only induces McTN growth in control cells, not CD44 KO cells. CD44 KO cells floating on HA matrix do not exhibit McTNs at the cell-gel interface. Few, short McTNs can be observed in other z-planes of the cell as indicated by white arrows. Scale=10 µm.

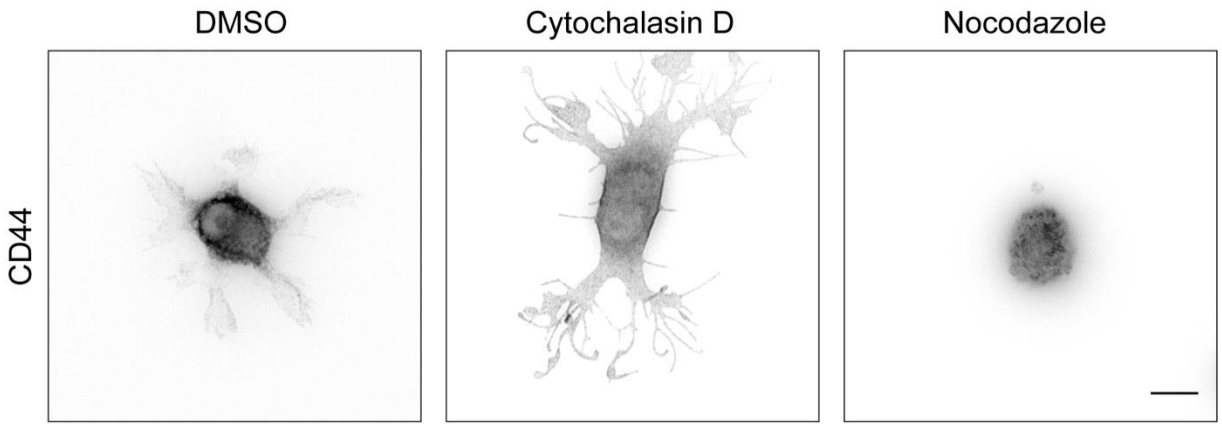

Figure S8. U-87 MG cells treated with cytochalasin D and nocodazole show similar expression pattern of CD44 as DMSO-treated control on HA-matrix at the cell-gel interface, with CD44 localized throughout the membrane. Scale=10 µm.

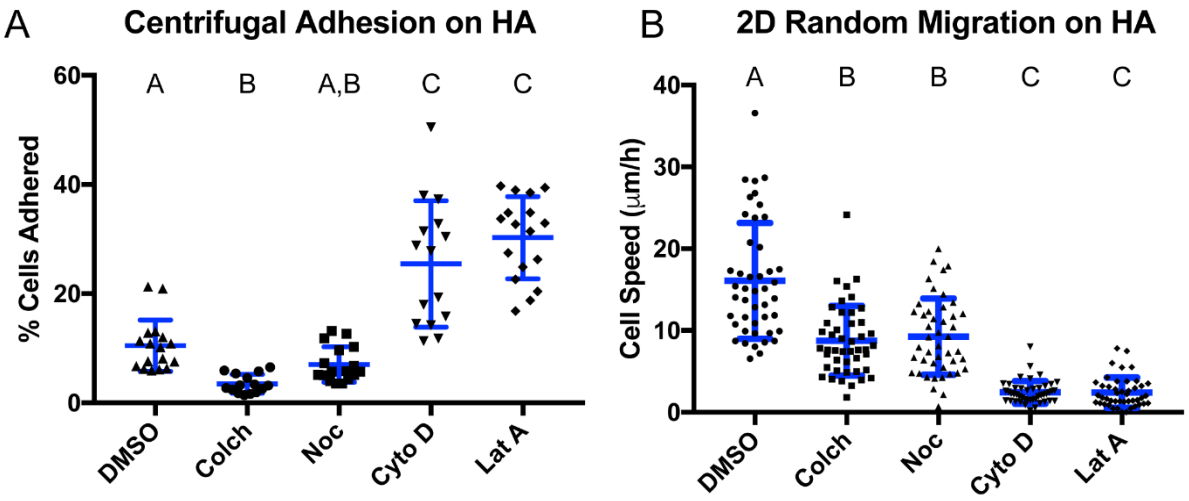

Figure S9. Actin and microtubule inhibitors have similar effects on centrifugal adhesion and 2D random migration on HA matrix in U-251 MG cells as in U-87 MG cells. A) Centrifugal adhesion assay of U-251 MG on HA matrix. N=15-17 total gels analyzed from 3 independent experiments. Letters represent statistical families with $p<0.05$ by ANOVA followed with Tukey Kramer's multiple comparison's test. Blue lines represent mean and standard deviation. B) 2D random migration speeds of U-251 MG cells on HA matrix. N=45 total cells analyzed from 3 independent experiments. Letters represent statistical families with $p<0.05$ by ANOVA followed with Tukey Kramer's multiple comparison's test. Blue lines represent mean and standard deviation.

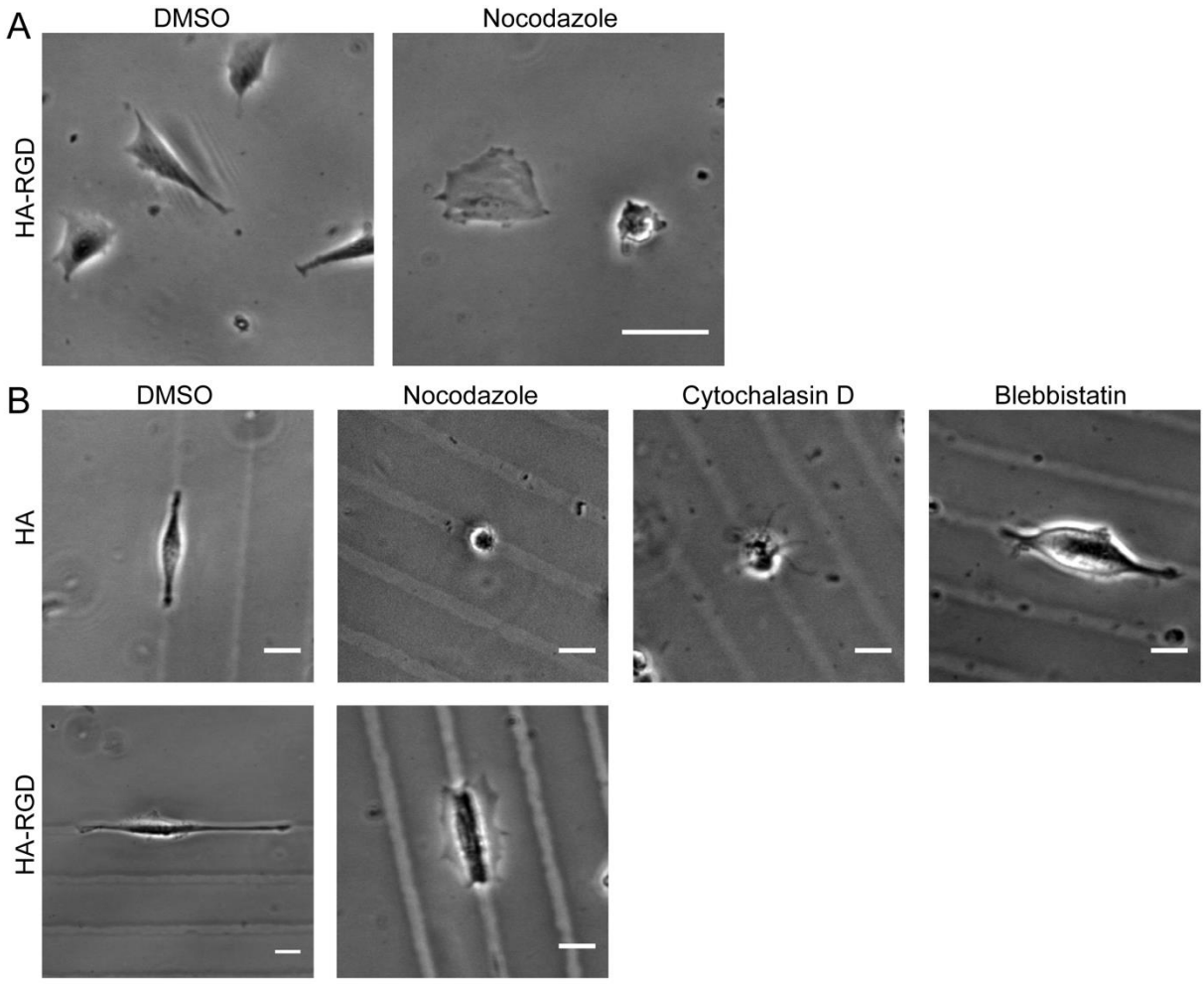

Figure S10. Morphology of cells on HA-RGD. A) Randomly migrating cells on 2D HA-RGD treated with pharmacological inhibitors. Nocodazole-treated cells show reduced spreading and polarity compared to control cells. Scale=50 µm. B) Morphology of U-87 MG cells migrating in 5 µm-wide HA or HA-RGD microchannels are affected by cytoskeletal inhibitors. Notably, nocodazole-treated cells in HA channels show dramatically reduced spreading compared to DMSO-treated controls, whereas in HA-RGD microchannels nocodazole treatment does not affect cell spreading as significantly compared to DMSO-treated controls. Cells treated with cytochalasin D induces McTN growth in all directions along the matrix. Cells treated with blebbistatin show similar spreading to controls. Scale=10 µm.

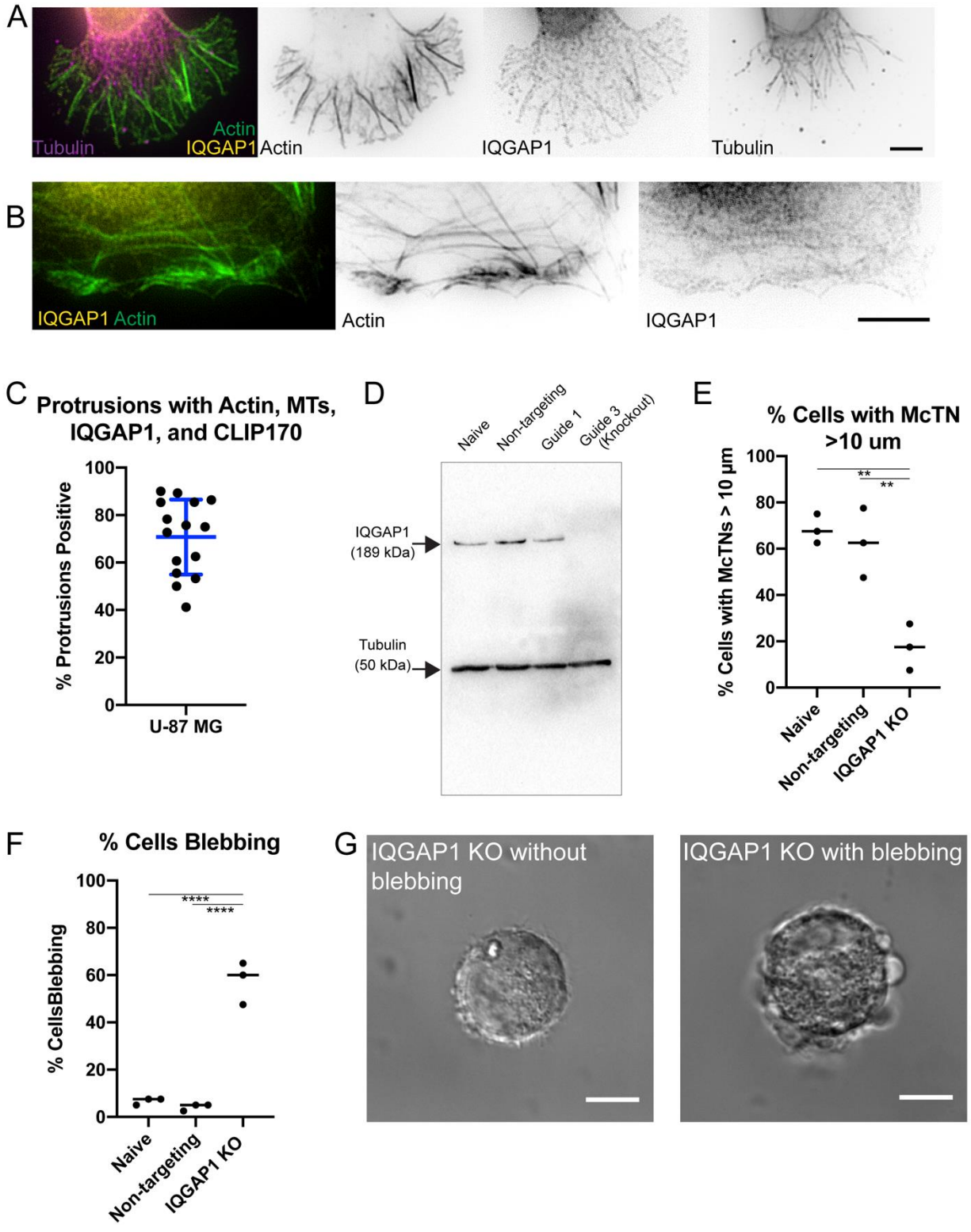

Figure S11. IQGAP1 localizes strongly to actin. A) IQGAP1 localizes strongly to actin or actin and microtubules in parallel in U-87 MG cells on HA matrix. Scale=5 µm. B) IQGAP1 also localizes strongly to actin in U-87 MG cells on HA-RGD. Scale=10 µm. C) Distribution

of percentage of protrusions positive for actin, microtubules, IQGAP1, and CLIP170 per cell on HA matrix. Each point represents one cell. N=15 total cells were analyzed from 3 independent experiments. D) Validation of IQGAP1 KO by Western blot. E) McTN length of U-87 MG cells on HA matrix was analyzed and categorized based on whether the cell exhibited any McTNs greater than 10 µm in length. Each point represents the fraction of 40 cells with McTNs greater than 10 µm in length for N=3 independent experiments. **p<0.01 by ANOVA followed by Tukey-Kramer's Multiple Comparison's test. Blue lines represent mean and standard deviation. F) U-87 MG cells were categorized based on whether the cell exhibited any McTNs greater than 10 µm in length. Each point represents the percentage of 40 cells with blebbing for N=3 independent experiments. **p<0.01 by ANOVA followed by Tukey-Kramer's Multiple Comparison's test. Blue lines represent mean and standard deviation. G) DIC imaging of example U-87 MG IQGAP1 KO without and with blebbing. Scale=10 µm.

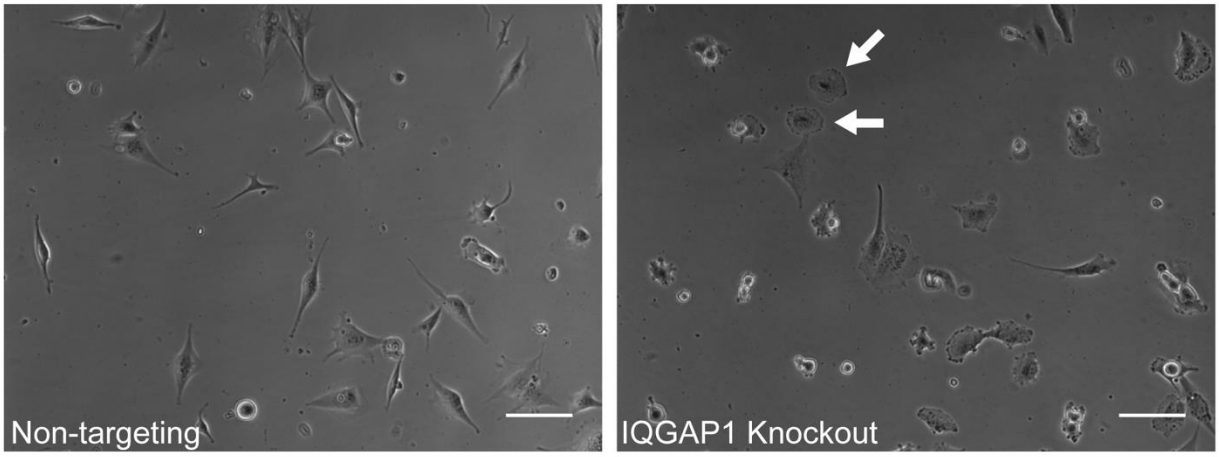

Figure S12. IQGAP1 KO cells compared to non-targeting controls on HA-RGD. IQGAP1 KO cells are less polarized and exhibit larger lamellipodia. Arrows point to circular, non-polarized cells. Scale=100 µm.

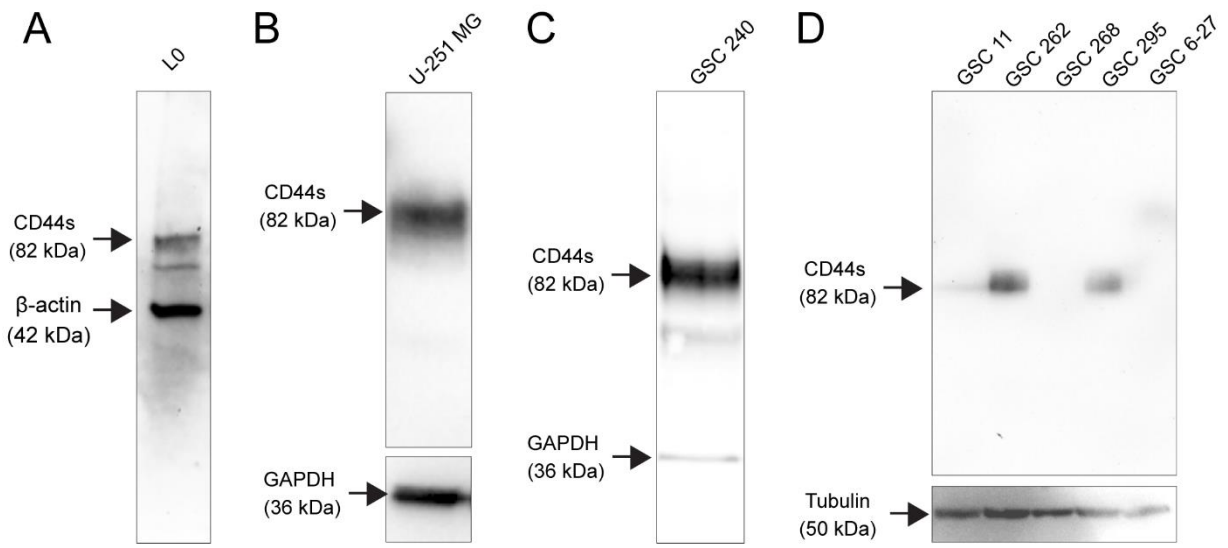

Figure S13. GBM continuous and stem cell lines express detectable levels of CD44s except GSC 268 and GSC 6-27. A) L0 cells show possible degradation product. B) U-251 MG cells express CD44s. Blot was probed initially for CD44, stripped, and probed for GADPH. C) GSC 240 cells express CD44s and possible degradation product. D) GSC 11, GSC 262, and GSC 295 cells express CD44s. GSC 268 and GSC 6-27 do not express detectable levels of CD44. Blot was probed for CD44, stripped and probed again for tubulin.

Table S1: Resources and Reagents

REAGENT or RESOURCE	SOURCE	IDENTIFIER
Antibodies		
Rabbit polyclonal anti-CD44	Thermo Fisher Scientific	Cat#PA5-21419; RRID: AB_11155593
Rabbit polyclonal anti-IQGAP1	Abcam	Cat#ab86064; RRID: AB_1925119
Mouse monoclonal anti-tubulin-α Ab-2 (clone DM1A)	Thermo Fisher Scientific	Cat#MS-581-P1ABX; RRID: AB_144075
Polyclonal rabbit anti-MYO10	Sigma-Aldrich	Cat#HPA024223; RRID: AB_1854248
Polyclonal goat anti-CLIP170	Novus Biologicals	Cat#NBP1-36749; RRID: AB_2082120
Monoclonal mouse anti-β-actin-peroxidase	Signa-Aldrich	Cat#A3854; RRID: AB_262011
Mouse monoclonal anti-CD44	R&D Systems	Cat#BBA10; RRID: AB_356933
Mouse monoclonal anti-tubulin, tyrosine	Millipore Sigma	Cat#T9029; RRID: AB_261811
Rabbit polyclonal anti-tubulin, detyrosinated	Millipore Sigma	Cat#AB3201; RRID: AB_177350
Mouse monoclonal anti-acetylated tubulin	Millipore Sigma	Cat#T7451; RRID: AB_609894
Mouse monoclonal anti-GAPDH (clone GAPDH 71.1)	Sigma-Aldrich	Cat#G8795; RRID: AB_1078991
Goat anti-Rabbit IgG (H+L) Secondary Antibody, HRP	Thermo Fisher Scientific	Cat#65-6120; RRID: AB_2533967
Goat anti-Mouse IgG (H+L) Secondary Antibody, HRP	Thermo Fisher Scientific	Cat#62-6520; RRID: AB_2533947
Goat anti-Mouse IgG (H+L) CF568	Biotium	Cat#20100; RRID: AB_10559038
Goat anti-Mouse IgG (H+L) Cross-Adsorbed Secondary Antibody, Alexa Fluor 488	Thermo Fisher Scientific	Cat#A-11001; RRID: AB_2534069
Goat Anti-Rabbit IgG H&L (Chromeo™ 546) (ab60317)	Abcam	Cat#ab60317; RRID: AB_954976
Goat anti-Rabbit IgG (H+L) Secondary Antibody, Alexa Fluor 488	Thermo Fisher Scientific	Cat#R37116; RRID: AB_2556544
Goat anti-Mouse IgG (H+L) Secondary Antibody, Alexa Fluor 405	Thermo Fisher Scientific	Cat#A-31553; RRID: AB_221604

Polyclonal donkey anti-goat IgG (H+L) Secondary Antibody, Alexa Fluor 568	Thermo Fisher Scientific	Cat#A11057; RRID: AB_2534104
Polyclonal goat anti-Mouse IgG (H+L) Secondary Antibody, Alexa Fluor® 647 conjugate	Thermo Fisher Scientific	Cat#A21235; RRID: AB_2535804
Goat Anti-Rabbit IgG H&L (Alexa Fluor® 647)	Abcam	Cat#ab150079; RRID: AB_2722623
Bacterial and Virus Strains		
Virus: LentiBrite™ GFP-Tubulin lentiviral Biosensor	Millipore Sigma	Cat#17-10206
Virus: RFP-LifeAct in pFUG-IP lentiviral backbone	Lee et al. Biomaterials 2016	N/A
Bacteria: NEB 5-alpha E. coli (high efficiency)	New England Biosciences	Cat#C2987
Chemicals, Peptides, and Recombinant Proteins		
Alexa Fluor® 647 Phalloidin	Cell Signaling Technology	Cat#8940S
Alex Fluor 546 Phalloidin	Thermo Fisher Scientific	Cat#A22283
Acti-stain 488 phalloidin	Cytoskeleton, Inc.	Cat#PDHG1
4′,6-Diamidine-2′-phenylindole dihydrochloride (DAPI)	Sigma-Aldrich	Cat#10236276001
Glutaraldehyde	Electron Microscopy Sciences	Cat#16310
Methacrylic Anhydride	Sigma-Aldrich	Cat#276685
Poly-L-Lysine Hydrobromide	Sigma-Aldrich	Cat#P1274
Viafect Transfection Reagent	Promega	Cat#E4981
Sodium Pyruvate	Thermo Fisher Scientific	Cat#11360070
MEM Non-Essential Amino Acids Solution	Thermo Fisher Scientific	Cat#11140050
Penicillin/Streptomycin	Thermo Fisher Scientific	Cat#15140
Fetal Calf Serum	JR Scientific	Cat#44709
Trypsin-EDTA 0.25%, phenol red	Thermo Fisher Scientific	Cat#25200
Dulbecco’s Modified Eagle Medium (DMEM)	Thermo Fisher Scientific	Cat#11965118
Sodium borohydride	Spectrum Chemical	Cat#S1187
Sodium Hyaluronate, 66 kDa - 99 kDa	Lifecore	Cat#HA60K-5

ICT Accutase Cell Detachment Solution	Innovative Cell Technologies	Cat#AT104
Dulbecco's Modification of Eagle's Medium/Ham's F-12 50/50 Mix (DMEM/F12)	Corning	Cat#10-090-CV
Fibroblast growth factor (FGF)	R&D Systems	Cat# 233-FB-025/CF
B-27 Supplement	Gibco	Cat#17504-044
Epidermal growth factor (EGF)	R&D Systems	Cat# 236-EG-01M
RGD Peptide (Ac-GCGYGRGDSPG-NH2)	Anaspec	N/A
Goat serum	Thermo Fisher Scientific	Cat#16210064
Bovine Serum Albumin, heat shock fraction, pH 7, >=98%	Sigma-Aldrich	Cat#A9647
Triton X-100	Sigma-Aldrich	Cat#X100
Dithiothreitol (DTT)	Thermo Fisher Scientific	Cat#FERR0861
DMEM, high glucose, no glutamine, no phenol red	Thermo Fisher Scientific	Cat#31053028
SuperSignal West Dura Chemiluminescent Substrate kit	Thermo Fisher Scientific	Cat#34076
Radioimmunoprecipitation assay buffer (RIPA)	Sigma-Aldrich	Cat#R0278
Sodium fluoride	Sigma-Aldrich	Cat#215309
Sodium molybdate	Sigma-Aldrich	Cat#737860
4-12% bis-tris gels	Life Technologies	Cat#NP0335BOX
PVDF Pre-cut Blotting Membranes, 0.2 µm	Life Technologies	Cat# LC2002
Paraformaldehyde	Alfa Aesar	Cat#43368-9M
Blebbistatin	Sigma-Aldrich	Cat#B0560
ML-141 Inhibitor	R&D Systems	Cat#4266
Latrunculin A	Cayman Chemical	Cat#10010630;
Cytochalasin D	Sigma-Aldrich	Cat#C8273
Colchicine	Sigma-Aldrich	Cat#C9754
Nocodazole	Cell Signaling Technology	Cat#2190
Cytoseal 60	Thermo Fisher Scientific	Cat#8310
Glucose oxidase	Sigma-Aldrich	Cat#G2133
Catalase	Roche Applied Science	Cat#106810

Cysteamine	Sigma-Aldrich	Cat#M9768
Fibrinogen	Millipore Sigma	Cat#F8630
Thrombin	Millipore Sigma	Cat#T9549
SU-8 3005 photoresist	MicroChem Corporation	SU-8 3005
PDMS/crosslinker Sylgard 184 Silicone Elastomer kit	Dow Corning	DC4019862
FITC-cysteine	Genscript	NA
Experimental Models: Cell Lines		
Human glioblastoma: U-87 MG (male)	University of California, Berkeley Tissue Culture Facility	RRID: CVCL_0022
Human glioblastoma: U-251 MG (male)	University of California, Berkeley Tissue Culture Facility	RRID: CVCL_0021
Human glioblastoma: GSC-20 (previously classified as mesenchymal subtype)	MD Anderson Cancer Center[152]	NA
Human glioblastoma: GSC-11 (previously classified as proneural subtype)	MD Anderson Cancer Center[507]	NA
Human glioblastoma: L0 (previously classified as classical subtype)	Previously obtained from Dr. Brent Reynold's lab[72]	NA
Human glioblastoma: GSC-28 (previously classified as mesenchymal subtype)	MD Anderson Cancer Center[152]	NA
Human glioblastoma: GSC-262 (previously classified as proneural subtype)	MD Anderson Cancer Center[152]	NA
Human glioblastoma: GSC-295 (previously classified as proneural subtype)	MD Anderson Cancer Center[152]	NA
Human glioblastoma: GSC-267 (previously classified as mesenchymal subtype)	MD Anderson Cancer Center[152]	NA
Human glioblastoma: GSC-268 (previously classified as classical subtype)	MD Anderson Cancer Center[152]	NA

Human glioblastoma: GSC6-27 (previously classified as classical subtype)	MD Anderson Cancer Center[152]	NA
Human glioblastoma: GSC-248 (previously classified as proneural subtype)	MD Anderson Cancer Center[152]	NA
Experimental Models: Organisms/Strains		
Mouse (NOD.Cg-prkdc scidil2) *ex vivo* tissue culture slice, female, age 18 months	The Jackson Laboratory	Cat#005557
Oligonucleotides		
Table S2		
Recombinant DNA		
pSpCas9(BB)-2A-GFP (PX458)	Addgene	Plasmid#48138
Software		
ImageJ	NIH	https://imagej.nih.gov/ij/
GraphPad Prism Version 8.0.2 (159)	GraphPad	https://www.graphpad.com
Zen 2010	Zeiss	https://www.zeiss.com/microscopy/us/products/microscope-software/zen.html
PrairieView Software v. 5.3 U3	Bruker	https://www.bruker.com/products/fluorescence-microscopes/ultima-multiphoton-microscopy.html
Other		
Transwell inserts, sterile, 5.0 µm pore polyester membrane	Corning	Cat#8600A59
Silicon Wafer	WaferNet	S45065
Anton Paar Physica MCR 310 Rheometer	Anton Paar	https://www.anton-paar.com
ChemiDocXRS+ molecular imager	Bio-Rad	http://www.bio-rad.com/en-us/product/chemidoc-xrs-

		system?ID=NINJHRKG4
35 mm Dish, No. 0 Coverslip, 20 mm Glass Diameter, Uncoated	MatTek Corporation	Cat#P35G-0-20-C

Table S2. Primers used to incorporate guide RNA sequences into PX458 backbone.

	Forward Guide 5'-3'	Reverse Guide 5'-3'
Non-targeting	CACCGGCACTACCAGAGCTAACTCA	AAACTGAGTTAGCTCTGGTAGTGCC
CD44-1	CACCGAATATAACCTGCCGCTTTGC	AAACGCAAAGCGGCAGGTTATATTC
CD44-2	CACCGATCCAGGGACTGTCTTCGTC	AAACGACGAAGACAGTCCCTGGATC
IQGAP1-1	CACCGCAGCCCGTCAACCTCGTCTG	AAACCAGACGAGGTTGACGGGCTGC
IQGAP1-2	CACCGACGAGGCGCGATTTTCCTGG	AAACCCAGGAAAATCGCGCCTCGTC
IQGAP1-3	CACCGCCCGTCAACCTCGTCTGCGG	AAACCCGCAGACGAGGTTGACGGGC